Universität der Bundeswehr München

Dissertation

On Mechanical Shear-Models in Reinforced and Prestressed Concrete Constructions

By
Thomas Hertle

On Mechanical Shear-Models in Reinforced and Prestressed Concrete Constructions

Thomas Hertle

Vollständiger Abdruck der von der Fakultät für Bauingenieurwesen und Umweltwissenschaften der Universität der Bundeswehr München zur Erlangung des akademischen Grades eines

Doktor-Ingenieurs
- Dr.-Ing. -

genehmigten Dissertation.

Gutachter:

1. Prof. Dr.-Ing. habil. Norbert Gebbeken (EE)
2. Univ.-Prof. Dr.-Ing. Dipl.-Wirt. Ing. Oliver Fischer
3. Univ.-Prof. Dr.-Ing. Jürgen Feix

Die Dissertation wurde am 10. Februar 2023 bei der Universität der Bundeswehr München eingereicht und durch die Fakultät für Bauingenieurwesen und Umweltwissenschaften am 02. September 2023 angenommen. Die mündliche Prüfung fand am 27. November 2023 statt.

Abstract

Advancement of standards is generally assumed to be one of two things. Either the introduction of more efficiency into the prediction, or the eradication of previously unknown and unwanted effects. Both are strived for and welcomed by the community, as it allows for the reduction of material and cost, while ensuring the required degree of safety. This, however, can not be said for the development of the shear verification method of reinforced and/or prestressed concrete slender beams. The latest chapter of this development being written by the Eurocode 2, where the partaking of the concrete compression zone, amongst other influences, in the shear-bearing capacity of said specimens is neglected, leading to far higher conservatism in design. Since neither damages or failures nor new research results exist, pointing towards an unsafe design prior to it, this increased safety is not warranted. Therefore the following work aims to showcase the impact, strength and weaknesses and reasoning of the current design standards as well as provide a design approach, incorporating multiple shear-bearing mechanisms, that mimics reality more closely.

Facing the challenge of having biased test databases, leaning strongly on single span test setups under concentrated loads, basically eliminating interactions of normal and shear stresses, as well as small cross-sections, a numerical modelling approach is developed. It is validated against tests reported in literature and allows for a more precise investigation as well as acknowledgement of certain parameters, when being compared to physical testing. Further on it is used to create a set of tests in accordance to the *Design of Experiments*, allowing assertions about the dependence of the test results on individual variables. The modelled test setup aims to represent bridge girders at intermediate supports, as research shows large discrepancies between the calculable critical load for the old and new standards at these points. Spotlighted variables consist of the span length, the slenderness and the transverse reinforcement ratio. Especially the allocable independence of the predicted critical load from the transverse reinforcement ratio in case of compression stresses, resulting from bending or prestressing, coinciding with the large shear stresses shows the inability of the currents design standard to correctly predict the physical behaviour of the reinforced and/or prestressed concrete slender beams. Furthermore the interaction of the overlapping point of large normal stresses and large shear stresses partaking in this effect needs to be stated.

Based on these findings an engineering model approach is developed, accounting for the partaking of the uncracked concrete compression zone in the shear-bearing mechanisms, in form of the compression arch with tension chord. Interaction of bending moment and transverse forces is ensured by the model via the shape of the compression arch and the coupling of the individual systems via the deformation. This ensures a stiffness dependency

of the model, which is used to allocated the load onto the individual systems. Partaking of the transverse reinforcement is covered by a smeared truss system, similar to the one in Eurocode 2. The applicability of the approach is determined on basis of compatibility of deformation.

For evaluation of the engineering model approach, the deformation of the smeared truss at its individual load-bearing capacity is taken and applied to the compression arch with tension chord, resulting in an additional load, that the combined system is able to bear, before reaching the failure load of the smeared truss subsystem. In coupling these subsystems in this way, the physical behaviour of the beam is mimicked. In this the engineering model approach differentiates itself from many existing shear models, which more often than not add individual load-bearing mechanisms, that are mostly assumed to be indifferent to each other as well as the actual physical behaviour of the specimen they attempt to predict.

Due to its stress dependency, aka the acknowledgement of stress interactions, the ratio of the load-bearing capacities of the two subsystems are dependent on the structural system as well as the loading. This is the major difference to the current design standards, which does not account for this effect due to it being grounded on a biased test database.

Zusammenfassung

Im Allgemeinen gibt es zwei mögliche Ursachen für die Weiterentwicklung von Normen. Entweder die Verbesserung der Vorhersage, oder die Reduzierung von zuvor unbekanntem und ungewolltem Verhalten. Jede davon ist von der Ingenieursgemeinschaft erwünscht, und ermöglicht eine effiziente Material- und Kostengestaltung im Rahmen der geforderten Sicherheitsanforderungen. Diese Maxime trifft jedoch nicht auf den Querkraftnachweis von schlanke Stahlbeton- oder Spannbetonbalken zu. In der aktuellen Fassung des Eurocodes liefert der Querkraftnachweis durch die Vernachlässigung der Betondruckzone verstärkt konservative Ergebnisse im Vergleich zu den Nachweisen, welche gegen Ende des 20. Jahrhunderts gegolten haben. Da weder bekannte Schäden oder Einstürze noch neue Forschungsergebnisse vorliegen, ist die somit gewonnene Sicherheit nicht begründbar, sondern führt vor allem im Zuge von Nachrechnungen zu erheblichen Problemen oder unnötigen von Verstärkung. Aus diesem Grund zeigt die vorliegende Arbeit den Einfluss, die Stärken und Schwächen als auch die Begründung des derzeitig gültigen Nachweises auf und stellt ein Nachweisverfahren vor, welches mehrere Querkrafttragmechanismen vereint und somit die Realität besser abbildet als der derzeit gültige Eurocode.

Für die Untersuchung einzelner Parameter wird ein numerisches Modell entwickelt, welches anhand von Versuchen aus der Literatur validiert wird. Somit wird die Abhängigkeit der folgenden Auswertung von Versuchsdatenbanken, welche hauptsächlich auf Versuchen an Einfeldträgersystemen unter Einzellasten und geringen Querschnittsabmessungen beruhen, vermieden und schwierig realisierbare Versuchszusammenstellungen ermöglicht. Mit dem numerischen Modell wird eine Versuchsreihe nach den Empfehlungen des *Design of Experiments* entwickelt, wodurch Aussagen bezüglich der Abhängigkeiten der Versuchsergebnisse von einzelnen Parametern ermöglicht wird. Als statisches System wird ein einseitig eingespannter Einfeldträger gewählt, da dieser die Situation an einem Zwischenauflager gut wiederspiegelt. Ausschlaggebend dafür ist die oft festgestellte starke Abweichung zwischen den Ergebnissen nach alten und neuen Bemessungsansätzen an diesen Stellen. Die Abhängigkeit der Versuchsergebnisse von den Parametern Spannweite, Schlankheit und Querkraftbewehrungsgrad werden im Detail untersucht. Es kann vor allem festgestellt werden, dass die numerisch berechneten Versagenslasten, unter der gewählten Situation, weitestgehend unabhängig von dem Querkraftbewehrungsgrad sind. Dies weist eine starke Diskrepanz zum derzeitig gültigen Nachweisverfahren für schlanke Stahlbeton- und Spannbetonbalken auf, welches maßgeblich auf diesem Parameter beruht. Ursächlich hierfür ist unter anderem eine Interaktion von Normal- und Schubspannungen, welche in den gängigen Nachweisverfahren nicht berücksichtigt wird.

Basierend auf diesen Ergebnissen wird ein Ingenieurmodell entwickelt. Hierfür wird ein

Betondruckbogenmodell mit Zugband mit dem gängigen verschmierten Fachwerkmodell gekoppelt. Somit wird neben der Querkraftbewehrung auch der ungerissene Betonquerschnitt für die Lastabtragung berücksichtigt. Die Spannungesinteraktion von Normal- und Schubspannungen wird hierbei hauptsächlich vom Druckbogen übernommen, da seine Formgebung und somit die Steifigkeit davon beeinflusst wird.

Für die Auswertung des Ingenieurmodells, wird vereinfacht die Tragfähigkeit des Fachwerkmodells als Modellbestimmend angenommen. Die Verformung, welche das Fachwerkmodell unter dieser Last erfährt, wird auf den Druckbogen angewendet. Die dafür benötigte Kraft wird zusätzlich zu der kritischen Last des Fachwerkmodells angesetzt. Durch diesen Ansatz wird das physische Verhalten des Balkens durch die zwei darin angesetzten Subsysteme nachgestellt. Hierdurch unterscheidet sich der Ansatz des Ingenieurmodells von vielen existierend Querkraftmodellen, welche meistens eine Aufaddierung verschiedener Tragmechanismen ansetzen, welche im Allgemeinen als untereinander ebenso wie Realität unabhängig betrachtet werden.

Durch die Spannungs- und somit Steifigkeitsabhängkeit des entwickelten Ingenieursmodells wird die Traglastaufteilung auf die zwei Tragmechanismen (Druckbogen und Fachwerk) direkt von Belastungsart und statischem System abhängig. Hierin liegt auch der größte Unterschied zu den aktuell gängigen Nachweisverfahren, welche auf die begrenzte Varianz der Versuchsdatenbaken zurückgehen.

Contents

1. Introduction

1.1. Motivation

Society's highest priority should always be a responsible and sustainable handling of its resources. One major portion of these resources can be found in the building infrastructure. Ranging from transporting infrastructure over power plants to hospitals, schools and governmental buildings, this building infrastructure can be seen as the backbone of modern society. Hence the maintenance of it is vital, but expensive and therefore an efficient allocation of resources is necessary. In light of this, enabling and continued use of existing infrastructure is most of the time preferable to rebuilding, cutting not only costs but also construction surrounding impacts and disruptions.

Enabling structures to last its intended and designed for life-expectancy, or even surpassing it is however easier said than achieved. While the design philosophy always has set life-expectancies for different types of structures, the rules and regulations always account for knowledge and boundary conditions of their time. Hence, with changing standards, the need for reevaluation of the existing infrastructure arises. In case of Germany this last major upheaval happened with the introduction of the Eurocodes in the early 2010s. In this context, special attention was paid to reinforced and prestressed concrete bridges, sporting 86.0% of bridges of the long-distance road-network in Germany [12]. Reasons behind this lie in the combination of updated design loads (EC1 [40]) and a change in the design approach for shear-bearing capacity (EC2 [41]). Some early research [52, 69] shows that nearly 60% of the investigated bridges did not conform to the requirements set by the new standards, when being recalculated. Most of the blame for this can be directed towards the fundamental changes in the design approach, rather than changing load models. Reasoning behind this can be found in the composition of the acting forces on the bridge. Generally speaking reinforced and prestressed concrete bridges require the majority of their load-bearing capacity to carry their own dead load. In light of the approximately 75 – 80% load-bearing capacity being reserved for this type of loading, an increase of the remaining acting loads, namely the design load model of vehicles, has a diminishing effect. This can be seen by the lack of calculable differences concerning bending [52]. Therefore the main culprit for the shear strength dilemma has to be the changed design approach, further supported by the lack of damages and failures on reinforced and prestressed concrete bridges in Germany due to shear.

Since the apparent discrepancies, when facing the recalculation of reinforced and prestressed concrete specimens in accordance with the Eurocodes (EC2 [41]) lie in the shear design methodology, a short recapture of its development and the inherent difficulties is in

order. While being largely disregarded in the first half of the 20^{th} century, research into the shear-bearing capacity was jump-started by two similar collapses of US Air Force warehouses in the mid 1950s [46]. The prolonged interest in this topic is documented by figure 1.1, where the number of shear tests on concrete beams over a nearly 60 year span are documented.

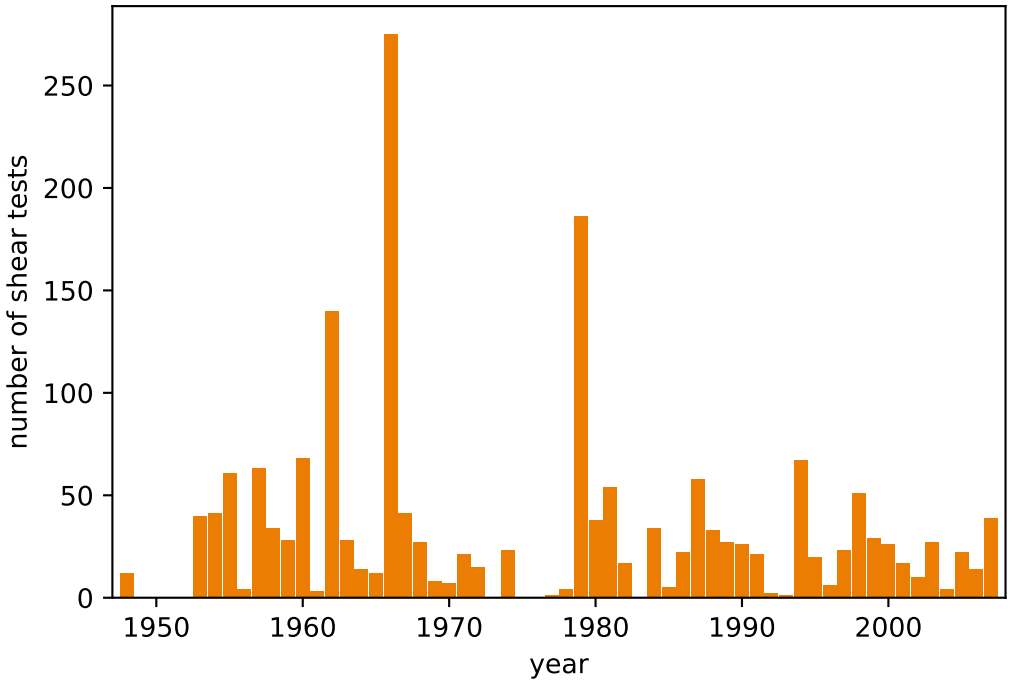

Figure 1.1.: Number of shear tests on concrete beams with and without reinforcement in terms of publication date as provided in [31]

Sparking a number of shear models and design approaches, like the smeared truss analogy, compression field models or fraction mechanic models, this longevity of shear testing did not manage to solve the riddle of shear in reinforced or prestressed concrete specimens satisfactorily. Figuratively for this, tests showcasing the critical failure load being more than double of the calculated expected failure load in accordance with the applicable standards exist [59]. Similar conclusions can be reached by the calculable shortcoming of the existing infrastructure not evidencing themselves in sizeable damage, linked to prolonged overloading, or a near failure loading [51, 64].

Pinpointing the reasoning for this proves to be challenging. The simple answer of the change in design philosophy needs to be further investigated to allow for improvement of the status quo. A starting point can be gathered from `Fischer` et al. [52], who highlighted the intermediate supports of multi-span girders as a point of special interest regarding differences in the amount of present shear reinforcement and the by recalculation required

amount of it for existing bridges. Hence recent research into prestressed concrete slender beams [78, 156] suggests a return to the partition of failure zones as previously supported by the DIN 4227 [39], the predecessor of the EC2 [41]. Circumventing the inability of the design approach to account for stress interactions, based on evaluation of biased tests.

This biased testing can be seen in the 2200+ shear tests on reinforced concrete beams with and without shear reinforcement that were conducted over the last 70 years [139, 140], being predominantly single-span test setups subjected to concentrated loads. While a lot of information could be gained from these tests, ranging from aggregate interlock and dowel action to shear-slenderness and size effect, the interaction of large normal stresses and large shear stresses was overlooked. Furthermore an abundance of beams with a height of less than 40.0 *cm* has to be noted, which do not represent most shear-critical beams, especially for wide spanning structures like bridges, where the main girders are usually exceeding 150.0 *cm*. Even so these circumstances are relatable due to limitations resulting from the equipment and the practicability, their shortcomings in reflecting reality need to be recognised and addressed. For this reason large scale tasting has become more prominent in the recent years, incorporating different boundary conditions like clamped supports [50, 53, 60, 61, 78, 81, 128, 156].

Tackling these aspects seems necessary to create a better understanding of shear within reinforced and prestressed concrete specimens, combining and embracing load interactions, rather than subdividing them. Only then the design methods are able to better predict the physical behaviour of the real life specimen and unintended conservatism can therefore be reduced.

1.2. Objective of Work and Unique Selling Points

As mentioned in the motivation, today's engineering standards concerning reinforced concrete beams are mostly based on tests, that do not reflect the reality satisfactorily. While distributed loads are difficult to achieve in test setups due to experimental limitations, they are the majority of loads used in today's design. Furthermore the neglecting of interactions of the internal stress distribution due to the abundance of similarly designed tests with regard to the structural system needs to be addressed. Achieving a good predictability resulting from test series has always been one of the challenges in designing experiments, either sacrificing broad applicability by focusing on singular influences, or informative value due to limitations on tests not being able to either cover each individual variable satisfactorily or combining variables resulting in an indistinguishability on the individual influences. To combat this, modern methods of the so called *Design of Experiments* (DoE) can be employed, enabling the minimisation of physical tests by extending them with computer simulations. By a lack of physical experiments in the scope of this work, the DoE approach is performed purely numerically. The numerical model and simulation are evaluated against tests taken from the literature, showcasing the validity of this approach.

To advance towards solving the riddle of shear a more thorough investigation into not only

material investigations of failure mechanisms, but also structural load-bearing mechanisms and stress-paths within the specimen need to be performed. In this context the developed and introduced shear model approach focuses on the mechanical and statical aspects, combining internal load-bearing subsystems by coupling their deformation. This approach allows for a stiffness based attribution of the acting forces towards each subsystem, enabling an investigation into individual subsystem failure loads as well as the critical shear load for the cracked specimen. Due to the aforementioned topicality, the method is tuned to work for bridge relevant dimensions and systems, focusing on the situation at intermediate supports and linear distributed loading conditions. The developed and introduced shear model approach focuses on the compatibility of the theoretical structural model and the real live behaviour of the reinforced and prestressed concrete, and aims to portrait a possible approach to shear validation. However it is neither intended nor evaluated to be used as a shear verification model without further development concerning limiting and failure criteria, as well as additional load bearing considerations, as explained and discussed within the scope of the presented work.

In this context the interaction of normal stresses and shear stresses are investigated, showcasing the shortcomings of the currently applicable German design standards and their limits of applicability when attempting to recalculate existing reinforced concrete beams. For this reason the research is constrained to normal strength concrete and slender beams. Hence the findings of this work can not be adopted to high-strength or light weight concrete as well as deep beams, slabs or shell-like structures without further investigation.

2. Shear in Reinforced and Prestressed Concrete Beams - Mechanisms and Models

2.1. Overview

Throughout the development of the modern shear models for reinforced and pre-stressed concrete beams, several mechanisms were discovered, examined and described to improve the prediction of the shear load-bearing capacity of reinforced concrete beams. While some of the load-bearing mechanisms and their mathematical definition are widely accepted, some others are still to this day under debate on their correct expression. The shear models presented in this section vary in this regard due to their time of development and focuses given by their respective researchers.

2.2. Shear Bearing Mechanisms

2.2.1. General

Following the general approach of the static limit analysis within the theory of plasticity theorem, the imposed shear force must be opposite and equal to the beams internal shear resistance. This internal shear resistance, in case of reinforced concrete slender beams, consists of the combination of the following widely accepted shear transfer mechanisms (figure 2.1):

- V_{cd} – Direct strut or arch action within concrete members
- V_{cc} – Shear stresses in the uncracked compression zone
- V_{ct} – Residual tensile stress in the crack processing zone
- V_{ai} – Shear stresses transferred by crack friction and aggregate interlock
- $V_{s,t}$ – Tensile forces in transverse reinforcements
- $V_{s,dw}$ – Dowel action in the longitudinal reinforcements
- V_p – Vertical component of prestressing tendons

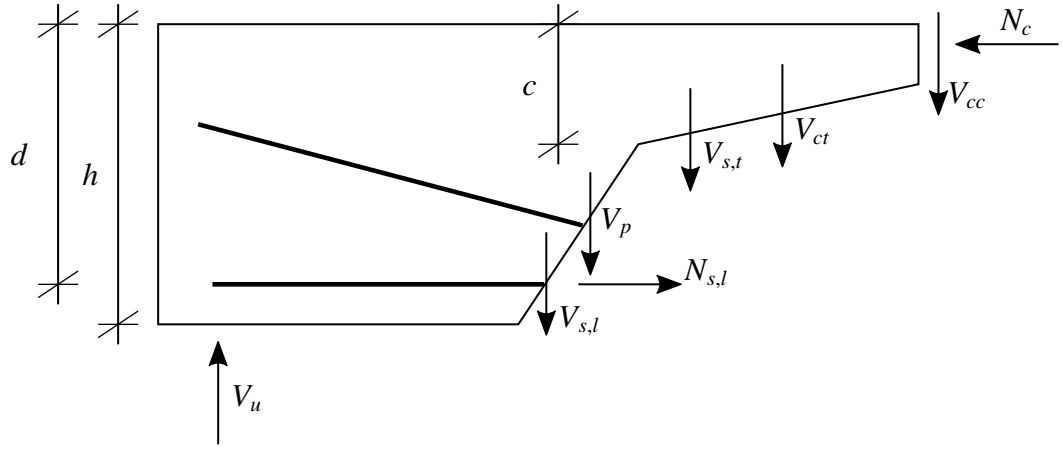

Figure 2.1.: Shear bearing mechanisms within a reinforced concrete beam

The mathematically expression for the static limit analysis theorem including the previously stated mechanisms is given by equation 2.1, with a detailed description of each individual mechanism being provided in the following subsections.

$$V_{u,crit} \geq V_{cd} + V_{cc} + V_{ct} + V_{ai} + V_{s,t} + V_{s,dw} + V_p \tag{2.1}$$

2.2.2. Direct Actions – Strut and Arch (V_{cd})

The simplest form of direct action can be found in a strut and is generally acknowledged for forces introduced close to supports, allowing for a direct flow of the stresses into it. They can be approximated well using strut and tie models or stress fields (section 2.4.2). `Muttoni` reckons that a direct strut can form for loads introduced as far has 1.5 times the statical height of the concrete beam from the nearest support [119]. Standards usually cover these areas with the definition of the critical control section for shear. Eurocode 2 for example defines the location as 1.0 times the statical height of the concrete beam from the nearest support [41], disregarding shear forces closer to it, since they are assumed to flow directly into the support.

Prestressing or large compression forces can lead to an increase of the area, where direct action is relevant [78], opening discussions of the position of the critical control section. Especially the development of a so called elbow or arch can be achieved by this. This effect can be seen for test 8-1 [103] in figure 2.2, where the elbow forms due to cracks crossing the theoretical compression strut, while the smaller shear slenderness of test 4 [103] does allow for a direct strut to form, which follows the theoretical compression strut.

Even so the strength of direct actions are reduced with increasing slenderness due to disruption resulting from flexural shear crack development, `Yang` does attribute residual load capacity generated after dowel failure to these direct actions [186].

Additionally experiments show that, while the slenderness does effect the amount of force being carried by direct actions, this influence decreases when comparing single-span sys-

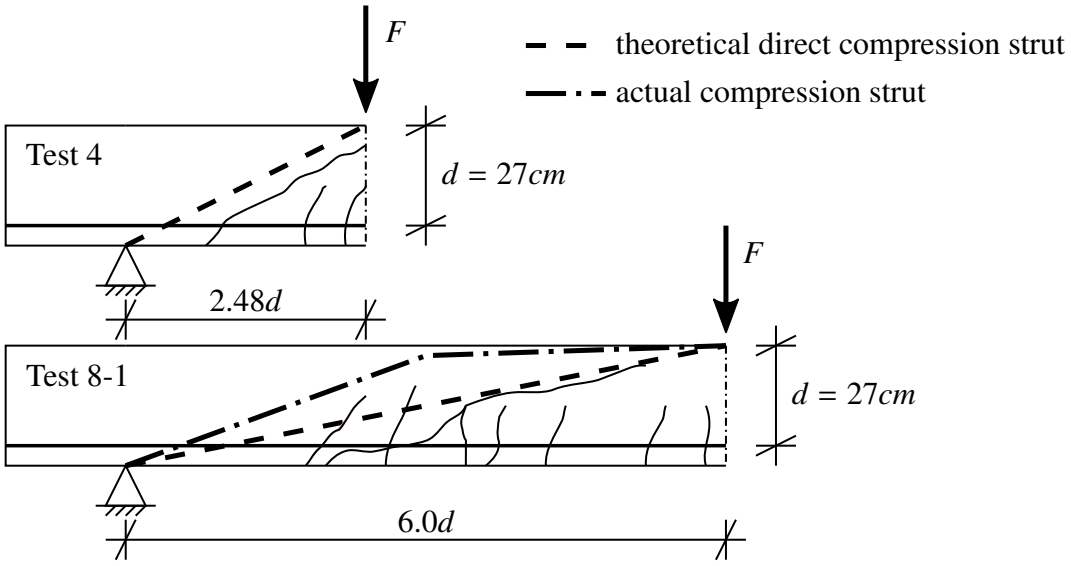

Figure 2.2.: Theoretical direct strut and elbow strut constructed for beams of different slenderness taken from [103]

tems to multi-span continuos systems [156]. Furthermore the direct action can be linked to the type of loading, which is discussed in more detail in section 2.3.4.

2.2.3. Shear stresses in the Uncracked Compression Zone (V_{cc})

In the uncracked concrete compression zone, stresses still follow the theory of elasticity and can be calculated depending on the boundary conditions of the uncracked concrete. Since the boundary conditions of the uncracked concrete are almost impossible to determine exactly, a number of approximations result in different approaches to determine the shear-bearing capacity.

On one side the truss models, strut and tie models as well as the arch and tension belt models often have an inclined compression belt, which can also be seen by a varying compression zone depth. Here the shear-bearing capacity of the uncracked concrete is determined using the vertical component of the principle stresses. On the other side, approaches based around a constant compression zone depth (parallel chords), use integration over the shear stresses to determine the shear-bearing capacity. The first simplified expression of this is given by `Mörsch`, who assumed a parabolic shear stress distribution above the neutral axis [122].

These two approaches result in very similar results, since the shear stresses in the case of a constant compression zone depth can be transformed to the vertical components of the

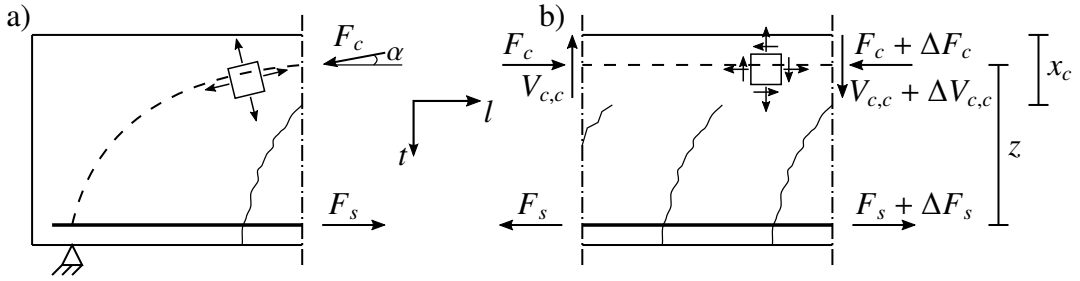

Figure 2.3.: Load-bearing of the uncracked concrete compression zone: a) varying compression chord; b) constant compression chord

principle stress in the case of a varying compression zone depth.

$$\text{for Figure 2.3 a)} \quad V_{cc} = F_c \cdot sin(\alpha) \tag{2.2}$$

$$\text{for Figure 2.3 b)} \quad V_{cc} = \int_0^{x_c} \int_0^{b_{eff}} \tau_{lt}(t) dy dt \tag{2.3}$$

Over the years, a number of different shear stress distribution curves within the uncracked concrete were suggested [47, 166]. However, as a comparison of experimental data with the parabolic shear stress distribution proposed by Mörsch sufficiently verified the assumption, where the experimental results attributed the shear-bearing capacity of the uncracked concrete with 24.0% of the critical load and the parabolic distribution attributes 21.0% of the applied load to the uncracked concrete. A reassignment of the uncracked concrete compression zone and its height results in a limited influence on the shear-bearing capacity of a reinforced concrete beam according to Albrecht and Schnell [7]. This showcases the persistence of shear-bearing mechanism that is based on concrete compression.

Taylor [166] as well as Zink [193] also come to the conclusion, that the shear-bearing capacity of the uncracked concrete is an important component of the overall shear-bearing capacity of the reinforced concrete beam. The latter even naming it the foundation of the shear-bearing capacity of beams without transverse reinforcements.

2.2.4. Residual Tensile Stress (V_{ct})

Firstly measured by Evans and Marathe [45], Hillerborg et al. were the first researchers to describe the residual tensile stress mathematically and include it in their Fictitious Crack Model [73]. Since then especially research linked to fracture mechanics (section 2.4.5) did spearhead further development regarding the tensile softening behaviour of concrete, with one of the most prominent models being derived by Hordijk and Reinhardt [74, 145] concerning the tensile stress - crack width relationship.

Overall, while the function of tensile stress after cracking is still not agreed upon by most researchers and further research points towards a very low significant of it in the case of

shear cracks, it will not be presented in further detail. Overviews on this specific topic are provided by [4, 19, 171].

2.2.5. Aggregate Interlock (V_{ai})

Aggregate interlock happens due to the shearing movement of the shear crack (figure 2.4). It is mostly influenced by the roughness of the developing crack surface, and hence purely depending on the composition of the concrete material, with major factors being the strength relation of the cement matrix and the aggregate. Where high performance concrete sees a shift in this strength, where the strength of the cement matrix matches the one of the aggregate, leading to crack development breaking the aggregate, cracks in normal concrete usually develop around the aggregates, leading to a much rougher surface. It can therefore be stated that the ability to transfer shear forces across the crack at normal concrete strength due to aggregate interlock is more potent than in high performance concrete.

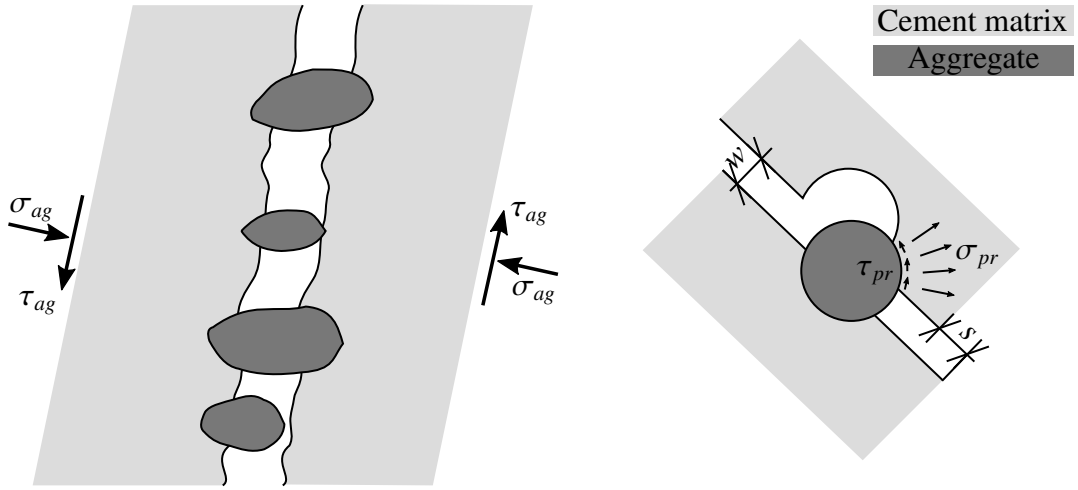

Figure 2.4.: Load-bearing of the cracked concrete caused by aggregate interlock

Aggregate interlock is well researched due to its large impact on the shear transfer across cracks [117, 143, 154, 183]. `Albrecht` and `Schnell` [7], f. e. did attribute aggregate interlock with about 51% of the critical shear failure load in reinforced concrete beams without transverse reinforcement. `Walraven`, based on his work in [180], published his ground breaking two-phase model in [181], where the concrete is viewed as consisting of two components, the spherical aggregates and the surrounding cement matrix (figure 2.4). Assuming strictly plastic material behaviour, the stresses acting at the contact between aggregate and cement matrix can be calculated, and therefore the transferable forces. Later on the model was expanded upon to account for none normal strength concrete, in which the crack can propagate through the aggregate [182].

Some alternative models revolving around aggregate interlock were derived by [58, 108].

2.2.6. Transverse Reinforcement ($V_{s,t}$)

Transverse reinforcement subjected to shear stresses function equivalently to longitudinal reinforcement subjected to normal stresses, meaning it is activated due to crack development within the reinforced concrete specimen. Hence the resistance of reinforcement, no matter if transversal or longitudinal, is largely governed by the bond behaviour, summarised in detail in the following literature [24, 100, 109, 147]. While the bonding behaviour is well investigated and the influencing parameters, like the reinforcement diameter, concrete strength or reinforcement surface amongst others, it mostly influences the crack development and spacing. In this context Schramm investigated the influence of none standard reinforcement shapes towards the shear load-bearing capacity of prestressed reinforced concrete beams, as well as their consideration towards shear verification [156, 157].

While the resistance of the transverse reinforcement is well documented and covered by most models like the truss models (section 2.4.1) research showed a dependency on the cross-section as well as the width of the web towards the stresses within the transverse reinforcement [103]. This research did result in the definition of a minimal shear reinforcement that is required by modern codes like the ACI 318 [2] or the EC2 [41, 42].

2.2.7. Dowel Action ($V_{s,dw}$)

First acknowledged as early as 1908 [122], the dowel action results from the interaction of concrete with embedded longitudinal reinforcement bars in the context of differential tangential displacement at the location of a vertically moving crack. Based on first experimental results on beams performed by Krefeld and Thurston [93], Baumann and Rüsch conducted a further extensive test series focusing on dowel action with regards to various influencing variables [14]. Figure 2.5 shows the origin of the force attributed to dowel action.

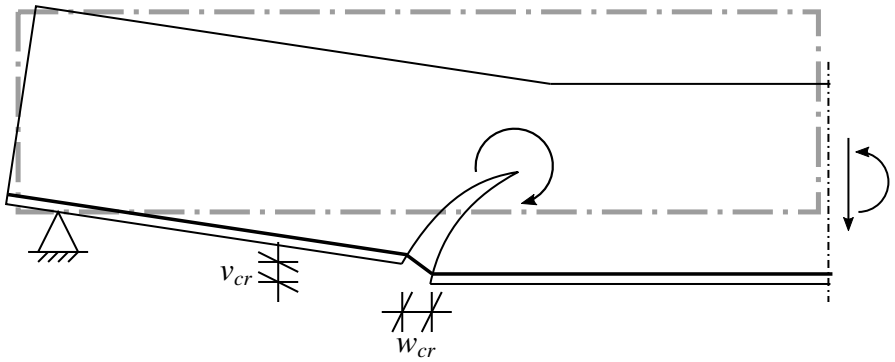

Figure 2.5.: Differential movement of a shear crack

The qualitative effect of the dowel action is viewed critically, with some researchers like Zink [193] and others [83] advocating for a disregarding of the dowel action in the light

of shear strength determination of reinforced concrete specimens, while other researchers attribute it with about 15 – 25% of the shear-bearing capacity and therefore advocate for an inclusion [7, 47, 136, 166].

Quantification of the dowel action can be done using equation 2.4, first defined by Baumann and Rüsch [14] and modified to fit modern concrete parameters like the concrete strength f_{ck} in MPa by Reineck [138]. It provides the critical force $V_{s,dw,cr}$, at which a dowel crack is developing, which follows the longitudinal reinforcement.

$$V_{s,dw,cr} = 1.476 \cdot w_{w,net} \cdot d_l \cdot f_{ck}^{1/3} \tag{2.4}$$

with:

$$w_{w,net} = w - \sum d_l$$

Clearly deductible is the linear influence of the reinforcement diameter d_l in mm confirmed by multiple researchers [14, 138, 177]. The cross-section geometry of the reinforced concrete is regarded by its net width $w_{w,net}$, which is the width w in mm reduced by the width of the combined longitudinal reinforcement. An alternative formulation for the calculation of the force, resulting from dowel action can be found in [193], however it is shown, that they differ only slightly for concrete strength up to 80.0 MPa.

It needs to be mentioned that the inclusion of transverse reinforcement leads to an increase of $V_{s,dw,cr}$, since the exceeding shear force gets transferred into the transverse reinforcement, where the developing horizontal crack crosses it [14]. Chana showed that the formation of a dowel crack, and resulting loss in dowel force, along the longitudinal reinforcement bars always closely precedes the opening of the critical shear crack and corresponding failure of a beam due to shear [26]. This is contradicted by a number of experiments, including [156], which show dowel action occurring simultaneously or shortly after reaching the critical shear load, further questioning the applicability of inclusion of the dowel force in the determination of the critical shear force [193].

2.2.8. Prestressing (V_p)

While the vertical forces, resulting from a none horizontal line of tendons is straight forward to determine, other effects need to be mentioned as well. Huber stated that the shear load-bearing capacity of an angled tendon is the combination of the vertical component of prestressing $V_{p,0}$, depending on age and quality of prestressing, and the added prestressing, due to deformation of the crack ΔV_p [78]. Using his expressions the vertical component of the prestressing in regard to the prestressing force P_0 and the added prestressing resulting from crack opening ΔP can be given for a single tendon to:

$$V_p = (P_0 + \Delta P) \cdot sin(\alpha_p). \tag{2.5}$$

The calculation of ΔP can be taken from [78, 152].

A secondary effect of prestressing is the influence it has on the stress distribution within the cross-section. Zararis and Zararis included the influence of the stresses within the

longitudinal direction in their generalized theory of shear strength of slender reinforced concrete beams [192]. However, since axial forces can also result from loading conditions, this influence can not be attributed solely to prestressing.

2.3. Influences on the Shear Bearing Capacity of Reinforced and Pre-Stressed Concrete Beams

2.3.1. General

One of the major reasons on there not being a generally accepted approach to precisely determine the shear bearing capacity of reinforced and pre-stressed concrete beams is the number of influencing parameters and their interactions with each other. These influencing parameters can be vaguely grouped into cross-section, longitudinal system and loading conditions. Each of which can only be viewed separately by specifically designed experiments, usually focusing on a single influence parameter. This makes a classification of the combinations rather difficult to predict and in generally hard to determine out of independent and separately conducted experiments. A better understanding of these parameters and their interactions is vital to further improve the prediction of the shear bearing capacity in reinforced and prestressed concrete members. Here the advanced numerical analysis (chapter 3) and the options provided by the *Design of Experiments* (DoE) [161] need to be employed at a large scale to further substantiate the experimental databases, that are covered in chapter 4.

The following subsections summarise the current understanding of the influencing parameters on the shear bearing capacity of reinforced and pre-stressed concrete beams. To avoid doubling up on influencing factors already covered by section 2.2 the influences provided by changing material properties, as well as reinforcement, pre-stressing and quality of bonding between concrete and reinforcement are not stated in this section.

2.3.2. Cross-Section

As engineer, one of the important decisions during the design process is the definition of the cross-section. In general a lot of factors play into the finally used shape of the beams cross-section, spanning from optical preference, practicability, provided space and ease of use to economical aspects. Especially for wide spanning beams, usually the latter of these factors proves to be decisive, often resulting in cross-sections with efficient shapes and possibly variable depth. However one of the most basic influences that needs to be studied lies in the size effect. Otherwise conclusions gained by small scale tests can not be transferred to large scale specimens.

Size Effect

While scaling is a generally applicable practice in scientific research, often necessary due to limited conditions but scalable or independent variables, like material properties, the concrete beams without shear reinforcement subjected to shear failure are one of the exceptions. Early tests by Leonhardt and Walther [103] and Kani [88] showed a reduction of the nominal shear strength ($\tau = V/(wd)$) with an increase of the statical height d. Even so the width w of the specimen is included in the nominal shear strength, it does not impact in the case of slender beams. An influence can however be proven for large width, where the beam transitions towards a slab [186].

An early attempt at linking the scaling relationship of nominal shear strength to the effective height of the beam was related to the *Weakest Link Theory* by Weibull [184]. However Bažant an Kazemi [17] did confirm Walraven's findings, that the *Weakest Link Theory* can not be applied to neither flexural shear failure nor tension failure [179].

Similarly the size effect as described in *Linear Elastic Fracture Mechanics* [15, 16, 20, 132] is unable to capture the link between nominal shear strength and the statical height. In this case the reason can be found in the quasi-brittle material behaviour of concrete, compared to the brittle materials, for which the *Linear Elastic Fracture Mechanics* was developed.

Further attempts describing the size effect with singled out influences like the aggregate interlock [32] can be torpedoed by research with neglecting or decreasing influences of aggregate interlock [186]. Hence mostly empirical approaches are deployed and can be found in standards like the EC2 [41]. While still present at reinforced concrete beams, the size effect gets mitigated when transverse reinforcement is present [187]. Therefore the main focus of all research done in the field of size effect concentrates on beams without transverse reinforcement.

Shape

Multiple researchers showed that the shape of the cross-section does influence the shear load-bearing capacity of reinforced concrete beams [103, 104, 156, 167, 170, 188].

Nearly all of the research concerning the influence of the shape focus on T-shaped cross-sections, with some of it also covering I-shapes, in comparison to a rectangular cross-section. This is expected, as these are the predominant shapes that are widely deployed. Comparison between rectangular and T-shaped cross-section concerning the change in shear-bearing capacity needs to be viewed critically however, since there has to be a differentiation between which dimensions can be compared, and which cannot. Leonhardt and Walther for example showed in their experiments reported in [104], that the width of the web does influence the shear-bearing capacity greatly, similarly to how a wider rectangular cross-section also is attributed with a higher shear-bearing capacity. Hence the usual comparison made in literature, linking T-shape to rectangular shape is done via the web width and total height. Attributed with the increase in load-bearing capacity, which in general is

not covered by most standards, is the flange due to the change in the compression zone and resulting load bearing-capacity increase resulting from it (section 2.2.3) [156, 188].

Considerations of this effect are attempted by some researchers focusing on their respective model, like Tureyen et al. [170] showcasing three approaches to extend models derived for rectangular cross-sections to T-cross-sections. Similar to Zararis [188], Tureyen et al. specified a form factor accounting for a direct influence of the flange towards the shear bearing capacity, which further supports the assumption that the increase is linked to the compression zone resulting from loading. Görtz [65] showed in numerical investigations, that the effective width of T-shaped cross-sections should be taken as an increase of the web width by 30% of the flange height for each side, when applying the standardised formula for rectangular cross-sections provided in the EC2 [41].

Variable Cross-Section Depth – Haunch

Due to the more complex shape as well as the larger specimen size that is required to properly account for a variable cross-section along the longitudinal length of a beam, only limited research is available on its influences. One of the first test series conducted, focusing on its influence was conducted by Rostásy et al. [149]. Their research focused on the influence of the compression strut angle and therefore had the test specimens increase their height towards the span mid. While the findings provide some valuable insight into the influence of an angled compression chord, in it reducing the acting tension stresses within the web, showing additional load-bearing reserves when being present, they find limited practical use, since the shape is rarely present outside of short overhangs or roofing constructions.

Caldentey et al. [25] did conduct tests on cantilevers with variable depth, finding an increase of load-bearing capacity, partially linked to the type of loading (section 2.3.4), further confirming the interdependencies of different factors on the total shear-bearing capacity of reinforced concrete beams. Attributed with this increase in load-bearing capacity was, likewise to [149], the "inclination of compression chord carrying shear".

2.3.3. Longitudinal System

Rarely considered in the context of design verifications, the statical system can have a relevant influence on the shear-bearing capacity of reinforced and/or prestressed concrete slender beams. Partially determined by economical aspects resulting from geometrical boundaries or visual preferences, the statical system influences the stress distribution within the beam, possibly leading to interaction of different load-bearing systems as widely recognised for steel structures [43].

Structural System

One of the earliest comprehensive investigation on the influence of the statical system was performed by Leonhardt et al. [106]. Their findings showed a decreased influence of the

moment-shear-relation for two-span girders when compared to single span girders, noting the reduction of the main tensile stress due to overlapping of stresses resulting from bending and shear as one of the influences for it.

Huber et al. [79] noted that an increase ranging between $30 - 50\%$ is encountered when comparing intermediate supports to end supports, for the same critical control section respective to each support. Moving this control section further away from the intermediate support yielded more comparable results and fall in line with Herbrand's argument of it being located near the point of counterflexure for continuous beams under uniformly distributed loads [70]. While this approach does acknowledge the influence of bending moments on the shear bearing capacity, trying to reduce its influence by moving the critical control section closer to the point of counterflexure, it is merely a work around instead of a solution to its implicated complexity. In this also lies the foundation of the influence that is linked to the statical system, where the interaction of the acting forces result in them influencing each others load-bearing mechanisms.

Further research conducted on shear using other statical systems than a single span girder were performed in [25, 61, 158].

2.3.4. Loading Conditions

Usually governed by the design code, the type of loading is none negotiable, approximating the relevant loading during the structures lifetime. The same can be said for the loading position, even so this can partially be controlled by design, like geometrical restrictions or choice of coupling location. However these two influences need to be studied and considered in the context of reinforced and/or prestressed concrete slender beams, since they control the stress distribution.

Loading Position - Shear-Slenderness

One major influence factor on the shear-bearing capacity of reinforced concrete members can be found in the load position, also known as shear-slenderness or simply slenderness in the context of shear. It is generally given as $\lambda = a/d$, where a describes the distance between the support and the applied load and d is the static height of the reinforced concrete beam. First described by Rüsch et al. [153] it was also used by Kani in his development of the strength envelop (figure 2.6), where $M_{fail} \hat{=}$ moment at shear failure and $M_{bend} \hat{=}$ resisting bending moment [86].

The shear-slenderness is equivalent to the bending moment-shear relation $M/(V \cdot d)$ used by Leonhardt and Walther [103] to determine the influence of the interaction of the internal forces on the shear-bearing capacity of reinforced concrete beams.

Seeing, as the beam strength is associated with the shear-span to depth ratio a/d, it can be determined that there is an influence on the beams shear-bearing resistance, depending on the point of loading. This highlights, that not only the type of loading needs to be considered, but also the location of it.

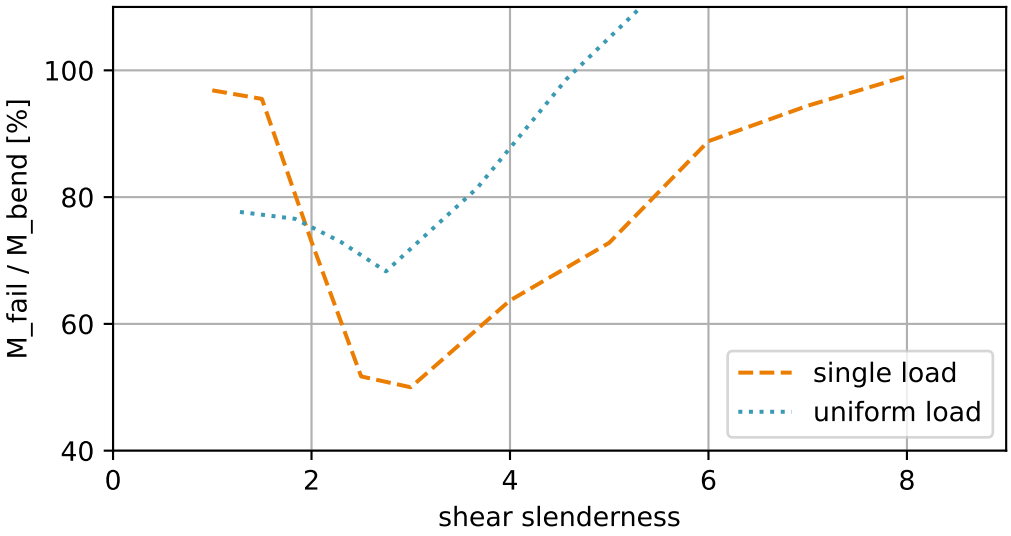

Figure 2.6.: Shear valley following Kani [87] based on tests taken from Leonhardt and Walther [103]

Type of Loading

Early research conducted into the influence of different loading types on the shear-bearing capacity of reinforced concrete beams was performed by `Leonhardt` and `Walter` [103]. Based on their tests they concluded, that the shear-bearing capacity of a single span beam increases by $20 - 40\%$ when comparing distributed loading to single point loading, attributing it mainly to the shear-stress bending moment interaction as well as the increasing strength of the compression zone (section 2.2.3). `Kani` included their tests on uniformly distributed loads in his paper concerning the influences different parameters on the shear-bearing capacity of reinforced concrete beams [87]. When plotting the `Kani` strength envelop for those tests (figure 2.6), it can be determined, that uniformly distributed loads are somewhat favourable towards the shear-bearing capabilities of reinforced concrete beams when compared to point loads.

To include the dependencies of loading conditions and type of loading into design codes, `Brown` et al. created a test series, focused on these parameters [23]. Of this test series three sub-series were presented, comparing asymmetric concentrated loads and concentrated loads to uniform loads. The tests showcased a significant difference between uniform and concentrated loads, as well as backed up the importance of the shear-span to depth ratio a/d, as discussed above, when designing reinforced concrete beams for shear. Strain measurements showed a clear difference between the different types of loading. While the strut was clearly visible for the concentrated loads, the strain under uniformly distributed loads followed the trajectories, and by that a compression arch within the concrete can be seen.

Next to their research on the influence of variable depth of the reinforced concrete beam

regarding shear resistance (section 2.3.2), Caldentey et al. also evaluated the influence of load distribution [25]. They also state that the type of loading has a significant effect on the shear-bearing capacity of slender reinforced concrete beams without transverse reinforcement. Out of their test series it can be seen, that an increase of the shear-bearing capacity of 25 – 30% can be achieved under uniformly distributed loads with respect to a concentrated load, and even upwards of 100% when a triangular load distribution was applied. This wide range of measured shear-resistances further adds to the importance loading has on the shear-bearing capacity of reinforced concrete beams, that is mostly disregarded in today's codes and standards.

Considering the type of loading Herbrand did note that for single span girders, the effect of taking the critical control section of the shear failure load as being located at a distance of the statical cross-section height does nullify the impact of a uniformly distributed load compared to single loads [70]. It was also noted, that the critical control section for continuous beams under uniformly distributed loads can not be defined that easily, further highlighting the interdependence of influence factors concerning the shear load-bearing capacity of reinforced concrete beams.

2.4. Shear Bearing Models

The development of the first shear bearing model goes back to the late 19^{th} century when Ritter published his basic theories of reinforced concrete in *Die Bauweise Hennebique* [148]. Back then Ritter formulated some of the fundamentals still applicable to modern reinforced concrete design. Mörsch followed up in the early 20^{th} century. His extensive book *Der Eisenbetonbau, seine Theorie und Anwendung* from 1908 [122] summarized all theories, verification methods and experiments developed so far for the then new composite material. The strut-and-tie model, which still forms the basis for shear verification methods in modern standards like the *Eurocode 2* [41] or the *SIA* [160], was first introduced in it.

The second half of the 20^{th} century brought with it some improvements to the strut-and-tie model. The introduction of the variable angle of the compression strut by Kupfer [95] was taken up by Leonhardt and resulted in the modified truss model [101] (section 2.4.1).

Drucker combined the strut-and-tie model with the theory of plasticity in the early 1960^{th} [44]. The so called stress fields were created which are used in standards like the SIA [160] and the FIB Model Code [48]. The stress field method will be examined in section 2.4.2 in more detail.

The compatibility-aided truss models, better known as compression field models (section 2.4.3) resulted from extensive tests on reinforced concrete membrane elements. While the strut-and-tie model is the result of an equilibrium approach when applying the principle of a truss-like load-bearing system within reinforced concrete beams, the compatibility-aided truss adds to this proven model by introducing compatibility conditions and further expanding the model by taking the tensile strength of concrete into account. The oldest of

these models is the Modified Compression-Field Theory by Vecchio and Collins [174]. However Hsu also published the so called Softened Truss Model in the late 1980^{th} [76] and followed it up in cooperation with Pang with an improved iteration of his previously published model [129].

While the previously stated mechanical approaches are widely acknowledged in its applicability to determine the shear load-bearing capacity of reinforced or prestressed concrete beams with shear reinforcement, reinforced concrete beams without shear reinforcement are written on a different page. Since the transverse reinforcement usually takes the brunt of the shear force, other load-bearing mechanisms can be simplified or even forgone in the name of resilience and/or safety. Since this can not be translated to reinforced concrete beams without transverse reinforcement, a whole plethora of different models are instead being used across the world.

Most prominently featured in the approaches to determine the load-bearing capacity of reinforced concrete beams without transverse reinforcement are the empirical methods. The *ACI Code* from 1995 [3] still featured 43 empirical equations solely for the determining of the shear load-bearing capacity. More analytically and mechanically sound approaches include Kani's Teeth Model [86] (section 2.4.4) and the separately by Reinhardt [144] and Bazant [18] pioneered fracture mechanic based models (section 2.4.5). A different approach can ge found in the Critical Shear Crack Model(section 2.4.6), in which Muttoni took account on the shear-bearing mechanisms, depending on the crack development within the reinforced concrete.

One of the latest additions to the shear models of reinforced concrete beams are the compression zone models (section 2.4.7), which focus on the shear bearing mechanism of the uncracked compression zone (Section 2.2.3).

2.4.1. Truss Models

The classical 45° truss model first mentioned by Ritter [148] and defined by Mörsch [122] is the first established shear bearing model. As the model name suggests the load-bearing capacity is entirely attributed to the transverse reinforcement $V_{s,t}$, while being limited by the crushing of the concrete compression strut. Depending on the angle of the transverse reinforcement α, the vertical component of the trusses tension strut can be calculated and used as verification in the general stress based manner. Following the limit analysis theory this marks the first step towards the determining of the actual shear load-bearing capacity of reinforced concrete beams.

Figure 2.7 showcases some of the possible trusses within transverse reinforced concrete beams. The depicted trusses follow Mörsch's first assumption, which states that the tension and compression belts are parallel. In fixing the angle of the compression struts ϑ to 45°, the second assumption is fulfilled. However Kupfer used the principle of stationary action to show, that the angle ϑ of the compression strut can vary from Mörsch's assumption,

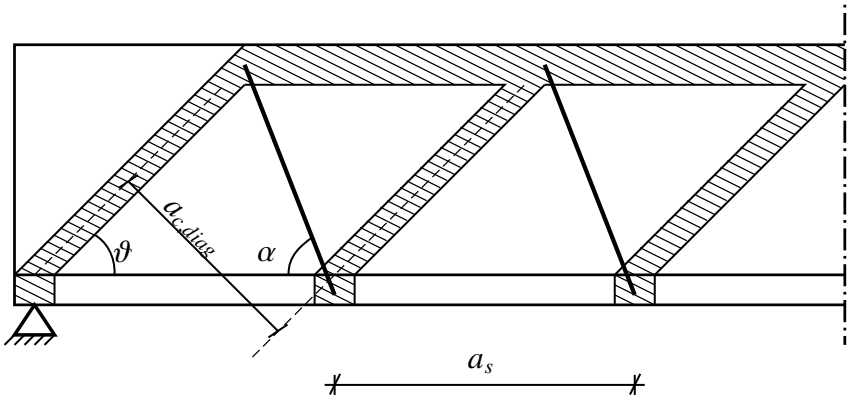

(a) Staticaly determined truss

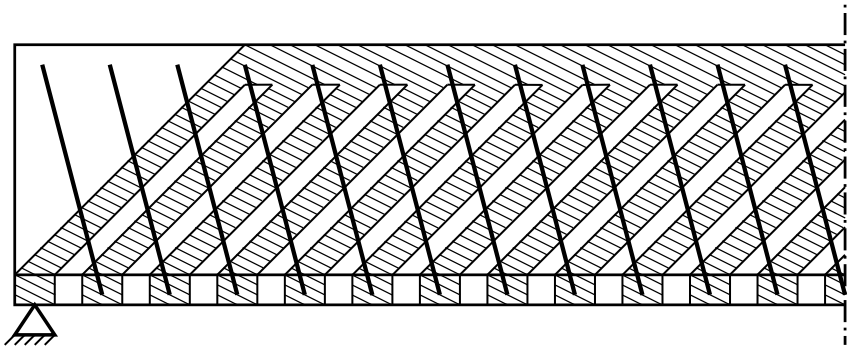

(b) Lattice truss

Figure 2.7.: Trusses of the classical truss analogy

depending on the beams geometrical as well as reinforcement parameters [95]. By that Kupfer formulated one of the earliest compression field models (section 2.4.3).

The difference of complexity of calculation between the statically determined truss (figure 2.7 a)) and the highly statically undetermined lattice truss (figure 2.7 b)) can be clearly stated. Also the major influence factor on the type of truss developing within a reinforced concrete beam with transverse reinforcement can be determined to be the spacing of the transverse reinforcement a_s. To tackle the bottle neck of computing power when dealing with variations of the lattice truss, Mörsch derived the approach of deconstructing the developing lattice truss into overlaying statically determined trusses, like the one given in figure 2.7 a). In this concept lies the foundation of the truss analogy.

Following Kupfer's finding of the variable angle of the compression strut as well as the shear tests conducted in Stuttgart ([103, 104, 105, 106, 107]), Leonhardt derived the so called modified truss analogy depicted in figure 2.8 [101].

As shown in figure 2.8, Leonhardt cast aside the assumption of parallel belts for a more arch like shape of the compression belt for his modified truss analogy. Various parameters, including the amount of shear reinforcement and the form of the cross-section, lead to this arch like shape as well as the variable angle of the compression strut ϑ. Thus resulting in a

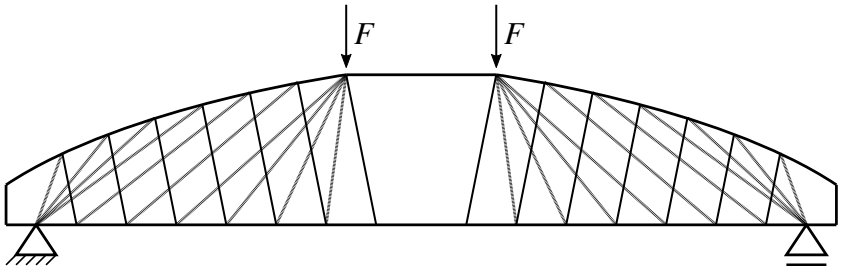

Figure 2.8.: Modified truss for single span beams

theoretical shear load-bearing capacity, which shows a better agreement with experimental data than the one according to the classical truss analogy.

Some of today's standards still use the varying angle truss analogy, assuming parallel compression and tension belts, for the calculation of the shear load-bearing mechanisms in reinforced or prestressed concrete beam with shear reinforcement. Due to its mechanical description of the major load-bearing mechanism and the following simple calculation scheme it is implemented in the Eurocode 2 [41], which gives the shear load-bearing capacity of the transverse reinforcement to:

$$V_{s,t} = \frac{A_{s,t}}{a_s} \cdot z \cdot f_{y,t} \left(cot(\vartheta) + cot(\alpha)\right) sin(\alpha). \tag{2.6}$$

2.4.2. Stress Fields

In general stress fields require the cross-section to be split into plane sections, which are then assigned a specific load-bearing behaviour. For reinforced concrete beams the cross-section is split into compression/upper and tension/bottom chords as well as the web, which functions as the stress field. Having this theoretical disassembly of the cross-section in mind, it becomes clear, that, similar to the truss analogy, not all load-bearing effects/systems, like f.e. the arch action (section 2.2.2), can be properly taken account of when applying this method [162]. Within the stress fields there exists a gradation of models with different degrees of approximation. The rigid-plastic stress fields, the extended rigid-plastic stress fields and the elastic-plastic stress fields [152].

Rigid-plastic stress fields, also known as the classical stress fields (CSF), were developed in Denmark and Switzerland in the late 1970^{th} [119, 126, 168]. They are based on the plasticity theorem formulated by `Drucker` [44], which states that any loading is smaller or equal to the critical loading, if a statically correct stress state within the cross-section can be derived. CSFs were improved upon by taking account of the strain compatibility conditions, which resulted in the extended rigid-plastic stress fields, also known as generalised stress fields (GSF) [163].

In the model of the rigid-plastic stress fields the beam is split into parallel stress fields in the areas without external forces and fan-like stress fields in the areas where concentrated external forces are applied (figure 2.9). These different sections are separated by discontinuity

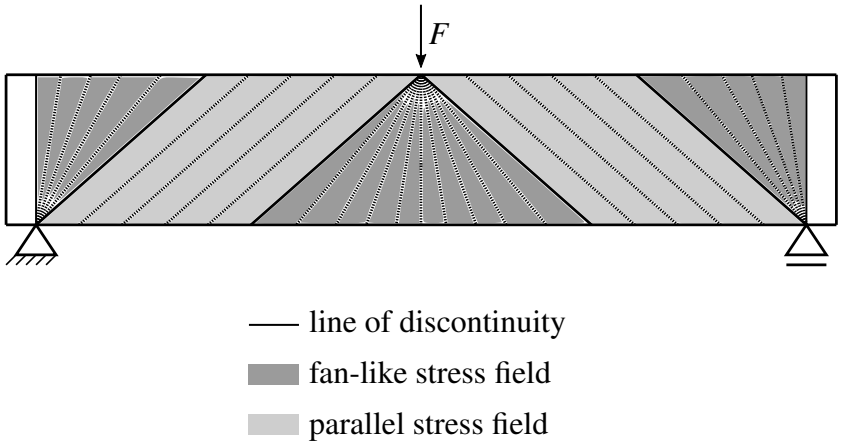

Figure 2.9.: Classical stress field

lines, which shows the model abstraction, since these sections are furthermore viewed individually. This shows parallels to the model version given by Kupfer [95]. The rigid-plastic material formulation in this approach allows for the equilibrium conditions to remain intact, even if the stresses parallel to the discontinuity line at the discontinuity line are of different sizes. The angle of concrete compression following the CSF is given by:

$$\vartheta = arcsin \left(\sqrt{\frac{\rho_l f_y l}{f_{cm}}} \right) \leq 45° \tag{2.7}$$

Attempting to improve upon the CSF, the GSFs were developed by Kaufmann and Marti [89] as well as Sigrist and Hackbarth [163]. They extended upon the purely force equilibrium conditions of the CSF by adding a strain compatibility component. In contrast to the models following the compression field approach (section 2.4.3), the compatibility component in the GSFs is limited to the strain compatibility at a single control cross-section height. Using this added degree of approximation, the resulting angle of the concrete compression ϑ changes from Eq. 2.7 to Eq. 2.8.

$$\vartheta = arctan \left(\frac{\epsilon_x - \epsilon_2}{\epsilon_y - \epsilon_2} \right)^{0,5} \tag{2.8}$$

In limiting the material behaviour of the reinforcement steel and the concrete to be elastic-plastic, while still neglecting the tensile strength of the concrete, the elastic-plastic stress fields (EPSF) incorporate a further generalisation of the CSF and GSF.

Ruiz and Muttoni showcased a finite element approach to stress fields on the basis of EPSF to tackle the generally applicable limitations of stress fields, like the freedom in choice of the underlying load-bearing mechanisms and not ensured alignment of the reinforcement with the stress fields [151].

2.4.3. Compression Field Models

Compression field models are derived from the classical 45° truss model. Baumann [13] generalised Kupfer's [95] work, which resulted in a description for the principal compressive stress direction in orthogonally reinforced concrete panels in plane stress (eq. 2.9).

$$tan^2(\vartheta)\rho_l(1 + n\rho_t) + tan(\vartheta)\rho_l\frac{\sigma_t}{\tau_{lt}} = cot^2(\vartheta)\rho_t(1 + n\rho_l) + cot(\vartheta)\rho_t\frac{\sigma_l}{\tau_{lt}} \tag{2.9}$$

For this case the appendices l and t symbolise the longitudinal and transversal direction applicable to the reinforcement ratio ρ and the normal as well as shear stresses σ and τ receptively, with ϑ providing the angle of the compression strut.

Vecchio and Collins [173] developed a non-linear approach by conducting experiments on orthogonally reinforced concrete panels that were loaded in different stress configurations, expending on the previously stated linear approach by Kupfer and Baumann. The non-linear definition of the compression field dates back to the compatibility equations by Mitchell and Collins [118], which were derived by torsion experiments. This allowed for a more mechanically sound model description of the shear load-bearing behaviour of reinforced concrete members. A test setup for the reinforced membrane elements subjected to shear used by Hsu in later tests of the same kind can be gathered from [77].

Due to the test setup a heavy emphasis on uniformly distributed reinforcement in each axis can be established. This uniformity within the membrane elements allows for the modelling of the composite material reinforced concrete as a single homogenous material with changing properties pre and post cracking [174], which was used in the development of the respective theory.

Modified Compression Field Theory

The *Modified Compression Field Theory* (MCFT) dates back to the mid 1980^{th} and is based on shear experiments on concrete membrane elements described in [173]. Using the experimental data and the assumptions given in [174], Vecchio and Collins deducted a stress-strain relationship within the reinforced concrete membranes. They state that the point of failure is reached when the reinforcement is not capable of transmitting the tension in the concrete across the crack. A revision and summary of the MCFT can be found in [22], while a detailed derivation of the equations and the theory are provided by [174].

Since the theory was developed for membrane elements, the application to beam-like elements is not that straight forward. A first approach in applying the theory to reinforced concrete beams was done by Vecchio and Collins and showcases the need to divide the beam cross-section into membrane sections in which the theory applies [175]. This can be seen as a parallel to the stress fields, where the beam also needs to be deconstructed into sections (section 2.4.2). Seeing the increased computational cost they also introduced some approximations to streamline the calculation procedure, making it more user-friendly. The best fit approximation provided was to define an effective section located between the top

and bottom reinforcement and to assume the shear flow as uniformly distributed over this section. Allowing for this section to be seen as controlling, concerning the shear resistance of the beam.

`Adebar` and `Collins` furthermore showed, that due to the compatibility based approach, the MCFT is not limited to reinforced concrete beams with shear reinforcement, but can also be applied to reinforced concrete members without shear reinforcement [5]. Following this approach the maximum shear stress τ_c in relation to the aggregate size a_g and the concrete strength f_{cm} is given by,

$$\tau_c \leq \frac{0,18\sqrt{f_{cm}}}{0,31 + \frac{24w}{a_g+16}}, \tag{2.10}$$

where the crack width w can be calculated, depending on the crack spacings in x and z direction (s_x, s_z), following equation 2.11.

$$w = \frac{1}{\frac{sin(\vartheta_c)}{s_x} + \frac{cos(\vartheta_c)}{s_z}} \cdot \epsilon_1. \tag{2.11}$$

The variables are showcased in figure 2.10.

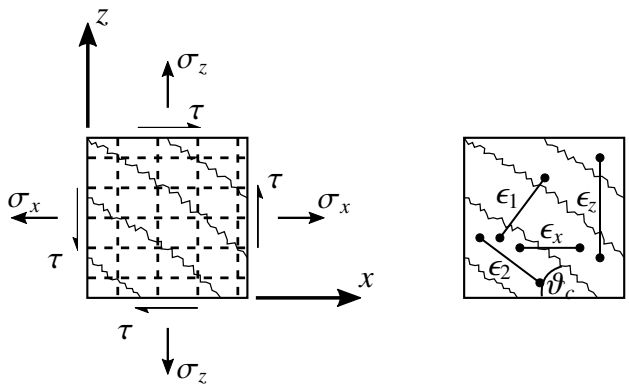

Figure 2.10.: Variables of the Modified Compression Field Theory

Seeing a further necessity of simplification `Bentz` et al. [22] proposed that the shear stress τ can be written as:

$$\tau = \tau_c + \tau_s = \beta\sqrt{f_{cm}} + \rho_t f_{yt} cot(\vartheta_c) \tag{2.12}$$

with:

$$\beta = \frac{0,4}{1 + 1500\epsilon_x} \cdot \frac{1300}{1000 + l_{cr,m}}$$

$$\vartheta_{crack} = (29deg + 7000\epsilon_x) \left(0,88 + \frac{l_{cr,m}}{2500}\right) \leq 75deg$$

$$l_{cr,m} = \frac{35s}{a_g + 16}$$

While ϵ is the strain as defined in figure 2.10 and f_{cm} and f_{yt} are the concrete compression strength and steel tension strength respectively, ρ_t describes the transverse reinforcement ratio.

The shear contribution of the concrete τ_c following equation 2.12 also reaches its maximum capacity in accordance to the MCFT (equation 2.10).

In 1996 "A General Shear Design Method" was proposed by `Collins` et al. [33]. It follows the widely accepted additive of shear resistance due to shear reinforcement and shear resistance due to the concrete, and pleads a case for a rational model in the light of the 43 empirical equations provided by the 1995 ACI Code [3]. In the face of a standardised approach the equations of the MCFT [174] were simplified and resulted in the following:

$$V_n = V_c + V_s + V_p \tag{2.13}$$

$$V_c = \beta \sqrt{f_{cm}} \cdot b_v d_v \tag{2.14}$$

$$V_s = \frac{A_v f_y}{s} d_v cot(\vartheta), \tag{2.15}$$

where β and ϑ are functions of the longitudinal strain ϵ_x, the shear stress τ and the crack spacing s_x given in tabular form. The shear stress and strain in longitudinal direction are given as:

$$\tau = \frac{V_n - V_p}{b_v d_v} \tag{2.16}$$

$$\epsilon_x = \frac{\frac{M}{d_v} + 0,5\,(N + Vcot(\vartheta)) - A_{ps} f_{p0}}{E_s A_s + E_p A_p} \tag{2.17}$$

In a final step the longitudinal reinforcement (A_s) as well as the prestressed reinforcement (A_{ps}) needs to be checked on its capacity using equation 2.18. To provide a characteristic result equation 2.18 does not including any safety factors or strength reduction factors.

$$A_s f_y + A_{ps} f_{ps} \geq \frac{M}{d_v} + 0,5N + \left(V - 0,5V_s - V_p\right) cot(\vartheta) \tag{2.18}$$

This approach now signifies a pen-and-paper version of the MCFT and is usable in the day to day work of structural engineers. It is incorporated in design procedures like the Canadian Standards for concrete design [34] and applicable to reinforced concrete beams with and without shear reinforcement.

Softened Truss Models

Improvements of the classical 45° angle truss model led to the development of the Softened Truss Model (STM) by `Hsu` [76]. Similarly to `Vecchio` and `Collins` equilibriums and compatibility equations [174], as well as a material law for softened concrete were used to create a theory that is applicable to shear and torsional loading of reinforced concrete

elements. Since the theory provides eleven equations with fourteen unknowns in the case of shear calculation, some boundary conditions are required to allow for application of the STM. Alternatively, some variables need to be determined iteratively. The STM is also known as Rotating Angle Softened Truss Model (RA-STM), since the theory includes the assumption of the rotating angle ϑ to coincides with the angle of the shear cracks ϑ_c.

Since the RA-STM is not capable of correctly predicting the shear resistance of reinforced concrete elements with low amounts of steel reinforcements in one direction [172], Pang and Hsu developed a variation of the STM called the Fixed Angle Softened Truss Model (FA-STM) [129]. By introducing a new constitutive law for concrete in shear, derived from full-size panel tests, the FA-STM is capable of taking the shear stress transfer across cracks into account. Differing to the MCFT, the concrete contribution to the shear-bearing capacity is not attributed solely on the tensile stress of concrete, but to the shear stress of concrete in case of the FA-STM.

Further Models

Based on the principal models given by the MCFT and the STM some other shear formulas have been developed. One of the most recent approaches was given by Lee [99]. Seeing the complexity of the MCFT when applied to reinforced concrete beams he proposed the following simplified equation:

$$V_n = \sqrt[3]{\left(\rho_t f_{yt} + \lambda \lambda_s \sigma_l\right)^2 \frac{700\rho_l}{\kappa\,(a_v/d - 1)}} b_w \tau \tag{2.19}$$

with:

$$\lambda = \begin{cases} 0,75 & \text{for lightweight concrete} \\ 1,00 & \text{for normalweight concrete} \end{cases}$$

$$\lambda_s = \left(\sqrt{\frac{200}{d}}\right)^{1,5} \leq 1,0$$

$$\kappa = \left(1 + \frac{\rho_t f_{yt}}{\beta_s f_{cm}}\right)^{0,9}$$

Equation 2.19 in kN is derived to express the shear strength of reinforced concrete beams, including the longitudinal and transverse reinforcement ration ρ_l and ρ_t respectively, the concrete compression strength f_{cm} and steel tensile strength f_{yt} as well as the strength reduction factor for concrete cracked in shear β_s ($0.6(1\check{}f_c/250)$ with f_c in MPa). The geometry is accounted for by a_v, being the distance between the support and the load introduction, d, being the statical height of the beam, and b_w, the width of the web.

2.4.4. Tooth Models

Tooth models got their name from the crack pattern of slender reinforced concrete beams at failure load (figure 2.11). While Kani was the first to define a model based on the state of

the reinforced concrete beam near failure [86], other researchers like Fenwick and Paulay [47] or Reineck [137] also created their models following this approach. They represent an early attempt towards a rational flexural shear failure model.

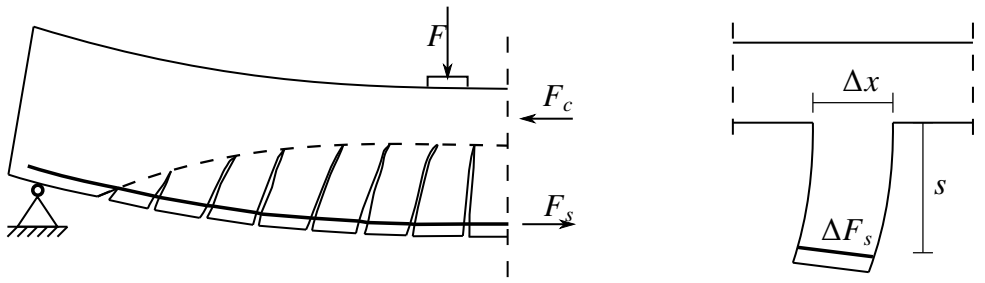

Figure 2.11.: Failure model basis for the tooth model

All tooth models have the same mechanical approximation in common, in them abstracting the concrete tooth as cantilevers, which are anchored in the compression zone of the beam and are loaded by the respective load $\Delta F_{s,l}$ due to the longitudinal reinforcement (figure 2.11). Kani stated that following this understanding of the internal mechanism of a reinforced concrete beam, the Euler–Bernoulli hypotheses that plane sections remain plane is inaccurate and leads to an inconsistent shear strength theory [86]. The concrete teeth in his model was loaded only by $\Delta F_{s,l}$, which leads to to a failure load of the concrete tooth per unit length at:

$$\frac{\Delta F_{s,l}}{\Delta x} = \frac{f_{ct} \cdot \Delta x}{6s} \cdot b_{eff} \tag{2.20}$$

When this condition is reached, it is assumed that the concrete teeth are being eliminated from the load bearing mechanisms, leading to an arch with tension belt as the remaining shear load bearing mechanism (section 2.2.2).

A series of tests performed by Fenwick and Paulay with manually arranged teeth within the test beams led to the first improvements of the teeth model [47]. The tests showed that aggregate interlock (section 2.2.5) should not be ignored when considering the tooth model by Kani. Taylor reached similar conclusions and extended the tooth model to further include dowel action [165]. Another approach, following Kani's model, is given by MacGregor and Walters, who also included aggregate interlock as well as dowel action [113]. In their example the shear-bearing capacity of these two mechanisms added up to 30 – 35 percent of the total load-bearing capacity, with aggregate interlock being the major contributor.

Reineck developed a stand-alone tooth model, in which the teeth are loaded due to aggregate interlock (figure 2.12 a)), bending of the teeth (figure 2.12 b)), dowel action (figure 2.12 c)) and global bending (figure 2.12 d)). The concrete tooth is defined by evaluation of test data to have a cracking angle ϑ_{crack} of 60° and a tooth length Δx of $0,7 \cdot (d - x)$, while the compression belt is assumed to be horizontal.

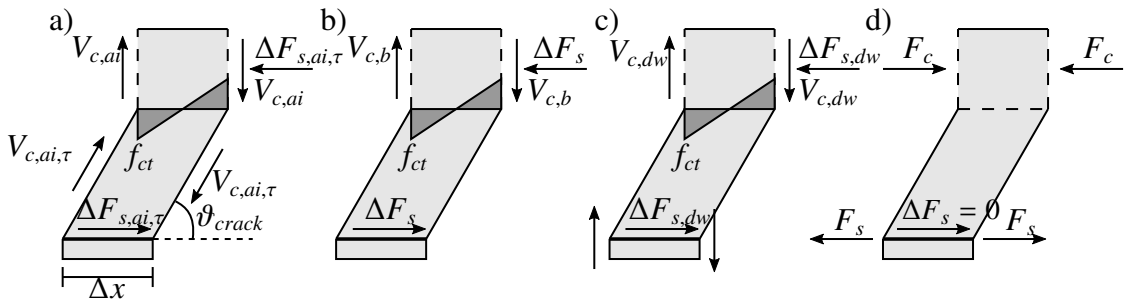

Figure 2.12.: Loading of the concrete tooth according to Reineck [137]: a) aggregate interlock; b) bending of the tooth; c) dowel action; d) global bending

Following Reineck's model, the crack fully develops after failure of the load-bearing mechanisms aggregate interlock and dowel action, which undergo an increase in loading after rotation of the concrete tooth due to bending of it. After failure of the concrete teeth, direct actions like the compressive arch (section 2.2.2) are made responsible for further increase of the shear-bearing capacity.

The size effect (section 2.3.2) is described by the crack width according to [137], hence Reineck attributes aggregate interlock to be a larger part in the shear-bearing of a reinforced concrete beam without transverse reinforcement than the dowel action. Reineck's model leads to a shear-bearing capacity of:

$$V_u = \frac{0,4 \cdot b_{eff} \cdot d \cdot f_{ct} + V_{c,dw}}{1 + 0,16 \cdot \frac{f_{ct}}{f_{ck}} \cdot \lambda \cdot \left(\frac{a}{d} - 1\right)}. \tag{2.21}$$

Seeing as this formulation excludes transverse reinforcement, the tensile strength f_{ct} as well as the compression strength f_{ck} of concrete is accounted for, next to the geometrical information like the slenderness λ, statical height d, distance of the loading from the support a and the effective width of the concrete beam b_{eff}.

Altering Reineck's approach to determine the forces within the concrete teeth by defining stress fields within each concrete tooth, Marti and Beck derived a hybrid model consisting of a tooth model extended by stress fields [116].

One of the latest entries, which can be sorted into the tooth models, Yang developed a model, focused in the shear force displacement relationship [186]. Yang's model allows for the calculation of the shear transfer mechanisms from the compression zone V_{cc}, aggregate interlock V_{ai} and dowel action V_{dw} with respect to the vertical crack opening at the tensile reinforcement. The mentioned shear transfer mechanisms need to be calculated iteratively until their sum converges with the applied shear force. While V_{dw} is assumed to be in line with the maximum dowel capacity given by Baumann and Rüsch [14] and V_{cc} is equal to

the sum of the average shear stresses over the compression zone depth, V_{ai} is calculated by:

$$V_{ai} = f_c^{0,56} s_{cr} b_{eff} \frac{0,03}{w - 0,01} \left(-978\Delta^2 + 85\Delta - 0,27\right), \tag{2.22}$$

where Δ is the relative displacement of the crack faces at the level of tensile reinforcement in the vertical direction, s_{cr} is the height of the crack and w is the crack opening at the level of the tensile reinforcement in the longitudinal direction. Equation 2.22 is a simplified equation based on `Walraven`'s model [180].

2.4.5. Fraction Mechanic Models

From the perspective of fracture mechanic, the quasi-brittle failure of reinforced concrete lies between the plastic limit analysis, that holds the correct results for small structures, and linear elastic fracture mechanics, which applies to very large structures. While these two extrema meet asymptoticly, the actual specimen behaviour follows a more gradual path (figure 2.13).

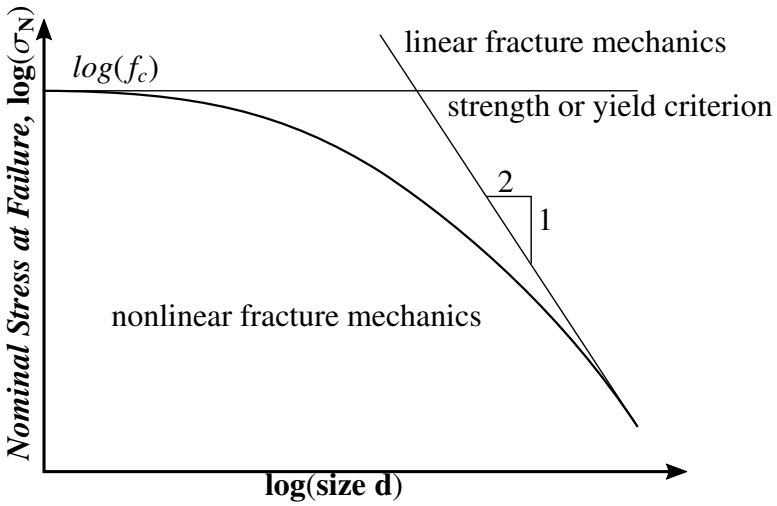

Figure 2.13.: Fracture modes used in shear models based on fracture mechanics

It is important to note, that the brittle shear failure of reinforced concrete consists of a number of individual failure modes, which include diagonal shear fracture of the concrete in the web, shear-compression fracture in the uncracked compression zone, interface bond fracture at the reinforcement bars and splitting fracture of the concrete cover (figure 2.14). As the fracturing behaviour of concrete in tension is rather complex, analytical equations for the shear capacity based purely on fracture mechanics are seldom, but mostly used in combination with regression analysis or finite element analysis. Basis for this is the suggested serial fracture processes triggering the shear failure of reinforced concrete beams, as suggested by some researchers.

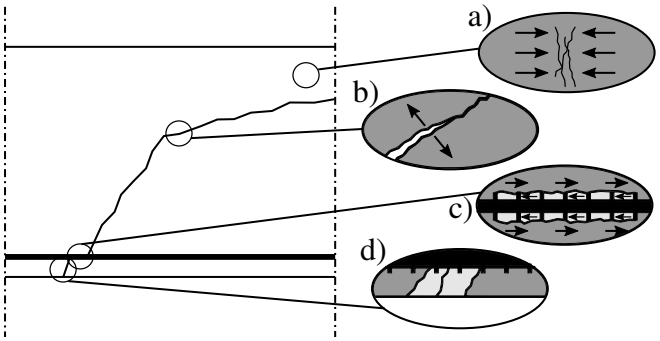

Figure 2.14.: Fracture modes used in shear models based on fracture mechanics: a) shear-compression fracture; b) diagonal shear fracture; c) interface bond fracture; d) splitting fracture

Since the shear failure of reinforced concrete beams represents a complex brittle fracture process, some models based on fracture mechanics are developed in an attempt to derive a physically sound analytical model. One of the earliest models was developed by Bazant in the mid 1980^{th} to describe the size effect observed in reinforced concrete beams without transverse reinforcements [15] (section 2.3.2). Bazant and Kim derived equation 2.23, which encapsulates a smooth transition between a plastic strength criterion and linear elastic fracture mechanics (figure 2.13). Equation 2.23 can be considered a semi empirical – semi fracture mechanics model [18], where ρ is the geometric reinforcement ratio and d_{ag} is the maximum aggregate size, while the statical height d as well as the effective beam width b_{eff} and the concrete compression strength f_c are equivalent to the previously introduced models.

$$V_c = \frac{8\sqrt[3]{\rho}}{\sqrt{1+\frac{d}{25d_{ag}}}} \quad 0,083\sqrt{f_c} + 20.7\left(\sqrt{\rho\ \frac{M}{Vd}}\right)^5 b_{eff}d \tag{2.23}$$

The size effect law derived in [15], taking into account a more sophisticated approach, based on the assumption of shear-bearing capacity being controlled by propagation of cohesive fracture or softening damage was confirmed by Bazant and Yu [20]. This led to the development of an improved fracturing truss model due to weighted least-square regression of a database, which is given by [21], where μ represents a safety-factor:

$$V_c = \left(\mu\rho^{3/8}\quad 1+\frac{d}{a}\right)\sqrt{\frac{f_c'}{1+\frac{d}{\kappa f_c'^{-2/3}}}}, \tag{2.24}$$

with:

$$\kappa = 3,8\sqrt{d_{ag}} \quad \text{if } d_{ag} \text{ is known,} \qquad \kappa = 3,33 \quad \text{if not.}$$

So and Karihaloo extended a previously developed fracture mechanic model [84], created with focus on the diagonal shear crack, to include the bond-slip relationship as well as dowel action and aggregate interlock [164].

A more recent semi empirical - fracture mechanics model was proposed by Xu et al. [185]. The model attempts to stray away from a formulation of the splitting tension fracture property of concrete to describe the shear failure of the reinforced concrete beam without transverse reinforcement. Instead it uses the sudden release of longitudinal reinforcement from the surrounding concrete, described by the shear fracture property along the interface between the steel bar and the concrete as the controlling shear mechanism.

Generally, the described methods require the assumptions of a simplified crack path as well as of the critical inclined crack to be the dominating shear failure mechanism. This also means, that shear-bearing mechanisms, like aggregate interlock and the shear-bearing capacity of the uncracked compression zone are usually disregarded in the fracture mechanics approach, resulting in a narrow range if applicability as can be seen in experiments of slender beams with high reinforcement ratio [186].

2.4.6. Critical Shear Crack Model

The critical shear crack theory (CSCT) was developed for slabs as well as beams without transverse reinforcements. It is based on the limit state analysis and was integrated into the Swiss standard, and currently represents the state of the art model for reinforced concrete members without transverse reinforcements [160]. It was developed by Muttoni at the beginning of the 1990^{th} [119]. While the stress fields by Drucker (section 2.4.2), based on the limit analysis, provide good results for reinforced concrete members with transverse reinforcements, they lead to unsafe design in members without transverse reinforcements.

At its core, the CSCT describes the development of the critical shear crack, including their responding shear-bearing mechanisms. Namely the aggregate interlock (section 2.2.5), dowel action (section 2.2.7) and direct actions (section 2.2.2) are included in the CSCT. According to it the critical shear crack propagates between the flexural cracks leading to a reduction of the aforementioned shear-bearing mechanisms when the concrete tensile strength within the reinforced concrete beam is reached [120].

Muttoni and Ruiz state, that the the arching action may develop within the beam even after the critical shear crack develops, allowing for further increase of the critical failure load [120]. Figure 2.15 shows the combination of the elbow-shaped strut [121] and the direct strut due to aggregate interlock in the critical shear crack. This showcases the respond of reinforced concrete member after development of the critical shear crack.

Following the CSCT the shear-bearing capacity of reinforced concrete members without transverse reinforcement is given by [120] to be:

$$V_{Rd} = \frac{0,3/\gamma_c}{1 + \frac{50}{16+a_g} \cdot \frac{f_{yk}}{\gamma_s \cdot E_s} \cdot d \cdot \frac{m_{Ed}}{m_{Rd}}} \cdot \left(b_w \cdot d \cdot \sqrt{f_{ck}} \right). \tag{2.25}$$

The relation $\frac{m_{Ed}}{m_{Rd}}$ here by is the bending moment to flexural strength, b_w the width of the web, d the statical height, a_g the aggregate size, f_{ck} and f_{yk} the characteristic concrete

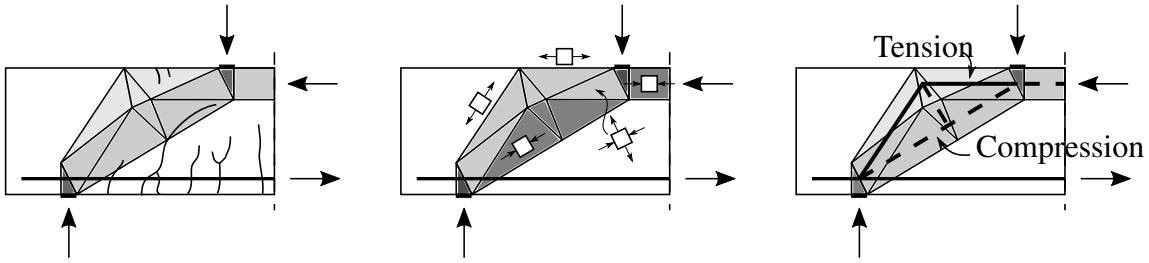

Figure 2.15.: Load-carrying mechanism after development of the critical shear crack (reproduced from [120])

compression strength and characteristic steel tensile strength respectively, with γ_s being a partial safety factor for steel and E_s being the Young's modulus of steel.

A simplified version of equation 2.25 is the given by the Swiss Code for structural concrete [160] for the verification of reinforced concrete members without transverse reinforcements.

2.4.7. Compression Zone Models

Some researchers approached the problem of defining the shear resistance depending on the predominant mode of failure. Failure controlled by tension or failure controlled by compression within the compression zone of intact concrete [29]. This approach gained popularity at the start of the 21^{st} century and sprawled a number of different models.

`Zararis` and `Papadakis` proposed a model focusing on the spilling of concrete in the compression zone [190]. It was extended in the following years to encompass rectangular [189] as well at T-shaped cross-sections [188] and generalised by adding axial forces [192]. Even the influence of the type of loading is established by a modified model for uniformly distributed loads [191]. Its development focuses around the shear load bearing capacity of reinforced concrete slender beams without transverse reinforcement. To allow the application in beams with transverse reinforcements, it uses the well established combining of separate load bearing capacities to account for the transverse reinforcement.

Based on the previous work by `Zink` [193], `Görtz` developed an approach fitted to address the gradual change from reinforced concrete beams without transverse reinforcement to reinforced concrete beams with transverse reinforcement [65]. By accounting for a shear-bearing capacity of the compression zone V_{cc}, which is added to the shear-bearing capacity of the transverse reinforcement $V_{s,t}$. This model was later on expanded upon by `Hegger` and `Görtz` for the application to beams with normal concrete and high performance concrete [66] as well as to encompass deep beams ($a/d < 3$) [67].

`Choi` et al.'s goal was to derive a formula that is not restricted to slender beams ($a/d > 2,5$), but can also be applied to deep beams ($a/d \leq 2,5$) [29]. In this approach the shear strength of concrete V_c is the combination of the shear contributions of tensile cracking V_{ct} and compression crushing V_{cc}. The simplified method published in [28] states that in case of

slender beams V_{cc} can be disregarded since the tensile crack penetrates the compression zone, leaving no room for concrete crushing to occur. Concerning the presence of transverse reinforcements Choi et al., like Zararis, comply with the approach of added shear strength of the reinforcement V_s given by standards like the ACI [2]. To ensure conservative results the contribution by the transverse reinforcement is restricted to the tension zone of the cross-section (height of the crack) [27].

One of the latest approaches was introduced by Cladera et al. [30]. The multiaction mechanical model for the shear design and assessment of reinforced and prestressed concrete beams was developed. The simplified model named the *Compression Chord Capacity Model* (CCCM) focuses on the concrete contribution, which is separated into shear resisted by the uncracked compression chord V_{cc}, the shear transferred across the web cracks, mostly by aggregate interlock V_{ai} and the dowel action V_{dw}. The shear resistance by transverse reinforcement $V_{s,t}$ follows closely the formula given by the EC2 [41]. The model provided by Cladera et al. incorporates dependencies on the size effect (section 2.3.2), normal forces, beam slenderness and effective shear width (section 2.3.4) and is applicable to rectangular, T- and I-cross-sections. The failure criterion of the model is provided by Kupfer's biaxial failure envelop [96] and is assumed to occur shortly after the first branch of the critical crack reaches the neutral axis. Figure 2.16 showcases the contributions accounted for in the CCCM.

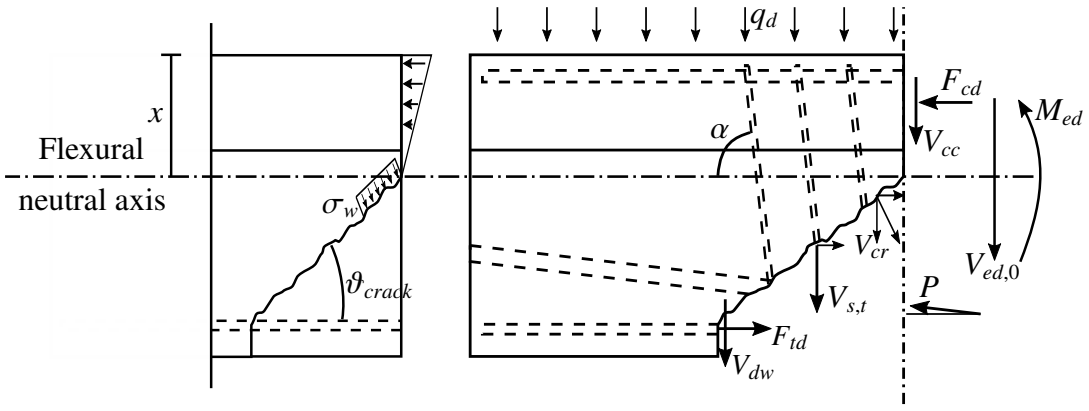

Figure 2.16.: Shear contributions of the CCCM for a simple supported beam (reproduced from [30])

In recent years, the assessment of existing prestressed concrete bridges grew more important. In light of this development Huber created the *Flexural-Shear Crack Model* (FSCM) [78]. The FSCM is named after the flexural-shear failure which it aims to predict. The model splits the total shear load bearing capacity into the components concrete V_c, transverse reinforcement V_s, vertical component of prestressing $V_{p,0}$ and added prestressing due to deformation ΔV_p. Since the load bearing capacities resulting from transverse reinforcement and prestressing are rather straight forward to determine and are independent on the

mode of failure the major concept is given by:

$$V_c = \frac{2}{3} \cdot \tau_{c,max} \cdot b_{V,eff} \cdot c \cdot \beta_{cc}, \tag{2.26}$$

where $\tau_{c,max}$ is the maximal shear stress within the concrete, $b_{V,eff}$ gives the width of the shear stress bearing cross-section, c is the depth of the compression zone and β_{cc} is a factor dependent on the type of loading.

An alternative approach describing the shear-bearing capacity of existing prestressed concrete bridges with varying depth of the tendons is given by `Gleich`. On the basis of the dated model theory of compression arches in the webs of reinforced concrete beams [102], previously validated by the *Compression Arch Model* (CAM) [91], the *Extended Compression Arch Model* (ECAM) was developed [61, 63]. By determining the shape of the compression arch, the ECAM allows for an added shear-bearing capacity by the compressed concrete respective to the direction and size of the principle stress (section 2.2.3). The ECAM differs from the CAM by its calculation of the arch shape. While the CAM assumes the Euler–Bernoulli hypotheses that plane sections remain plane and can only be applied to prestressed concrete beams prior development of the shear crack. The ECAM tackles this shortcoming by allowing for stress redistribution within the prestressed concrete beam and by that can be used to determine the critical loading post development of the shear crack.

2.5. Conclusion

Opposing the clearly and undisputed load-bearing capacity of bending, the load bearing capacity concerning shear in reinforced and/or prestressed concrete beams still is not solved satisfactory. The reason for this lies in the complex shear bearing mechanisms, which can not only interact, but sometimes even induce each other. An example of this interaction can be seen in the dowel action (section 2.2.7), which can be increased, and therefore influenced by the presence of transverse reinforcement. Furthermore the partially known influences, like the size effect (section 2.3.2) or the position and type of loading (section 2.3.4) do complicate the formulation of a generally applicable shear-bearing capacity of reinforced and/or prestressed concrete beams. Therefore a considerable amount of vastly different shear models were developed. Ranging from the simplistic truss models for beams with transverse reinforcement, mostly neglecting other shear-bearing mechanisms other than the transverse reinforcement, over fracture mechanic models, applicable to beams without transverse reinforcement, to compression zone models, where attempts are made to combine most of the shear-bearing mechanisms. It has to be pointed out that, even with the compression zone models showcasing an analytical approach to determining the shear strength of reinforced concrete beams they are not tested for a wide variety or parameters as mostly viewed by the shear-bearing influences. An example of this is given by `Choi` et al. stating, that the model does not consider web crushing failure in case of thin web cross-section types like I- or T-shaped beams [27].

In summary, even so the shear-bearing mechanisms are mostly recognised, the importance of some of them are still disputed and therefore are not accounted for consistently in the shear models, sometimes falling victim to conservative approaches and other times being viewed individually, without considering possible interactions between them. Hence no uniformly agreed description of shear in reinforced and/or prestressed concrete slender beams exists at this point.

3. Numerical Calculation

3.1. Overview

The numerical simulation and evaluation of experiments has come a long way. While in the last century it was the norm to validate theoretical approaches by physical experiments, the numerical modelling has risen to be a useful addition to this practice. Reducing the amount of necessary tests by supplementing them with numerical simulations allows for economical research when dealing with a wide variety of varying parameters. Particularly where the test setup is especially difficult to realize, or where geometrical restrictions concerning specimen size apply, it is a rational approach to extend the tests by numerical simulations validated against the same test setup.

Since computer simulations always yield the same outcome by constant input, it is even more important to understand the variance within the modelling as well as to calibrate the numerical model with the use of physical experiments [155]. In order to define the required physical and numerical tests the *Design of Experiments* (DoE) is a proven approach, yielding reliable results [161].

The following chapter aims to present different modelling approaches (section 3.2), evaluate them using documented tests (section 3.3) and define a best-use approach to numerical tests later used for parameter studies and sensitivity analysis (section 3.4).

3.2. Model Development

3.2.1. General Approach

The selected finite element software is ABAQUS [36], which has been proven to provide reliable results for reinforced and prestressed concrete beams subjected to shear [61, 68, 71].

3.2.2. General Approach

In general there are explicit and implicit methods used in numerical analysis. The major difference of these approaches can be summarised in their handling of calculations of different time steps. While explicit methods use an extrapolation of the previous/current time step to predict a later time step, implicit methods solve an equation, which uses variables of the previous/current time step as well as the later time step, resulting in a more complex

and time consuming calculation. These two approaches lead to different pros and cons, even though they should yield similar results when applied correctly.

Using explicit methods reduces the calculation time, since the equation to be solved does not need to be iterated to find the equilibrium, however using extrapolation of a previous time step to predict a later time step boundary conditions should be implemented to correct the extrapolation, and account for a change of behaviour.

Implicit methods do not need this kind of checking to ensure the calculation does predict the correct behaviour. However by needing to solve an equation relying on the previous/current time step as well as the later time step, a higher computing cost is required. Since implicit methods provide solutions based on the calculation of an equilibrium and by that, providing easy to evaluate results, they are usually chosen when modelling static or quasi-static loadings, while explicit methods are usually chosen for time step related problems like impact or dynamic simulations. However the introduction of a damage model (section 3.2.3) excludes the possibility of using implicit calculation, since, as soon as stiffness changes, depending on strains are introduced, the system can only be solved iteratively. Hence the numerical calculations featured in this work will use the explicit solvers. This choice has a number of implications for the numeric model, like the material models that are compatible with the solver.

3.2.3. Concrete Material Models

There exist a plethora of different material models for usage when performing numerical analysis on concrete elements. These models are developed to account for the highly non-linear behaviour of concrete, not only depending on the currently applied strain of the elements, but also accounting for the stress history of the elements and the resulting stiffness changes. Seeing this highly non-linear material behaviour, there is no single material model, that is widely accepted as the 'correct one' to model concrete. Generally speaking, any material model relies on a variety of parameters, which are mostly tuned using standardised material testing. Differences between the models usually derive from these parameters leading to varying influences on the resulting calculations, making it vital to understand and define each of the parameters of the material model.

The material models for concrete included in ABAQUS are the smeared crack concrete model (SCCM), the concrete damaged plasticity model (CDPM) and the brittle cracking model (BCM) (sections 4.5.1 - 4.5.3 in [36]). Since only the BCM and the CDPM are usable in combination with the explicit solver in ABAQUS, the SCCM is not covered in high detail.

SCCM is based on smeared crack models, that were developed to be used on brittle materials and go back to `Rashid` [135]. Using stress-strain relations, the initial isotropic stress-strain law is changed to an orthotropic law upon crack formation. Differing from discrete crack models, which track a crack within the material model using separation between element edges, leading to a huge cost of computing power needed for constant mesh

adaptation close to the crack, smeared crack models calculate stresses at the integration points of the numeric element, initiating a crack when a specified criterion is reached independently, meaning it does not track individual crack development [35, 150]. One of the most mentioned drawbacks of the smeared crack model is an apparent mesh sensitivity with respect to the shape/orientation of the finite elements and its size [131]. Crack development within the SCCM is numerically accounted for by a reduction of the material strength and stiffness, which influences calculation at the integration points of the finite element.

The CDPM, based on the work by `Lubliner` et al. [111] and later modifications by `Lee` and `Fenves` [98], is a constitutive model combining the plasticity theory with the damage model (figure 3.1). It combines the different modes of failure resulting from compression and tension in a general failure criteria, allowing analysis of cyclic and/or dynamic loading. To account for compressive as well as tensile failure the CDPM requires the complete description of the stress strain behaviour of the concrete, allowing for a more precise definition of the material when compared to the SCCM and BCM. Even so the CDPM is based on an empirical formulation, it is widely used in numerical calculations of reinforced concrete specimens, as can be gathered from publications [55, 57, 61, 71, 159].

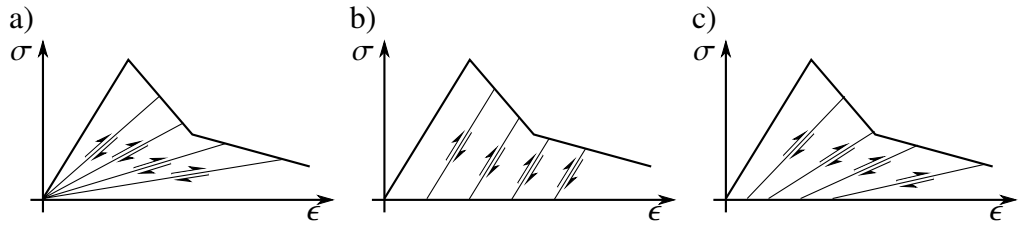

Figure 3.1.: Comparison of material behaviour following - a) damage theory b) plasticity theory c) combination of damage theory and plasticity theory

The focus on the brittle behaviour of a material is inherent of the BCM that is available in ABAQUS. By using smeared crack assumptions, the main points given for the SCCM can be translated to the BCM. A fixed orthogonal cracks model [150] is used to ensure that the crack face normal vectors are orthogonal within the finite element [36]. The BCM is defined by an elastic and a cracking strain rate in combination with cracking conditions and a cracking evolution law, which can namely be summarised as a pure elastic stress-strain relationship and a stress-crack-width relationship. In research, the BCM is often applied to other brittle materials like glass [92] or plexiglas [90]. The BCM can be interpreted as the SCCM, which is usable with explicit methods.

Analysing the pros and cons of the material models, the CDPM is chosen for the numerical analysis using ABAQUS in the context of this work. The major advantages of the CDPM over the other two models is mainly based around the more precise definition of the stress-strain relationship. Where the BCM and SCCM mostly account for linear elastic behaviour of concrete in compression and focus solely on the cracking behaviour, the CDPM presents a more complete material model for concrete. It also has the advantage to be usable in implicit as well as explicit calculations using ABAQUS (section 3.2.2). The

number of recently published research using CDPM to assess reinforced and prestressed concrete specimens under shear ([55, 57, 61, 71, 159]) further solidifies the usage of this material model for the here examined problem.

Concrete Damaged Plasticity

As stated above, the CDPM combines principles of the plasticity theory and the damage theory. The reduction of the stiffness resulting from increased loading (figure 3.1 c)) results from a progressive reduction of the cross-section due to damage propagation. In the CDPM the loading and unloading is influenced by these irreversible changes.

The behaviour of the CDPM is defined by the yield function, the yield criterion and the softening or stiffening law of the material. In this it follows material models based on the plasticity theory, which describe the total strain as the sum of the reversible elastic strain and the irreversible plastic strain. Contrary to the damage theory, the plasticity theory accounts for loading history and non-linear material behaviour. However the damage theory incorporates the material damage ($D > 0$), while the plasticity theory assumes an undamaged cross-section ($D = 0$). The CDPM was developed to extend the plasticity theory to include the influence of a damaged cross-section, so the following definitions of the yield function as well as the yield criterion are not restricted to the CDPM but also apply to material models based solely on the plasticity theory. For a detailed definition [114] can be used.

The yield function defines the boundary between elastic and plastic material behaviour. It can be interpreted as a surface (equation 3.1) in the Haigh-Westergaard stress space (principal stresses σ_1, σ_2 and σ_3) and limited by the yield-point k_f, which represents every plastic material state ($F = 0$) encompassing every combination of principal stresses resulting in a purely elastic material behaviour ($F < 0$). Combinations of principal stresses resulting in $F > 0$ can not be achieved by the material. In the CDPM the yield-surface is defined by a modified Drucker-Prager function, allowing for different rates of stiffness degradation depending on compression and tension (figure 3.2), with K_c being the ratio of the second stress invariant on the tensile meridian.

$$F(\sigma_1, \sigma_2, \sigma_3, k_f) = 0 \tag{3.1}$$

The evolution of the materials plastic strain is defined by the yield criterion. It describes softening or stiffening of the material after the yield-point is exceeded. Most materials will soften after the yield-point is reached, resulting in the general stress-strain diagram shown in figure 3.3.

Softening or stiffening laws describe the change of the yield criterion due to yielding. It is distinguished between isotropic softening or stiffening and kinematic softening or stiffening. While the isotropic change of the yield criterion results from a change of the yield-point due to reoccurring strain, the kinematic change describes a translation of the origin of

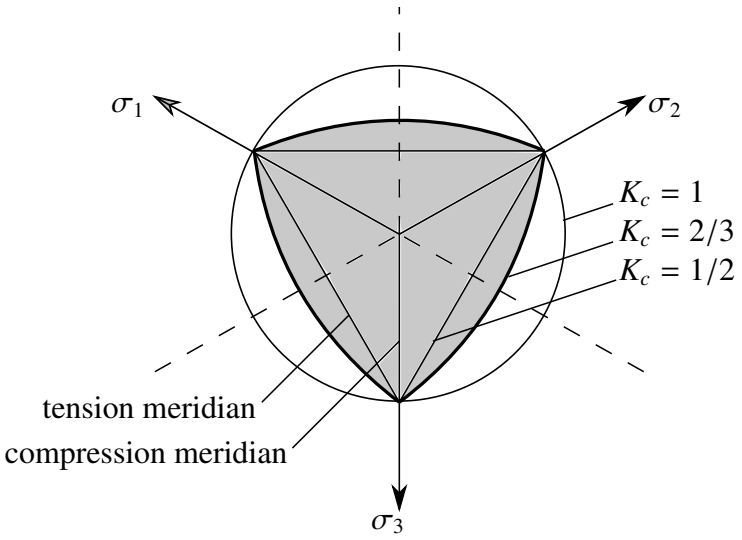

Figure 3.2.: Yield surfaces in the deviatoric plane, corresponding to different values of K_c, reproduced from [36] and [61]

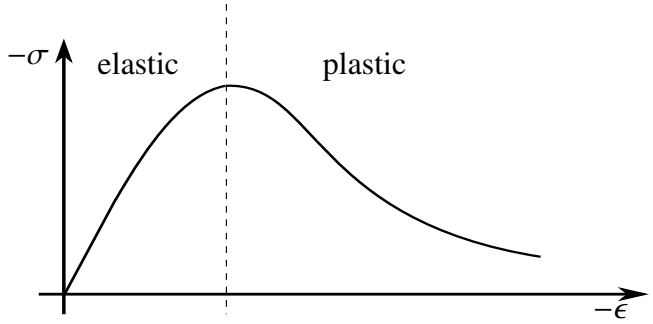

Figure 3.3.: General stress strain diagram of concrete in compression

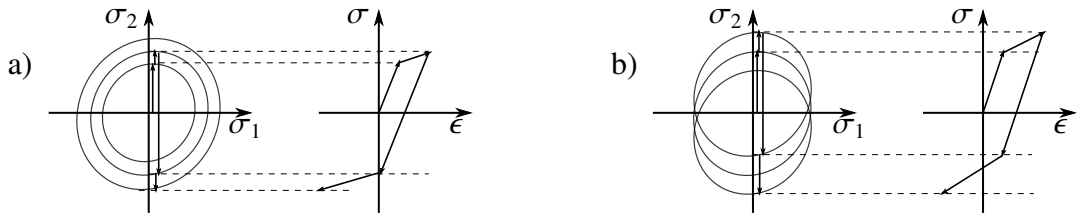

Figure 3.4.: Material stiffening - a) isotropic stiffening; b) kinematic stiffening

the stress space, while the yield-point stays relative to it (figure 3.4). This results in a constant but translating yield-surface, while the isotropic softening or stiffening law decreases or increases the yield-surface respectively [114].

The CDPM uses a Drucker-Prager potential function for the non associated yield criterion to describe the strain behaviour of the material after exceeding the yield surface [98].

Yield function

The main key in defining the CDPM, lies in the choice of the yield-function, that represents the real concrete. Figure 3.5 shows the yield surface as provided by [97], similar to the one used in ABAQUS, which is based on the model by `Lee` and `Fenves` [98]. It is conceptualised for in-homogeneous materials, as shown by the yield-functions that do not centre on the zero stress origin.

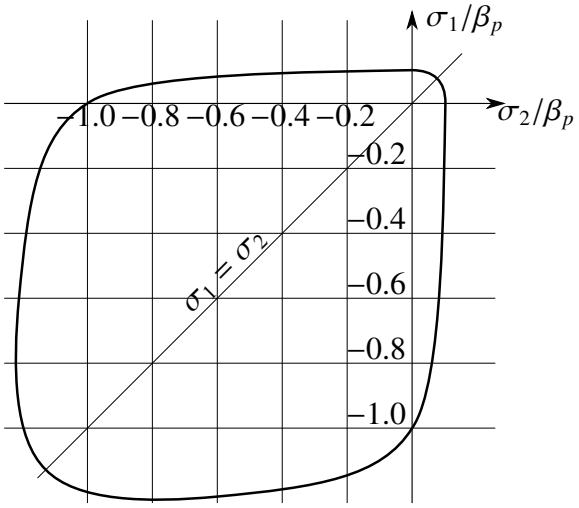

Figure 3.5.: Yield surface in plane stress taken from [97]

One of the most well known yield-functions for concrete under compression is given by the Eurocode 2 (equation 3.14 [41]) and the FIB Model Code 2010 (equation 5.1-26 [48]) used to determine the deformation of a concrete specimen. The equation 3.2 used in both standards uses the mean value of the concrete compressive strength f_{cm}. When using test data with known material properties, f_{cm} is replaced by $\sigma_{c,max}$, the experimentally determined compressive strength of the concrete.

$$\sigma_c = \frac{k\eta - \eta^2}{1 + (k-2)\,\eta} \cdot f_{cm} \tag{3.2}$$

with

$$\eta = \frac{\epsilon_c}{\epsilon_{c1}}$$

$$k = 1.05 \cdot E_{cm} \cdot \frac{|\epsilon_{c1}|}{f_{cm}}$$

The factor of 1.05 for the variable k is only included in the EC2, but not in the FIB Model Code 2010.

Concerning concrete in tension, the FIB Model Code 2010 [48] suggests a bilinear stress-strain relationship for uncracked concrete sections (equations 3.3 and 3.4) and a bilinear stress-crack opening relation for cracked concrete sections (equations 3.5 and 3.6). For equations 3.5 and 3.6 w represents the opening fo the crack in mm, G_F is the fracture energy in N/mm, E_{cm} is the Young's modulus in N/mm and f_{ctm} is the tensile strength of concrete in MPa and will be calculated in accordance with [48] to be $f_{ctm} = 0.3016 f_{ck}^{2/3}$ for cases, where the concrete tensile strength was not determined via testing.
The EC2 does not provide any concept for the inclusion of the tensile behaviour of concrete, due to its conservative approach in design.

$$\text{for} \quad \sigma_{ct} \leq 0.9 \cdot f_{ctm}$$
$$\sigma_{ct} = E_{cm} \cdot \epsilon_{ct} \tag{3.3}$$

$$\text{for} \quad 0.9 \cdot f_{ctm} < \sigma_{ct} \leq f_{ctm}$$
$$\sigma_{ct} = \left(f_{ctm} \cdot \quad 1 - 0.1 \cdot \frac{0.00015 - \epsilon_{ct}}{0.00015 - 0.9 \cdot f_{ctm}/E_{cm}} \right) \tag{3.4}$$

$$\text{for} \quad w \leq w_1$$
$$\sigma_{ct} = \left(f_{ctm} \cdot \quad 1.0 - 0.8 \cdot \frac{w}{w_1} \right) \tag{3.5}$$

$$\text{for} \quad w_1 < w \leq w_c$$
$$\sigma_{ct} = \left(f_{ctm} \cdot \quad 0.25 - 0.05 \cdot \frac{w}{w_1} \right) \tag{3.6}$$

with

$w_1 = G_F/f_{ctm}$ in mm when $\sigma_{ct} = 0.2 \cdot f_{ctm}$
$w_c = 5 \cdot G_F/f_{ctm}$ in mm when $\sigma_{ct} = 0$

However there also exist other definitions of the yield-function, like the one given by `Mark` [115], which include considerations for the numerical application, by making the loss of compression strength of concrete, due to compression failure, dependent on the volume V_E and the number of integration points n^{IP} of the numeric element used, or the slightly altered approach by `Alfarah` et al. [8].

Following these methods the stress-strain relationship of concrete can be divided into five regions (figure 3.6). For the material under compression the behaviour is given by a purely elastic compression stress-strain region (equation 3.7), the plastic compression stress-strain increasing region (equation 3.8) and the plastic compression stress-strain decreasing region

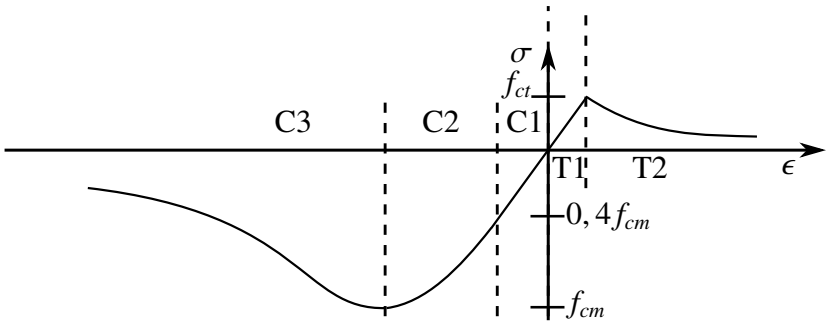

Figure 3.6.: Stress-strain diagram of concrete defined by `Mark` [115]

(equation 3.10).

$$\text{for} \quad \text{(C1)} \quad \sigma_c \leq 0.4 \cdot f_{cm}$$
$$\sigma_c = E_{cm} \cdot \epsilon_c \tag{3.7}$$

$$\text{for} \quad \text{(C2)} \quad 0.4 \cdot f_{cm} < \sigma_c \leq f_{cm}$$
$$\sigma_c = \frac{E_{ci}\left(\frac{\epsilon_c}{f_{cm}} - \frac{\epsilon_c}{\epsilon_{c1}}\right)^2}{\left(1 + E_{ci} \cdot \frac{\epsilon_{c1}}{f_{cm}} - 2\right)\frac{\epsilon_c}{\epsilon_{c1}}} \cdot f_{cm} \tag{3.8}$$

with

$$E_{ci} = \left(\frac{2}{3 \cdot E_{cm}} \cdot \frac{f_{cm}}{\epsilon_{c1}}\right)^2 - \frac{4 \cdot f_{cm}}{3 \cdot \epsilon_{\sigma_{c,max}}} + \frac{5}{3} \cdot E_{cm} \tag{3.9}$$

$$\text{for} \quad \text{(C3)} \quad \epsilon_c > \epsilon_{c1}$$
$$\sigma_c = \left(\frac{2 + \gamma_c \cdot f_{cm} \cdot \epsilon_{c1}}{2 \cdot f_{cm}} - \gamma_c \epsilon_c + \frac{\gamma_c \cdot \epsilon_c^2}{2 \cdot \epsilon_{c1}}\right)^{-1} \tag{3.10}$$

with

$$\gamma_c = \frac{0.5 \cdot \pi^2 \cdot f_{cm} \cdot \epsilon_{c1}}{\left[g_{cl}\left(\frac{f_{cm}}{2} - \epsilon_{c1} \cdot (1 - b_c) + \frac{b_c \cdot f_{cm}}{E_{cm}}\right)\right]^2} > 0 \tag{3.11}$$

$$g_{cl} = \frac{G_{cl}}{l_c} \tag{3.12}$$

$$l_c = \left(\frac{V_E}{n^{IP}}\right)^{1/3} \tag{3.13}$$

$$l_c \leq \frac{G_{ch}}{f_{cm}\left(\epsilon_{c1} \cdot (1 - b_c) + b_c \cdot \frac{f_{cm}}{E_{cm}}\right)} \tag{3.14}$$

In these equations G_{ch} is the compression equivalent to the fracture energy of concrete G_F.

While [115] assumes $G_{ch} = 15\ N/mm$ in accordance with and determined from [178]. The material flow potential will be calculated following equations 3.15 in accordance with [48] and 3.16 for the here pursued approach.

$$G_F = 0.073 f_{cm}^{0.18} \tag{3.15}$$

$$G_{ch} = \left(\frac{f_{cm}}{f_{tm}}\right)^2 G_F \tag{3.16}$$

The compression damage parameter $b_c = \frac{\epsilon^{pl}}{\epsilon^{in}}$ is assumed to be 0.7 and the equation 3.14 accounts for the "Snap-Back" effect to not be relevant [115, 133].

The material behaviour of concrete under tension is described by two regions and is based on the *Fictitious Crack Model* by `Hillerborg` [72]. The elastic tension stress-strain region (equation 3.17) and the plastic tension stress-strain decreasing region (equation 3.18).

$$\begin{aligned} &\text{for} \quad \text{(T1)} \quad \sigma_{ct} \leq f_{ctm} \\ &\sigma_{ct} = E_{cm} \cdot \epsilon_{ct} \end{aligned} \tag{3.17}$$

$$\begin{aligned} &\text{for} \quad \text{(T2)} \quad \epsilon_{ct} > f_{ctm}/E_{cm} \\ &\sigma_t = \left[\left(1 + \left(c_1 \cdot \frac{w}{w_c}\right)^3\right) \cdot e^{-c_2 \frac{w}{w_c}} - \frac{w}{w_c} \cdot \left(1 + c_1^3\right) \cdot e^{-c_2}\right] \cdot f_{ctm} \end{aligned} \tag{3.18}$$

with

$$c_1 = 3; \qquad c_2 = 6,93 \qquad [75]$$

Differing from the definition of w_c used by the FIB Model Code 2010, here the approach following `Mark` assumes a constant critical crack width for normal concrete to be 180 μm. The numerical verification of experimental results of shear experiments on reinforced concrete specimens of this approach can be found in [8, 61, 115].

Damage Parameters

Damage within the material is a vital indicator towards the stress distribution. The CDPM accounts for damages due to compression as well as tension via irreversible stiffness reduction of the material, where the strains exceed the defined limitations. `Müller` states that due to the nature of shear tests being performed under static loading, an inclusion of the isotropic damage accountability of the CDPM should not yield more accurate results [123]. Since the chosen approach of the developed method is based on stiffness relationships it is however important to account for stiffness changes to allow for a solid evaluation. A comparison calculation however will be performed and included in section 3.3.

The damage reduction factor d has a value between 0 and 1, relating to the percentage reduction of stiffness. So the material, while being undamaged has a damage reduction factor of 0, which increases, in theory, up to 1, where the materials stiffness is negligible. A

lot of damage parameter equations can be found in the literature like [8, 55, 82, 115]. Their approach usually is based on the same concept, a relation between strains as highlighted in figure 3.7.

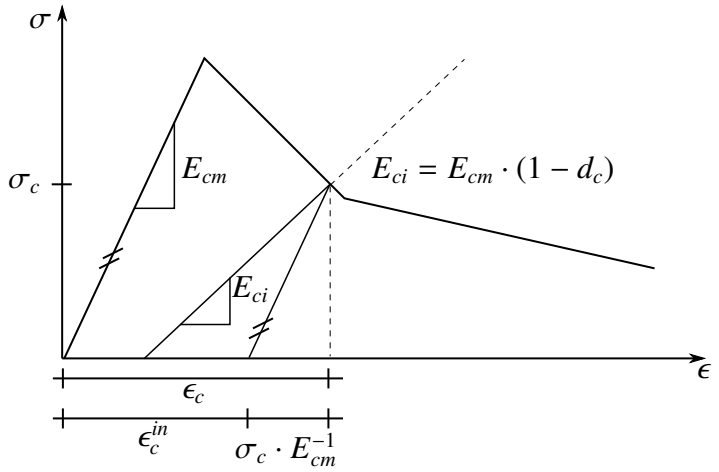

Figure 3.7.: Stress-strain relation used for determining the damage parameter of concrete

The major difference between the previously listed approaches lies within its mesh sensitivity. Here especially `Alfarah` et. al. [8] developed a definition of the damage parameters d_c and d_t for compression crushing and tension cracking damage respectively that is dependent on the size of the numeric element. This is important, since the damage parameter leads to an element consistent weakening of the material. A mesh-insensitivity verification can be found in the stated reference.

The equations 3.19 and 3.20 state the furthermore used definitions of d_c and d_t respectively. A comparison of the equations shows, that the approach is unified and independent of the strain direction.

$$d_c = 1 - \frac{1}{2 + a_c}\left[2(1 + a_c) \cdot e^{-b_c \epsilon_c^{in}} - a_c e^{-2b_c \epsilon_c^{in}}\right] \tag{3.19}$$

$$d_t = 1 - \frac{1}{2 + a_t}\left[2(1 + a_t) \cdot e^{-b_t \epsilon_{ct}^{in}} - a_t e^{-2b_t \epsilon_{ct}^{in}}\right] \tag{3.20}$$

The strains ϵ_c^{in} and ϵ_{ct}^{in} represent the inelastic strains in compression and tension respectively and can be calculated by subtracting the elastic strain from the total strain $\epsilon_{c/ct}^{in} = \epsilon_{c/ct} - \left(\sigma_{c/ct}/E_{cm}\right)$. While the parameters a_c and a_t are only depending on material parameters of compressive strength and tensile strength, the parameters b_c and b_t are mesh size dependent

with the inclusion of the characteristic length of the finite element l_{ch}.

$$a_c = 2\frac{f_{cm}}{f_{c0}} - 1 + \left(2\sqrt{\left(\frac{f_{cm}}{f_{c0}}\right)^2 - \frac{f_{cm}}{f_{c0}}}\right) \tag{3.21}$$

$$a_t = 2\frac{f_{ctm}}{f_{t0}} - 1 + \left(2\sqrt{\left(\frac{f_{ctm}}{f_{t0}}\right)^2 - \frac{f_{ctm}}{f_{t0}}}\right) \tag{3.22}$$

$$b_c = \frac{f_{c0} l_{eq}}{G_{ch}}\left(1 + \frac{a_c}{2}\right) \tag{3.23}$$

$$b_t = \frac{f_{t0} l_{eq}}{G_F}\left(1 + \frac{a_t}{2}\right) \tag{3.24}$$

Using equations 3.19 and 3.20 the damage parameter for any given strain exceeding ϵ_{c1} and ϵ_{t1} can be determined.

Summary of the CDPM

By applying the equations derived in the previous section, the behaviour of the concrete damaged plasticity model can be illustrated. Figure 3.8 shows the stress-strain curve for a C35/45 concrete under compression, while figure 3.9 provides the tension parameters. The damage parameter d is provided in % in both cases. The selected element size has an edge length of 20 *mm*. The here provided model will be used for the numerically derived shear-tests in section 4.5.

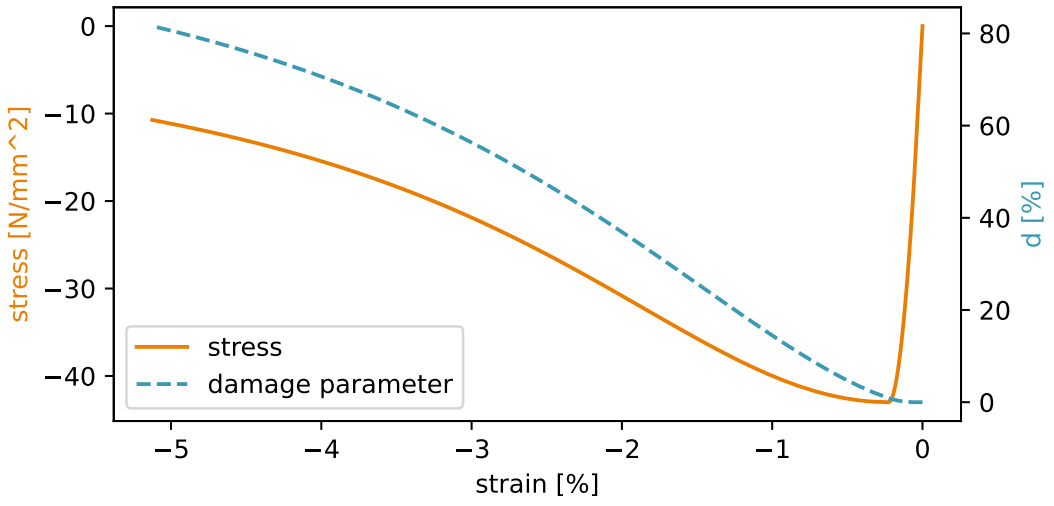

Figure 3.8.: Stress-strain and damage-strain relation of C35/45 under compression

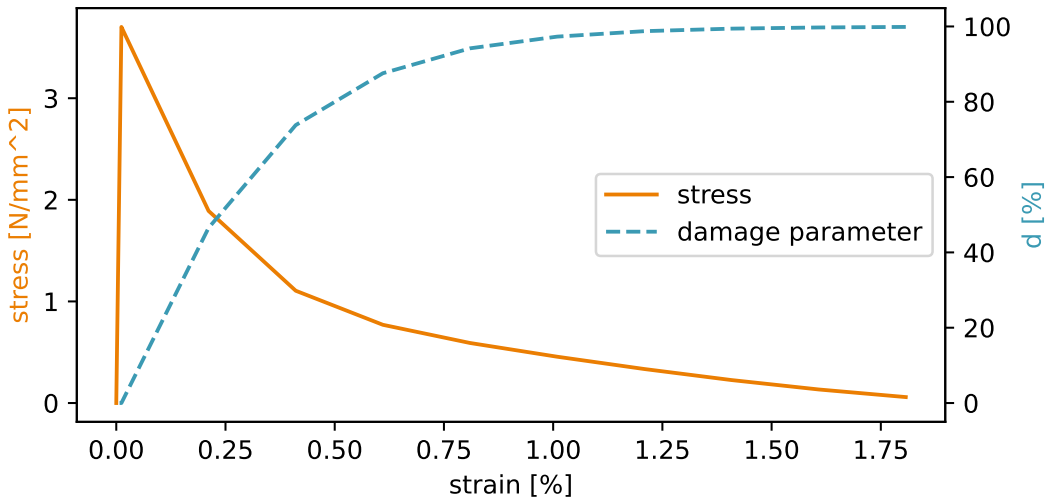

Figure 3.9.: Stress-strain and damage-strain relation of C35/45 under tension

3.2.4. Steel Material Model

Due to the homogeneous material properties of steel, the material model used for reinforcement and prestressing steel is a standard elastic-plastic material model as given in numerous standards [41, 48, 160]. Most often a bilinear stress-strain diagram is assigned to the steel. This approach will also be used in this numerical model, since the stress-strain relations of reinforcement and prestressing steel is rarely available in the experimental database.

For the steel used for support and loading plates a purely elastic material model is assumed, following the Young's modulus of 210 GPa.

3.2.5. Reinforcement

A number of factors must be considered, when selecting any modelling approach. In the case of reinforcement one of the major influence factors can be found in the definition of the bonding behaviour between the singular bars and the concrete. In case that the main interest of the simulation is within this interaction, a modelling strategy including a representation of the reinforcement as volume elements should be considered. Otherwise, if a more wholistic consideration of the reinforcement as part of a test specimen is the focus, like in the presented case, the modelling strategy should account for it, by not overvaluing certain interactions, while generalising other behaviours, like aggregate interlock (section 2.2.5) due to approximation and generalising of material behaviour.

Bonding of Concrete and Reinforcement

As touched upon in the section introduction there are different possibilities on defining the bond between reinforcement and concrete, depending on the chosen modelling approach. In general ABAQUS allows for reinforcement to be modelled as volume elements (3D-Elements) or wire elements (2D-Elements). Selecting to use 3D-Elements for the representation of the reinforcement enables the user to define the bonding in detail, including the slip criteria, friction between the steel and concrete surface and other interactions between the steel and concrete elements. Additionally the comparatively small dimensions of the reinforcement when compared to the beam would result in more extensive convergent studies and a more limited range of element sizes to counteract expected numerical problems like shear-locking and mashing. This results in a very detailed and computing cost expensive numerical model. Hence this modelling is usually done, when the main focus is set on the interaction of reinforcement and concrete, like the numerical evaluation of pull out tests [37, 49].

Especially larger specimens however are generally modelled under a more wholistic approach focusing on the load-bearing behaviour. In this case the modelling of the reinforcement is predominantly realised as 2D-Elements, that are fully embedded within the concrete. By using embedded wire reinforcement, the assumption of perfect bonding between the 2D-Elements and the 3D-Elements is being made. This assumption is applicable when studying the behaviour of the entire specimen under loading and using ripped reinforcement bars. When studying the behaviour of concrete specimens with plane reinforcement bars, this assumption needs more thorough investigation, since it may lead to unsafe results.

In addition the usage of embedded 2D-Elements is compatible with the chosen CDPM (section 3.2.3). Due to the reduction of stiffness induced by damage within the elements, the embedded elements experience the corresponding non-linear behaviour of strain happening at cracks. The pendent to *tension-softening* in the concrete [123], the *tension-stiffening* of the steel however is not necessary in accordance with [61, 91, 115, 123].

Chosen Elements

ABAQUS provides a number of truss elements, that can be used for linear 2D-Elements that are applicable for the modelling of reinforcement bars. The element type herby defines the number of integration points and the selected trial functions used for the calculation. Using an element type T3D2 f. e. only allows for truss like behaviour, neglecting bending, while the element type B31 includes the consideration of bending moments.

The T3D2 element is chosen due to the generally negligible bending stiffness of the longitudinal reinforcement and the irrelevant one for the stirrups.

Prestressing

In general there are two fundamentally different ways of modelling prestressed tendons for a finite-element analysis. A general overview can be taken from [1], which splits the modelling techniques into consideration of the prestressing as either additional loading on or additional load resisting elements in addition to the concrete member. While the first modelling technique solely focuses on the loading induced by prestressing tendons, it neglects the changes in the prestressing forces due to concrete deformation. The consideration of prestressing tendons as load resisting members similar to the previously discussed reinforcement allows for a more thorough inclusion of its effects on a reinforced concrete member [10].

When considering prestressing tendons as load resisting elements, the prestressing force needs to be introduced to a point, where the load resisting element is loaded to the same capacity as in reality. Modern finite-element software, like ABAQUS [36], allows for the prestressing of elements via certain functions. In the case of ABAQUS a predefined field can be generated, resulting in element local stresses. Alternatively a temperature change on the tendon-elements can be used to generate the prestressing load [146]. The uniformly applied temperature T in $°C$ to the prestressed elements can be determined following equation 3.25. The required variables are the coefficient of linear expansion c in $MPa/°C$, the modulus of elasticity E_p in MPa as well as the cross-sectional area of the prestressing tendon A_p in mm^2 and the desired prestressing force P in N.

$$T = -\frac{P}{c \cdot E_p A_p} \tag{3.25}$$

The chosen modelling approach follows the in [1, 10] favoured inclusion of the prestressing tendons as load resisting elements embedded in the concrete. Prestressing forces are applied using predefined fields in normal direction of the truss elements, which functioning as tendons, thus following the previously determined modelling approach for the general reinforcement.

3.3. Evaluation

3.3.1. General

A first evaluation of the modelling approach described in section 3.2 will be conducted on two beams where the load-displacement information is recorded. For the verification of the chosen element types and material models a beam without transverse reinforcement is used (section 3.3.2). Excluding any transverse reinforcement allows to focus on the usability of the CDPM as well as on the simplest and clearest load-bearing mechanisms. The second beam (section 3.3.3) will include transverse reinforcement to provide a validation of the changing load-bearing capacity this inclusion results in. Additionally it allows for a

validation of the chosen modelling approach for the reinforcement as discussed in section 3.2.5.

Both beams are taken from test series performed by `Leonhardt` and `Walther`, published in [103]. Main foci of the selection are put on the reported type of failure, recorded crack-pattern and load-displacement behaviour.

Further in-depth evaluation, using tests taken from literature, follows in section 4.3, investigating the capacity of the numerical model concerning singular changing variables.

3.3.2. Reinforced Concrete Beam without Transverse Reinforcement

The selected reinforced concrete beam without transverse reinforcement is presented in figure 3.10. As previously mentioned it is taken form [103] and failed due to sudden fracture resulting from shear. The presented test was conducted twice resulting in slightly varying points of failure which will both be presented for the numerical evaluation.

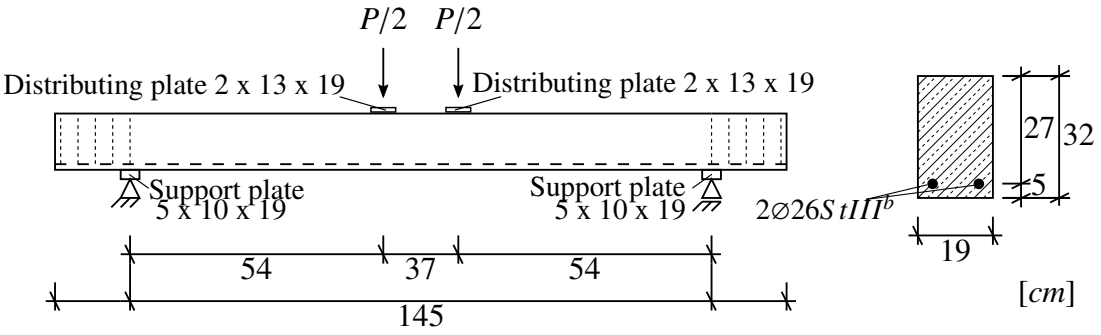

Figure 3.10.: Parameters of the tested reinforced concrete beam without shear reinforcement V3 taken from [103]

The beam was subjected to a 4-point bending experiment and did not include shear reinforcement. The material strength of the concrete was given to be 355 kg/cm^2, which, given the time period of the experiments, can be assumed to be derived from $20x20x20$ cm cubes, resulting in $\approx$ 29.2 MPa for todays cylindrical test specimens. The used reinforcement steel grade of $StIII^b$ has a nominal yield strength of 400 MPa for reinforcement with a diameter exceeding 18.0 mm and was not recorded further. The transverse reinforcement shown in figure 3.10 is located behind the supports and was only required construction wise to ensure a correct anchorage of the longitudinal reinforcement. It will not be modelled for the numerical calculation, since the longitudinal reinforcement will be taken to be fully embedded within the concrete, requiring no anchorage length to be considered. The dimensions for the support and loading plates can be taken from figure 3.10 and the purely elastic steel material is assumed as stated in section 3.2.4.

Figure 3.11 shows the calculated load-displacement curve of the numerical calculation with respect to different element sizes as well as the displacements as reported in [103]. It has to be noted, that due to the time period in which the tests were performed, the measurement of load-displacement data was not continuous via automated systems, but had to be done manually at given load intervals. Hence the displacement at the failure load is not provided by the literature.

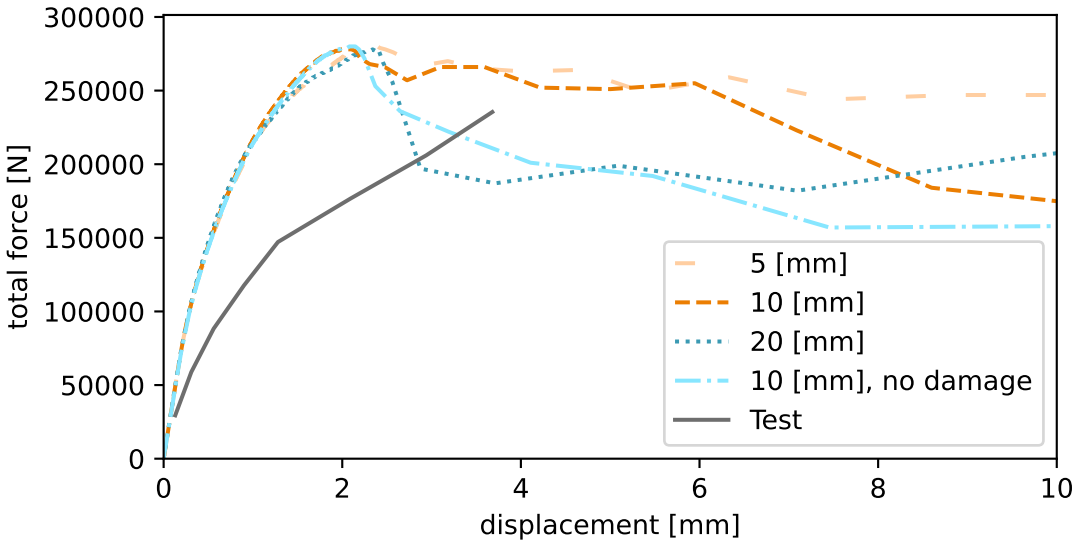

Figure 3.11.: Load-displacement diagram for V3

A mesh independent behaviour of the numerical model up to the critical load can be deduced from the load-displacement diagram, with some discrepancies being found at the post-failure behaviour. Since the post-failure behaviour however is not part of the performed investigation this can be disregarded. Henceforth, considering V3 is a beam without transverse reinforcement, the mesh independence of the concrete material model as constituted in section 3.2.3 can be confirmed for the presented case.

Additionally, even though the load-displacement curve resulting from the numerical simulation behave stiffer than the recorded values from the test, the critical load provided in table 3.1 fall within a less than 6 % range.

Table 3.1.: Critical loads of beam V3

	Test	FEM-5	FEM-10	FEM-20
P_{crit} $[kN]$	294.2	280.68	277.96	277.80

Furthermore the good relation between the numerical simulation and the physically performed test can be taken from the similarity of the critical shear crack as provided by figure 3.12. Especially at smaller mesh sizes the crack angle as well as the crack development

mimic the recorded one exceptionally well. However the predominantly visual asymmetry present at the larger element sizes needs to be addressed. Since the boundary conditions are not precisely copied by the numerical model. While the physical test setup had no actual horizontal support, the numerical model required it. Therefore one support plate was fixed horizontally, resulting in a slight asymmetry of the beams stiffness, which explains the asymmetric crack pattern.

The most prominent difference between the numerical simulated tests and the physical test now lies within the previously mentioned differing stiffness behaviour 3.11. Looking at the provided data from the literature [103] it has to be stated that, even so the concrete strength is given, no further information were provided. The previously assumed test specimen size of a $20x20x20$ *cm* cube is mentioned at a different section of the report and henceforth can be assumed to conform with the test specimen for the recorded material. It also has to be noted that this does contradict the information provided in [141] about the same test series. Since neither a stress-strain relationship, nor the Young's modulus has been provided in the original test report they were calculated, using the in section 3.2.3 introduced approach. All of this, as well as the perfectly assumed and modelled support conditions and the other previously stated assumptions and simplifications can be the origin of this recorded differences. Since the main failure criterion, that is defined by the critical load does however correspond well to the recorded values, the modelling approach can be endorsed for further usage.

3.3.3. Reinforced Concrete Beam with Transverse Reinforcement

Varying from the previously discussed beam V3 (section 3.3.2) the selected reinforced concrete beam with transverse reinforcement has a T-cross-section. Its reported type of failure is given to be shear failure resulting from plastic deformation of the transverse reinforcement leading to the destruction of the web and the compression zone [103]. The parameters of the test specimen ET3 are provided in figure 3.13.

The beam was subjected to a 4-point bending experiment and its material strength of the concrete was recorded to be 285 kg/cm^2. Given the time period and the assumed test specimen being a $20x20x20$ *cm* cubes this translate to ≈ 22.4 MPa for todays cylindric test specimen, used for the numerical simulation. While steel of the grade $StIII^b$ with a nominal yield strength of 400 MPa was used for the longitudinal reinforcements, the transverse reinforcement was made out of 6 *mm* diameter bars and a steel grade StI, corresponding to a nominal yield strength of 220 MPa. The transverse reinforcement was spaced at 11.0 *cm* between the supports and loading points. Anchorage failure was avoided by the reduced spacing of 5.0 *cm* between the supports to the specimens ends. Due to undisclosed precise location information of the reinforcement, other than the static height, a constant spacing of 5.0 *cm* was assumed for the longitudinal reinforcement, with the stirrups enclosing it. The constructively required reinforcement within the compression zone of the cross-section was ignored for the numerical model.

Crack pattern recorded by the test

Element size 5 [*mm*]

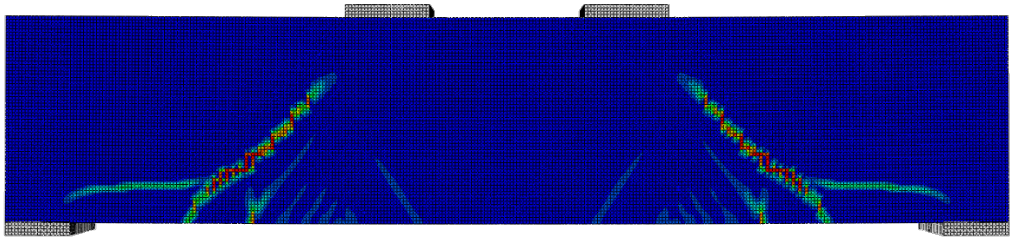

Element size 10 [*mm*]

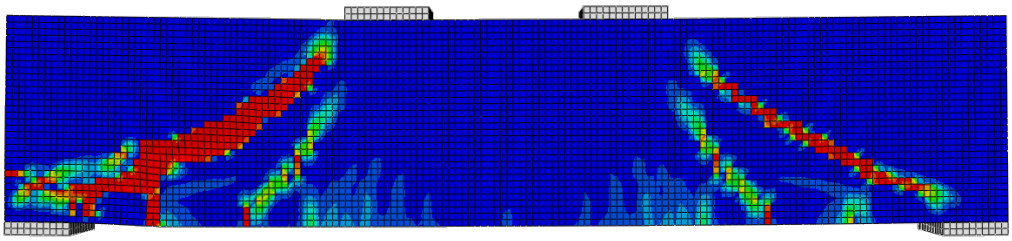

Element size 20 [*mm*]

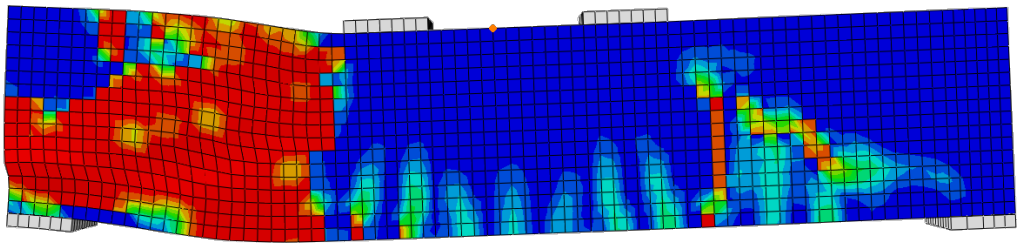

Figure 3.12.: Comparison of the numerically derived crack patterns for V3 with the literature [103]

Missing precise information, the distributing plates and support plates are assumed to be covering the entire width of the respective part of the cross-section and to have a geometry as disclosed in figure 3.13. This assumption is based on previously provided dimension from the same literature as well as the determined minor influence on the size of the loading plates [103].

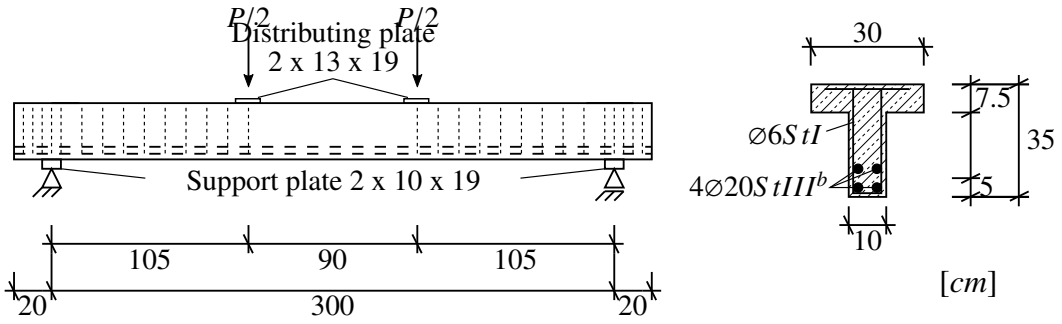

Figure 3.13.: Parameters of the reinforced concrete beam with shear reinforcement ET3 taken from [103]

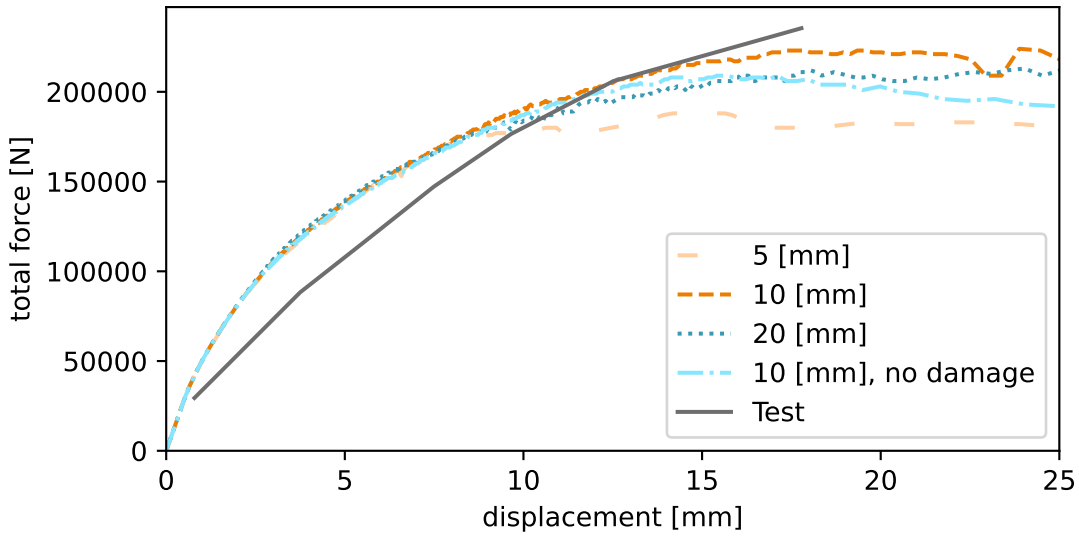

Figure 3.14.: Load-displacement diagram for ET3

Figure 3.14 provides the load-displacement curve of the numerical simulation with regards to different mesh sizes as well as the reported displacements of the test taken from [103].

At lower loads the trend of the numerical model behaving stiffer than the physical test as previously seen in section 3.3.2 can be confirmed. In contrast with the investigation of the beam without transverse reinforcement, a softening of the beam at higher loadings can be observed. This behaviour can be attributed to an underestimation of the Young's modulus, or the neglecting of aggregate interlock and dowel effects due to the modelling approach [71]. A comparison of the cracking patterns is provided in figure 3.15, showing good correlation, especially for the smaller mesh sizes.

Noteworthy, the noticeable asymmetry at the 5 *mm* elements. This stems from the asym-

Crack pattern recorded by the test

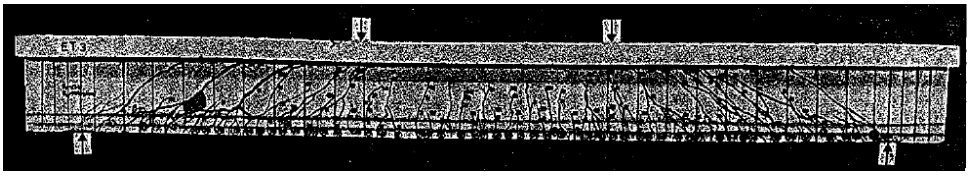

Element size 5 [*mm*]

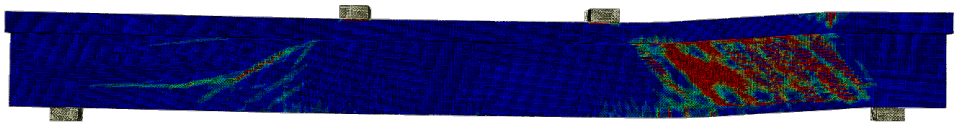

Element size 10 [*mm*]

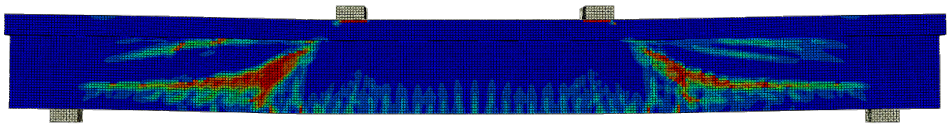

Element size 20 [*mm*]

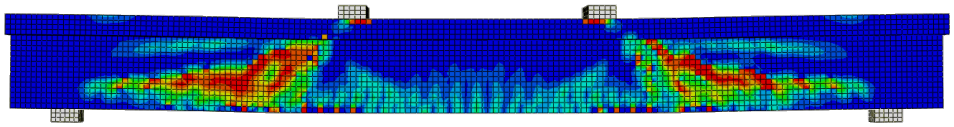

Figure 3.15.: Comparison of the numerically derived crack patterns for ET3 with the literature [103]

metric boundary conditions used in the numerical model, where only one side was fixed in beam direction. The increased cracking is located on the side without that boundary conditions.

Since neither the longitudinal nor the transversal reinforcement steel material was described in more thorough detail than their respective steel grade, the previously stated yield strength was assumed in unison with historical data. Figure 3.16 provides the stresses within the steel reinforcement in total and the transverse reinforcement in particular at failure load.

Table 3.2.: Critical loads of beam ET3

	Test	FEM-5	FEM-10	FEM-20
P_{crit} [kN]	250.07	200.77	222.01	225.69

As can be seen, the transverse reinforcement as well as the longitudinal reinforcement

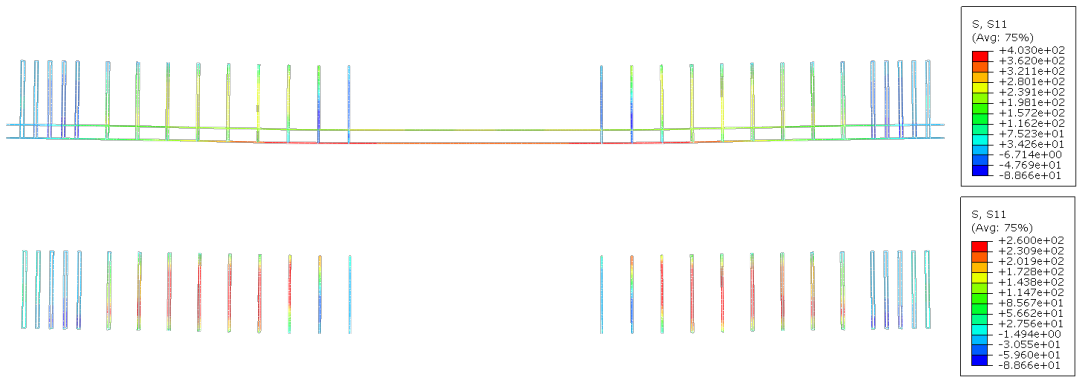

Figure 3.16.: Steel stresses for ET3 with element size of 10 [mm]

reaches plasticity after the critical shear crack has developed. Accordingly the critical load at failure is directly influenced by the yield strength present at the cracked beam location.

Due to the incomplete data of these parameters of the reinforcement in particular the variance in the stiffness near the critical load as well as the value of the critical load itself (table 3.2) can be justified.

3.4. Conclusion

Evaluation of the two tests investigated in section 3.3 provides a general understanding of the applicability of numerical simulations for the recalculation of physical tests. While the loads at failure matched well between the numerical simulations and the recorded test values, the behaviour of the beam, mainly attributed to the stiffness, showed some discrepancies. Since the load-bearing capacity as well as the damage propagation within the concrete and the resulting crack-patterns fitted well with the recorded data this can however be attributed to some modelling assumptions like the perfect tie between the support plates and the beam or the boundary conditions with the added support in beam direction. Additionally the influence of the mesh size can be defined as negligible for the presented examples. The major influence of mesh size can be determined to lie in the more precise definition of the crack pattern, which provides only a small qualitatively bonus, but does not influence the behaviour, nor the critical load when compared to the material model without the inclusion of damage parameters.

All in all a good applicability of the chosen material models and modelling approach has to be determined and will be used for the further conducted numerical simulations in section 4.3, where the capability of the numerical model is investigated on more variables.

4. Evaluation Database

4.1. Overview

In general, a database has to consist of enough separate and independent data over a range of variables to provide a reliable informative value on a given approach. Concerning shear tests on reinforced and prestressed concrete beams a database consisting of tests published has been created by cooperation of the *American Concrete Institute* (ACI) and the *Deutscher Ausschuss für Stahlbeton* (DAfStb) with regards to reinforced concrete beams without transverse reinforcement [139, 142] as well as with transverse reinforcement [140]. In light of the databases consisting purely out of single span girder tests that are predominantly tested under concentrated loading, with ≈ 70 % of them having a total beam height of less then 40.0 *cm* and only about 7.5 % having a height of 100.0 *cm* or more, a bias towards small beams can be assumed when performing any kind of statistical evaluation on the database. In light of shear-critical beams, as discussed in chapter 1, usually exceeding of least 50.0 *cm* in height and the possibility of resulting scale effects an evaluation of shear-formulas and -models based on these databases needs to be viewed critically.

As the developed approach is aimed at evaluating existing structures, mainly bridges, it has to be concluded, that a validation based purely on the aforementioned databases can not be assumed to be accurate. Especially in light of the major difference in stresses, resulting form different loading and structural systems, when comparing multi-span bridge girders with the experimental database, a different approach is to be pursued. The focus on construction related configurations of the reinforced concrete member also excludes any experiments without transverse reinforcement. Hence a small database was created numerically that covers a number of relevant variations as well as realistic dimensions (section 4.5).

Attempting to mimic the principles of the *Design of Experiments* (DoE) [161] (section 4.2), pairs of tests are taken from the recorded databases to represent maxima and minima of the specific influence factors, whereas the rest of the defined influence factors are kept as similar as possible. Seeing as the selected tests to validate the numerical model (section 4.3) are taken from a number of different researchers, studying varying aspects of shear within reinforced concrete members over multiple decades, some leeway from the ideal theoretical tests has to be accepted. An overview of the applicability and representability of the numerical approach on the basis of physical tests is provided in section 4.4.

4.2. Design of Experiments

When investigating a system, there is a controllable input which leads, under consideration of interferences, to a result (figure 4.1). The so called *Design of Experiments* (DoE) was founded to describe and explain the variation of information and their influences. Therefore the DoE encompasses methods aimed to analyse the relation of input variables to results.

One of the most well known methods for generating test data using simulation is the Monte-Carlo-Method (MCM) [11, 94, 124]. It is usually used in computer-aided engineering (CAE), since the required amount of test combinations can not be achieved by physical test setups. Hence different methods were created prior to the spread of numerical methods. The DoE describes a statistical approach to the design of test specimens, generally developed for physical tests and later on extended to CAE [155, 161].

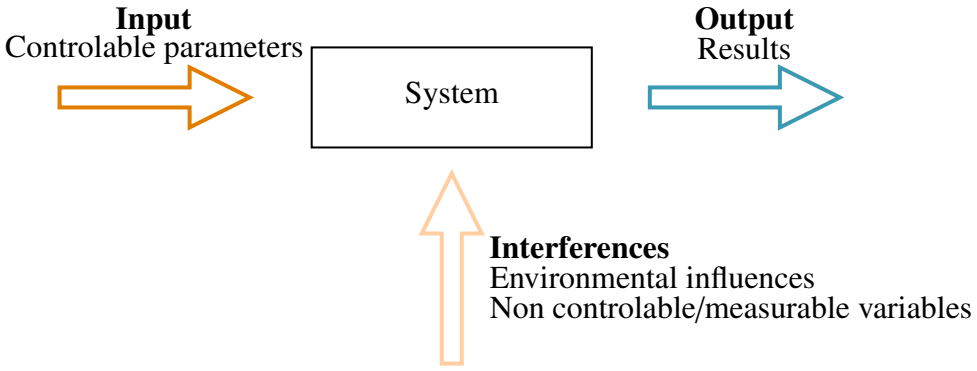

Figure 4.1.: System visualisation for DoE

As soon as multiple input variables are to be included in a test study the full factorized design should be considered. Here every combination of input variables are included in the tests. Depending on the required level for each variable n_l, meaning the gradation to account for non-linear effects, this leads to:

$$n_r = n_l^{n_f} \tag{4.1}$$

required tests, with n_f being the number of variables, also known as factors. Following equation 4.1 the amount of tests required to cover seven factors being investigated at two levels results in 128 test specimens. If quadratic effects are assumed and correspondingly the required level raised to three, the resulting number of test specimens accumulates to 2187. Since these numbers are often impossible achieve physically due to time and costs, restrictions methods like the so called *Screening Design* (e.g. Definitive Screening Design [85, 112]) or the *Central-Composite-Design* (CCD) were developed [161].

While the previously described test specimens following the full factorised design, it can be imagined as the corner points of a n-dimensional dice, in case of a second level investigation, where n symbolises the number of investigated variables (e.g. for three variables

the resulting shape in the three-dimensional space is a cube as shown in figure 4.2), the CCD adds additional tests in the centre points of the surfaces. These additional tests can be imagined as the tips of a star shape, with every tip centring in the surfaces of the dice, and the centre point of the dice. These additional tests are designed to determine any non-linearity of the variables. To allow for the most precise results these additional tests should exceed the defined variable ranges in the positive as well as the negative direction. If, due to limitations, this exceedance can not be achieved a special case of the CCD is derived. The so called *Face-Centered-Central-Composite-Design* (FCCCD) is depicted in figure 4.2 for the three-dimensional space. As can be seen for the FCCCD the star (light orange), sits on the faces of the dice limited by the defined variable ranges (orange).

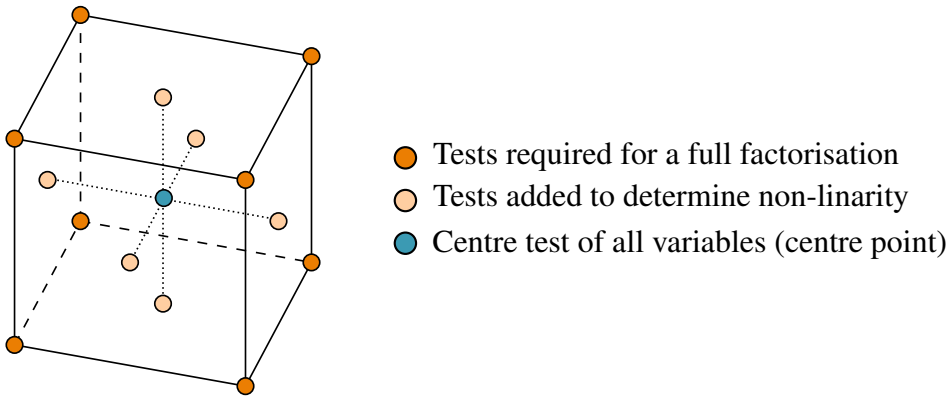

Figure 4.2.: Face-Centered-Central-Composite-Design for a level two investigation of three factors

The CCD does provide more thorough understanding of the relations between input parameters and measured output when compared to the FCCCD [161]. However additional test series can be conceptualised in case achieved results from the FCCCD warrant a more precise investigation.

4.3. Composition of the Experimental Database

4.3.1. General

Seeing the need for an unbiased evaluation, that confirms the general applicability of a shear model, this section briefly introduces the tests, which form the cornerstones of the validation of the numerical model. To ensure maximum applicability, the chosen tests encompass a number of shear influencing factors defined in section 2.3 (section 4.3.3). Before diving into the topic of shear influences, the general accuracy of the numerical model has to be validated using a set of basic experiments to control the influence of different shear-bearing mechanisms. Especially the correct influence of the transverse and the longitudinal reinforcement, as well as the concrete strength needs to be verified (section 4.3.2). Every

numerical model will be calculated using three different mesh sizes, following the progression of 1 : 2 : 4, to evaluate the possibility of mesh dependencies for each investigated aspect on the shear-bearing capacity of reinforced and prestressed concrete slender beams.

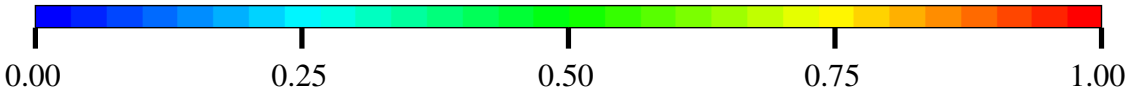

Figure 4.3.: Legend scale for tension damage factor d_t

Figure 4.3 provides the legend scale for the tension damage factor for all numerical results in this section. It is equivalent to the tension damage factor d_t from section 3.2.3.

Further clarification has to be noted for the provided load-displacement diagrams in the following sections. Since some of the recorded tests from the literature were performed at a time without the ability of continuously recording and measurement of data, some load-displacement curves do not provide the final deformation at the point of failure, but rather the last loading step prior to it, at which a manual measurement of the beams deformation was taken. Hence the shown load-displacement diagrams do not coincide with the recorded failure load, that is also provided and discussed.

4.3.2. Benchmark Experiments

Experiments Concerning the Influence of Transverse Reinforcement

As discussed in section 2.2.6 the transverse reinforcement is the major load-bearing mechanism attributed with the shear-bearing capacity of a reinforced concrete beam. Being able to tune the shear load-bearing capacity of a reinforced concrete beam without needing to adjust the cross-section is the most influential property of reinforcement in general and for stirrup in particular. Hence there has been a huge number of tests being performed with the focus on the transverse reinforcement of reinforced concrete beams [105, 134, 140, 176].

Concerning the influence of the transverse reinforcement two main variables need to be investigated. The first being the amount of transverse reinforcement, while the second focuses on the spacing of it. Both of these factors can be linked via the variable ρ_t, which expresses the amount of transverse reinforcement for a one meter long section of the beam.

The investigated pair of tests was conducted by `Leonhardt` and `Walther` and published in [105]. The test setup was a single span girder beam with a span length of $3,00\ m$ and a T-shaped cross-section. According to the documented results the test TA13 failed due to bending-shear, while TA4's mode of failure was due to plasticity of the transverse reinforcement. Figure 4.4 provides the experimental set up as well as the geometry.

As previously mentioned, the major difference between the tests TA4 and TA13 is the amount of transverse reinforcement, namely the cross-section of it. While the first mentioned was fitted with $\varnothing 6\ mm$ stirrups, the latter had double the diameter with $\varnothing 12\ mm$

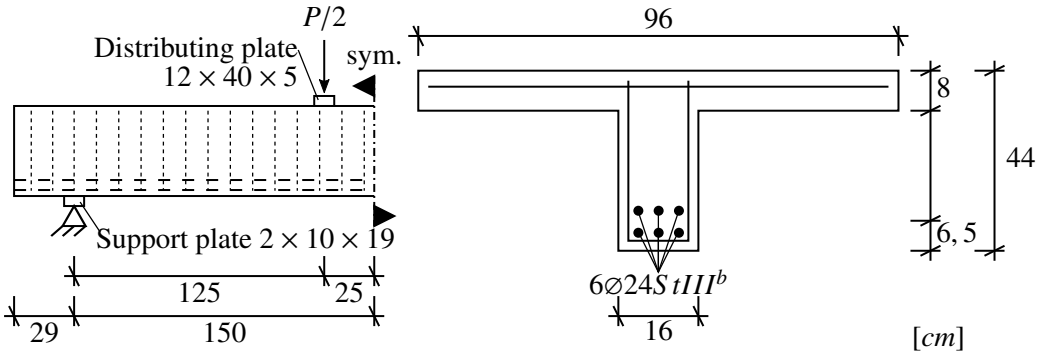

Figure 4.4.: Dimensions and geometry of transverse reinforcement tests TA4 & TA13 taken from [105]

stirrups. The spacing between the transverse reinforcement is constant at $113,0\ mm$. Furthermore the concrete strength varied slightly between the two tests. All required variables for the tests are summarised in table 4.1.

Table 4.1.: Material properties of beams TA4 and TA13 from [105]

	TA4	TA13
concrete strength		
$f_{ck,cyl}\ [N/mm^2]$	$\approx 15,0$	$\approx 17,8$
longitudinal reinforcement		
$\varnothing\ [mm]$	$24,0$	
$f_{y,l}\ [N/mm^2]$	$\approx 410,0$	
$E_{y,l}\ [N/mm^2]$	$\approx 200.000,0$	
transverse reinforcement bars		
$\varnothing\ [mm]$	$6,0$	$12,0$
$f_{y,t}\ [N/mm^2]$	$\approx 427,0$	$\approx 440,0$
$E_{y,t}\ [N/mm^2]$	$\approx 190.000,0$	$\approx 205.000,0$

One minor difference between the tests discussed here, is the strengthening of the longitudinal reinforcement's anchorage done for TA13 in comparison with TA4. The reason for this was slipping of the longitudinal reinforcement for TA1 - TA3, which were identical to TA4. Since TA4 did not show any slip, the numerical model will include the strengthening done for TA13 for both beams, which is already included in figure 4.4. For the tests two different kinds of strengthening where performed. At one end a doubling of the anchorage length was done, while at the other end 'anchorage rebars' were implemented. Since, the reinforcement is assumed to be fully embedded (section 3.2.5), neither modification should influence the simulation results.

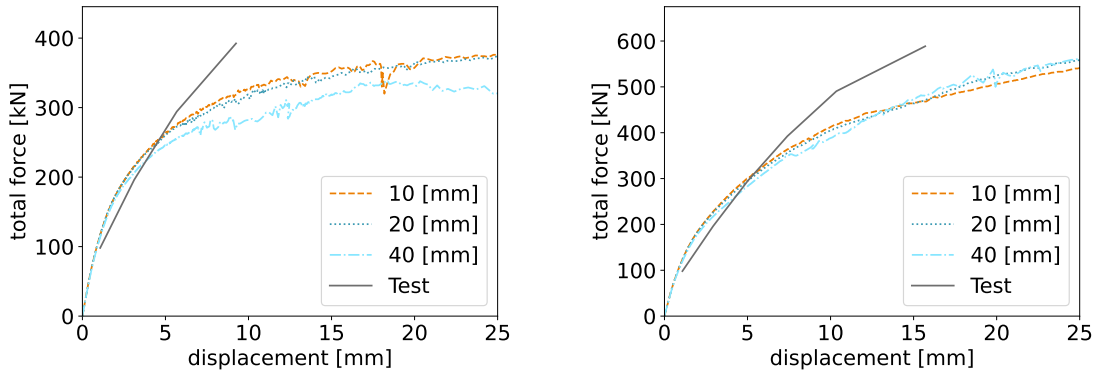

Figure 4.5.: Load-displacement diagrams for TA4 (a) and TA13 (b)

The general trend already mentioned in section 3.3 of the numerical test being softer than the physical test can be seen in the load-displacement diagrams given in figure 4.5. While the load-displacement curves for the physical tests also show a softening of the test specimen at approximately similar loads, the numerical model does show a far greater reduction of its stiffness. This effect can be attributed to the development of cracks, the final stages of them being provided in figures 4.6 and 4.7.

While the crack patterns and crack development of the numerical models provides a similar behaviour as the recorded test information, additional effects like dowel action and aggregate interlock, more simply put as friction, are not present in the chosen modelling approach. Another influence can be attributed to the application of the load. Since the discussed tests were performed using force controlled loading [105], the simulation also was performed using the load as the controlling variable. As previously discussed in section 3.3 this can lead to higher critical loads and less specific points of failure when compared to displacement controlled tests.

Additionally the incomplete data concerning material parameters like the concrete tension strength, which generally can vary rather strongly, can also impact the results which can be achieved by numerical simulation.

Next to the good comparison of the numerically achieved crack patterns to the recorded ones, the critical loads provided in table 4.2 show a good correlation between physical test and numerical simulation in the case of varying transverse reinforcement.

The variation of the critical load between the physical test and the numerical simulation has a maximum divergence of less than 15%, with most of them being less than 10%. The influence of the transverse reinforcement can therefore be seen as being accurately represented in the numerical simulation.

It must be noted, that the numerical simulation was able to replicate the tests behaviour in light of the varying transverse reinforcement correctly. The deviations between the numer-

Crack pattern recorded by the test

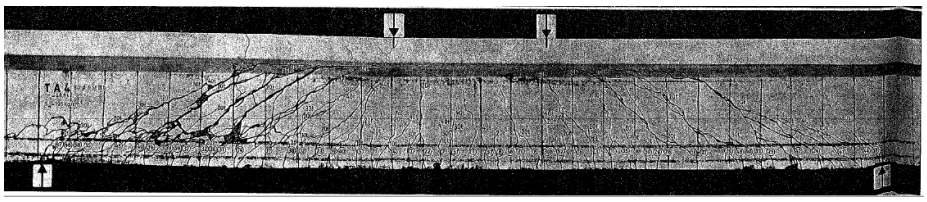

Element size 10 *mm*

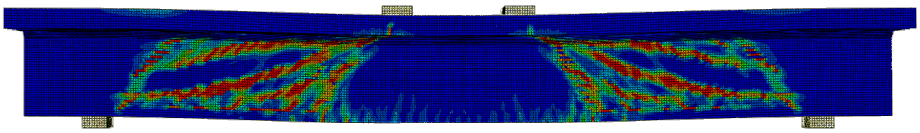

Element size 20 *mm*

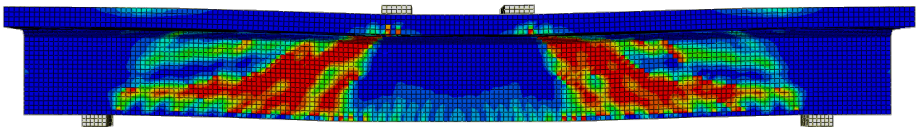

Element size 40 *mm*

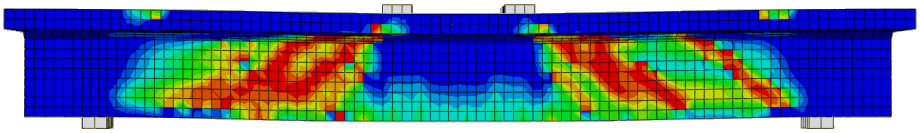

Figure 4.6.: Comparison of the numerically derived crack patterns for TA4 with the literature [105]

Table 4.2.: Critical Loads of beams TA4 and TA13

	TA4	TA13
$P_{crit,test}$ $[kN]$	$458,95$	$686,47$
$P_{crit,FEM,10}$ $[kN]$	$389,05$	$615,07$
$P_{crit,FEM,20}$ $[kN]$	$404,77$	$642,11$
$P_{crit,FEM,40}$ $[kN]$	$422,21$	$642,35$

ical and the recorded data are present at both tests to the same degree and can be attributed to incomplete data and approximations made by the numerical model.

Experiments Concerning the Influence of Prestressing

Since prestressing can have an influence on the shear-bearing capacity of reinforced concrete beams 2.2.8, it has to be ensured that it is correctly accounted for in the numerical simulation. For this reason a comparison between two prestressed concrete beams with

Crack pattern recorded by the test

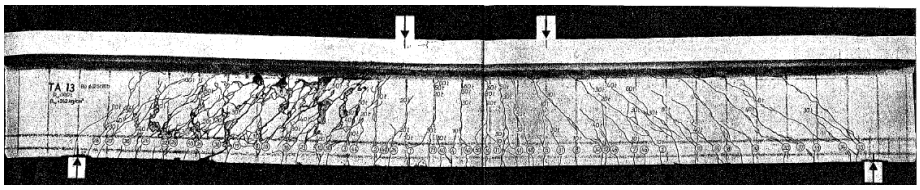

Element size 10 *mm*

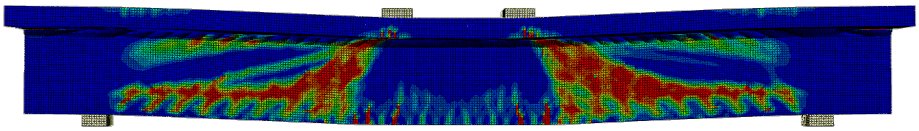

Element size 20 *mm*

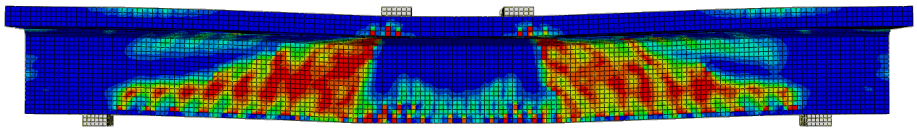

Element size 40 *mm*

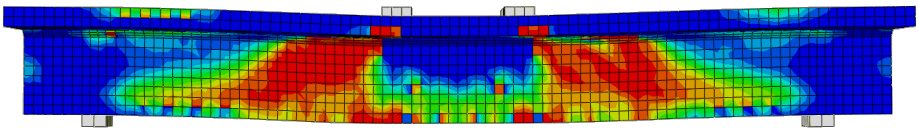

Figure 4.7.: Comparison of the numerically derived crack patterns for TA13 with the literature [105]

differing degrees of prestressing force is analysed. The selected tests are taken from [102] (IP1 and IP3) and are shown in figure 4.8.

As it can be gathered from figure 4.8, the cross-section of the selected test specimens follows an I-shape and the two prestressing tendons are parallel to the bottom flange. The tendons were made up of 12 individual strands with diameters of 12.2 *mm* each and a steel grade of $SIGMA\ St\ 125/140$ with $b_{0,2}$ of 1201.3 N/mm^2. Further material parameters are given in table 4.3.

Since the concrete strength was tested on $20 \times 20 \times 20$ *cm* cubes table 4.3 already includes the conversion following [110] to todays standard of a $30/15$ *cm* cylinder.

While IP1 was prestressed to the maximum allowed force of $\approx$ 995.4 *kN* per tendon, IP3 was only subjected to a prestressing of 99.5 *kN*, corresponding to about 10% of the allowed prestressing force. These forces however decreased to 890.9 *kN* and 90.2 *kN* per tendon for IP1 and IP3 respectively at the time of testing due to the time-depending behaviour of concrete - creep, shrinkage - and anchor-slip.

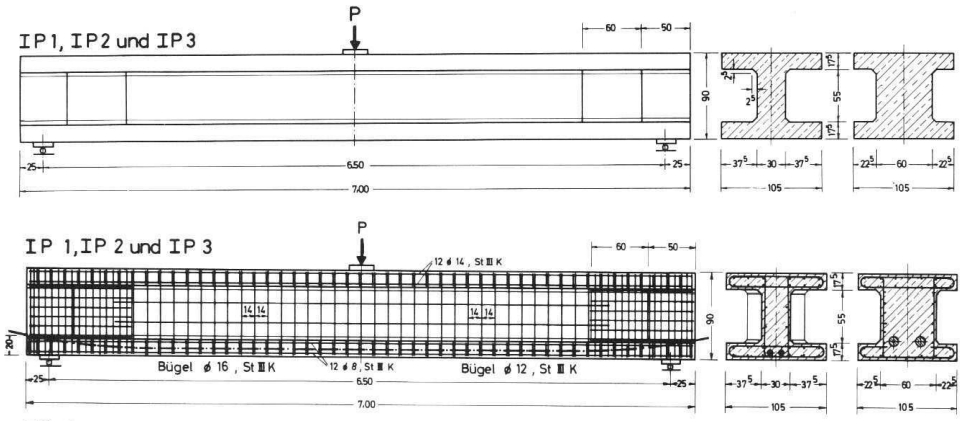

Figure 4.8.: Dimensions and geometry of prestressing tests taken from [102]

Table 4.3.: Material properties of beams IP1 and IP3 from [102]

concrete strength		
	IP1	IP3
$f_{ck,cyl}$ $[N/mm^2]$	≈ 25.9	≈ 29.5
E_{ck}	≈ 26772.2	≈ 26085.7
longitudinal reinforcement		
	Web/Flange Bottom	Flange Top
∅ $[mm]$	8.0	14.0
$f_{y,l}$ $[N/mm^2]$	≈ 451.1	≈ 389.3
$E_{y,l}$ $[N/mm^2]$	≈ 195,000.0	≈ 200,000.0
transverse reinforcement bars		
	IP1	
∅ $[mm]$	12.0	16.0
$f_{y,t}$ $[N/mm^2]$	≈ 490.0	≈ 392.0
$E_{y,t}$ $[N/mm^2]$	≈ 200,000.0	≈ 191,230.0
	IP3	
∅ $[mm]$	12.0	16.0
$f_{y,t}$ $[N/mm^2]$	≈ 505.0	≈ 470.0
$E_{y,t}$ $[N/mm^2]$	≈ 201,000.0	≈ 198,000.0
prestressing tendons		
A_p $[mm^2]$	≈ 1403.0	
f_p $[N/mm^2]$	≈ 1200.0	
E_p $[N/mm^2]$	≈ 200,000.0	

The load-displacement diagrams for the underside of the beam at mid-span is given by figure 4.9. While it shows a great fit for the strongly prestressed IP1, including the negative deformation resulting from the prestressing before loading, a slightly stronger difference

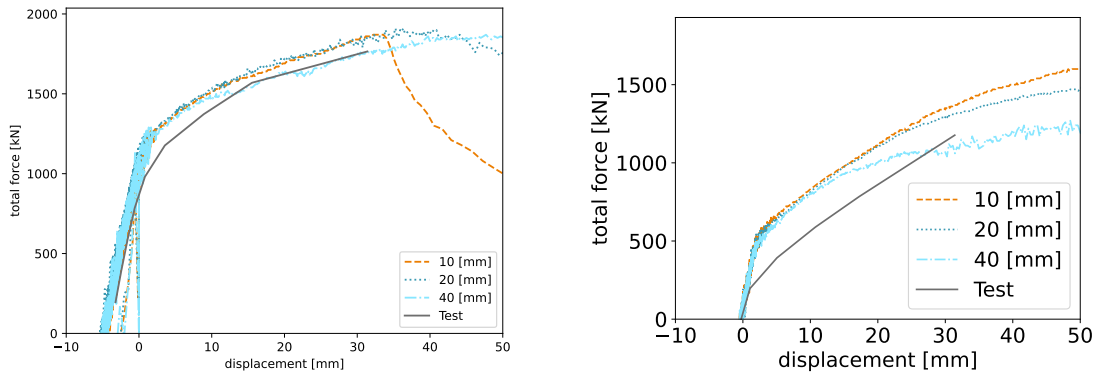

(a) (b)

Figure 4.9.: Load-displacement diagrams for IP1 (a) and IP3 (b)

can be seen for the less prestressed IP3. However this results mostly from the pre-crack-behaviour of the concrete, due to possibly incomplete data. The post-cracking increase in loading follows the test astonishingly well, like it does for IP3. Even so slight decrease of quality can be determined for the largest element size of 40 *mm* edge length when compared to the smaller ones.

The crack-patterns as shown in figures 4.10 and 4.11 need to be discussed more closely since a clear change of quality can be seen for them between IP1 and IP3. While IP1 on the one hand is represented well in the numerical simulation, even so fewer cracks did form than are shown in the test report, their direction, even the ones resulting from direct arching action, can be clearly determined. Like previously discussed the increasing mesh size again leads to less defined cracks.

IP3 on the other hand seems to be a rather different story. While the smallest element size does show good agreement with the test report, the larger element sizes seem to show the beam to be completely damaged due to tension. Taking the load-displacement diagram (figure 4.9) into account and the fact that the crack-patterns were recorded for the same loading prior to failure the conclusion that the larger elements are able to display the rather tightly spaced cracks, resulting from the high amount of reinforcement present in the beam, correctly is reached. Correspondingly this needs to be taken into account when evaluating likewise tests with a high reinforcement ratio using the CDPM. The good agreement of the critical load (table 4.4) with less than 7.5 % in total and less than 3.5 % when comparing the numerical results further highlights the separation between the visually represented crack-patterns and the actual calculated results concerning the shear-bearing capacity.

In light of the tests IP1 and IP3 it can be stated, that the influence of prestressing reinforced concrete beams is captured accurately by the numerical model. Especially IP1 shows a good fit of the load-deformation curve as well as the critical load highlighting the numerical implementation of the prestressing. IP3 needs to be viewed more critically when focusing on the critical load, which has a much higher discrepancy. However, when studying the load

Crack pattern recorded by the test

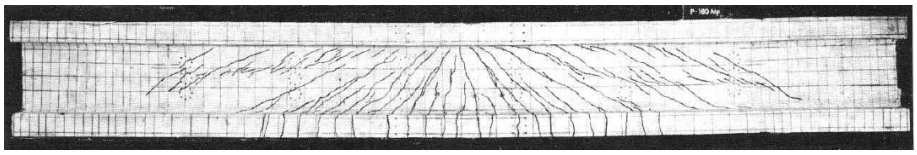

Element size 10 *mm*

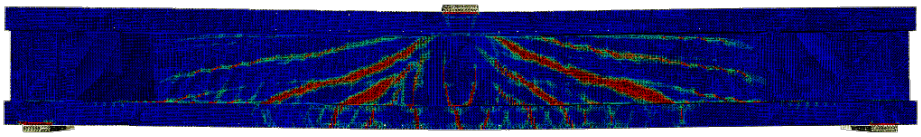

Element size 20 *mm*

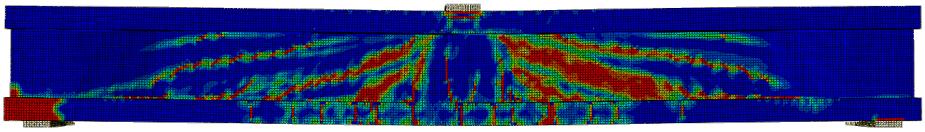

Element size 40 *mm*

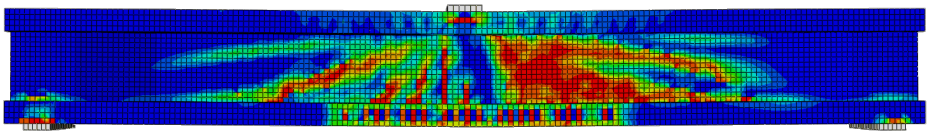

Figure 4.10.: Comparison of the numerically derived crack patterns for IP1 with the literature [102]

Table 4.4.: Critical Loads of beams IP1 and IP3

	IP1	IP3
$P_{crit,test}$ $[kN]$	1,897.59	1,701.45
$P_{crit,FEM,10}$ $[kN]$	1,873.94	1,780.06
$P_{crit,FEM,20}$ $[kN]$	1,914.08	1,769.51
$P_{crit,FEM,40}$ $[kN]$	1,862.32	1,829.89

displacement curve a similar behaviour can be seen with the sole difference being the point of crack initiation, aka the end of the elastic deformation. Subtracting the elastic influence it has to be stated, that the plastic behaviour of the numerical model does follow the recorded test behaviour exceptionally well. Figure 4.12 does provide the load-displacement curves for IP3 with and without prestressing.

Seeing as the elastic deformation of the recorded test data still fails prior to the numerical simulation where the prestressing force is neglected, the difference must be found in the

Crack pattern recorded by the test

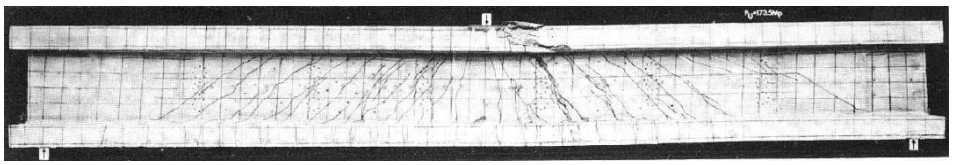

Element size 10 *mm*

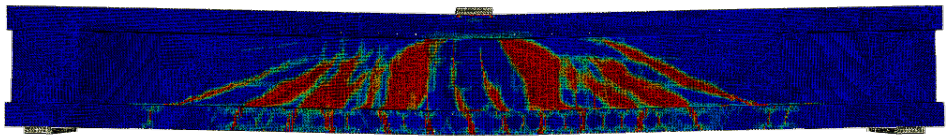

Element size 20 *mm*

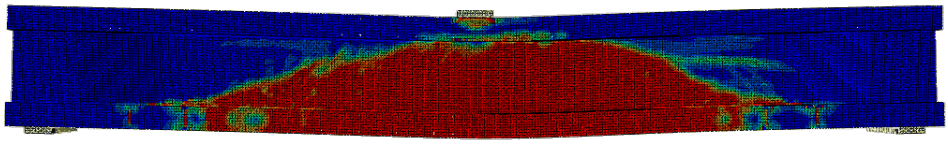

Element size 40 *mm*

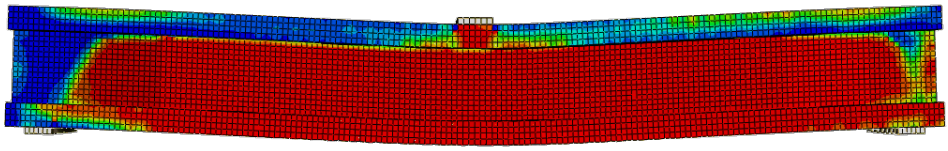

Figure 4.11.: Comparison of the numerically derived crack patterns for IP3 with the literature [102]

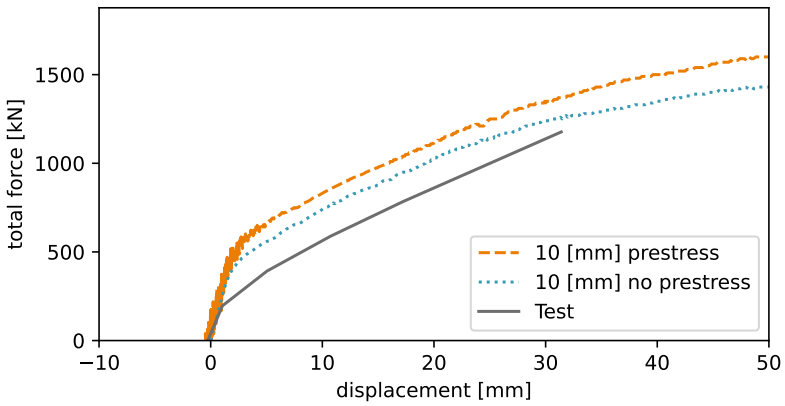

Figure 4.12.: Load-displacement diagrams for IP3 with and without prestressing

material, geometrical inconsistencies or damages. Since the test was taken from the literature a detailed analysis on the exact reasons for the discrepancies can not be made, but

should not fault the quality of the numerical simulation concerning prestressing.

Since the general behaviour and trend does, however, follow the test data and a clear influence of the prestressing force can be seen between IP1 and IP3 as well as in figure 4.12 it has to be stated that the influence of prestressing is represented well in the numerical modelling approach and simulations.

Experiments Concerning the Influence of Concrete Strength

Any influence can best be measured when other mechanisms are eliminated. Hence the impact of varying concrete strengths on the shear bearing capacity of reinforced concrete beams should be evaluated on the basis of tests performed on beams without transverse reinforcement. `Angelakos's` showed for this case that no measurable influence of the varying concrete strength (20 MPa to 80 MPa) was existent [9]. Same results have also been recorded by [66, 105].

The addition of transverse reinforcements however showcases a split in behaviour between normal strength concrete and high strength concrete. Within each of these two categories the influence of the concrete strength was negligible, but a clear difference when comparing them needs to be taken into account. This phenomenon is also seen in recent tests on ultra high performance concrete (UHPC) [6]. Since the focus of the presented work is based around the evaluation of existing structures, high performance concrete and UHPC are not regarded further. For future applications however this topic should be revisited.

4.3.3. Influence Experiments

Experiments Concerning the Influence of Loading Conditions

A rarely investigated, but important influence factor on the shear capacity of reinforced concrete beams presents itself in the loading conditions as discussed in section 2.3.4. Since the numerical model consists of 3-D volumetric elements the correct stress distribution within the modelled reinforced concrete beam is supposed to be reached. However the extend of its influence on the selected modelling approach needs to be quantified. For this verification the previously investigated test V3 (section 3.3.2) will be paired with test V11/1 from the same reference [103].

Both tests share the same cross-section as well as reinforcement, however, varied slightly in its span-length ($1,45\ m$ for V3 and $1,50\ m$ for V11/1) as well as their concrete strength. While the test setup of V3 can be found in figure 3.10, the one for V11/1 is given by figure 4.13.

To allow for an easy comparison of the two beams the material properties are given in table 4.5.

As discussed in section 3.3.2, due to a lack of information in the yield strength of the reinforcement a yield strength of 400.0 N/mm^2 was used in the finite-element calculation.

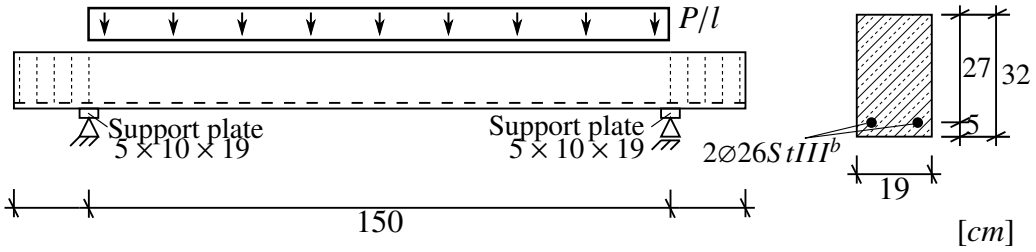

Figure 4.13.: Parameters of the reinforced concrete beam without shear reinforcement V11/1 taken from [103]

Table 4.5.: Material properties of beams V3 and V11/1 from [103]

	V3-1	V11/1
concrete strength		
$f_{ck,cyl}$ $[N/mm^2]$	≈ 29.2	≈ 31.1
longitudinal reinforcement		
∅ $[mm]$	24.0	
$f_{y,l}$ $[N/mm^2]$	≈ 400.0	

While the test V3 was loaded using loading plates with known properties, the uniformly distributed load in test V11/1 was introduced using a fire hose as distribution surface between the loading press and the beam to ensure a constant stress over the beam, even when deformed. In the numerical model the distributed load is introduced directly on the beam surface making use of a pressure field, which distributes the load directly on the surface nodes independent on their current deformation. This also ensures the ideally perfectly constant load distribution along the beam axis. Figure 4.14 provides the load-displacement curves for tests V3 and V11/1.

While the load-displacement curve for beam V3 has been discussed in detail in section 3.3.2, it shows a great fit for V11, with small discrepancies concerning the large mesh size. Especially when compared to V11 it shows a much better correlation to the recorded test data, furthermore confirming the chosen material model and modelling approach as being capable of providing realistic data and depicting the real specimen behaviour adequately.

The crack-patterns provided in figures 4.15 and 4.16 further attest the capabilities of the numerical model. Keeping in mind that both beams did not include transverse reinforcement the development of a shear-crack leads to sudden failure. Hence the crack patterns at failure for V3 (figure 4.15) being partially provided post failure, where part of the beam is already destroyed. The distributed loading on V11 on the other-hand allows for a more gradual development of the shear-crack resulting in a better comparison between the recorded crack pattern and the numerical representation.

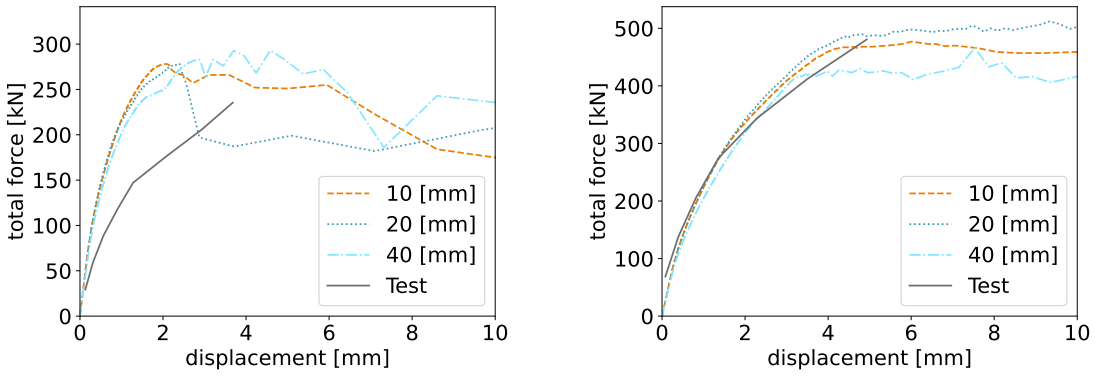

Figure 4.14.: Load-displacement diagrams for V3 (a) and V11 (b)

Crack pattern recorded by the test

Element size 10 *mm*

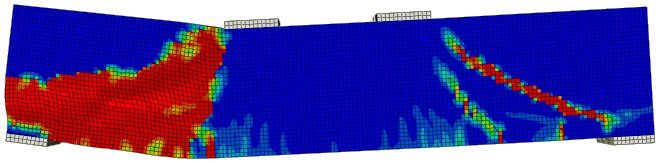

Element size 20 *mm*

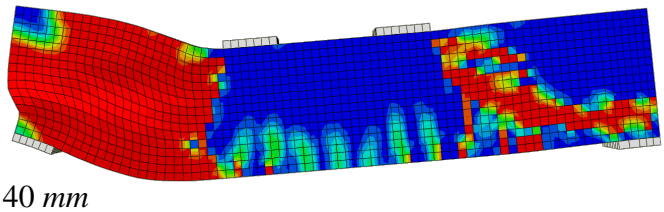

Element size 40 *mm*

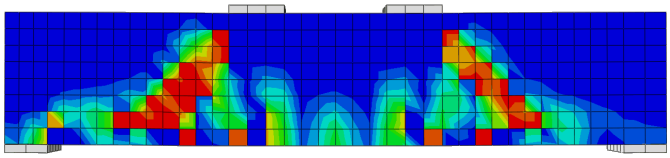

Figure 4.15.: Comparison of the numerically derived crack patterns for V3 with the literature [103]

The comparison of the critical loads (table 4.6) does confirm the previously stated tenden-

Crack pattern recorded by the test

Element size 10 *mm*

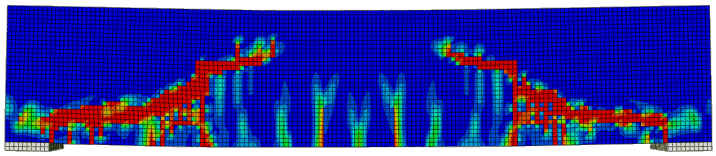

Element size 20 *mm*

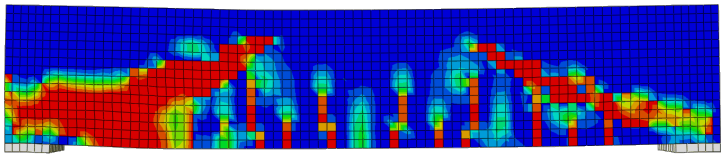

Element size 40 *mm*

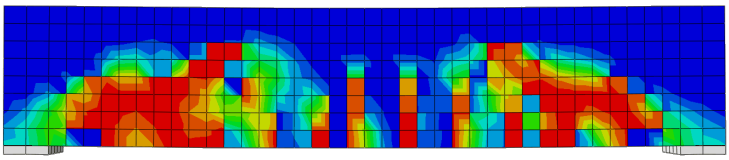

Figure 4.16.: Comparison of the numerically derived crack patterns for V11 with the literature [103]

Table 4.6.: Critical Loads of beams V3 and V11

	V3-1	V11/1
$P_{crit,test}$ $[kN]$	294, 2	535.44
$P_{crit,FEM,10}$ $[kN]$	277, 96	477, 09
$P_{crit,FEM,20}$ $[kN]$	277, 80	504, 78
$P_{crit,FEM,40}$ $[kN]$	277, 84	439, 52

cies, with only the 40 *mm* mesh size for V11 strafing further from the reported test results.

In conclusion of the comparison of V3 and V11 it has to be stated, that, the numerical model was able to thoroughly compute the different types of loading.

4.4. Summary of the Experimental Database

Remodelling existing experiments provides some further insight in the applicability of numerical simulations for the case of shear failure in reinforced and prestressed concrete slender beams. While the generally expected convergence with reducing element size can be seen in all highlighted tests of section 4.3 some details need to be pointed out.

- Firstly the point of failure can be seen more clearly the smaller the element size was chosen. This is mostly due to the nature of running a force controlled test. If the tests were rerun using a displacement controlled loading, the cut-off points would be seen more prominently for larger elements as well.

- Secondly the good fit of the behaviour of the numerical model across the different element sizes. Seeing the very similar behaviour does confirm the adjustments made in 3.2.3 to account for the changing element size.

- Thirdly the trend of a decrease in critical load with regards to smaller numerical element sizes. It has to be stated, that the decrease is minimal with it being $< 5\%$ for every element step, and an expected variance due to the explicit solver. While this effect is linked to the first point, it does not, however, result from the nature of the loading control, but from the inclusion of the damage propagation. By introducing tension and compression damage in the material model (section 3.2.3) the ability of an element focused weakening of the structure is given, which is visualised in the crack-patterns. Since this weakening is linked to the volume of the element it can not be translated coherently and directly for different element sizes, leading to different areas being weakened to different degrees. With reduced element size a more prominent weakening at the same strain is realistic, since the physically forming crack is smeared over a smaller area. As by-product of this the failure load can be determined more precisely for smaller element sizes.

- Fourthly the visualisations of the crack-patterns do greatly improve with decreasing numerical element size. As stated in the previous detail, this effect is directly linked to the material model and its method of introducing material weakening on an element basis.

To summarize the remodelling of existing experiments it can be stated that the chosen modelling approach and all its decisions as provided in chapter 3 provide good results and can be applied to theoretical as well as design problems. For further evaluations an element size of $20 \times 20 \times 20$ *cm* will be used as they provide results with the required degree of accuracy.

4.5. Numerical Database

4.5.1. Test series

As previously stated the need for an unbiased database can be gathered from the limited variance the test databases [139, 140] provide due to physical limitations of sensible test setups. Nowadays more real-size tests are performed like shown in [53, 62], however they are limited to a small number and can rarely be used in the sense of a test series, since there usually are not multiple tests with varying parameters when it comes to large scale tests setups.

Hence the need for a numerically derived database of simulated tests arises. As discussed in section 4.4 numerically simulated tests can not account for every physically present aspect and effect concerning shear-tests in reinforced and prestressed concrete beams. However the general influences and trends as seen in the physical tests can also be seen in the numerical simulations, when using the approach as described in chapter 3. More detailed models might be capable of including additional effects like bond-slip, dowel action (section 2.2.7) or aggregate interlock (section 2.2.5). Since the proposed engineering model (chapter 5) focuses on a global approach it is vital not to get tangled up in local effects, which in the end could even obscure or have interplay with the monitored influences. An extension of the proposed numerical model should be considered under these aspects. Any modification requires further detailed analysis of any added parameters and influences.

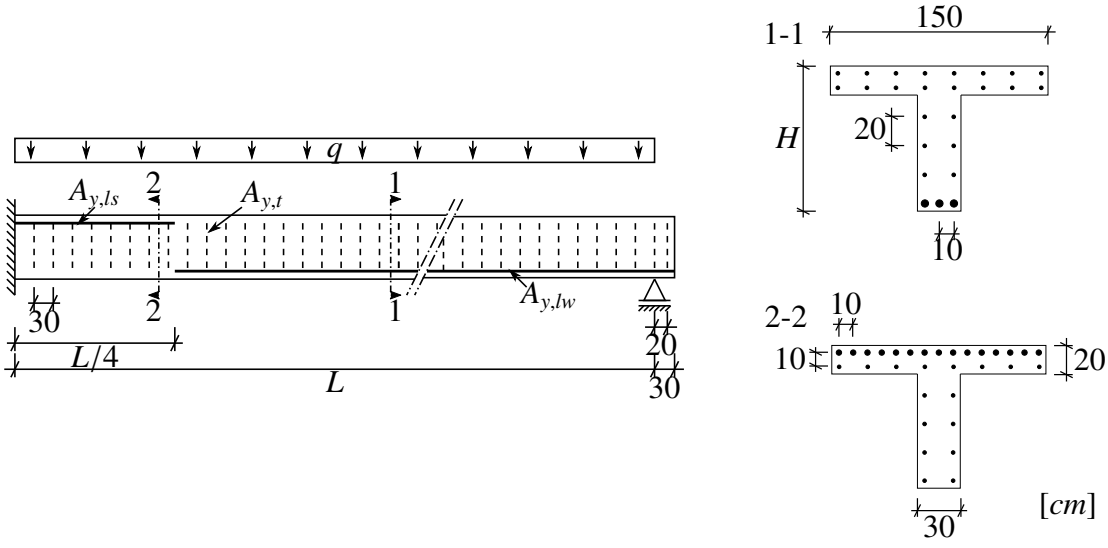

Figure 4.17.: Setup of the numerical tests

The parameters for the numerical tests performed when elaborating this thesis are chosen in light of the problem portrayed in the introduction (chapter 1) and are based on scenarios typically encountered at bridges. The cross-section with its variables as well as the statical system can be taken from figure 4.17. A one-sided clamped single span girder is chosen

to investigate the generally accepted controlling conditions at intermediate bearings, while the slab-girder cross-section is the most used cross-section for bridges due to its economic feasibility. Table 4.8 in combination with the maximal (+), mean (0) and minimal (-) values defined in table 4.7 provide the changing and constant variables.

The test series is designed following the FCCCD as described in section 4.2 and depicted in figure 4.2. It is designed to investigate the influences span-length L, the slenderness λ and the amount of shear-reinforcement $A_{y,t}$ with regard to the shear-bearing capacity of one sided clamped reinforced concrete single span girders. In this regard the first eight tests according to table 4.8 represent the required tests according to a fully factorised design, while the latter seven tests are included to account for quadratic effects.

Table 4.7.: Variables ranges of the numerical experiments in accordance with DoE

	+	0	-
L $[m]$	20.0	15.0	10.0
λ	20	15	10
$A_{y,t}$ $[mm^2]$	153.94	102.10	50.26

The varying cross-sections as assigned in table 4.8 can be found in Appendix A and vary only in their total height in accordance with the variable λ.

Rather than modelling the vertical supports separately, requiring a consideration of the tie between support elements and beam elements, the beam is fixed directly. While the support conditions of the hinged support is modelled using line supports, the clamped support is modelled consisting of two parts. The moment bearing is achieved by restricting the cross-section to deform in beam direction, while the vertical support is modelled assuming a $10.0 \cdot b_w$ cm^2 area at the bottom of the web. Further information about the modelling approach can be taken from chapter 3.

For the beam presented in figure 4.17 a minimal amount of shear reinforcement of ∅8 every 30.0 cm is chosen since the resulting shear-reinforcement-ratio (ρ_t) of 0.112% is between the minimal shear-reinforcement-ratio ($\rho_{t,min}$) of 0.105% or $0,118$% in accordance with EC2 [41] and NA Germany [42] respectively. A $\rho_t = 0.342$%, being roughly three times the minimal ρ_t, min, was achieved by ∅14 stirrups every 30.0 cm and marks the upper bound of the investigated range. The mean variable ('0' in table 4.7) is the purely theoretical diameter of 11.4 mm providing a shear-reinforcement-ratio of 0.227%.

The amounts of longitudinal reinforcement are determined to ensure shear failure of the beams and are kept constant for the same cross-section a span-length pairing as provided by table 4.8. To allow for some degree of comparability between the tests, the amount of longitudinal reinforcement is determined to withstand the critical moment resulting from $V_{Rk,s}$ (equation 6.8 EC2 [41]) assuming the maximal allowed $cot(\theta)$ of 3.0 in accordance with the German national annex to EC2 [42] and the maximal amount of shear reinforcement as defined in table 4.7. The precise values of the resulting amount of reinforcement

Table 4.8.: Definition of the numerical test specimens variables and ids

	T10-1-1	T10-1-2	T10-2-1	T10-2-2	T20-1-1	T20-1-2	T20-2-1	T20-2-2	T10-0-0	T20-0-0	T15-1-0	T15-2-0	T15-0-1	T15-0-2	T15-0-0
L	-	-	-	-	+	+	+	+	-	+	0	0	0	0	0
λ	+	+	-	-	+	+	-	-	0	0	+	-	0	0	0
$A_{y,t}$	-	+	-	+	-	+	-	+	0	0	0	0	-	+	0
H $[m]$	0.500		1.000				2.000		0.667	1.333	0.750	1.500	1.000		
$f_{ck,cyl}$ $[N/mm^2]$	43.0														
f_{ct} $[N/mm^2]$	3.2														
E_c $[N/mm^2]$	31,451.0														
$f_{yk,c}$ $[N/mm^2]$	500.0														
$f_{yk,t}$ $[N/mm^2]$	500.0														
$f_{yk,l}$ $[N/mm^2]$	700.0														
$A_{y,ls}$ $[mm^2]$	4584		5583		9215		11162		5083	10189	6903	8372	8968		
$A_{y,lw}$ $[mm^2]$	2481		2678		4977		5380		2580	5179	3729	4029	3814		
E_y $[N/mm^2]$	210,000.0														
$s_{y,t}$ $[mm]$	30.0														

are used for the numerical analysis, hence the unusual amounts that can not be replicated by generally available reinforcement bars.

Additional simulations are conducted on equivalent cantilever beams, to isolate the failure section from the overall beam behaviour for tests T10-2-1, T10-2-2, T20-2-1 and T20-2-2. The test setup is provided in Appendix B section B.1.

The results of these additional simulations will also be discussed in the following evaluation of the test series.

4.5.2. Evaluation of the Test Series

The evaluation of the test series needs to be viewed under two aspects. On the one hand the design of experiments view, focusing on the influences of the observed variables and on the other hand the failure mechanisms and total ultimate forces. In a first step however a convergence study, as well as the investigation on certain numerical peculiarities needs to be discussed.

Convergence and Numerical Peculiarities

The mesh size is chosen to 20 *mm* in accordance with the previous simulations provided in section 4.3. A separate convergence study is performed on test T10-2-2, to further solidify the selection. The results are provided in figure 4.18.

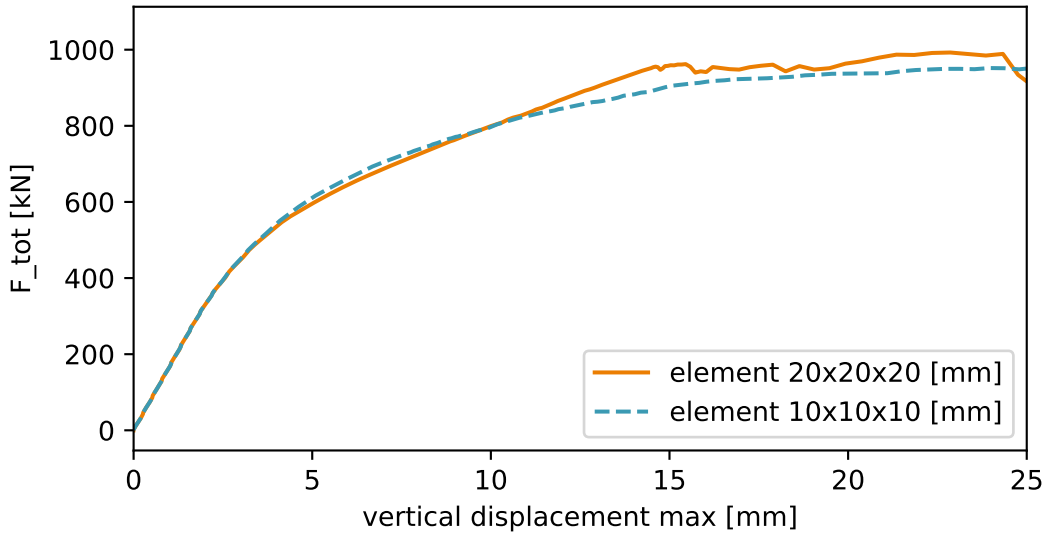

Figure 4.18.: Convergence study for T10-2-2

As can be seen, especially the loading behaviour up to the failure load matches. The slight discrepancies when comparing the load-displacement curves can be traced back to a weakening of the beam near the mid-span due to tension in the concrete elements, which are

more present at the 10 *mm* mesh size. This effect was also observed at the T20-2-1 and T20-2-2 beams for the chosen mesh size of 20 *mm* (appendix A.4). Comparing the load-displacement curve for T10-2-2 (figure 4.18) with the visualisation of the tension damage, aka cracks, (figure 4.19) shows that the numerically derived cracks at the point of maximal moment do not influence the beams behaviour.

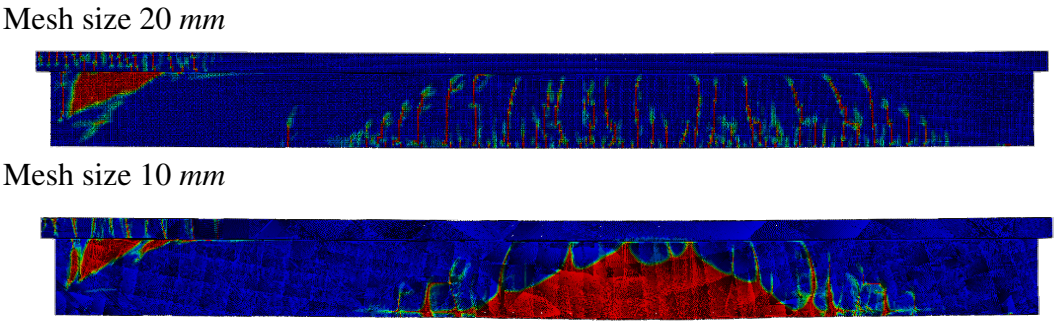

Figure 4.19.: Numerically derived tension damage of T10-2-2 for different mesh sizes

As can be gathered from figure 4.18 that numerical peculiarity leads to a slight decrease in stiffness when approaching the failure load, but does not influence it in a measurable way. This can further be highlighted by using a corresponding cantilever model and comparing its failure load as well as its load-displacement curve to the one-sided clamped single span girder (figure 4.20).

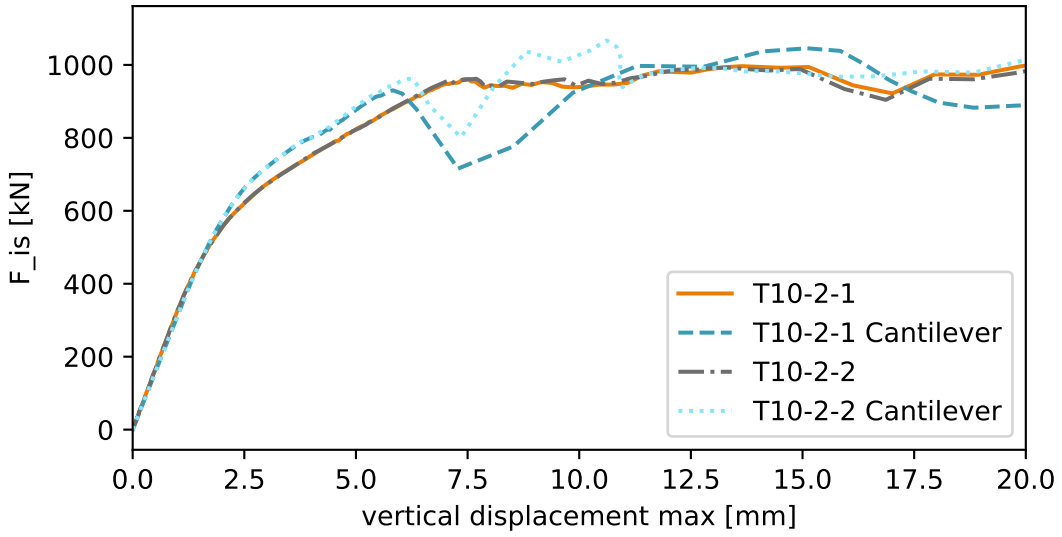

Figure 4.20.: Comparison of load-displacement curves for T10-2-1 and T10-2-2 and their corresponding cantilevers

Critical Loads and Type of Failure

The first thing that needs to be addressed and defined in the context of evaluation is: What categorises the point of failure? In the simplest case for civil engineering this question can be answered with the circumstances under which a structure collapses. Another definition could be an irreversible change, which prevents further intended usage. Figuratively speaking a failure of a part or a section may result in limited usability, but does not necessarily lead to total collapse of a structure. Standards touch on this subject by differentiating between an ultimate limit state and a limit state of usability [41].

Since the test series can be described as consisting of only single parts, namely the reinforced concrete beam, tested separately, the definition of failure and its resulting critical load F_{crit} should be the point of collapse. The values resulting from this definition are provided in table 4.9 for the shear force at distance d of the clamped support ($V_{crit,is}$) and the theoretical critical shear force $V_{Rc,EC2-NA}$ (further referenced as theoretical shear force) using the angle of the compression strut $cot(\vartheta)$ resulting from [41] in combination with [42]. Furthermore the visually deductible angle of the compression strut ϑ_{sim} is provided and can be gathered from the appendix (A.4).

Table 4.9.: Numerical and theoretical critical shear forces of the test series at distance d from the support

Test ID	$V_{crit,is}$ $[kN]$	$V_{Rc,EC2-NA}$ $[kN]$	$cot(\vartheta)_{calc}$	$cot(\vartheta)_{meas}$
T10-1-1	483.98	103.22	1.52	8.14
T10-1-2	467.97	319.02	1.54	11.43
T10-2-1	865.05	229.0	1.6	2.14
T10-2-2	853.53	704.48	1.61	2.25
T20-1-1	645.3	258.2	1.8	6.31
T20-1-2	692.52	764.58	1.74	6.31
T20-2-1	1152.49	572.94	1.95	2.36
T20-2-2	1254.94	1669.61	1.85	1.6
T10-0-0	660.17	287.67	1.52	4.33
T20-0-0	899.0	697.87	1.78	2.48
T15-1-0	607.07	348.53	1.63	5.67
T15-2-0	1059.95	773.05	1.74	1.66
T15-0-1	747.15	241.67	1.69	4.33
T15-0-2	846.82	706.36	1.61	5.14
T15-0-0	820.37	473.73	1.63	5.14

Three things catch the eye when viewing table 4.9. Firstly the general underestimation of $V_{crit,is}$ by the standards. Secondly the independence of the numerical shear-failure load on the reinforcement ratio, contradicting the theoretical approach from EC2. And lastly the two anomalies of T20-1-2 and T20-2-2, where the theoretical shear forces exceed the numerical ones.

For the first mentioned statement, supported by a number of tests by different researchers [52, 69, 127], the indifference of the standards towards moment-shear interaction needs to be addressed. While the formulation for $V_{Rc,EC2-NA}$ includes a variable angle of the compression strut ϑ, this angle is depending on two major factors. On the one hand the normal-stress at the cross-sections centre of gravity, which in the case of pure bending becomes irrelevant and consequently only accounts for effects resulting from external normal forces or prestressing forces. On the other hand the ration of $V_{Rd,cc}/V_{Ed}$, where a higher ratio results in a smaller ϑ, resulting in more stirrups being activated and an increased $V_{Rc,EC2-NA}$. Table 4.9 provides the $cot(\vartheta)$ resulting from EC2 NA when substituting V_{Ed} with $V_{crit,is}$. Analysing them provides the generally applicable understanding, that the angle of the compression strut, being assumed equivalent to the shear-crack angle, gets steeper for larger acting shear forces. This statement is confirmed by the measured compression strut angle ϑ_{meas} provided in table 4.9.

Even so ϑ being used to determine the length over which the stirrups get activated in case of a shear crack, the main influence parameter for the theoretical shear-failure force can be found in the reinforcement ratio ρ_t, leading to the second statement. The numerical simulations provide a vastly different view on its influence. Probably best described using the tests T15-0-0, T15-0-1 and T15-0-2, where the only changing parameter is ρ_t (figure 4.21).

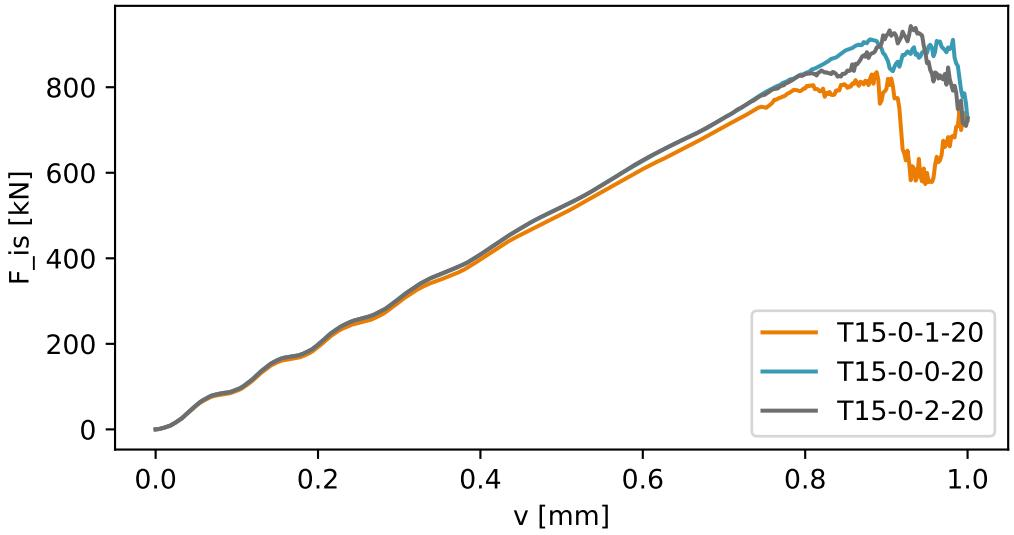

Figure 4.21.: Influence of the changing transverse reinforcement ratio on the critical failure load at the clamped support

Two aspects have to be considered when comparing the results. Firstly the span of the results from lowest to highest reinforcement ratio, which provide an increase in shear force at failure of $99,67\ kN$ for the numerical simulations and $681,69\ kN$ for EC2 NA. Therefore a reduction of 700% solely focusing on ρ_t can be stated. Secondly the varying degree of

conservatism, or safety when comparing the numerically determined failure load to the theoretical one. Here the range spans from 3.09 for the small reinforcement ratio to just 1.20 for the large one. Seeing the conservatism decrease by a factor of ≈ 2.5, the question of intent has to be asked. Studying the regulations however does not provide any acknowledged intent on the increased caution when dealing with small reinforcement ratios, introduced with the introduction of the Eurocodes, sparking a number of new research focusing on small amounts of shear reinforcement in the recent years [56, 80, 134, 169].

Additionally the extreme cases T10-1-1 and T10-1-2, resulting from the measured crack angle ϑ_{meas}, and the constant failure load between them need to be inspected more closely. Figure 4.22 provides the van Mises stresses within the concrete as well as the stresses of the transversal reinforcement for T10-1-1.

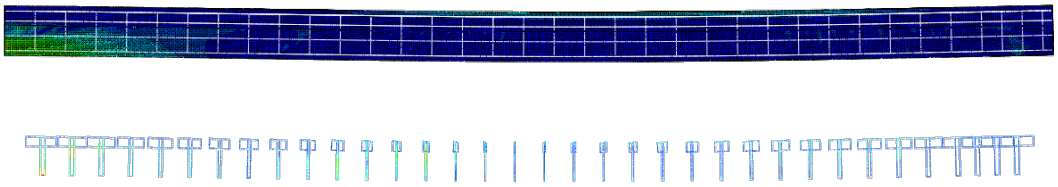

Figure 4.22.: Stresses within the transversal reinforcement and the concrete in N/mm^2 at the section in which failure occurred for beam T10-1-1

Two aspects need to be mentioned. Firstly the transverse reinforcement does not reach its yielding strength, and secondly the compressive strength of the concrete, visualised by the Mises stresses is reached for virtually the entire height of the web at the clamped support. This does lend itself to the assumption of the beams not failing due to shear, but due to bending. Further strengthening this argument is the recalculation of the main tensile stress for $V_{crit,is}$, where, even under the assumption of the normal stress only reaching 40.0 N/mm^2 and the shear stress resulting from 480.0 kN being 3.2 N/mm^2 in case of the T10-1-1, the main compression stress and main tension stress are calculated to be -40.25 N/mm^2 and 0.25 N/mm^2 respectively. Seeing as the main tensile stress does not reach f_{ct} of the concrete, which is at 3.2 N/mm^2, no cracks resulting from shear develop, hence the failure of beams T10-1-1 and T10-1-2 has to be noted as bending failure.

Lastly the anomalies mainly evident in tests T20-1-2 and T20-2-2, where $V_{Rc,EC2-NA}$ exceeds $V_{crit,is}$. The first assumption made after review of the simulation results, mainly the crack-pattern (figure 4.23) is the previously mentioned large failure area at the section of positive bending moment.

However, as already discussed under the subsection 'Convergence and Numerical Peculiarities', this visually presented major anomaly, when compared to the rest of the test series (appendix A.4), does not represent the correct influence. In fact the described beams do fail due to compression failure within the concrete induced by the shallow shear crack angle.

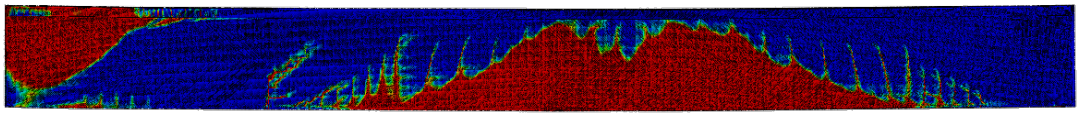

Figure 4.23.: Numerically determined cracking pattern of test beam T20-2-2

Figure 4.24 shows the equivalent cantilever for the test T20-2-2 providing the van Mises stresses within the concrete as well as the tension damage.

a) 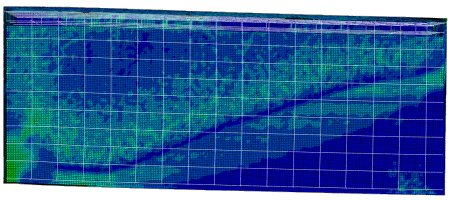 b) 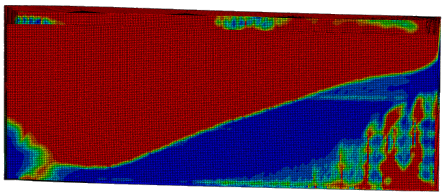

Figure 4.24.: Van Mises stresses (a)) and tension damage (b)) in the concrete for the T20-2-2 equivalent cantilevers

The main connection between these two parameters can be seen when studying the edge of the shown tension crack. The high stresses do run parallel to it and reach the f_{ck} of the used concrete, hence the lower $V_{crit,is}$.

Influence of Span Length, Slenderness and Shear-Reinforcement Ratio

The 15 beams encompassing test series focuses on the influence of the span length L, the slenderness λ and the shear reinforcement ration ρ_t. Their influences on the critical load at failure can be gathered from figure 4.25. It has to be noted, that the tests T10-1-1, T10-1-2, T20-1-2 and T20-2-2, which had different failure modes, are included in these effect diagrams.

The effect diagrams are derived by determining the mean-result for all tests sharing the same value for the separate variables. Hence the trend of the variables effect on the selected result parameter can be seen. The first major effect apparent from figure 4.25 is the comparable small influence the amount of transverse reinforcement has on the critical load of a one-sided clamped single span girder. In stark contrast to this the influence of the slenderness can be seen. Here a linear dependency of the critical load can be gathered, prompting a decrease in it for larger values of λ. This effect however does not surprise and is regarded in standards like the EC2 [41] by the lever of the internal forces z which is linearly depending on λ when set to $z = d/2$. More surprising is the apparent increase of load bearing capacity with an increase of the span length. Considering a change in span length

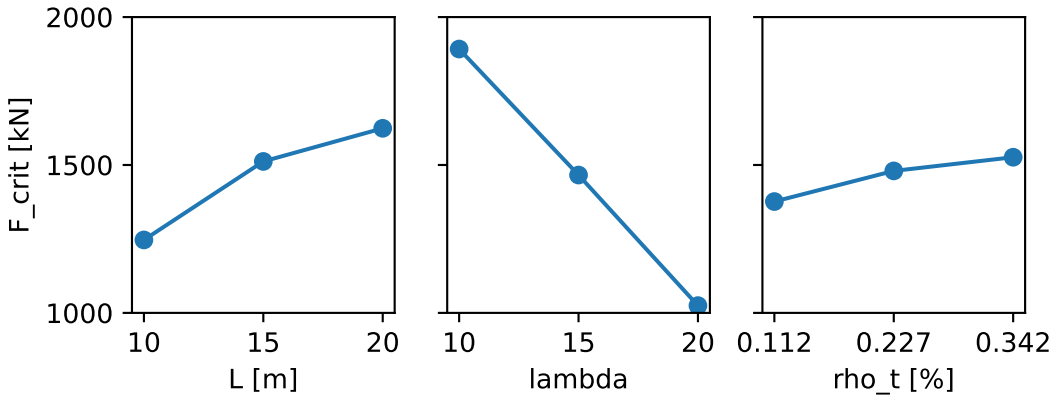

Figure 4.25.: Effect diagrams for the influence variables L, λ and ρ_t

leads to a change in clamped moment to support force at the clamped support this can be attributed to be one of the main causes of it. However the effect of L gets counteracted by λ if the cross-section is kept constant, since the size of the impact of a change in L is smaller than the impact of a change of λ.

Also an important aspect gained by the effect diagrams is, that L and ρ_t have an non-linearly influence on the critical shear-load. This is more prominent for the span length, providing another indication that the stress distribution at the point of shear failure, resulting from the bending moment, has a noticeable influence on the shear-load bearing capacity. This conclusion is derived, the bending moment and its resulting stress-distribution is the only factor changing none-linearly with a change in L.

4.6. Conclusion

Based on the previously introduced and tested numerical modelling and simulation approach, the test series, consisting of 15 individual varying specimens, shows a diminishing influence of the transverse reinforcement ratio on the shear-bearing capacity. While this statement can be taken from the presented results, it has to be broken down to its limiting factors, since the test series does focus around the case of overlapping high shear stresses and high normal stresses at the location of failure. Hence the statement can firstly be limited to this case and not be applied directly to the huge amount of test data gathered in literature, for which the numerical modelling approach was benchmarked.

The usage of DoE focusing on three different variables, that could influence the shear-bearing capacity, as well as the restricted application usage of multi-span girders, which the test series is supposed to mimic, a clear restriction of the gained information has to be stated, that focuses on the influences of span length, slenderness and shear-reinforcement ratio in light of overlapping high shear stresses and high normal stresses. Hence the transfer of this knowledge to single span girders can not be performed without further investi-

gations. However the same has to be stated vice-versa and the knowledge that is gained by excessive, but still mostly restricted tests based on single span girder set-ups can not be universally applied to alternate configurations. The inability to do this does come from the interlinking load-bearing mechanisms within reinforced or prestressed concrete specimens, that are currently not acknowledged within the standards but can be seen by the numerical tests provided in this chapter.

5. Mechanical Shear Model for Reinforced and Prestressed Concrete Beams

5.1. Overview

The recently resurfaced discussion on shear verification of reinforced and prestressed concrete beams founded the motivation to develop a mechanical shear model in the scope of an engineering model fitted to this task. While a high level of conservatism is welcomed in the design process of long lasting constructions, the introduction of EC 2 [41] brought with it a number of changes in its verification procedures, leading to a number of inconveniences, which are mostly founded and confined to national regulations and application of the introduced design standards. In Germany for example due to the requirement to reevaluate existing structures of high importance for the public infrastructure, like bridges, engineers are faced with the task to apply these newly introduced standards with their usually higher degree of conservatism to constructions designed following a different philosophy as well as standards. Concluding from this challenge a number of new guidelines like the *Nachrechnungsrichtlinie* [125] in Germany were developed, requiring a more thorough investigation of the construction and introducing changes to the verifications that might be applied for the sole purpose of reevaluating of existing constructions.

While these guidelines extend and/or differ upon/from the limits set by the codes and standards they do not engage in the origin of the existing discrepancies. For this reason an engineering model focused on the physically compatibility of the individual mechanical shear-bearing mechanisms is developed. To unify these individual parts a calculable variable is required. As an obvious choice the vertical deformation resulting from loading can be chosen for this purpose. Furthermore by coupling multiple systems via a common resulting variable provides the pleasant byproduct of determining the internal load distribution among the systems, since each individual deformation is directly linked to the loading. Simply said the stiffness of the individual system determines the distribution of the load across them, to ensure the same behaviour.

The engineering of the proposed model focused on coupling individual shear-bearing mechanisms to work in parallel with each other is showcased in this chapter. First an approach to determine the actual stiffness of a reinforced and prestressed beam is provided in section 5.2. It can be used to determine the deformation, which can further on be used to link the

subsequent load-bearing sub-systems. The proposed model includes the compression arch with tension chord and the truss which are introduced in section 5.3. An evaluation of the applicability of the proposed engineering model with regard to the test series (section 4.5) can be taken from section 5.4.

5.2. Beam Stiffness

5.2.1. Overview

This section showcases the approach on how to determine the stiffness of a general beam. It can be applied to prestressed or none prestressed beams, yielding its stiffness in case of recalculation, where not all parameters, like the state of the prestressing force are known.

5.2.2. General Approach

The basis for the showcased approach lies within the Euler–Bernoulli beam theory, which states that the beam must be slender, plain cross sections remain plain after deformation and that cross sections that were perpendicular to the beams longitudinal axis prior to deformation remain perpendicular to the beams longitudinal axis post deformation. By taking these assumptions into account the following general differential equations of the beam can be derived with regard to the distributed force loading $q(x)$, distributed moment loading $m(x)$ and an externally applied curvature $\kappa^e(x)$, f.e. resulting from temperature loading or eccentric forces, at the given location x along the beam. The internal shear force ($V(x)$) and bending moment ($M(x)$), as well sa the beam dependent parameters of the Young's modulus E and the area moment of inertia $I(x)$, are also variable along the beams axis.

$$\frac{dV(x)}{dx} = -q(x) \tag{5.1}$$

$$\frac{dM(x)}{dx} = V(x) + m(x) \tag{5.2}$$

$$\frac{d\varphi(x)}{dx} = -\left[\frac{M(x)}{E \cdot I(x)} + \kappa^e(x)\right] \tag{5.3}$$

$$\frac{dw(x)}{dx} = \varphi(x) \tag{5.4}$$

Equation 5.5 can be derived by rearranging Equation 5.3. It allows for the calculation of the local stiffness depending on the bending moment and the resulting curvature.

$$E \cdot I(x) = -\frac{M(x)}{\frac{d\varphi(x)}{dx} - \kappa^e(x)} \tag{5.5}$$

Assuming that the internal forces as well as the initial state of the beam are known, the curvature resulting from these parameters is required to derive the beams stiffness. The

curvature therefore can be determined by the cross-sections strain distribution. The parameters needed for the next steps can be taken from figures 5.1 and 5.2.

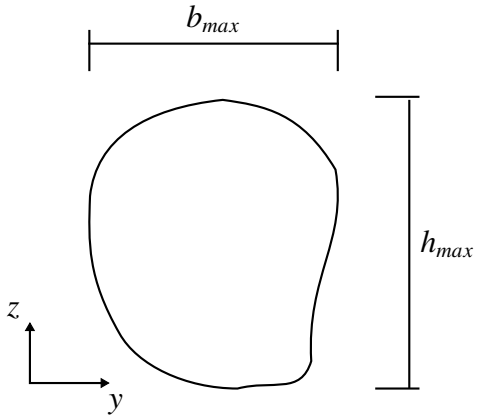

Figure 5.1.: General cross section

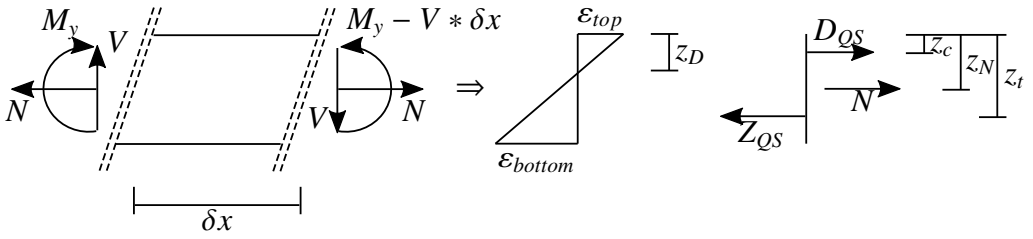

Figure 5.2.: Equilibrium of forces at a section

Figure 5.1 shows a general homogenous cross section. It has a maximal height of h_{max} and depending on the height coordinate a varying width. The width will be referred to by $w(z)$. The equilibrium of forces at a given section of the beam is defined in figure 5.2. The two following equations (equations 5.6 and 5.7) result from it.

$$C_{CS} - T_{CS} = N \tag{5.6}$$

$$C_{CS} \cdot (z_t - z_c) + N \cdot (z_t - z_N) = M_y \tag{5.7}$$

As long as the stress and strain within the cross section are depending on each other, the resulting force can hence be given by:

$$F_{CS} = \int_0^{h_{max}} \sigma(\varepsilon(z)) \cdot b(z) dz(.) \tag{5.8}$$

Using the equilibrium equations 5.6 and 5.7 as well as equation 5.8 a system of equations depending on the stress $\sigma(\varepsilon(z))$ can be derived. The resulting equations for the equilibrium of forces and moments are given by equations 5.9 and 5.10 respectively.

$$\int_{z_0}^{h_{max}} \sigma(\varepsilon(z)) \cdot b(z)dz - \int_{0}^{z_0} -\sigma(\varepsilon(z)) \cdot b(z)dz = N \tag{5.9}$$

$$\int_{z_0}^{h_{max}} \sigma(\varepsilon(z)) \cdot b(z)dz \cdot (z_c - z_t) + N \cdot (z_N - z_t) = M_y \tag{5.10}$$

Combining the equation for $\sigma(\varepsilon(z))$ with the assumption, that the strain distribution is linear over the cross section height, the following two variables are unknown:

- z_0 ,
- ε_{top} or ε_{bottom}.

Determining the unknowns using the equations of equilibrium is then possible.

If the strain distribution is known within the cross-section, equation 5.11 can be used to calculate the curvature at that point.

$$\kappa(x) = \frac{\varepsilon_{top} + \varepsilon_{bottom}}{h_{max}} \tag{5.11}$$

Using equation 5.3 in combination with the calculated curvature for a given stress distribution yields the beams stiffness at that location (equation 5.12).

$$E \cdot I_y = \frac{M(x)}{\kappa(x) - \kappa^e(x)} \tag{5.12}$$

The given approach has the advantage that the local stiffness can be determined independent of its cross section, material and statical system.

5.3. Development of the Mechanical Model

5.3.1. Arch with Tension Chord

Theory

As previously discussed, one of the shear-bearing mechanisms that make up the behaviour of a reinforced or prestressed concrete beam is the compression arch with tension chord (section 2.2.2). Some advanced shear models incorporating this mechanism like the ECAM (section 2.4.7) already exist and are able to showcase its compatibility in determining the shear-bearing capacity of a reinforced concrete beam.

For the stiffness based approach pioneered here it is necessary to determine the stiffness of the compression arch with tension chord within the reinforced concrete beam. This allows a coupling of it to other sub-systems to predict the distribution of loading amongst them.

Simply Supported Beam

The differential equations of the arched beam can be derived, providing the necessary geometry and boundary conditions (figure 5.3). Even so the differential equation can be

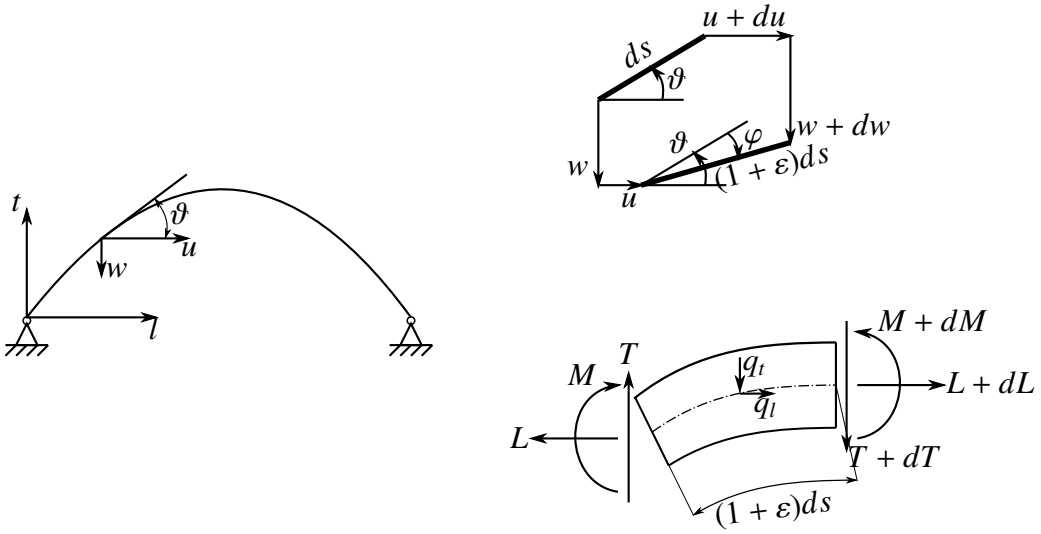

Figure 5.3.: Deformation and equilibriums states of an arch

developed using polar-coordinates, for the further use and compatibility with the beam and the subsequent shear-bearing mechanisms the Cartesian-coordinate system (l, t) is chosen in accordance with [130]. Following figure 5.3 the arch section-length ds is defined by $\sqrt{ds^2} = \sqrt{dl^2 + dt^2}$ and provides the relation between global deformations u, w, the local strain ε and the local rotation angle due to bending φ to be:

$$dw = dt - (1 + \varepsilon)ds \cdot sin(\vartheta + \varphi) \tag{5.13}$$

$$du = -dl + (1 + \varepsilon)ds \cdot cos(\vartheta + \varphi). \tag{5.14}$$

Applying small-angle approximation for φ and as a result imposing $\varphi \cdot \varepsilon = 0$ equations 5.13 and 5.14 can be rearranged to:

$$\varphi = \frac{dw}{ds} \cdot cos(\vartheta) + \frac{du}{ds} \cdot sin(\vartheta) \tag{5.15}$$

$$\varepsilon = \frac{du}{ds} \cdot cos(\vartheta) - \frac{dw}{ds} \cdot sin(\vartheta). \tag{5.16}$$

For the following equations the differentiation with respect to the coordinate l will be marked as $'$. This results in a rewriting of equations 5.15 and 5.16 into equations 5.17 and 5.18 respectively, where the beam and cross-section parameters Young's modulus E, area moment of inertia I and area A as well as the temperature t_t in $°K$ and temperature

variable α_t in $1/^\circ K$.

$$\varphi = w' + \varepsilon tan(\vartheta) \tag{5.17}$$

$$\varepsilon = u' - \varphi \cdot tan(\vartheta) \tag{5.18}$$

$$\varepsilon = \frac{N}{EA(l)} + \alpha_t t_t \tag{5.19}$$

$$\varkappa = -\frac{M}{EI(l)} \tag{5.20}$$

Implementing Hooks' law (equations 5.19 and 5.20), where $\varkappa = \frac{\varphi'}{cos(\vartheta)}$ is the curvature resulting from bending, in the rearranged equations (5.17 and 5.18) for u' and w'' results in:

$$u' = \left(\frac{N}{EA(l)} + \alpha_t t \right) \left(1 + tan^2(\vartheta(l))\right) + w' tan(\vartheta(l)) \tag{5.21}$$

$$w'' = -\frac{M}{EI(l)} \cdot \frac{1}{cos(\vartheta(l))} \left(- \left[\frac{N}{EA(l)} + \alpha_t t_t \right) \cdot tan(\vartheta(l)) \right]' \tag{5.22}$$

The equilibriums equations gathered from figure 5.3 are stated below and combine with the elasticity law (equations 5.23 - 5.25) to a coupled non linear system of differential equations (equations 5.26 and 5.27).

$$L' + q_l(1 + u') = 0 \tag{5.23}$$

$$T' + q_t(1 + u') = 0 \tag{5.24}$$

$$M' - T(1 - u') + L(tan(\vartheta) + w') = 0 \tag{5.25}$$

Since horizontal loadings on beams are in general rare and minor in size ($q_l \to 0$), in a first step this system of differential equations can be simplified. Thus for the further equations $L' = 0 \to L = \text{const.}$ is valid.

$$T'(l) + q_t(l)(1 + u'(l)) = 0 \tag{5.26}$$

$$\begin{aligned} \left[EI(l) \cdot cos(\vartheta(l)) \left(w''(l) + \left[\frac{N(l)}{EA(l)} + \alpha_t t \right) \cdot tan(\vartheta(l)) \right]' \right) \right]'' + \\ + L\left(tan'(\vartheta(l)) - w''(l)\right) + T'(l) + \left[T(l)u'(l)\right]' = 0 \end{aligned} \tag{5.27}$$

Equation 5.27 is derived by differentiating equation 5.25 with respect to l and substituting M with equation 5.22.

The derived system of differential equations can only be solved numerically. When considering the compression arch as an internal system of a reinforced or prestressed concrete beam it is sufficient to calculate the deformation in accordance with first order analysis. Including stability related influences introduced in higher order analysis in fact can lead to a decrease of plausibility since these influences mostly related to slenderness of the calculated system and therefore do not occur when being embedded within the complete load-bearing structure.

As with all differential equations, the boundary conditions need to be considered. One major point of influence considering the system stiffness in the context of an internal load-bearing system of a reinforced concrete beam is given by the tension chord, affecting the horizontal displacement.

Alternatively further well known engineering approaches can be used to determine the deformation of the compression arch with tension chord, like the principle of virtual work and energy.

Application to a General Reinforced or Prestressed Concrete Beam

Substituting part of the load bearing capacity of a reinforced or prestressed concrete beam with a compression arch with tension chord requires some consideration concerning its geometry, since they need to coincide with the beams dimensions, loading and boundary conditions. Since the arch shape, within the external geometrical limitations, tries to mimic the moment curve to create an arch which is as moment free as possible, the fix points in arch direction resulting from this can be determined as follows:

- Supports,
- Minima/Maxima of the Moment Curve,
- 0-Points of the Moment Curve.

Additionally the verification of the cross-section, which provides the compression zone height, is required to finalise the shape of the arch. The generally applicable formulas for the verification can be taken from EC2 [41] or FIB Model Code 2010 [48]. Equations 5.28 and 5.29 are used for the relation between the stress σ_c and strain ε_c in the concrete (compare to section 3.2.3), while the generally applicable bi-linear stress-strain relation is assumed for the reinforcement steel.

$$\sigma_c = f_{cm} \qquad \text{while} \quad \varepsilon_c > \varepsilon_{c1} \tag{5.28}$$

$$\sigma_c = \frac{k\eta - \eta^2}{1 + (k-2)\cdot\eta} \cdot f_{cm} \qquad \text{while} \quad \varepsilon_c \leq \varepsilon_{c1} \tag{5.29}$$

with

$$\eta = \varepsilon_c / \varepsilon_{c1}$$

$$k = 1.05 \cdot E_{cm} \cdot |\varepsilon_{c1}| / f_{cm}$$

Combining the cross-sectional geometry with the centre of gravity of the resulting compression zone provides the height coordinates of the compression arch at the previously mentioned fix points corresponding to the minima/maxima of the moment curve. At the 0-points the cross-sectional centre of gravity and at the boundary conditions the respective support locations provide further coordinates. Using a polynomial of the degree equal to the amount of determined boundary conditions, aka fix points, the shape of the compression arch can be constructed.

In addition to the shape, the cross-sectional values along the arch as well as the internal forces under loading are needed to determine the arches deformation. It has a varying area which can be determined at the fix points according to either the compression zone at moment minima/maxima, the entire cross-section at moment 0-points and support areas at exterior boundary conditions. Between these calculated values the cross-sectional values are assumed to behave linear. Alternatively constant values could be assumed, leading to slightly larger deformations under the same loads. In both cases the compression zone under moment load bearing capacity according to the amount of longitudinal reinforcement is used.

When this constructed arch is then loaded, the deformation can be calculated following the before mentioned differential equations or alternate methods.

The application of this approach is highlighted in the following section for a beam from the numerical test series (section 4.5).

Example Beam T10-2-2

As exemplary application beam T10-2-2 of the numerical test series is used (section 4.5 and annex A.4). The beam as well as the resulting compression arch with tension chord are shown qualitatively in figure 5.4. Applying the previously described approach a com-

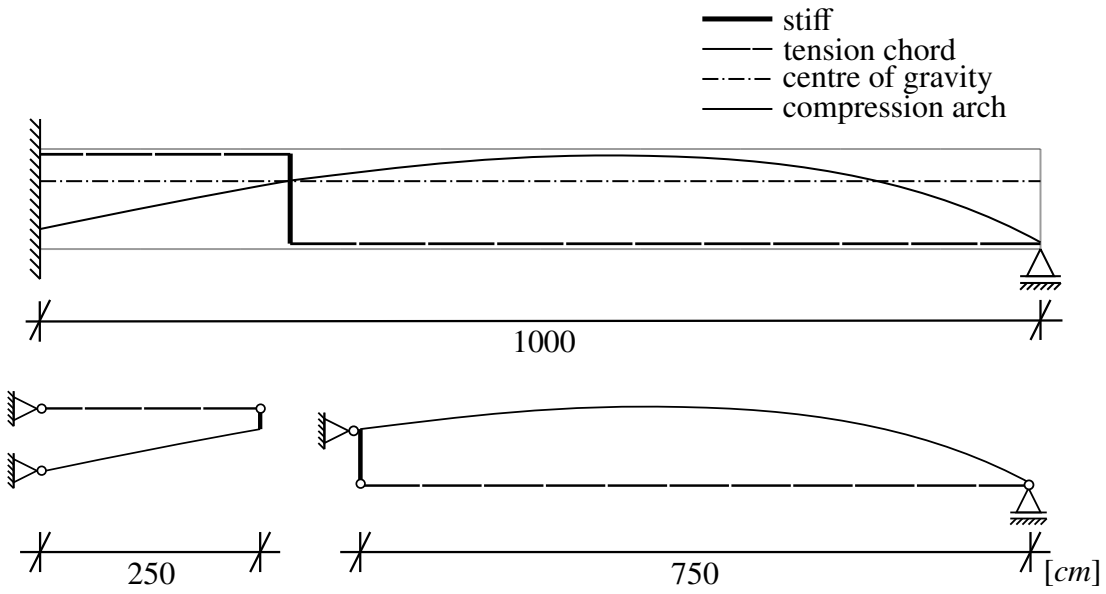

Figure 5.4.: Beam T10-2-2 and the corresponding compression arch with tension chord

pression arch as depicted in figure 5.4 can be derived. The shape showcases the influence the T-shaped cross-section and its centre of gravity, leading to it being much flatter in the area of a positive moment, while being steeper near the clamped support. Another point

can be taken considering the mentioned fix points. While the arch coincides with the cross-sections centre of gravity at the location of the 0-moment, it does follow the generally assumed compression zone at the clamped support, while falling all the way to the moment free support to allow for a physically sound stress transfer into the support.

In addition the disassembled structural systems, which make up this compression arch with tension chord are depicted, allowing for a straight forward calculation of the internal forces. The positioning of the moment couplings are decided to ensure the tension chord, aka the reinforcement, to be moment free, following their stress distribution and load-carrying part within the reinforced concrete beam. This is system compliant, since the statical systems depicted are reduced to their idealised system lines, even so their cross-section at the point of 0-moment does theoretically conform to the entire beam cross-section. Doing this removes unwanted eccentricities, which would provide unrealistic stress flow, contradicting the expected flow from a stress fan. Since these systems are merely sub-systems they also transmit the forces at the section where they are connected within the beam.

With the structural systems the forces within the sub-systems compression arch with tension chord can be determined with regard to a unified load following the actual loading. Disregarding the moment which is expected in the unsymmetrical shape, limited by the beams dimensions, the tension forces in the reinforcement can be calculated directly, leading to the compression forces along the arch. This follows standard assumptions for subsystems, like the classical truss analogy (section 2.4.1) and can be done due to the theoretical system actuality being embedded in a larger specimen and its actual load-bearing mechanism being more complex. This also voluntarily induces a degree of conservatism, generally appreciated in engineering models breaking down complex mechanisms to workable approximations.

Parallel to the arch's shape the cross-sectional parameters need to be determined. For this the moment load-bearing capacity is needed resulting from the amount of longitudinal reinforcement, from which the compression zone height and the corresponding area can be gained. Proceeding this step the area can be assumed either constant for each subsection, or linear changing with the minimum being the area attributed to the compression zone under moment load-bearing capacity and the support areas either being the complete cross-section in case of the moment 0-point, or the external contact area of the supports. Table 5.1 provides the determined areas at the arches fix points, while figure 5.5 showcases the influence between the constant and a varying cross-section approach.

Table 5.1.: Cross-sectional areas at the fix points of the arch (clamp (A_{clamp}), moment 0-point (A_{0M}), maximal moment (A_{maxM}) and moment free support (A_{sup}))

A_{clamp}	A_{0M}	A_{maxM}	A_{sup}
$[mm^2]$			
1282.5	5400.0	900.0	265.9

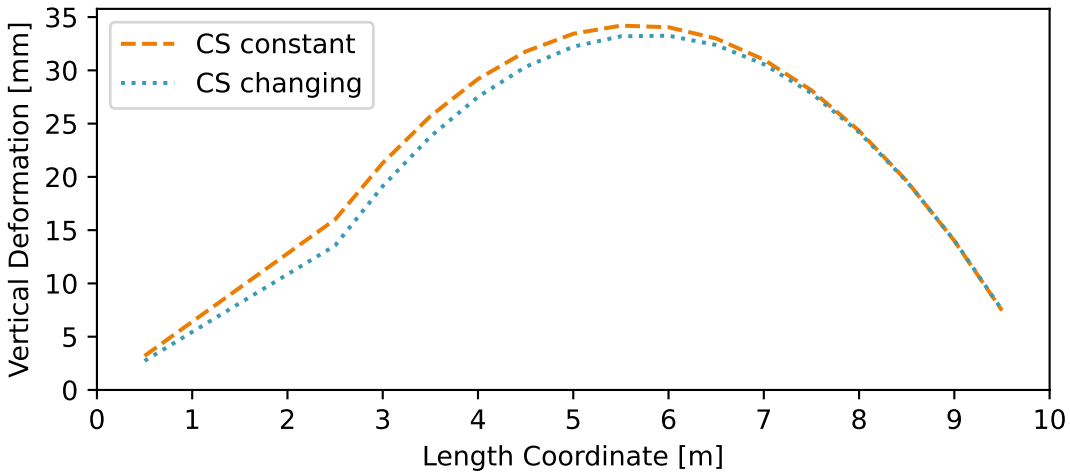

Figure 5.5.: Comparison of deformation of the sub-system compression arch with tension chord for T10-2-2 with regard to the area subjected to a uniformly distributed load of 100 kN/m

Figure 5.5 shows the rather small difference of the deformational behaviour as well as the maximal deformation resulting from the comparison of the different cross-sectional areas under the same load. Especially considering the difference of less then 3% for the maximal deformation highlights its negligible influence. To confirm with the physical model however the more precise approach of a changing cross-section for the compression arch is used.

5.3.2. Truss

Theory

Since trusses are considered to only carry normal forces within its members, the stiffness of a truss girder can be considered to consist purely off of the shear stiffness based on the diagonals and the verticals of its structure. The following definitions and equations in this section are in relation with a truss element as seen in figure 5.6. The equations can not be applied to different truss shapes. If a different truss shape is present, the equations need to be re-evaluated.

Following [130] the shear-stiffness of the presented truss-segment can be calculated by:

$$\frac{1}{GA_{truss}} = \frac{d^3}{EA_{diag}ab^2} + \frac{b}{EA_{vert}a}, \tag{5.30}$$

where the annotations $_{truss}$, $_{diag}$ and $_{vert}$ are attached to the beam parameters Young's modulus E or shear modulus G in combination with the area A to signal the parameters for the truss equivalent beam, the trusses diagonal beam or vertical beam respectively.

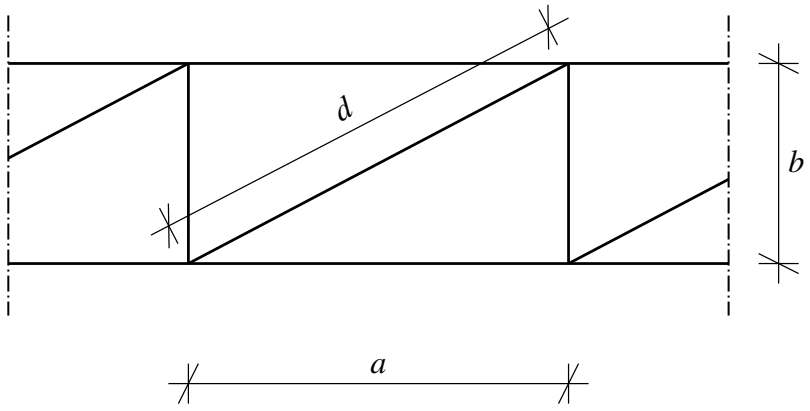

Figure 5.6.: Truss system on the basis of the truss analogy according to [41]

Using equation 5.30 allows for a truss-segment individual determination of the stiffness, neglecting the deformation of the belts, since it is already included in the compression arch with tension chord. This can be used in the case of the truss-model assigned for the shear-bearing capacity of reinforced concrete beams to account for the varying cross-section of the concrete compression diagonal, leading to a staggered increase of shear stiffness when looking at the truss-girder from its support towards the mid-span, when looking at the discrete systems. Figure 5.7 can be used as an example, where the changing variables are the cross-section of the diagonals (A_{diag}) and the cross-section of the vertical (A_{vert}) truss members, but the cross-section parameters of the compression diagonals are changing. Due to symmetry only half of the truss is shown.

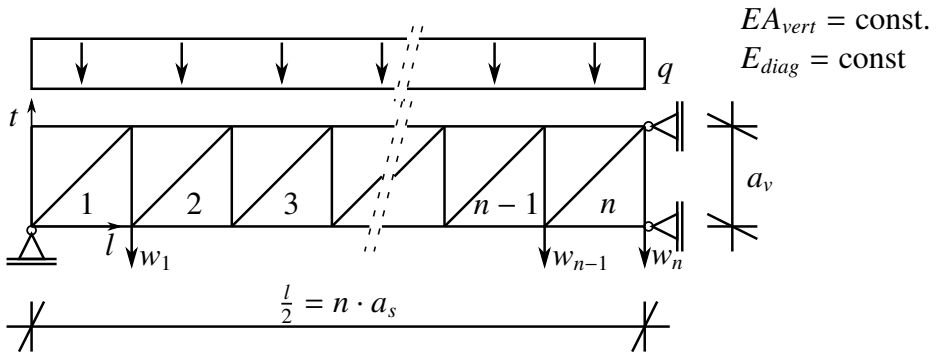

Figure 5.7.: Truss with varying section properties

Using equation 5.30, the shear-stiffness of each truss segment can be calculated (equation 5.31) under the assumption that $A_{diag} = \frac{T_n}{\sigma_{diag}}$, where A_{diag} is depending on the shear-force T_n of the segment and the diagonal compression stress σ_{diag}, which in case of verification calculations is set to the material strength $\sigma_{diag} = f_{diag}$.

$$\frac{1}{GA_n} = \frac{\left(\sqrt{a_s^2 + a_v^2}\right)^3 \cdot \sigma_{diag}}{E_{diag} T_n a_s a_v^2} + \frac{a_v}{EA_{vert} a_s} \tag{5.31}$$

As a disclaimer it has to be mentioned, that the above given equation can only be applied to trusses of the in figure 5.7 portrayed design. The design is chosen due to its applicability to the truss analogy in accordance with Eurocode 2 [41] and the predominantly vertically installed transverse reinforcement. For other truss designs, resulting f.e. from angled transverse reinforcements, the necessary supplementary equations can be gained from [130], or need to be determined individually.

The vertical deformation at the end of a given segment can be calculated as follows:

$$w_n = \sum_{1}^{n} \frac{1}{GA_n}. \tag{5.32}$$

A relation between the compression force in the diagonals and the shear-stiffness can be established.

Since a plethora of discrete trusses can be formed within a reinforced concrete beam, depending on the compression diagonal angle and the spacing of the shear reinforcement, all of them need to be accounted for when using them as a sub system for the shear load-bearing capacity. This can be achieved by either putting this plethora of discrete systems in parallel and distributing the acting load amongst them with regard to their stiffness, or by accounting for them more generally as a smeared truss system, which combines their resistances as it is usually done in standards like the EC2 [41]. It needs to be mentioned, that one further difference between these two approaches lies in the compression diagonal angle. While it is gathered out of the geometry for the discrete trusses, it needs to be chosen in case of the smeared truss. For this a first approximation can be done by following the recommendations given by EC2.

Example Beam T10-2-2

While the smeared truss is generally well known, the influence of the compression diagonal angle needs to be visualised, to enable the use of it in tandem with the compression arch with tension chord (section 5.3.1). Therefore beam T10-2-2 (section 4.5 and annex A.4) will be used to quantify the influence of the selected angle on the truss' vertical deformation. The beam and its reinforcement are shown in figure 5.8 with all relevant measurements.

Including the possible compression diagonals resulting from an angle that ranges between $\approx 25°$ to $\approx 60°$ showcases the large quantity of different discrete trusses, that would needed to be accounted for if choosing that approach. They coincide with the stress fields as

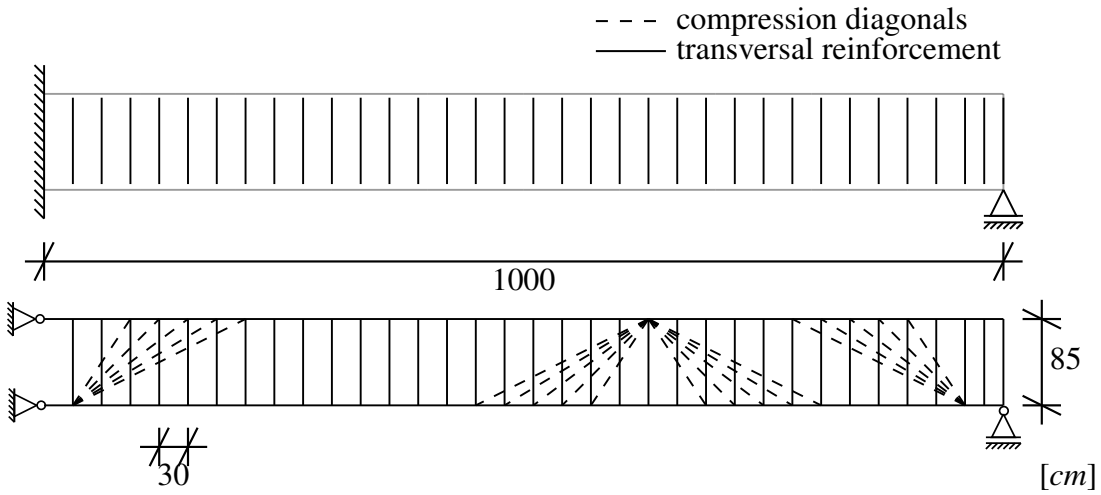

Figure 5.8.: Beam T10-2-2 and its possible discrete trusses

discussed in section 2.4.2 with their fan-like shape close to the supports and the parallel stress fields where the individual trusses are overlapping each other.

Since the proposed approach uses smeared trusses the most important variable can be found in the angle of the compression diagonal. The variance that results from it is provided in figure 5.9.

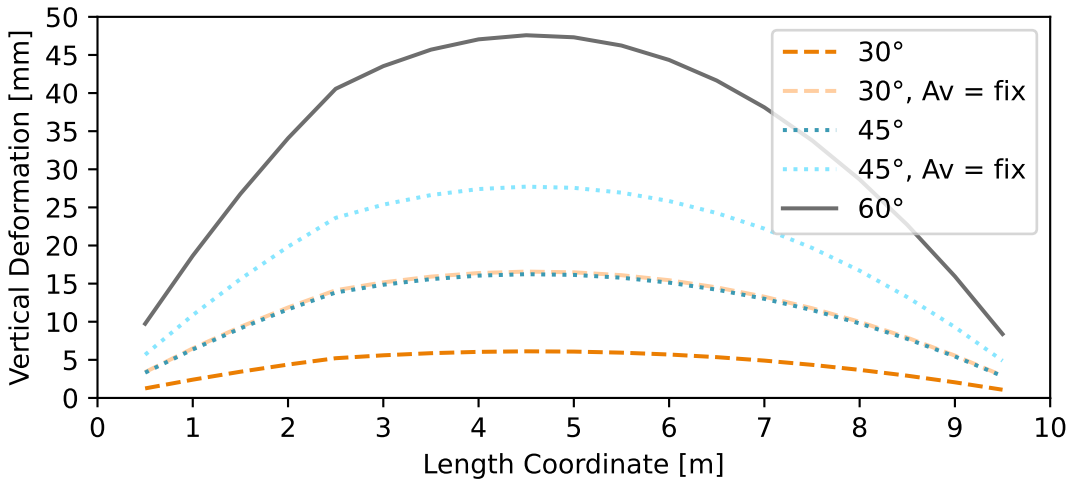

Figure 5.9.: Comparison of deformation of the sub-system smeared truss for T10-2-2 with regard to the angle of the compression diagonal

A clear dependency of the deformation on the selected angle of the compression diagonal can be established by figure 5.9. Originating from the correlation between the angle and

the corresponding amount of transverse reinforcement A_{vert}, decreasing with an increase of the angle, this variance in shear stiffness can be explained by equation 5.31. Especially the areas close to the supports, where the largest shear forces are present lead to this stark variance in the total deformation. When comparing them to the deformation resulting from a constant area of the vertical truss elements, the stiffening effect of the area increase depending on the angle can be highlighted. As fixed A_{vert} the area corresponding to the 60° is used, resulting in 257.0 mm^2.

5.4. Evaluation

5.4.1. Numerical Database

Quality of a method can be assessed from its ability to reproduce trends from changing variables, that coincide with the reality, as well as the actual accuracy of the prediction, in the investigated case this can be found in the critical failure load F_{crit}.

To allow an evaluation of the first mentioned behavioural correctness of the method, the previously introduced effect diagrams derived in section 4.5.2, spotlighting the influences of span length L, slenderness (λ) and shear-reinforcement ratio (ρ_t), are normalized (figure 5.10). The mean-result for the mean-value of each variable is used for this normalisation, hence they define the scale of the effect diagram at a value of 1.0. As discussed in the evaluation of the numerical test series, beams T20-1-2 and T20-2-2 did fail due to concrete crushing at the clamped support, while T10-1-1 and T10-1-2 failed due to bending. Hence these four tests will be excluded in the effect diagrams.

As the pioneered engineering model as well as the smeared truss model of EC2 allow for an engineer sided selection of the compression strut angle, it will be fixed at 30.0° for the purpose of this evaluation, to ensure an objective comparison. The diagrams featuring alternative angle selections are provided in annex C section C.1.

Generally speaking it can be seen that trends, that are present for the numerical simulations, are followed by the models, but with varying degree of accuracy. The two verification methods, the engineering model and the EC2, do match well with each other, but do show some differences to the numerical simulations for the investigated case of a shear failure in a shear and normal strain coinciding cross-section.

Especially the effect diagram showing the influence of the transverse reinforcement ratio does provide an understanding of the aforementioned overweighting of that variable. Since this diagram is normalised and therefore does merely provide a trend, it has to be stated that the numerical simulation does not show any evidence of the reinforcement ratio influencing the critical failure load in the investigated case of a one-sided clamped single span girder loaded by a uniformly distributed load, leading to an overlapping of high normal stresses with high shear stresses. Concerning the other two variables no mentionable deviation can be observed using the test series data.

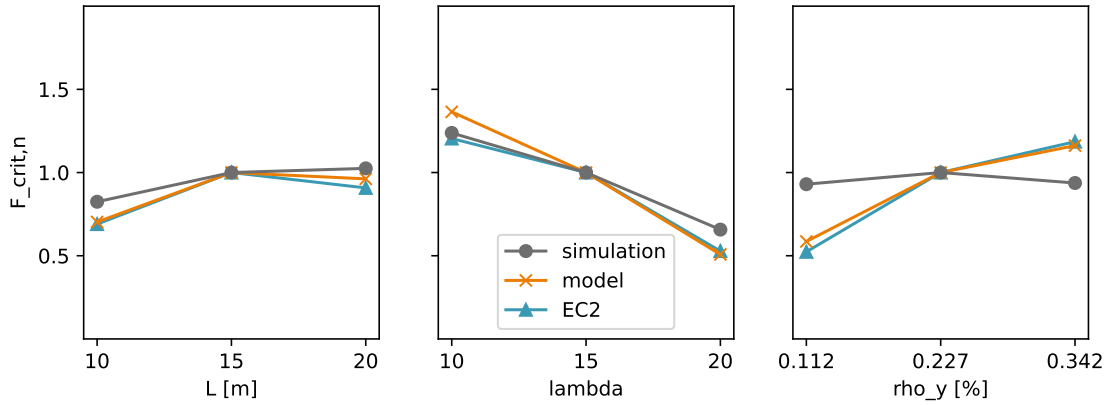

Figure 5.10.: Normalised effect diagrams for the variables span length, slenderness and reinforcement ratio

While the effect diagram does provide some value in showing similar behaviour of different methods, an evaluation of the critical load prediction is equally necessary to determine the quality of the suggested verification model introduced in section 5.3.

Next to the ability of a model to follow trends, the quality of a method is also linked to the accuracy of its predicted results. At this point it has to be pointed out, that the values derived by the engineering model use the failure load of the smeared truss system as its limiting factor. This means, that the critical failure load according to the engineering model consists of the failure load of the smeared truss subsystem and the added load of the compression arch, at the point of equal deformation to the smeared truss system. It is included in figure 5.11 under the tag *Model*. Figure 5.11 provides a standardised diagram for the critical failure load $F_{crit,n}$ for each beam in the test series, comparing them with the the EC2 model as well as the CCCM as described in [30] (also mentioned in section 2.4.7) and the suggested improvement to [125] as provided by [68], further noted as *NRR*.

Other models sometimes suffer when being applied to this investigated case, due to their improvements to general shear models, resulting from verification against the shear database with its over representation of simply supported single span tests. In the case of the model following [78], one improvement does concern the location of the critical control section, being defined as the location of the closest crack due to bending to the investigated support, making it impossible to be applied to a clamped supports.

Further diagrams showcasing alternate angles for the EC2, the NRR, the CCCM and the engineering model as well as non normalised results can be found in annex C section C.2.

The following evaluation of the engineering model is done in comparison to the model from EC2. The scientific models are exempt for the further evaluation, but highlight the short comings of the current standards, as well as possible additions to the engineering model approach, that can be included in the development of a verification method.

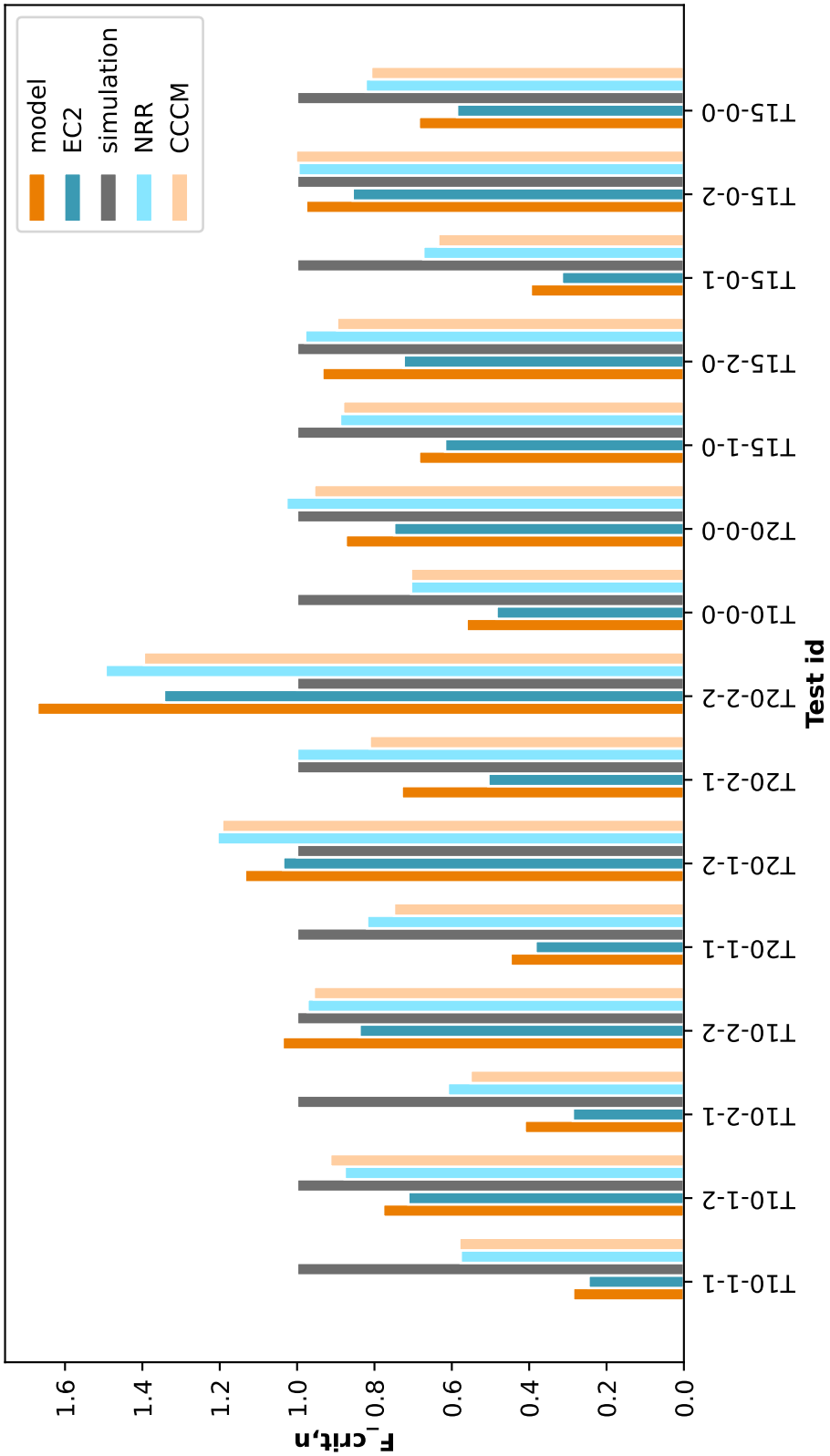

Figure 5.11.: Standardised failure loads of the test series

Since both engineering model in its current theoretical approach as well as the smeared truss model of the EC2 are unable to account for the complex failure modes of experiments T10-1-1, T10-1-2, T20-1-2 and T20-2-2 (section 4.5.2), they will be exempt from the following discussion and values provided. However these cases do provide ground to discuss limits of applicability of the models, following the model evaluation.

While the engineering model provides a fluctuating quality of the failure load when compared to the numerically derived one, it can be stated that it does perform better than the current standard of the EC2.

Comparing the two verification methods provides on average a failure load of 67.7% and 56.2% compared to the numerical results for the engineering model and the EC2 respectively, which do still follow the same trend when looking at the individual beams. This similarity is founded in the engineering model merely expending on the smeared truss model provided in EC2, by introducing another load-bearing system in the compression arch, by which an increase of 21.7% on average can be noted for the configuration currently discussed.

Furthermore the engineering model links the quantitative participation of the compressive arch to the angle of the compression strut by coupling them using their respective stiffness. In case of the test series, the proportional increase of the critical failure load of the engineering model in comparison with EC2 does decrease from 33.2% for a 45° compression strut to the afore mentioned 21.7% at 30°. This effect is linked to the decrease in deformation as visualised in figure 5.9, leading to a smaller load required to deform the compression arch, which is independent of the truss, to the same degree.

However the varying accuracy of the prediction that is inherent of the EC2 shear verification method, especially at small transverse reinforcement ratios (section 4.5.2), is still apparent for the engineering model. While a considerable increase in the predicted critical failure load is achieved, it still does fall short when compared to the numerically determined results. Still the 29.2% relative increase of the predicted loads of the tests with small amounts of transverse reinforcement compared to 15.6% in case of the large amounts of transverse reinforcement show a fading influence of the compression arch with an increase in transverse reinforcement. This does highlight the practicability of the engineering model, since an increase of transverse reinforcement does in fact lead to a diminishing influence of other factors on the shear-load bearing capacity due to its overshadowing stiffness and strength.

As mentioned the excluded cases of T10-1-1, T10-1-2, T20-1-2 and T20-2-2 provide clues towards the limits of the model, that need to be defined. For the first case of T10-1-1 and T10-1-2, failing due to bending, the high normal stresses compensate the tensile stresses, leading to an inability of a shear crack to form within the web, hence the transverse reinforcement can not be activated. For this case a simple verification of the main tensile and compressive stress can be used as a first point of notion. If the compression zone resulting from bending does encompass the height of the web at the critical control section, and the main tensile stress is negligible compared to the tensile strength of the concrete, no failure due to shear can occur and the shear models discussed can not be applied. The second case

present at beams T20-1-2 and T20-2-2, where a failure of the compression strut within the concrete is present can be tackled the same way, but instead of the main tensile stress, the main compressive stress needs to be evaluated. Hence an investigation into the main stresses should be part of every evaluation to pinpoint the correct modes of failure and therefore apply the corresponding verification methods.

5.4.2. Prestressed Cantilever Beams

Looking at more recent physical shear-testing, it becomes clear that the current focus lies on continuous systems under prestressed conditions [54, 68, 62]. While the presented shear model focuses on stiffness relations in its ability to distributed the acting loads on the arch with tension chord and the smeared truss presented in reinforced and prestressed concrete beams it is vital to have a precise understanding of the system. However in the attempt to maximise the use of test specimens, by altering parameters between the spans, like the amount of shear reinforcement [68], and strengthening the section of failure to continue testing the other span, leads to convoluted stiffness distributions between the spans as well as prior and post failure of the first span. Remodelling these changes in stiffness and resulting system behaviour for the presented mechanical shear model could be done via boundary conditions, but would require thorough data and measurements.

Alternatively cantilever beams, modelled and loaded to confirm with these aforementioned tests were performed, allowing for precisely controlled boundary conditions [54, 68]. These tests are used to apply the concept of the presented mechanical shear model to prestressed beams. The tests further investigated are provided in [54] and focus on the influence of the longitudinal reinforcement in the shear-bearing capacity of prestressed concrete beams.

By keeping the prestressing force to provide 2.5 MPa of normal stress on the gross cross-section, varying the amount of longitudinal reinforcement inadvertently results in an alteration of the normal stresses acting on the concrete. This influence can be seen by the beams T25 and R25 resulting in a reduced failure load when compared to the T18 and R18 beams, despite of having nearly double the amount of longitudinal reinforcement. This decrease of the failure load can partially be retraced mathematically. Firstly the main stress can be calculated following

$$\sigma_{I/II} = \frac{\sigma_x}{2} \pm \sqrt{(\frac{\sigma_x}{2})^2 + \tau^2}. \tag{5.33}$$

By substituting $\sigma_{II} = f_{c,t}$ as well as $\sigma_x = \sigma_{c,prestress}$, where $f_{c,t}$ is the tensile strength of concrete and $\sigma_{c,prestress}$ is the normal stress acting on the concrete, the resulting main tension stress, that can be linked to the critical shear stress τ in the investigated example, can be calculated.

The acting normal stress on the concrete for the beams of the test series can be calculated in accordance with the ideal cross-section, resulting in the case of the T25 and T18 beam to be 2.21 MPa and 2.36 MPa respectively. Following equation 5.33 the resulting shear

stresses τ can be derived to be 4.15 MPa and 4.48 MPa in accordance with equation 5.33 and provided having in mind, that the splitting tensile strength $f_{ct,sp}$ leads to f_{ct} by the well known relation $f_{ct} = 0.9 \cdot f_{ct,sp}$. This increase of about $8,1\%$ of the shear stress bearing capacity of the concrete without the activation of transverse reinforcement can provide some reason on the critical load increase of $13,5\%$ when comparing T18 to T25. Assuming τ to only act on the concrete net shear cross-section, the qualitative increase of critical load with the decrease of the amount of longitudinal reinforcement can be calculated to approximately 9.5%. The calculated critical failure loads resulting from this consideration of the tensile strength of the concrete, as well as the critical failure loads in accordance to [54] are provided in table 5.2.

Table 5.2.: Failure loads of prestressed cantilever tests with varying longitudinal reinforcement [54]

	$F_{crit,calc}$ $[kN]$	$F_{crit,test}$ $[kN]$
T18	577.9	578.8
T25	528.0	509.9
R18	478.7	584.6
R25	462.5	483.9

With the exception of R18, the attempt at predicting the critical failure loads of the cantilever tests solely based on the main tensile strength of the concrete performed exceptionally well. While this does provide valuable insight in the predominant load bearing system, it also highlights the negligible influence of the transverse reinforcement. Speaking of the mechanical shear model presented in this work, this showcases the interplay of the subsystems working in parallel within their own physical limits regarding individual failure as well as activation. For these cantilever tests the subsystem direct action, developing as a compression strut with tension chord as shown in figure 5.12, gets activated right from the start of loading, and its failure also marks the failure of the beam, since stresses at the point of failure of this subsystem can not be redistributed onto the smeared truss system, which instantly exceeds its load bearing capacity. The transverse reinforcement does however partake in the load bearing system mainly at the point of loading as well as the clamped support. However the supporting plates used for loading on one site and supporting on the other of the cantilever, allow the shear stresses to distribute themselves over the height of the cross-section rather than concentrate on a singular line support as would be the case in a real world situation with point supports underneath the girder's web.

Further substantiating this mechanical load-bearing system are the recorded crack patterns, which suggest the development of a compression strut with a shallow angle of around 20° as observed during the experiments. Accounting for stress distribution due to loading and boundary conditions at the end, that is mainly aided by the transverse reinforcement, as well as the stress distribution within the compression strut and the resulting cross-section, this shallow angle compression strut allows for the transfer of the shear forces along the length of the test specimens.

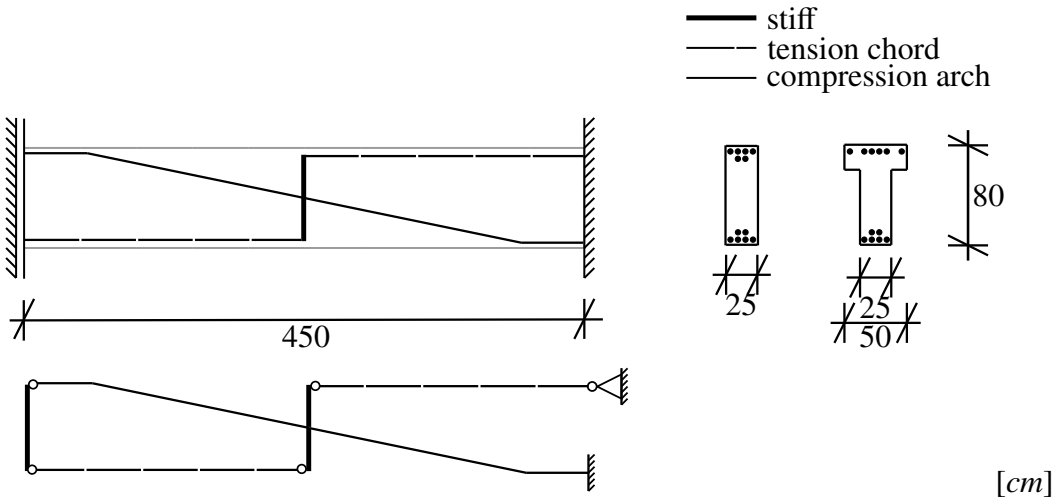

Figure 5.12.: Dimensions of the cantilever tests [54] and the superposed theoretical model

Application of the previously introduced shear model to this test scenario consists solely of this aforementioned compression strut with tension chord, depicted in figure 5.12. The deformations in accordance to the loading as described in [54] are provided in figures 5.13 and 5.14.

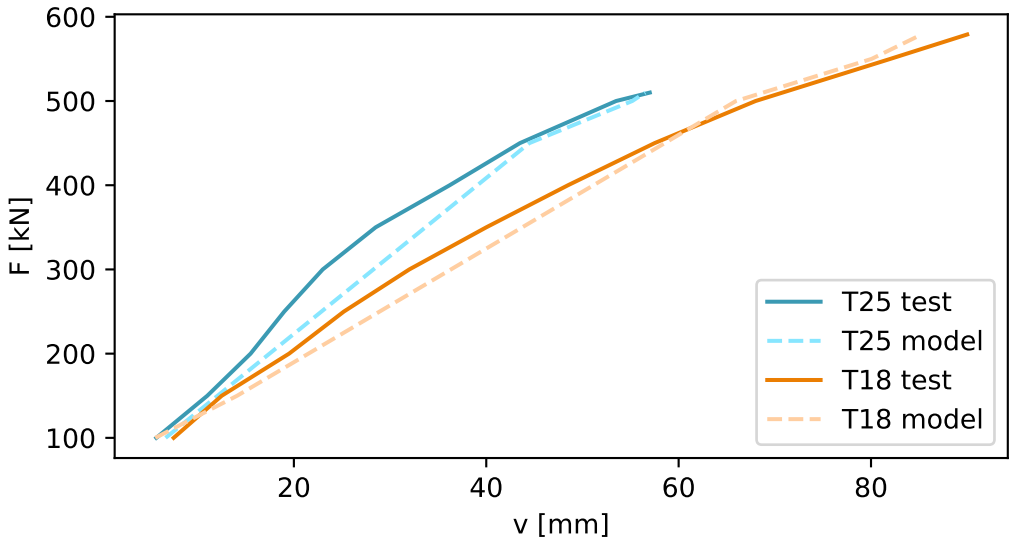

Figure 5.13.: Comparison of deformation of the cantilever tests for T-cross-section taken from [54]

The achieved deformation, when applying the simplified compression strut with tension chord matches exceptionally well with the measured deformations of the test specimens.

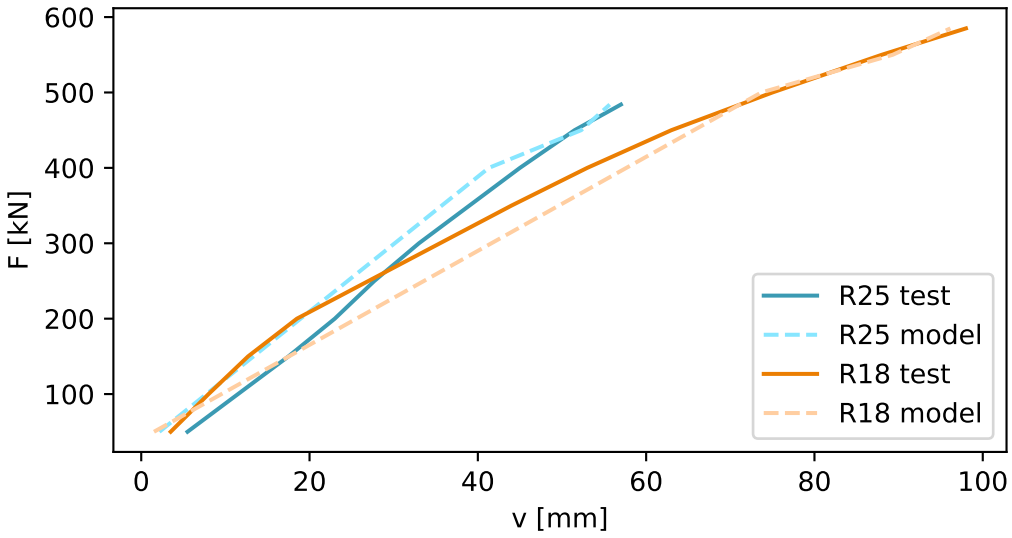

Figure 5.14.: Comparison of deformation of the cantilever tests for R-cross-section taken from [54]

Especially when taking into account, that at lower loads the Young's modulus is larger than the provided value due to testing. The softening at loads beyond $0.4 f_{cm}$ has been accounted for to achieve a good match at the point of failure.

Even so only the direct action load-bearing capacity is activated in this case it showcases the potential of combining the different load-bearing models, in providing the load-deformation behaviour of the beam. It also highlights the necessity of accounting for activation and failure of the load-bearing subsystems, when establishing a shear verification or shear design model on this concept.

5.5. Conclusion

In summary it can be stated that the proposed engineering model approach reaches beyond the smeared truss model of the EC2. The wholistic approach of combining global load bearing mechanisms and linking them via the deformation of the beam does hold potential in its ability of distributing stresses to different load-bearing mechanisms based on the specimens deformation.

Especially the investigation of the large clamped test specimens performed in section 5.4.2, showed the possibility on deriving a sound shear verification model. By accounting for the subsystems individual limits, the failure load of the direct action model was provided, as well as the inability of the smeared truss model to compensate for it, at the point of individual subsystem failure.

The evaluation of the numerical test series in section 5.4.1 on the other hand provided

insight in the ability of the model approach to account for changing variables and reproduce the investigated trends. While the model approach was performed solely with focus on its capability, no design model required definition of failure criteria, accounting for all limiting factors of the subsystems was made. At a reasonable first approach the limiting factor, taken as failure criterion, was provided by the load-bearing capacity of the smeared truss.

Both investigations showcase the potential of the presented approach in being implemented into a shear model grounded on physical behaviour of the concrete beam under load. However it has to be stated, that, if a shear verification model, based on this approach is to be developed, the limits of the included subsystems have to be accounted for.

6. Summary and Outlook

6.1. Summary

Economical design and sustainable as well as responsible use of resources has always been a fundamental trait of engineering. This core competence has come under increased focus of public interests in recent years, coinciding with some major changes in design standards as well as longevity of our building infrastructure. Facing this constellation, the economical maintenance and prolongation of the service life of structures can be seen as a significant contribution factor of civil engineers towards a responsible use of society's resources. To fulfil this duty realistic models, mimicking the structural behaviour and load bearing capacities, are crucial to avoid wasteful design and constructions. At this point, severe discrepancies between reality and design concerning the shear-bearing capacity of reinforced or prestressed concrete slender beams for certain real world conditions are noted by independent researchers. This disagreement forms the basis of this work.

Focusing on the multiple shear models in existence and use, spanning from single standing approaches like the fracture mechanic based models, attributing failure down to the fracture energy released in the crack propagation, to the more generally applicable models like the Compression Field Models, which base their behaviour on a more wholistic stress-strain relationships within the reinforced concrete members, it becomes clear, that the riddle of shear is still far from being solved satisfactorily. Enabling this plethora of distinct approaches is the inhomogeneous material reinforced concrete, providing multiple different mechanisms counteracting shear loading. Furthering this complexity are secondary influences deriving from external influences like loading conditions, selection of cross-section and longitudinal system.

Cutting down the abundance of parameters by focusing on high priority applications of reinforced or prestressed concrete slender beams in bridges, the case of a one-sided clamped single span girder loaded by a distributed load, mimicking internal as well as end supports, was chosen to be investigated further. Reasoning behind this choice lies in the stress distribution, allowing for overlapping of high normal stresses and high shear stresses at the clamped support. Compared to the usual test setup of a single span girder, this allows for load-bearing interactions to be considered. Highlighting the ability of the design of experiments approach, a numerical test series is designed around the variables slenderness, span length and transverse reinforcement ratio, consisting of 15 tests. While these tests do not have physical reference data, the numerical model and approach is validated against multiple tests from the literature, showing good agreement with the recorded data.

Evaluation of the numerical test series shows the aforementioned differences between the expected shear-bearing capacities according to the current design model and the simulated critical failure loads. Especially the low impact of the transverse reinforcement ratio on the critical failure load can be noted for the numerical results. They only provide a maximal increase of the critical failure load by 13% for a doubling of the transverse reinforcement ratio. In comparison, this difference, according to the EC2 shear design approach should be 200%, assuming the compression diagonal does not fail prior. This further showcases the shortcoming of the EC2 shear design approach in representing reality, as well as provide evidence that the reduction of the transverse reinforcement ratio does not compromise the safety of the structure significantly in case of coinciding normal compression stresses and shear stresses at the location of the critical control section. Reasoning for this behaviour influence can be found in the stress interaction of normal stresses, resulting from bending moments and the shear stresses. They control the allocation of loads and resulting contribution of the individual load-bearing mechanisms.

This stark difference highlights the biased databases, which were used in the development of the EC2 design approach, being almost purely consisting of single span experiments under concentrated loading and hence neglecting more complex stress distributions and interactions. Furthermore the lack of consideration of the shear bearing capacity of the concrete compression zone can be noted. While the design of reinforced concrete without transverse reinforcement does acknowledge some shear-bearing capacity of the concrete cross-section, it is disregarded as soon as transverse reinforcement is included. Hence the qualitative prediction improvement of the design method with increasing transverse reinforcement ratio can be fathomed, since the shear-bearing capacity of the concrete has a diminishing influence with an increase of other shear-bearing mechanisms.

Due to the shortcomings of the current design method to reliably predict the failure load of the test series' beams a structural engineering model is derived, focusing on global load-bearing mechanisms. It incorporates the smeared truss model as well as the compression arch model as subsystems of the beam, while disregarding localised mechanisms like the aggregate interlock or dowel action. Since these two models act simultaneously and work in parallel, coupling them is done via the deformation. This approach accounts for the possibility of changing stiffness relation and a resulting altering of the load distribution among them. As by-product this method allows for allocation of the acting load onto the subsystems in accordance to their stiffness, enabling the calculation of stresses in individual parts for any loading. Furthermore the coupling of the subsystems allows for redistribution of the loads in case of failure of a subsystem. However, failure of one subsystem can be synonymous to failure of the main structure in case of the subsystems being integral to the overall load-bearing mechanism, as present in this here case.

Using the beams from the numerical test series the design approach of the structural engineering model is showcased. In light of the presented method showcasing the potential of the approach, rather than it being a fleshed out verification model, the chosen failure criterion is taken to be governed by the smeared truss subsystem, disregarding limiting factors of the direct action model, presented as the compression arch with tension chord.

While these loads at coinciding deformation at the point of failure coincide with the trends of the three investigated variables resulting from the current design method of Eurocode 2, since the smeared truss model is the main load-bearing system, a qualitative improvement of the predicted failure loads is achieved. Comparison of the predicted failure loads shows a relative increase from the EC2 standard ranging from 15.6% for the large transverse reinforcement ratio to 29.2% for the small one when applying the structural engineering model instead. Decrease of the relative improvement with increasing transverse reinforcement ratio highlights the diminishing partaking of the concrete compression zone in the shear-bearing, as previously mentioned in the evaluation of the numerical test series, that is accounted for in the structural engineering model. Therefore it has to be stated that the developed and introduced model approach of parallelisation of load bearing mechanisms, allowing for interaction, does yield the potential of improvement predicted failure loads for the investigated case of a reinforced concrete one-sided clamped single span girders under uniformly distributed load.

Applicability and transferability of these results to prestressed concrete beams originates from the comparable stress situation is showcased by the evaluation of large scale cantilever tests. Especially the adaptability of the approach, based on the coupling of subsystems with individual load-bearing behaviour and limits, as well as possible a possible failure criterion are provided and proofed to yield good results for the investigated tests.

The numerical test series as well as the large scale cantilever tests do highlight the role of normal stresses at the critical control section. Particularly the normal stresses resulting from negative bending moments at the clamped support, even at the lack of normal forces within the beam, contribute significantly to the shear-bearing capacity of reinforced concrete beams, which can be accounted for by mechanical models regarding direct action. This effect is amplified when prestressing forces are present, as seen by the large scale tests.

6.2. Outlook

Apparent from all the shear models and lasting research in the field, the quest for the final shear model is far from over. Three major fields can be determined from this work for which further research is necessary to edge closer to it. Firstly a critical investigation of the existing shear tests of reinforced concrete slender beams in light of unintended bias seems necessary. Tools provided by approaches like the *Design of Experiments* should be applied retrospectively, as well as forming the foundation of further test series. Especially the combination of physical tests with numerical simulations needs to be pursued, allowing for economical design of test series, while not compromising the quality of knowledge gained. Therefore the evaluation of new models and methods should not be conducted using a statistical approach spanning a large number of physical tests, but rather on its quality to predict known and researched trends, leading to a more thorough understanding of strength

and weaknesses of each method as well as clearly identifying areas with potential of further investigation, research and improvement.

Secondly shear models as well as design philosophies need to clearly state their simplifications as well as reasoning behind it to allow for application as well as comparison to other models. In the case of the EC2 [40] in comparison to its predecessor in Germany DIN 1045 [38] and DIN 4227 [39], does completely neglect the partaking of the concrete compression zone in the shear bearing mechanisms, but only for transverse reinforced specimens, while acknowledging it in specimens without it. This not only shows inconsistencies in the design methodology but also makes a comparison to the previous standards extremely difficult. Therefore the reevaluation of existing structures using the new standards can not be quantified in its safety aspects as well as applicability. But most importantly the fact that a more recent version of a design verification does stray further from the observed physical behaviour can therefore be caught early on and adjustments can be made, since going backwards in the understanding of structural behaviour is never advised nor strived for.

Thirdly the introduced structural engineering model, allowing and recognising interactions of load-bearing mechanisms showed to be an obvious improvement over the current standard. While the predominant design approaches for concrete, dividing load-bearing mechanisms and viewing them as independent, are conservative, they can not represent the reality, as recognised by design approaches for different materials. Therefore the acknowledgement of interactions in load-bearing mechanisms can lead to a far more economical design for reinforced concrete structures, not just limited to shear. One obvious research field, which should be considered for this approach is the even more obscure load-bearing mechanisms concerning torsional moments in reinforced concrete specimens. The ability to break the load bearing mechanism down to individual subsystems not only allows for clear cut definition of the subsystems as well as evaluation using streamlined tests for them, but by coupling them the actual load-bearing capacity can be approached conservatively and on structural sound foundation.

Bibliography

[1] B. O. Aalami. Structural Modeling of Posttensioned Members. *Journal of Structural Engineering*, 126(2):157–162, 2000.

[2] ACI 318. *Building Code Requirements for Structural Concrete (ACI 318-08)*. American Concrete Institute, 2008.

[3] ACI 318-95. *Building Code Requirements for Reinforced Concrete (ACI 318-95) and Commentary ACI 318 R-95*. American Concrete Institute, 1995.

[4] ACI Committee 446. *446.1R-91: Fracture Mechanics of Concrete: Concepts, Models and Determination of Material Properties (Reapproved 1999)*. American Concrete Institute, 1991.

[5] P. Adebar and M. P. Collins. Shear Strength of Members without Transverse Reinforcement. *Canadian Journal of Civil Engineering*, 23:30–41, 1996.

[6] S. Ahmad, S. Bahij, M. A. Al-Osta, and S. U. Adekunle, S. K.and Al-Dulaijan. Shear Behaviour of Ultra-High-Performance Concrete Beams Reinforced with High-Strength Steel Bars. *ACI Structural Journal*, 116(4):3–16, 2019.

[7] C. Albrecht and J. Schnell. Zum Einfluss einzelner Traganteile auf die Querkrafttragfähigkeit von Stahlbetondecken mit integrierten Hohlräumen. *Beton- und Stahlbetonbau*, 112(e):133–143, 2017.

[8] B. Alfarah, F. López-Almansa, and S. Oller. New methodology for calculating damage variables evolution in Plastic Damage Model for RC structures. *Engineering Structures*, 132(8):70–86, 2017.

[9] D. Angelakos. *The influence of concrete strength and longitdunal reinforcement ratio on the shear strength of large-size reinforced concrete beams with, and without, transverse reinforcement*. PhD thesis, University of Toronto, 1999.

[10] A. Ayoub and F. C. Filippou. Finite-Element Model for Pretensioned Prestressed Concrete Girders. *Journal of Structural Engineering*, 136(4):401–409, 2010.

[11] A. Barbu and S.-C. Zhu. *Monte Carlo Methods*. Springer Nature Singapore Pte Ltd., 2020.

[12] BASt - Bundesanstalt für Straßenwesen. Brückenstatistik. https://www.bast.de/DE/Statistik/statistik-node.html, Sept. 2021. 15.12.2022.

[13] T. Baumann. Zur Frage der Netzbewehrung von Flächentragwerken. *Der Bauingenieur*, 47:367–377, 1972.

[14] T. Baumann and H. Rüsch. *Versuche zum Studium der Verdübelungswirkung der Biegezugbewehrung eines Stahlbetonbalkens*. Beuth Verlag GmbH Berlin-Wien-Zürich, 1970.

[15] Z. P. Bažant. Size Effect in Blunt Fracture: Concrete, Rock, Metal. *Journal of Engineering Mechanics*, 110(4):518–535, 1984.

[16] Z. P. Bažant. Size effect. *Internatinal Journal of Solids and Structures*, 37:69–80, 2000.

[17] Z. P. Bažant and M. T. Kazemi. Size Effect on Diagonal Shear Failure of Beams without Stirrups. *ACI Structural Journal*, 88(3):268–276, 1991.

[18] Z. P. Bažant and J.-K. Kim. Size Effect in Shear Failure of Longitudinally Reinforced Beams. *ACI Journal*, 81(5):456–468, 1984.

[19] Z. P. Bažant and J. Planas. *Fracture and Size Effect in Concrete and Other Quasibrittle Materials*. Routledge, 2019.

[20] Z. P. Bažant and Q. Yu. Designing Against Size Effect on Shear Strength of Reinforced Concrete Beams Without Sitrrups: I. Formulation. *Journal of Structural Engineering*, 131(12):1877–1885, 2005.

[21] Z. P. Bažant and Q. Yu. Designing Against Size Effect on Shear Strength of Reinforced Concrete Beams Without Sitrrups: II. Verification and Calibration. *Journal of Structural Engineering*, 131(12):1886–1897, 2005.

[22] E. C. Bentz, F. J. Vecchio, and M. P. Collins. Simplified Modified Compression Field Theory for Calculating Shear Strength of Reinforced Concrete Elements. *ACI Structural Journal*, 103(4):614–624, 2006.

[23] M. D. Brown, O. Bayrak, and J. O. Jirsa. Design for Shear Based on Loading Conditions. *ACI Structural Journal*, 103(4):541–550, 2006.

[24] J. Cairns, G. L. Balázs, J. Cairns, R. Eligehausen, S. Lettow, G. Metelli, S. Pantazopoulou, G. Plizzari, M. A. Aiello, C. Alander, J. Den Uijl, P. Gambarova, G. Genesio, A. Muttoni, C. Pellegrino, R. Tepfers, A. Wildermuth, and K. Zandi. *fib Bulletin 72. Bond and anchorage of embedded reinforcement: Background to the fib Model Code for Concrete Structures 2010*. fib. The International Federation for Structural Concrete, May 2014.

[25] A. P. Caldentey, P. Padilla, A. Muttoni, and M. F. Ruiz. Effect of Load Distribtion and Variable Depth on Shear Resistance of Slender Beams without Stirrups. *ACI Structural Journal*, 109(5):595–603, 2012.

[26] P. S. Chana. Investigation of the mechanism of shear failure of reinforced cocnrete beams. *Magazine of Concrete Research*, 39(141):196–204, 1987.

[27] K.-K. Choi, J.-C. Kim, and H.-G. Park. Shear Strength Model of Concrete Beams Based on Compression Zone Failure Mechanism. *ACI Structural Journal*, 113(5):1095–1106, 2016.

[28] K.-K. Choi and H.-G. Park. Unified Shear Strength Model for Reinforced Concrete Beams - Part II: Verification and Simplified Method. *ACI Structural Journal*, 104(2):153–161, 2007.

[29] K.-K. Choi, H.-G. Park, and J. K. Wight. Unified Shear Strength Model for Reinforced Concrete Beams - Part I: Development. *ACI Structural Journal*, 104(2):142–152, 2007.

[30] A. Cladera, A. Marí, J. Bairán, C. Ribas, E. Oller, and N. Duarte. The Compression Chord Capacity Model for the Shear Design and Assessment of Reinforced and Prestressed Concrete Beams. *Structural Concrete*, 17(6):1017–1032, 2016.

[31] M. P. Collins, E. C. Bentz, and E. G. Sherwood. Where is Shear Reinforcecment Required? Review of Research Results and Design Procedures. *ACI Structural Journal*, 105(5):590–600, 2008.

[32] M. P. Collins and A. Kuchma. How Safe are Our Large, Lightly Reinforced Concrete Beams, Slabs and Footings? *ACI Structural Journal*, 96(4):482–490, 1999.

[33] M. P. Collins, D. Mitchell, P. Adebar, and F. J. Vecchio. A General Shear Design Method. *ACI Structural Journal*, 93(1):36–45, 1996.

[34] CSA A23.3:19. *Design of concrete structures*. CSA Group, 2019.

[35] R. de Borst, J. J. C. Remmers, A. Needleman, and M.-A. Abellan. Discrete vs smeared crack models for cocnrete fracture: bridging the gap. *International Journal for Numerical and Analystical Methods in Geomechanics*, 28(7):583–607, 2004.

[36] Dessault Systèmes. *ABAQUS: Abaqus 6.14 Online Documentation*, 2014.

[37] A. Dey, D. Valiukas, R. Jakubovskis, A. Sokolov, and G. Kaklauskas. Experimental and Numerical Investigation of Bond-Slip Behaviour of High-Strength Reinforced Concrete at Service Load. *Materials*, 15(1):293, 2022.

[38] DIN 1045. *DIN 1045 - Beton- und Stahlbetonbau, Bemessung und Ausführung*. Beuth Verlag GmbH, 1972.

[39] DIN 4227. *DIN 4227 - Spannbeton Richtlinien für Bemessung und Ausführung*. Beuth Verlag GmbH, 1953.

[40] DIN EN 1991-2:2003 + AC:2010. *Eurocode 1: Einwirkungen auf Tragwerke - Teil 2: Verkehrslasten auf Brücken; Deutsche Fassung*. Deutsches Institut für Normung, 2010.

[41] DIN EN 1992-1-1:2004 + AC:2010. *Eurocode 2: Bemessung und Konstruktion von Stahlbeton- und Spannbetontragwerken - Teil 1-1: Allgemeine Bemessungsregeln und Regeln für den Hochbau; Deutsche Fassung*. Deutsches Institut für Normung, 2011.

[42] DIN EN 1992-1-1/NA:2011-01. *Nationaler Anhang - National festgelegte Parameter - Eurocode 2: Bemessung und Konstruktion von Stahlbeton- und Spannbetontragwerken - Teil 1-1: Allgemeine Bemessungsregeln und Regeln für den Hochbau*. Deutsches Institut für Normung, 2011.

[43] DIN EN 1993-1-1:2005 + AC:2009. *Eurocode 3: Bemessung und Konstruktion von Stahlbauten - Teil 1-1: Allgemeine Bemessungsregeln und Regeln für den Hochbau; Deutsche Fassung*. Deutsches Institut für Normung, 2010.

[44] D. C. Drucker. On Structural Concrete and the Theorems of Limit Analysis. *IVBH-Anhandlungen*, 21:49–59, 1961.

[45] R. H. Evans and M. S. Marathe. Microcracking and stress-strain curves for concrete in tension. *Matériaux et Constructions*, 1(1):61–64, 1968.

[46] J. Feld and K. L. Carper. *Construction Failure, 2nd Edition*. Wiley-Interscience, 1996.

[47] R. C. Fenwick and T. Pauley. Mechanism of Shear Resistance of Concrete Beams. *Journal of the Structural Division*, 94(10):2325–2350, 1968.

[48] fib MC2010. *fib Model Code for Concrerte Structures 2010*. International Federation for Structural Concrete, 2013.

[49] C. Fischer, J. Ožbolt, and C. Gehlen. Experimentelle und numerische Untersuchungen zum Einfluss der Bewehrungskorrosion auf das Verbundverhalten zwischen Stahl und Beton. *Beton- und Stahlbetonbau*, 105(5):284–293, 2010.

[50] O. Fischer, S. Gehrlein, J. Landler, and T. Oberndorfer. In-Situ Shear Tests on a 64-year-old Road Bridge. In *5th International fib Congress*, pages S. 338–339, Melbourne, Australia, Oct 2018.

[51] O. Fischer, T. Lechner, M. Wild, A. Müller, and K. Kessner. *Nachrechnung von Betonbrücken - Systematische Datenauswertung nachgerechneter Bauwerke*. Berichte der Bundesanstalt für Strassenwesen - Brücken- und Ingenieurbau (B). Fachverlag NW in Carl Ed. Schünemann, Bremen, Germany, 1 edition, Feb. 2016.

[52] O. Fischer, A. Müller, T. Lechner, M. Wild, and K. Kessner. Ergebnisse und Erkenntnisse zu durchgeführten Nachrechnungen von Betonbrücken in Deutschland. *Beton- und Stahlbetonbau*, 109(2):107–127, 2014.

[53] O. Fischer, N. Schramm, and S. Gehrlein. Experimentelle Untersuchungen zur wirklichkeitsnahen Beurteilung der Querkrafttragfähigkeit bestehender Spannbetonbrücken. In M. Pahn, C. Thiele, and C. Glock, editors, *Vielfalt im Massivbau - Festschrift zum 65. Geburtstag von Prof. Dr.-Ing. Jürgen Schnell*, pages S. 69–90. Ernst & Sohn, 2018.

[54] O. Fischer, S. Thoma, J. Hegger, and M. Schmidt. Weiterentwicklung der Nachrechnungsrichtlinie - Validierung erweiterter Nachweisformate zur Ermittlung der Schubtragfähigkeit bestehender Spannbetonbrücken. resreport 189, Bundeanstalt für Straßenwesen, 2023.

[55] P. Francis. *The influence of shear connection strength and stiffness on the resistance of steel-concrete composite sandwich panels to out-of-plane forces*. PhD thesis, The University of Surrey, 2018.

[56] C. Fust. *Zum Tragverhalten von gering querkraftbewehrten Stahlbetonbalken*. PhD thesis, Ruhr-Universität Bochum, 2017.

[57] J. Gallwoszus. *Zur Ermüdung von Verbundkonstruktionen mit Verbunddübelleisten*. PhD thesis, Rheinisch-Wästfälische Technische Hochschule Aachen, 2014.

[58] P. G. Gambarova and C. Karakoc. A New Approach to the Analysis of the Confinement Role in Regularly Cracked Concrete Elements. *Transactions of the 7. Internatinal Conference on Structural Mechanics in Reactor Technology*, H(5):251–261, 1983.

[59] S. Gehrlein and O. Fischer. Großversuche zur Querkrafttragfähigkeit bestehender Spannbetonbrücken an der Saalebrücke Hammelburg. *Beton- und Stahlbetonbau*, 113(10):696–704, Sept. 2018.

[60] S. Gehrlein, J. Landler, T. Oberndorfer, and O. Fischer. Großversuche zur Querkrafttragfähigkeit bestehender Spannbetonbrücken an der Saalebrücke Hammelburg, Teil 1: Konzeption, Beurteilung des Bestands und Durchführung der Versuche. *Beton- und Stahlbetonbau*, 113(9):667–675, 2018.

[61] P. Gleich. *Das Erweiterte Druckbogenmodell zur Beschreibung des Betontraganteils bei Querkraft*. PhD thesis, Technische Universität Dortmund, 2020.

[62] P. Gleich and R. Maurer. Investigations into the shear load bearing capacity of a prestressed two-span concrete beam - findings from a large scale experiment. In *Proceedings to fib Symposium in Copenhagen*, 2015.

[63] P. Gleich and R. Maurer. Das Erweiterte Druckbogenmodell für die Nachrechnung von Spannbetonbrücken - Theoretische Hintergründe. *Bauingenieur*, 95(11):430–439, 2020.

[64] A. Goris and J. Hegger. *Stahlbetonbau aktuell 2011*. Bauwerk, 2011.

[65] S. Görtz. *Zum Schubrissverahlten von Stahlbeton- und Spannbetonbalken aus Normal- und Hochleistungsbeton*. PhD thesis, Rheinisch-Westfäischen Technischen Hochschule Aachen, 2004.

[66] J. Hegger and S. Görtz. Querkraftmodell für Bauteile aus Normalbeton und Hochleistungsbeton. *Beton- und Stahlbetonbau*, 101(9):695–705, 2006.

[67] J. Hegger and S. Görtz. *Querkrafttragfähigkeit von Stahlbeton- und Spannbetonbalken aus Normal- und Hochleistungsbeton*. Number 557 in DAfStb - Schriftenreihe. Beuth Verlag GmbH Berlin-Wien-Zürich, 2007.

[68] J. Hegger, M. Herbrand, V. Adam, R. Maurer, P. Gleich, E. Stuppak, O. Fischer, N. Schramm, W. Scheufler, K. Zilch, and R. Tecusan. Beurteilung der Querkraft- und Torsionstragfähigkeit von Brücken im Bestand – erweiterte Bemessungsansätze. resreport 150, Bundeanstalt für Straßenwesen, 2020.

[69] J. Hegger, A. Karakas, E. Pelke, and U. Schölch. Zur Querkraftgefährdung bestehnder Spannbetonbrücken Teil I: Grundlagen. *Beton- und Spannbetonbau*, 104(11):737–746, 2009.

[70] M. Herbrand. *Shear Strength Models for Reinforced and Prestressed Concrete Members*. PhD thesis, RWTH Aachen University, 2017.

[71] M. Herbrand, D. Kueres, M. Claßen, and J. Hegger. Einheitliches Querkraftmodell zur Bemessung von Stahl- und Spannbetonbrücken im Bestand. *Beton- und Stahlbetonbau*, 111(2):58–67, 2016.

[72] A. Hillerborg. *Fracture Mechanics of Concrete (Developments in civil engineering)*, chapter Analysis of one single crack, pages 223–249. Elsevier, 1983.

[73] A. Hillerborg, M. Modeer, and P.-E. Petersson. Analysis of Crack Formation and Crack Growth in Concrete by Means of Fracture Mechanics and Finite Elements. *Cement and Concrete Research*, 6(6):773–782, 1976.

[74] D. A. Hordijk. *Local Approach to Fatigue of Concrete*. PhD thesis, Delft University of Technology, 1991.

[75] D. A. Hordijk. Tensile and tensile fatigue behaviour of concrete; experiments, modelling and analyses. *Heron*, 37(1):1–79, 1992.

[76] T. T. C. Hsu. Softend Truss Model Theory for Shear and Torsion. *ACI Structural Journal*, 85(6):624–635, 1988.

[77] T. T. C. Hsu, A. Belarbi, and X.-B. Pang. A Universal Panel Tester. *Journal of Testing and Evaluation*, 23(1):41–49, 1995.

[78] P. Huber. *Beurteilung der Querkrafttragfähigkeit bestehender Stahlbeton- und Spannbetonbrücken*. PhD thesis, TU Wien, 2016.

[79] P. Huber, T. Huber, and J. Kollegger. Influence of loading conditions on the shear capacity of post-tensioned beams with low shear reinforcement ratios. *Engineering Structures*, 170(6):91 – 102, 2018.

[80] P. Huber, B. Kromoser, J. Kollegger, and T. Huber. Experimentelle Untersuchung zum Querkrafttragverhalten von Spannbetonträgern mit geringer Schubbewehrung. *Bauingenieur*, 91(6):238–247, 2016.

[81] T. Huber. *Beurteilung der Querkrafttragfähigkeit bestehender Stahlbetonplattenbrücken mit Aufbiegungen*. PhD thesis, TU Wien, 2019.

[82] T. Jankowiak and T. Lodygowski. Identification of parameters of concrete damage plasticity constitutive model. *Foundations of Civil and Environmental Engineering*, 6:53–69, 2005.

[83] I. Jelić, M. N. Pavlović, and M. D. Kotsovos. A study of dowel action in reinforced concrete beams. *Magazine of Concrete Research*, 51(2):131–141, 1999.

[84] Y. S. Jenq and S. P. Shah. Shear Resistance of Reinforced Concrete Beams – A Fracture Mechanics Approach. *ACI Special Publication*, 118:237–258, 1990.

[85] B. Jones and C. J. Nachtsheim. A Class of Three-Level Designs for Definitive Screening in the Presence of Second-Order Effects. *Journal of Quality Technology*, 43(1):1–15, 2011.

[86] G. N. J. Kani. The Riddle of Shear Failure and Its Solution. *ACI Journal*, 61(4):441–467, 1964.

[87] G. N. J. Kani. Basic Facts Concerning Shear Failure. *ACI Journal*, 63(6):675–692, 1966.

[88] G. N. J. Kani. How Safe are Our Large Reinforced Concrete Beams. *ACI Journal*, 64(3):128–141, 1967.

[89] W. Kaufmann and P. Marti. Structural Concrete: Cracked Membrane Model. *Journal of Structural Engineering*, 124(12):1467–1475, 1998.

[90] A. J. Khan, N. Iqbal, H. A. Saeed, and W. A. Tarar. Development of material model for assessment of brittle cracking behaviour of plexiglas. *IOP Conf. Series: Material Science and Engineering*, 146:1–9, 2016.

[91] H. Kiziltan. *Zum Einfluss des Druckbogens auf den Schubwiderstand von Spannbetonbalken*. PhD thesis, Technische Universität Dortmund, 2012.

[92] M. Kozlowski, M. Kadela, and J. Hulimka. Numerical Investigation of Structural behaviour of Timber-Glass Composite Beams. *Procedia Engineering*, 161:990–1000, 2016.

[93] W. Krefeld and C. Thurston. Contribution of longitudinal steel to shear resistance of reinforced concrete beams. *ACI Journal*, 63(3):325–344, 1966.

[94] D. P. Kroese, T. Taimre, and Z. I. Botev. *Handbook of Monte Carlo Methods*. John Wiley & Sons, Inc., Hoboken, New Jersey, 2011.

[95] H. Kupfer. Erweiterung der Mörsch'schen Fachwerkanalogie mit Hilfe des Prinzips vom Minimum der Formänderungsarbeit. *CEB Bulletin d'Information*, 40:44–57, 1964.

[96] H. Kupfer. Behaviour of Concrete under Biaxial Stresses. *Journal of the Engineering Mechanics Division*, 99(4):853–866, 1973.

[97] H. Kupfer. *Das Verhalten des Betons unter mehrachsiger Kurzzeitbelastung unter besonderer Berücksichtigung der zweiachsigen Beanspruchung*. Number 229 in DAfStb - Schriftenreihe. Verlag Wilhelm Ernst & Sohn Berlin - München - Düsseldorf, 1973.

[98] J. Lee and G. L. Fenves. Plastic-Damage Model for Cyclic Loading of Concrete Structures. *Journal of Engineering Mechanics*, 124(8):892–900, 1998.

[99] J.-Y. Lee and J. Kim. Simplified Equation Based on Compatibility-Aided Truss Model for Shear Strength of Reinforced Concrete Beams. *ACI Structural Journal*, 113(6):1301–1312, 2016.

[100] L. Lemnitzer, S. Schröder, A. Lindorf, and M. Curbach. Bond behaviour between reinforcing stell and concrete under multiaxial loading conditions in concrete containments. In *20th Internatinal Conference on Structural Mechanics in Reactor Technology (SMiRT 20)*, 2009.

[101] F. Leonhardt. *Vorlesungen über Massivbau*. Springer-Verlag Berlin Heidelberg New York, 2 edition, 1973.

[102] F. Leonhardt, R. Koch, and F.-S. Rostásy. *Schubversuche and Spannbetonträgern*. DAfStb - Schriftenreihe. Verlag von Wilhelm Ernst & Sohn Berlin-München-Düsseldorf, 1973.

[103] F. Leonhardt and R. Walther. *Versuche an einfeldrigen Stahlbetonbalken mit und ohne Schubbewehrung*. Number 151 in DAfStb - Schriftenreihe. Verlag von Wilhelm Ernst & Sohn, 1962.

[104] F. Leonhardt and R. Walther. *Versuche an Plattenbalken mit hoher Schubbeanspruchung*. Number 152 in DAfStb - Schriftenreihe. Verlag von Wilhelm Ernst & Sohn, 1962.

[105] F. Leonhardt and R. Walther. *Schubversuche an Plattenbalken mit unterschiedlicher Schubbewehrung*. Number 156 in DAfStb - Schriftenreihe. Verlag von Wilhelm Ernst & Sohn, 1963.

[106] F. Leonhardt and R. Walther. *Schubversuche an Durchlaufträgern*. Number 164 in DAfStb - Schriftenreihe. Verlag von Wilhelm Ernst & Sohn, 1964.

[107] F. Leonhardt, R. Walther, and W. Dilger. *Schubversuche an indirekt gelagerten, einfeldrigen und durchlaufenden Stahlbetonbalken*. Number 201 in DAfStb - Schriftenreihe. Verlag von Wilhelm Ernst & Sohn, 1968.

[108] B. Li, K. Maekawa, and H. Okamura. Contact Density Model for Stress Transfer across Cracks in Concrete. *Journal of hte Faculty of Engineering, The University of Tokyo*, 40(1):9–52, 1989.

[109] A. Lindorf. *Ermüdung des Verbundes von Stahlbeton unter Querzug*. PhD thesis, Technische Universität Dresden, 2011.

[110] M. Loch. *Beitrag zur Bestimmung von charakteristischen Werkstofffestigkeiten in Bestandstragwerken aus Stahlbeton*. PhD thesis, Technische Universität Kaiserslautern, 2014.

[111] J. Lubliner, J. Oliver, S. Oller, and E. Oñate. A plastic-damage model for concrete. *International Journal of Solids and Structures*, 25(3):299–326, 1989.

[112] O. Luzanin, V. Guduric, I. Ristic, and S. Muhic. Investigating impact of fice build parameters on the maximum flexural force in FDM specimens - a definitive screening design approach. *Rapid Prototyping Journal*, 23:1088–1098, 2017.

[113] J. G. MacGregor and J. R. V. Walters. Shear in Slender Reinforced Concrete Beams. *ACI Journal*, 64:644–653, 1967.

[114] H. A. Mang and G. Hofstetter. *Festigkeitslehre*, volume 4. Springer Vieweg, 2013.

[115] P. Mark. *Zweiachsig durch Biegung und Querkräfte beanspruchte Stahlbetonträger*. Habilitationsschrift, Ruhr-Universität Bochum, 2006.

[116] P. Marti and A. Beck. Querkraftwiderstand von Stahlbetonbauteilen ohne Querkfratbehwerung. *Beton- und Stahlbetonbau*, 111(11):716–727, 2016.

[117] A. H. Mattock, L. Johal, and H. C. Chow. Shear transfer in reinforced concrete with moment or tension acting across the shear plane. *PCI Journal*, 20(4):76–93, 1975.

[118] D. Mitchell and M. P. Collins. Diagonal Compression Field Theorie - A Rational Model for Structural Concrete in Pure Torsion. *ACI Journal*, 71(8):396–408, 1974.

[119] A. Muttoni. *Die Anwendbarkeit der Plastizitätstheorie in der Bemessung von Stahlbeton*, volume 176 of *Bericht / Institut für Baustatik und Konstruktion ETH Zürich*. Birkhäuser Verlag Basel, 1990.

[120] A. Muttoni and M. F. Ruiz. Shear Strength of Members without Transverse Reinforcement as Function of Critical Shear Crack. *ACI Structural Journal*, 105(2):163–172, 2008.

[121] A. Muttoni and J. Schwartz. Behaviour of Beams and Punching in Slabs without Shear Reinforcement. *Proceedings of the IABSE Colloquium*, 62:703–708, 1991.

[122] E. Mörsch. *Der Eisenbetonbau, seine Theorie und Anwendung*. Konrad Wittwer, 3 edition, 1908.

[123] M. Müller. *Zum schubfesten Anschluss von Druckgurten in Hohlkastenbrücken*. PhD thesis, Technische Universität Dortmund, 2016.

[124] T. Müller-Gronbach, E. Novak, and K. Ritter. *Monte Carlo-Algorithmen*. Springer-Verlag Berlin Heidelberg, 2012.

[125] Nachrechnungsrichtlinie. *Richtlinie zur Nachrechnung von Straßenbrücken im Bestand (Nachrechnungsrichtlinie)*. Bundesministerium für Verkehr, Bau und Stadtentwicklung, Abteilung Straßenbau, 2011.

[126] M. P. Nielsen, M. W. Braestrup, and F. Bach. Rational Analysis of Shear in Reinforced Concrete Beams. *IABSE Proceedings*, 2:1–16, 1978.

[127] J. Nilimaa, J. Bagge, J. Häggström, T. Blanksvärd, G. Sas, B. Täljsten, and L. Elfgren. More Realistic Codes for Existing Bridges. In *IABSE Conference 2016: Bridges and Structures Sustainability - Seeking Intelligent Solutions*, volume 106 of *IABSE Symposium Report*, pages 376–384, 2016.

[128] B. H. Oh and K. S. Kim. Shear Behaviour of Full-Scale Post-Tensioned Prestressed Concrete Bridge Girders. *ACi Structural Journal*, 101(2):176–182, 204.

[129] X.-B. Pang and T. T. C. Hsu. Fixed Angle Softened Truss Model for Reinforced Concrete. *ACI Structural Journal*, 93(2):197–207, 1996.

[130] C. Petersen. *Statik und Stabilität der Baukonstruktionen*. Friedr. Vieweg & Sohn, 1982.

[131] M. Petrangeli and Ožbolt. Smeared crack approaches - material modeling. *Journal of Engineering Mechanics*, 122(6):545–554, 1996.

[132] R. V. Pieri. *Size Effects in Linear Elastic Fracture Mechanics*. PhD thesis, Carnegie-Mellon University, 1987.

[133] R. Pölling. *Eine praxisnahe, schädigungsorientierte Materialbeschreibung für Stahlbeton*. PhD thesis, Ruhr-Universität Bochum, 2000.

[134] K. N. Rahal and K. S. Al-Shaleh. Minimum Transverse Reinforcement in 65 MPa Concrete Beams. *ACI Structural Journal*, 101(6):872–878, 2004.

[135] Y. R. Rashid. Analysis of prestressed concrete pressure vessels. *Nuclear Engineering and Design*, 7(4):334–344, 1968.

[136] P. E. Regan. Research on Shear a Benefit to Humanity or a Waste of Time. *The Structural Engineer*, 71(19):337–347, 1993.

[137] K.-H. Reineck. *Ein Mechnaisches Modell für den Querkraftbereich von Stahlbetonbauteilen*. PhD thesis, Universität Stuttgart, 1990.

[138] K.-H. Reineck. Ultimate Shear Force of Structural Concrete Members without Transverse Reinforcement Derived from a Mechanical Model. *ACI Structural Journal*, 88(5):592–602, 1991.

[139] K. H. Reineck, E. C. Bentz, B. Fitik, D. A. Kuchma, and O. Bayrak. ACI-DAfStb Database of Shear Tests on Slender Reinforced Concrete Beams without Stirrups. *ACI Structural Journal*, 110(5):867–876, 2013.

[140] K. H. Reineck, E. C. Bentz, B. Fitik, D. A. Kuchma, and O. Bayrak. ACI-DAfStb Databases for Shear Tests on Slender Reinforced Concrete Beams with Stirrups. *ACI Structural Journal*, 111(5):1147–1156, 2014.

[141] K.-H. Reineck, D. A. Kuchma, and B. Fitik. *Erweiterte Datenbanken zur Überprüfung der Querkraftbemessung für Konstruktionsbetonbauteile mit und ohne Bügel*. Number 597 in DAfStb Heft. Beuth Verlag GmbH Berlin-Wien-Zürich, 2012.

[142] K.-H. Reineck, D. A. Kuchma, K. S. Kim, and S. Marx. Shear Database for Reinforced Concrete Members without Shear Reinforcement. *ACI Structural Journal*, 100(2):240–249, 2003.

[143] R. Reineck. *Haftverbund und Rissverzahnung in unbewehrten Betonschubfugen*. PhD thesis, Technische Universität München, 2002.

[144] H.-W. Reinhardt. Maßstabseinfluß bei Schubversuchen im Licht der Bruchmechanik. *Beton- und Stahlbetonbau*, 76(1):19–21, 1981.

[145] H. W. Reinhardt and D. A. Hordijk. Tensile Tests and Failure Analysis of Concrete. *Journal of Structural Engineering*, 112(11), 1986.

[146] W. Ren, L. H. Sneed, Y. Yang, and R. He. Numerical Simulation of Prestressed Precast Concrete Bridge Deck Panels Using Damage Plasticity Model. *International Journal of Concrete Strucftures and Materials*, 9:45–54, 2015.

[147] L. Ritter. *Der Einfluss von querzug auf den Verbund zwischen Beton und Betonstahl*. PhD thesis, Technische Universität Dresden, 2013.

[148] W. Ritter. Die Bauweise Hennebique. *Schweizerische Bauzeitung*, 33/34(5,6 und 7):41–43/49–52/59–61, 1899.

[149] F.-S. Rostásy, K. Roeder, and F. Leonhardt. *Schubversuche an Balken mit veränderlicher Trägerhöhe*. Number 273 in DAfStb - Schriftenreihe. Beuth Verlag GmbH Berlin-Wien-Zürich, 1977.

[150] J. G. Rots and J. Blaauwendraad. Crack models for concrete: discrete or smeared? Fixed, multi-directional or rotating? *Heron*, 34:3–59, 1989.

[151] M. F. Ruiz and A. Muttoni. On Development of Suitable Stress Fields for Structural Concrete. *ACI Structural Journal*, 104(4):495–502, 2007.

[152] M. M. Rupf. *Querkraftwiderstand von Stahlbeton- und Spannbetonträgern mittels Spannungsfeldern*. PhD thesis, École Polytechnique Fédérale de Lausanne, 2014.

[153] H. Rüsch, F. R. Haugli, and H. Mayer. *Schubversuche an Stahlbeton-Rechteckbalken mit gleichmäßig verteilter Belastung*. Verlag von Wilhelm Ernst & Sohn, 1962.

[154] J. Sagaseta and R. L. Vollum. Influence of aggregate fracture on shear transfer through cracks in reinforced concrete. *Magazine of Concrete Research*, 63(2):119–137, 2011.

[155] T. J. Santner, B. J. Williams, and W. I. Notz. *The Design and Analysis of Computer Experiments*. Springer-Verlag New York, 2018.

[156] N. Schramm. *Zur Querkrafttragfähigkeit von Spannbetonbalkenelementen unter besonderer Berücksichtigung der Bügelform*. PhD thesis, Technische Universität München, 2021.

[157] N. Schramm and O. Fischer. Zur Anrechenbarkeit von nicht normgemäßen Bügelformen auf die Querkrafttragfähigkeit von Bestandsbrücken. *Bauingenieur*, 95(11):408–418, 2020.

[158] N. Schramm, S. Gehrlein, and O. Fischer. Querkrafttragverhalten von großformatigen Spannbetonbalkenelementen mit Plattenbalkenquerschnitt. *Beton- und Stahlbetonbau*, 115(1):2–12, 2019.

[159] E. Sharei. *Simulation concepts for concrete structures with discrete and smeared representation of reinforcement*. PhD thesis, Rheinisch-Westfälische Teschnische Hochschule Aachen, 2018.

[160] SIA 262. *SIA 262 Betonbau*. Schweizerischer Ingenieur- und Architektenverein, 2013.

[161] K. Siebertz, D. Bebber van, and T. Hochkirchen. *Statistische Versuchsplanung*. Springer-Verlag Berlin Heidelberg, 2010.

[162] V. Sigrist. Zur Querkraftbemessung von Stahlbetonträgern. *Beton- und Stahlbetonbau*, 100(5):390–397, 2005.

[163] V. Sigrist and B. Hackbarth. Querkrafttragfähigkeit von Stahlbetonträgern - Bemessung, Überprüfung, Beurteilung. *Beton- und Stahlbetonbau*, 105(11):686–694, 2010.

[164] K. O. So and B. L. Karihaloo. Shear Capacity of Longitudinally Reinforced Beams: A Fracture Mechanics Approach. *ACI Structural Journal*, 90(6):591–600, 1993.

[165] H. Taylor. *Fundamental Behaviour in Bending and Shear of Reinforced Concrete*. PhD thesis, The City Unversity, 1971.

[166] H. P. J. Taylor. The Fundamental Behaviour of Reinforced Concrete Beams in Bending and Shear. *ACI Spcial Publication*, 42:43–77, 1974.

[167] R. Thamrin, J. Tanjung, R. Aryanti, O. F. Nur, and A. Devinus. Shear strength of reinforced concrete T-beams without stirrups. *Journal of Engineering Science and Technology*, 11(4):548–562, 2016.

[168] B. Thürlimann. Plastic analysis of reinforced concrete beams. *IABSE reports of the working commissions*, 28:72–90, 1979.

[169] N. V. Tue, R. Ehmann, C. Betschoga, and N. D. Tung. Einfluss geringer Querkraftbewehrung auf die Querkrafttragfähigkeit von Stahlbetonbalken unterschiedlicher M/V-Kombinationen. *Beton- und Stahlbetonbau*, 114(4):217–230, dec 2018.

[170] A. K. Tureyen, T. S. Wolf, and R. J. Frosch. Shear Strength of Reinforced Concrete T-Beams without Transverse Reinforcement. *ACI Structural Journal*, 103(5):656–663, 2006.

[171] J. G. M. van Mier. *Concrete Fracture*. CRC Press, Oct. 2012.

[172] F. J. Vecchio. Analysis of Shear-Critical Reinforced Concrete Beams. *ACI Structural Journal*, 97(1):102–111, 2000.

[173] F. J. Vecchio and M. P. Collins. *Response of Reinforced Concrete to In-Plane Shear and Normal Stresses*, volume 82 of *Publication*. University of Toronto, Department of Civil Engineering, 1982.

[174] F. J. Vecchio and M. P. Collins. The Modified Compression Field Theory for Reinforced Concrete Elements Subjedted to Shear. *ACI Journal*, 83(2):219–231, 1986.

[175] F. J. Vecchio and M. P. Collins. Predicting the Response of Reinforced Concrete Beams Subjected to Shear Using Modified Compression Field Theorie. *ACI Structural Journal*, 85(3):258–268, 1988.

[176] F. J. Vecchio and W. Shim. Experimental and Analytical Reexamination of Classic Concrete Beam Tests. *Journal of Structural Engineering*, 130(3):460–469, 2004.

[177] E. N. Vintzeleou and T. P. Rassios. Mathematical models for dowel action under monotonic and cyclic conditions. *Magazine of Concrete Research*, 38(134):13–22, 1986.

[178] R. A. Vonk. A micromechanical investigation of solftening of concrete loaded in compression. *Heron*, 38:3–94, 1993.

[179] J. C. Walraven. *Influence of Member Depth on the Shear Strength of Lightweight Concrete Beams without Shear Reinforcement*, volume 5-78-4 of *Stevin Report*. Delft University of Technology, 1978.

[180] J. C. Walraven. *Aggreagte Interlock: A Theoretical and Experimental Analysis*. PhD thesis, Technische Universiteit Delft, 1980.

[181] J. C. Walraven. Fundamental Analysis of Aggregate Interlock. *Journal of the Structural Division*, 107(11):2245–2270, 1981.

[182] J. C. Walraven and J. Stroband. Shear Friction in high-Strength Concrete. *ACI Special Publication*, 149:311–330, 1994.

[183] J. C. Walraven, E. Vos, and H. W. Reinhardt. *Experiments on shear transfer in cracks in concrete. Part I: Discription of results*. Delft University of Technology, 1979.

[184] W. Weibull. A Statistical Distribution Function of Wide Applicability. *Journal of Applied Mechanics*, 18(3):293–297, sep 1951.

[185] S. Xu, X. Zhang, and H. W. Reinhardt. Shear Capacity Prediction of Reinforced Concrete Beams without Stirrups Using Fracture Mechanics Approach. *ACI Structural Journal*, 109(5):705–713, 2012.

[186] Y. Yang. *Shear Behaviour of Reinforced Concrete Members without Shear Reinforcemen*. PhD thesis, Technische Universiteit Delft, 2014.

[187] Q. Yu and Z. P. Bažant. Can Stirrups Suppress Size Effect on Shear Strength of RC Beams? *Journal of Structural Engineering*, 137(5):607–617, 2011.

[188] I. P. Zararis, M. K. Karaveziroglou, and P. D. Zararis. Shear Strength of Reinforced Concrete T-Beams. *ACI Structural Journal*, 103(5):693–700, 2006.

[189] P. D. Zararis. Shear Strength and Minimum Shear Reinforcement of Reinforced Concrete Slender Beams. *ACI Structural Journal*, 100(2):203–214, 2003.

[190] P. D. Zararis and G. C. Papadakis. Diagonal Shear Failure and Size Effect in RC Beams Without Web Reinforcement. *Journal of Structural Engineering*, 127(7):733–742, 2001.

[191] P. D. Zararis and I. P. Zararis. Shear Strength of Reinforced Concrete Beams under Uniformly Distributed Loads. *ACI Structural Journal*, 105(6):711–719, 2008.

[192] P. D. Zararis and I. P. Zararis. Shear Strength of Reinforced Concrete Slender Beams with or without Axial Forces - A Generalized Theory. *ACI Structural Journal*, 106(6):782–789, 2009.

[193] M. Zink. *Zum Biegeschubversagen schlanker Bauteile aus Hochleistungsbeton mit und ohne Vorspannung*. Springer-Verlag, Berlin Heidelberg New York, 2013.

Appendix

A. Results of the Numerical Test Series

This appendix provides the results of the numerical test series. They are split up into the following sections:

- A.1 Setup and Dimensions: Test setup as well as specimen dimension of the numerical simulation are provided in figures,
- A.2 Tables: Simulation results are provided in tabulated form,
- A.3 Diagrams: Simulation results are provided in diagrams for the test series,
- A.4 Visuals: Simulation results are provided in visual form.

A.1. Setup and Dimensions

In this section the test setup as well as the specimens cross-sections are provided. They are divided depending on the beams length into figures A.1 - A.3. Material data as well as the dimensions of the reinforcement are provided in section 4.5 table 4.8.

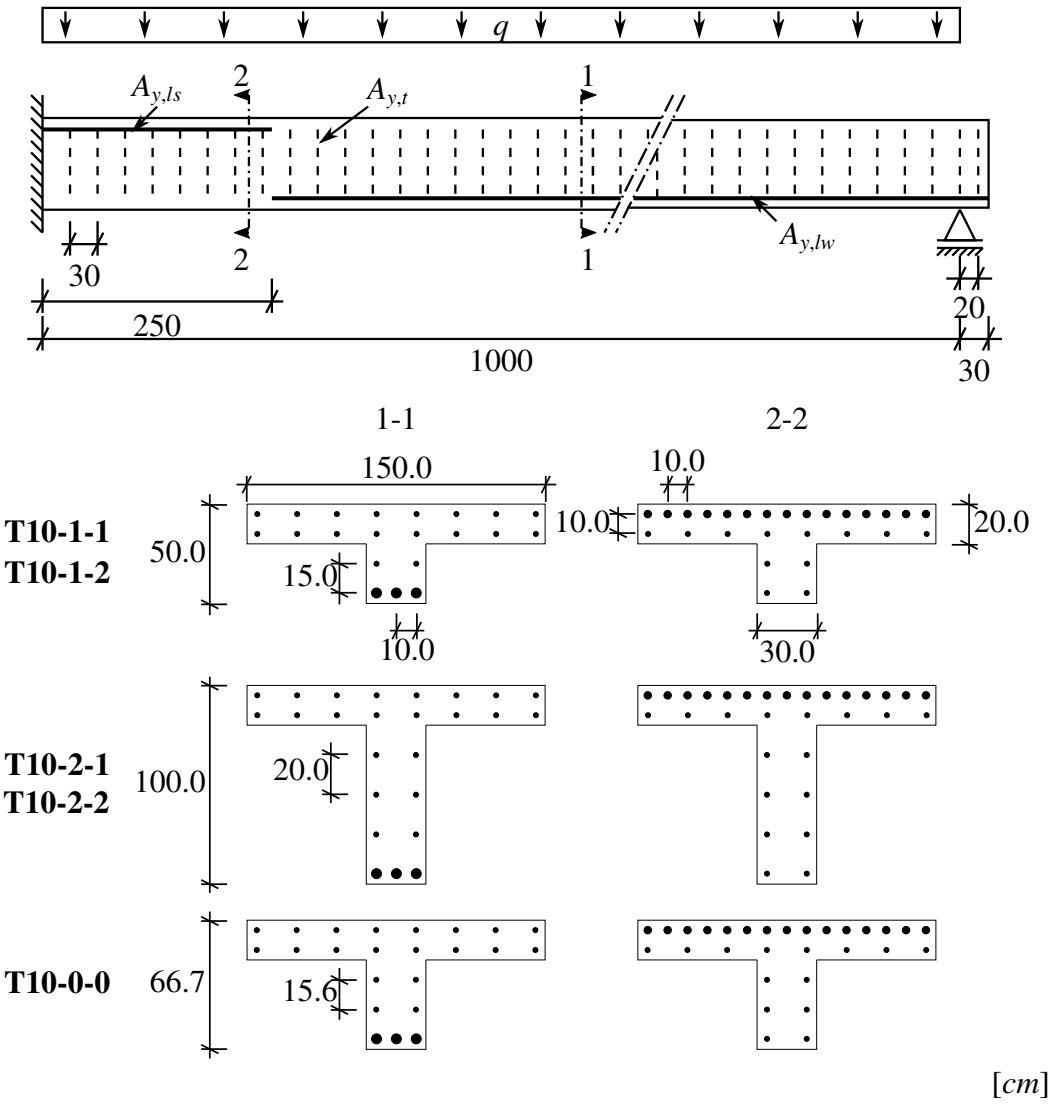

Figure A.1.: Setup of the numerical tests with a beam length of 10 *m*

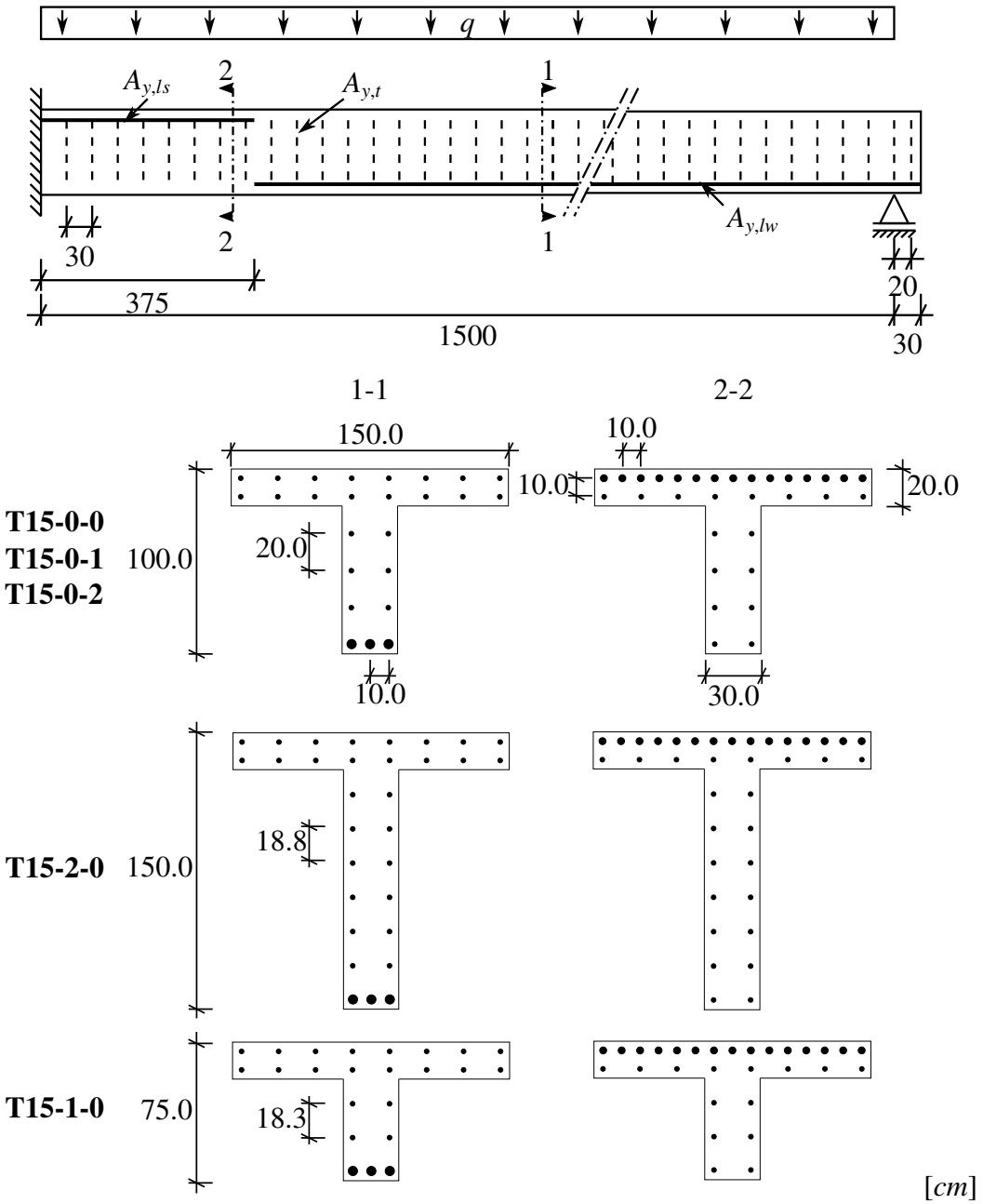

Figure A.2.: Setup of the numerical tests with a beam length of 15 *m*

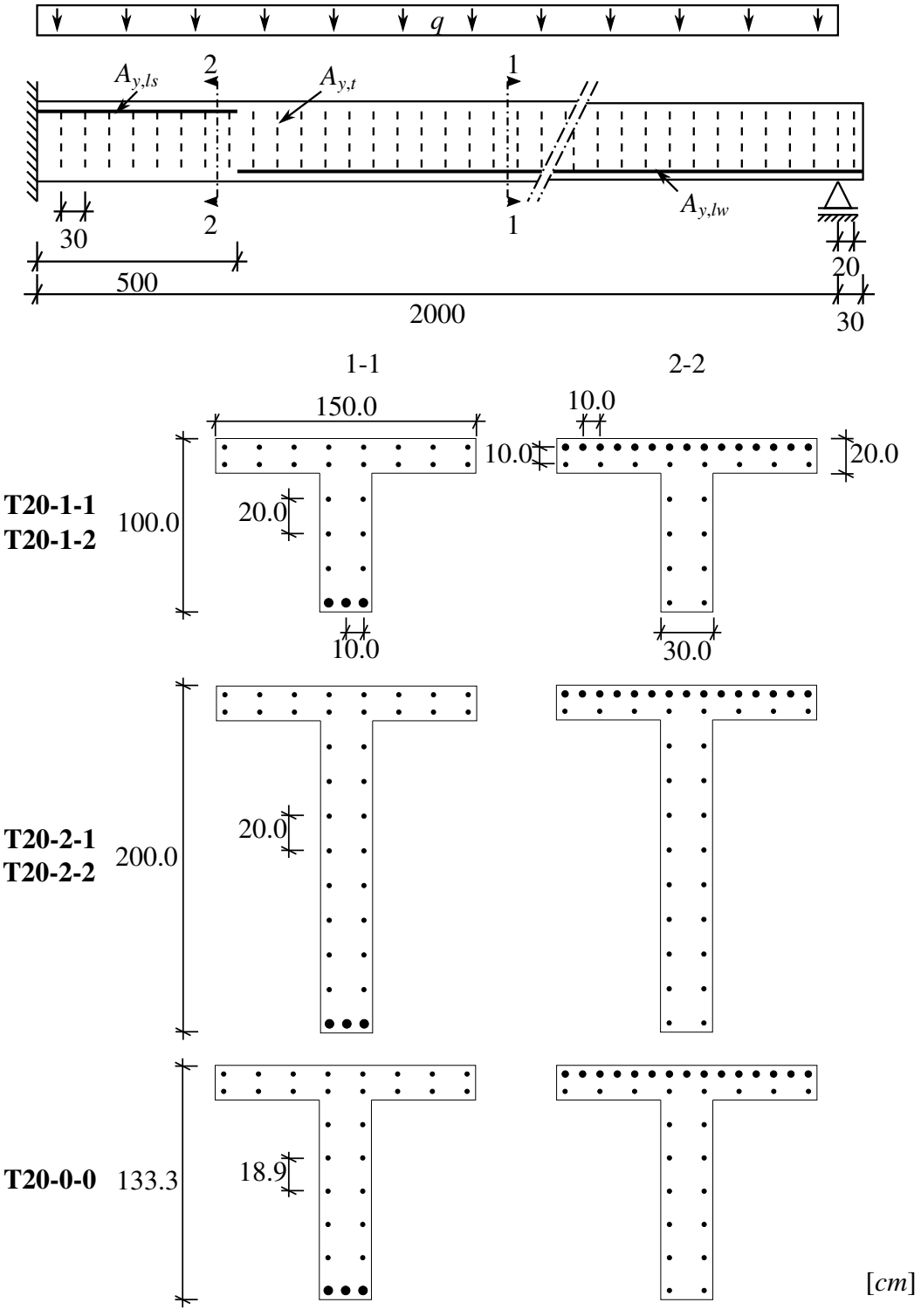

Figure A.3.: Setup of the numerical tests with a beam length of 20 *m*

A.2. Tables

In this section the results of the test series are provided in tabulated form. Table A.1 provides the critical failure force for the tests $F_{crit,tot}$ as well as the maximal reaction forces for the intermediate support (clamped) $F_{cirt,sc}$ and the end support (moment free) $F_{crit,sf}$.

The explicit solver is responsible that there is a discrepancy between the sum of $F_{cirt,sc}$ and $F_{crit,sf}$ when being compared to $F_{crit,tot}$. The reason for this lies in the interpolation method of the solver, resulting in different points of each maximal value. Since they do not coincide this discrepancy justified and small enough to be neglected in light of other uncertainties.

Table A.1.: Maximal values of the test series for total reaction force $F_{crit,tot}$, clamped support $F_{crit,sc}$ and moment free support $F_{crit,sf}$

Test ID	$F_{crit,tot}$ $[kN]$	$F_{crit,sc}$ $[kN]$	$F_{crit,sf}$ $[kN]$
T10-1-1	850.12	522.24	334.55
T10-1-2	821.96	504.86	326.13
T10-2-1	1655.31	1022.3	676.22
T10-2-2	1637.43	1005.17	668.8
T20-1-1	1122.57	698.62	472.06
T20-1-2	1225.08	750.71	482.88
T20-2-1	2187.71	1364.73	937.79
T20-2-2	2534.2	1502.03	1048.15
T10-0-0	1203.14	733.05	472.16
T20-0-0	1634.68	1003.88	636.99
T15-1-0	1058.0	656.41	429.52
T15-2-0	2066.22	1253.08	861.2
T15-0-1	1392.15	835.32	601.44
T15-0-2	1541.94	943.12	615.99
T15-0-0	1504.63	911.95	599.25

A.3. Diagrams

In this section the loading of the test beams, as well as their behaviour are provided. Figures A.4 - A.6 provide the total loading over time as well as the reaction forces for the intermediate support (clamped) and the end support (moment free).

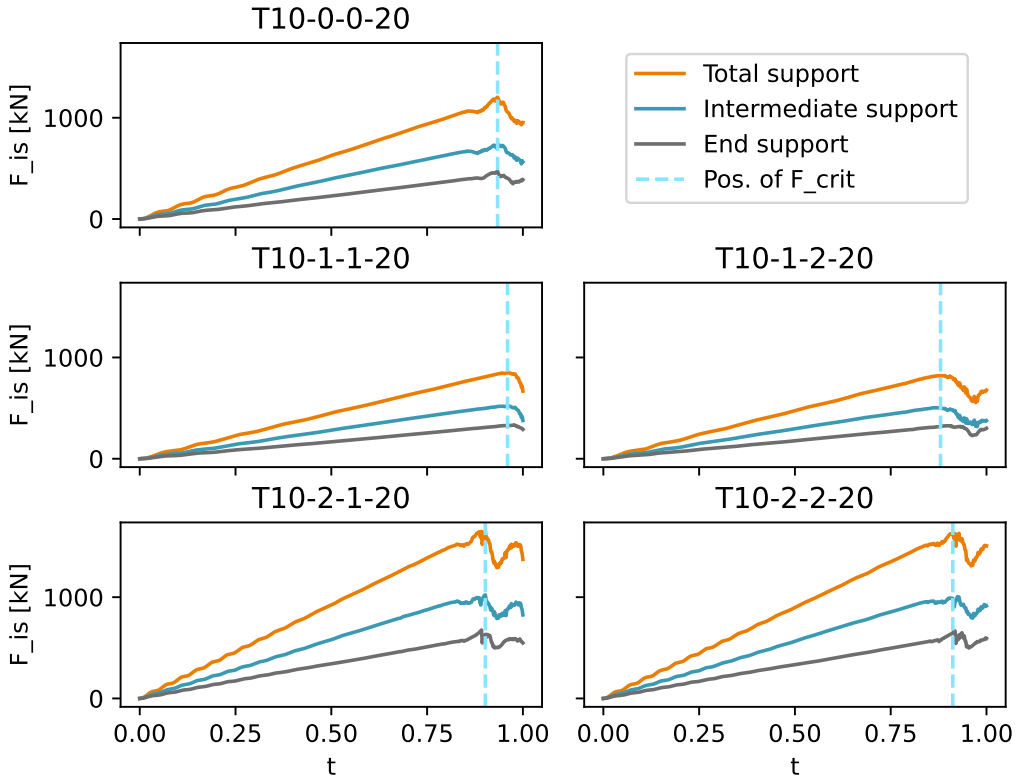

Figure A.4.: Diagrams showing the reaction forces of the 10 [m] beams of the numerical test series

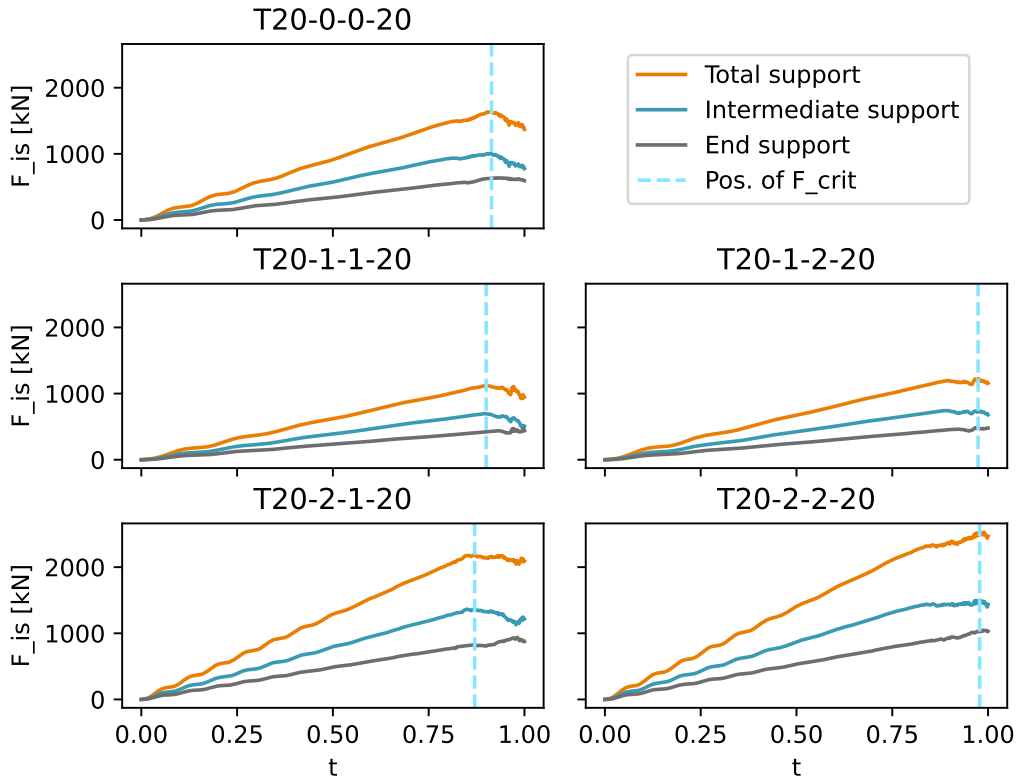

Figure A.5.: Diagrams showing the reaction forces of the 20 [m] beams of the numerical test series

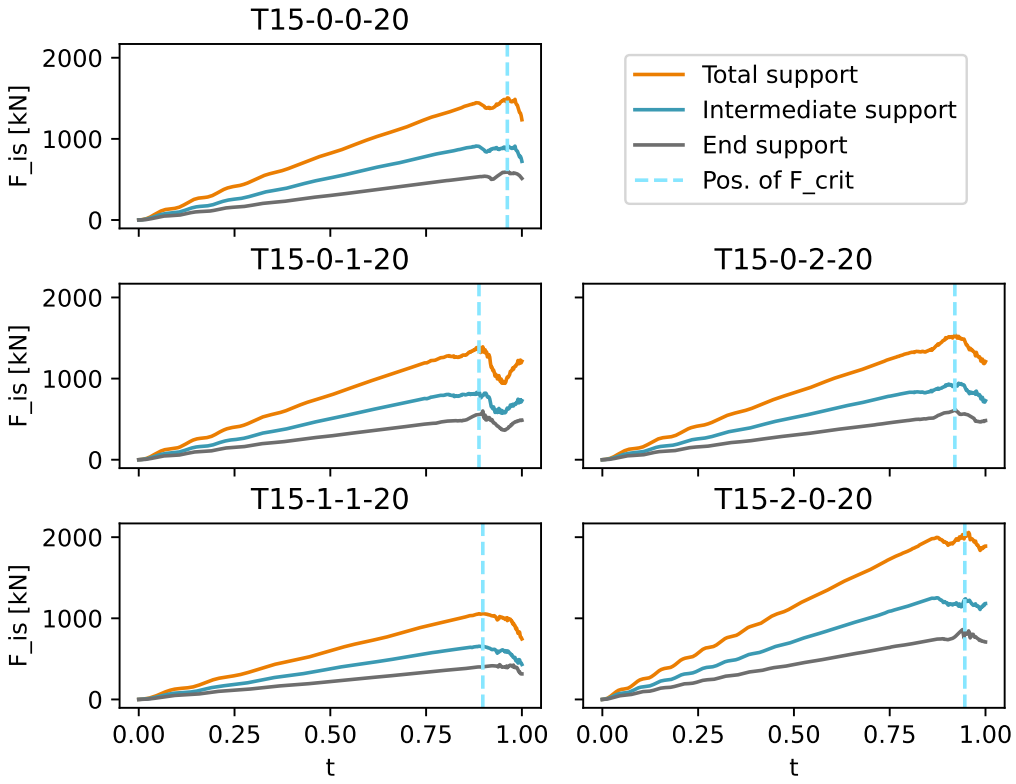

Figure A.6.: Diagrams showing the reaction forces of the 15 [m] beams of the numerical test series

A.4. Visuals

In this section the visual results of the numerical simulations are documented. The four parameters shown are the crack pattern as provided by the tension damage parameter, the main stresses given as the van Mises stresses as well as the normal stress within the transverse reinforcement and the longitudinal reinforcement.

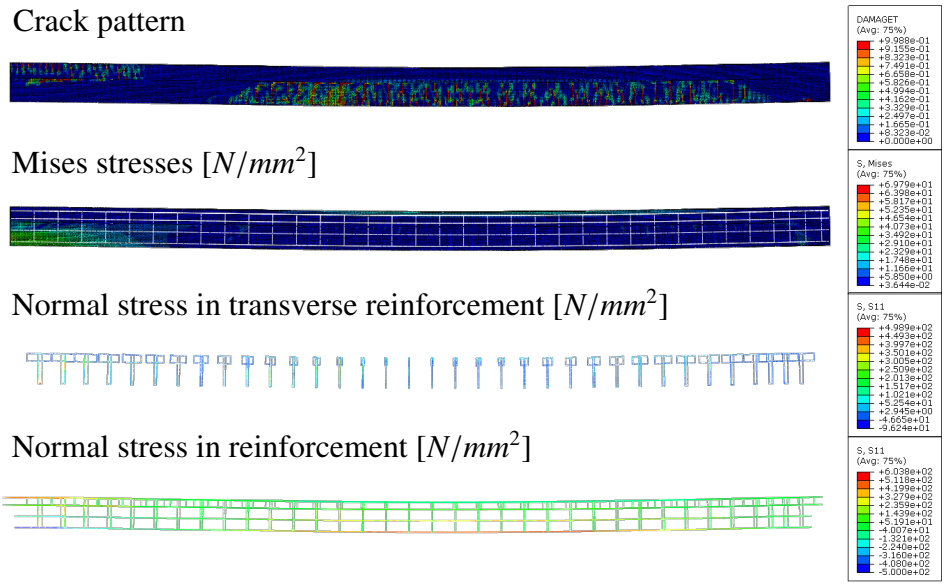

Figure A.7.: Numerical results for T10-1-1 at $F_{crit,tot}$

Crack pattern

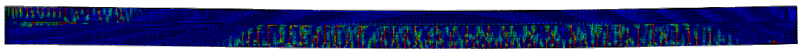

Mises stresses $[N/mm^2]$

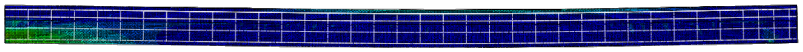

Normal stress in transverse reinforcement $[N/mm^2]$

Normal stress in reinforcement $[N/mm^2]$

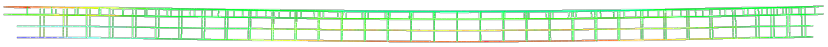

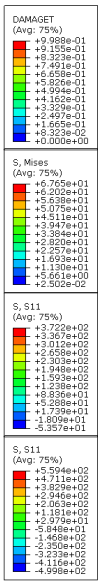

Figure A.8.: Numerical results for T10-1-2 at $F_{crit,tot}$

Crack pattern

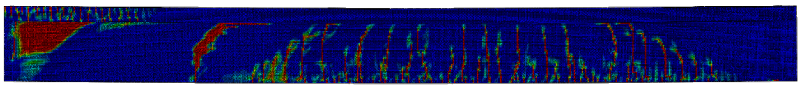

Mises stresses $[N/mm^2]$

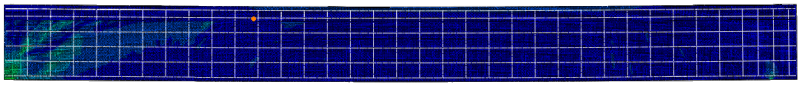

Normal stress in transverse reinforcement $[N/mm^2]$

Normal stress in reinforcement $[N/mm^2]$

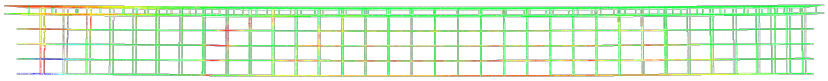

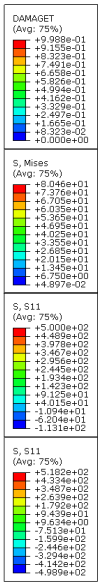

Figure A.9.: Numerical results for T10-2-1 at $F_{crit,tot}$

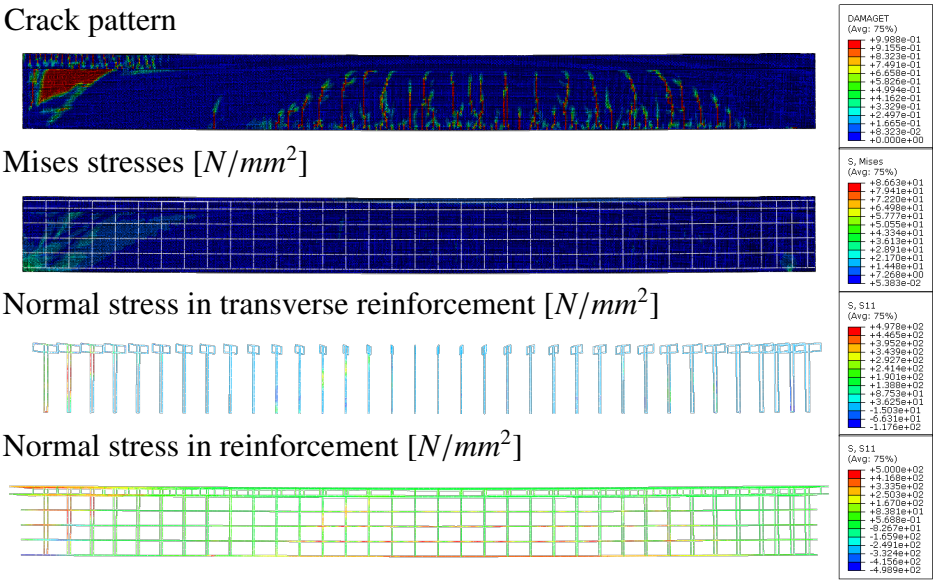

Figure A.10.: Numerical results for T10-2-2 at $F_{crit,tot}$

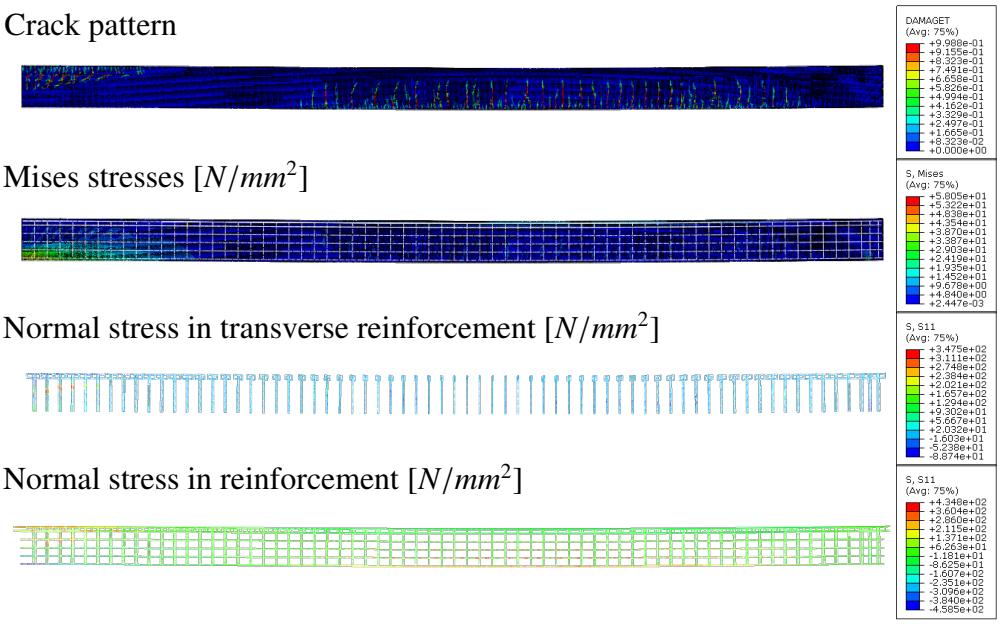

Figure A.11.: Numerical results for T20-1-1 at $F_{crit,tot}$

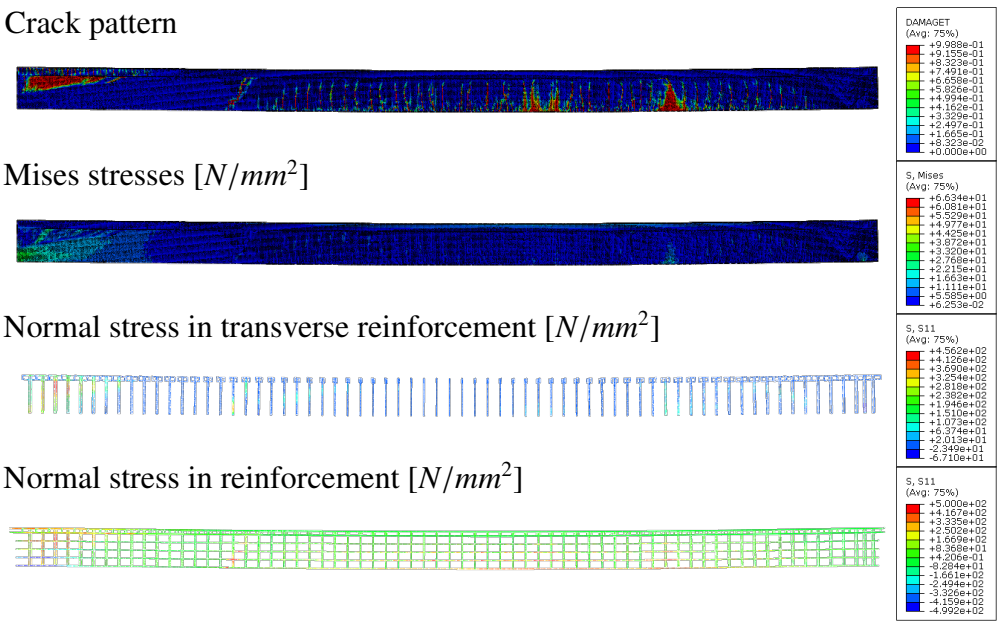

Figure A.12.: Numerical results for T20-1-2 at $F_{crit,tot}$

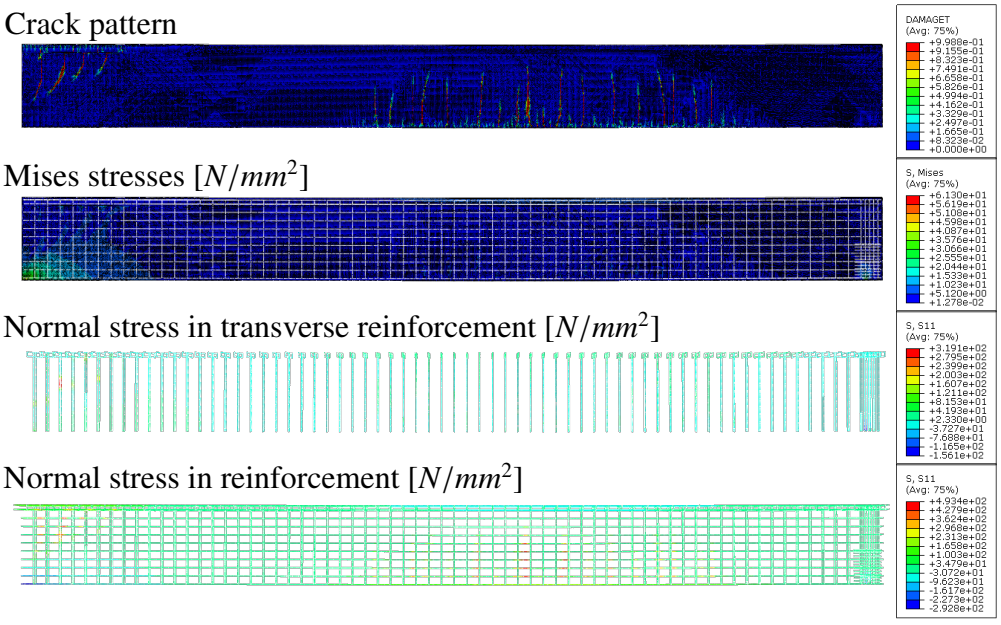

Figure A.13.: Numerical results for T20-2-1 at $F_{crit,tot}$

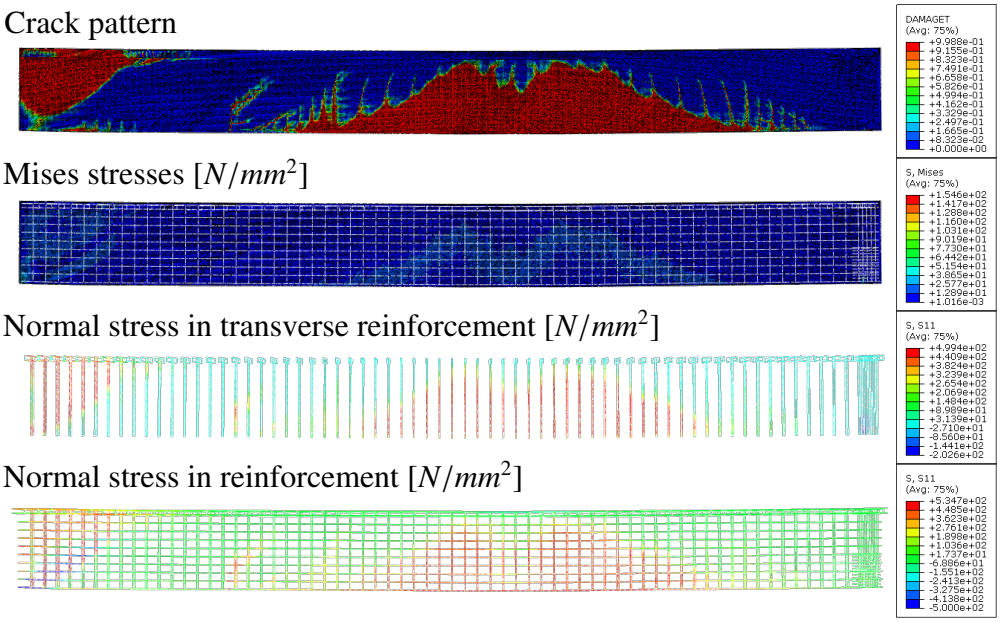

Figure A.14.: Numerical results for T20-2-2 at $F_{crit,tot}$

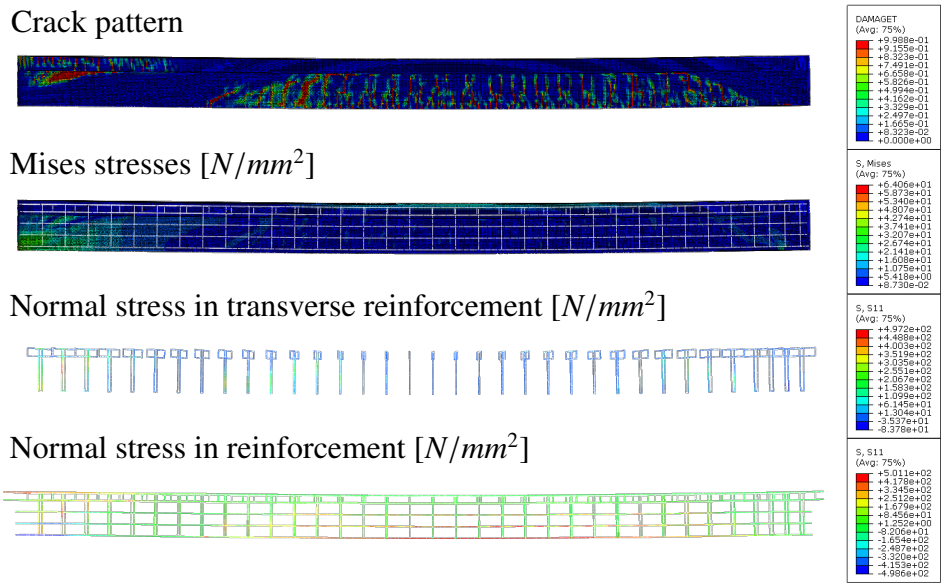

Figure A.15.: Numerical results for T10-0-0 at $F_{crit,tot}$

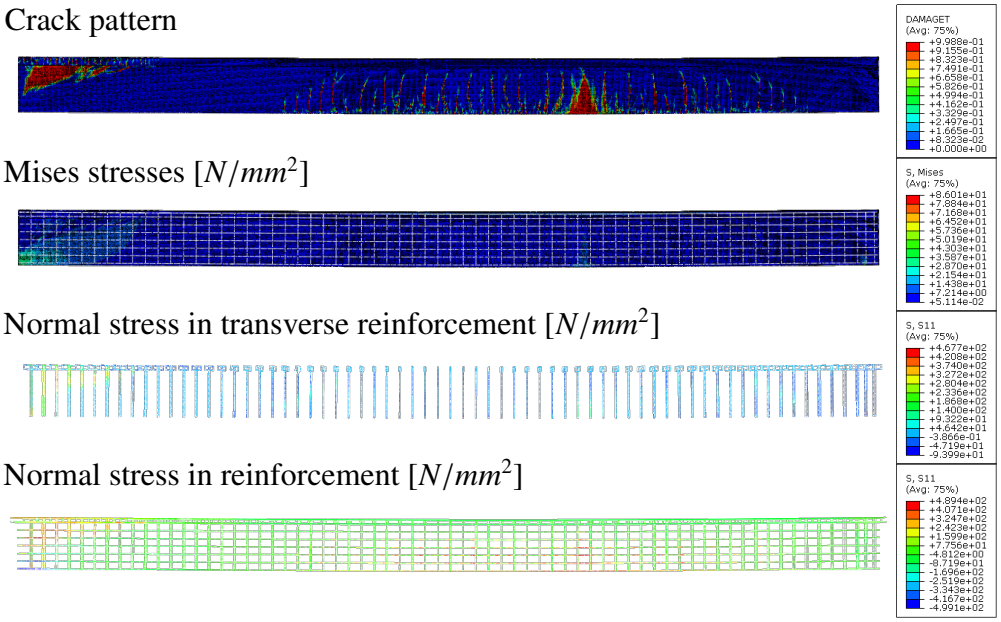

Figure A.16.: Numerical results for T20-0-0 at $F_{crit,tot}$

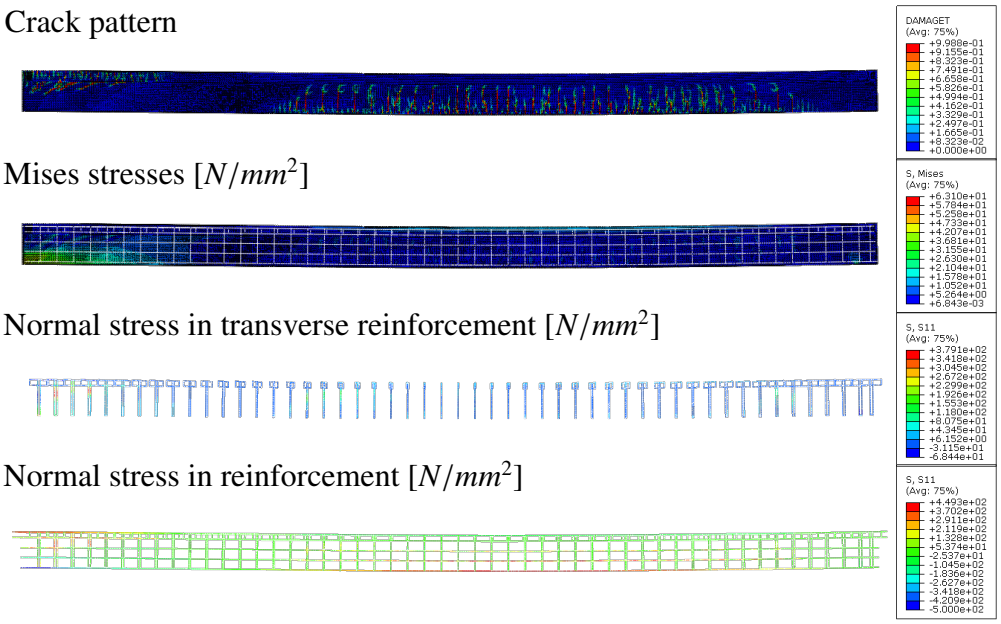

Figure A.17.: Numerical results for T15-1-0 at $F_{crit,tot}$

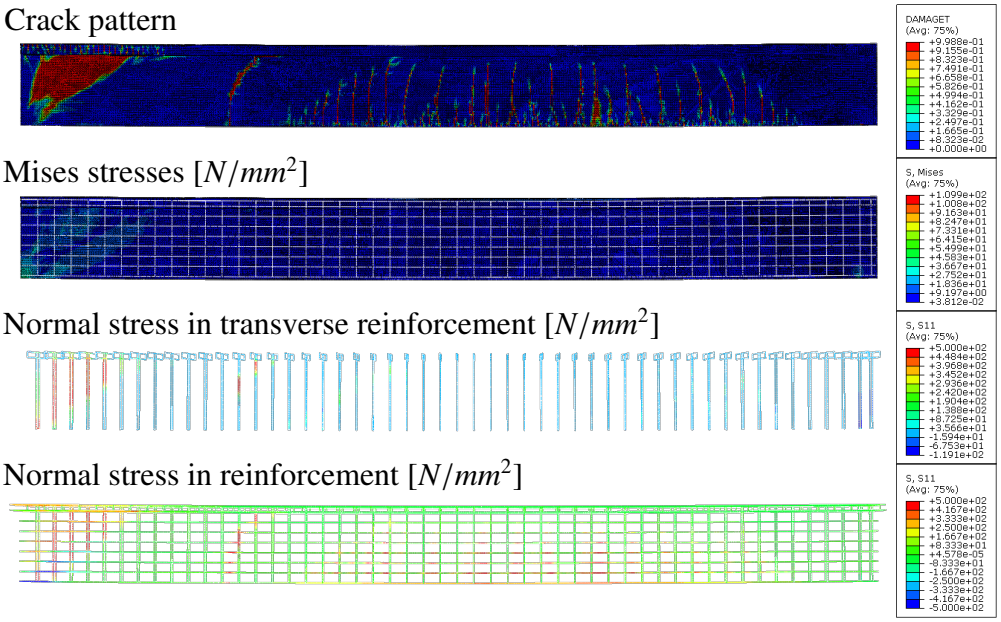

Figure A.18.: Numerical results for T15-2-0 at $F_{crit,tot}$

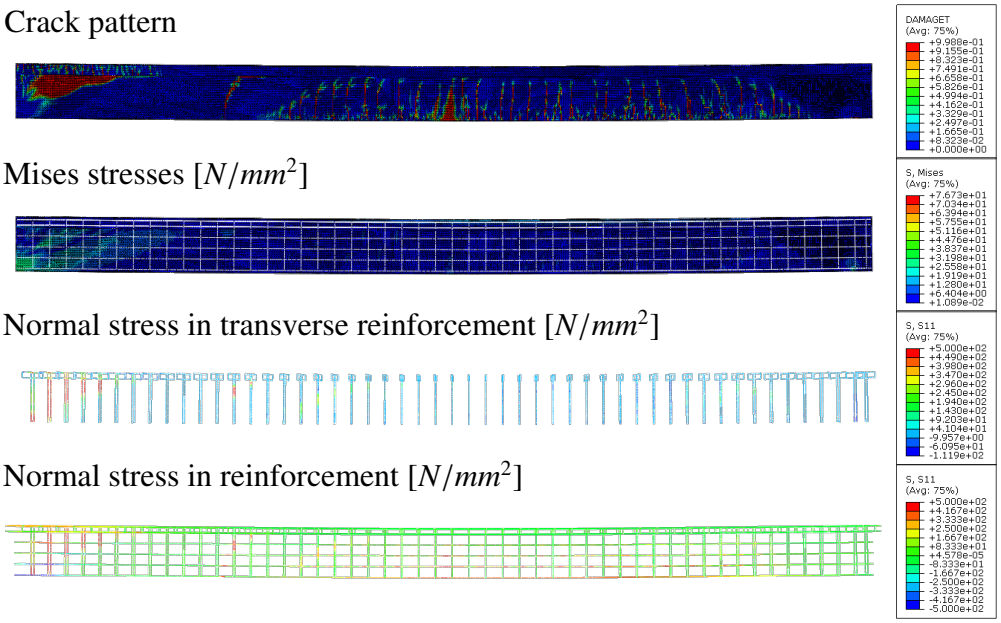

Figure A.19.: Numerical results for T15-0-1 at $F_{crit,tot}$

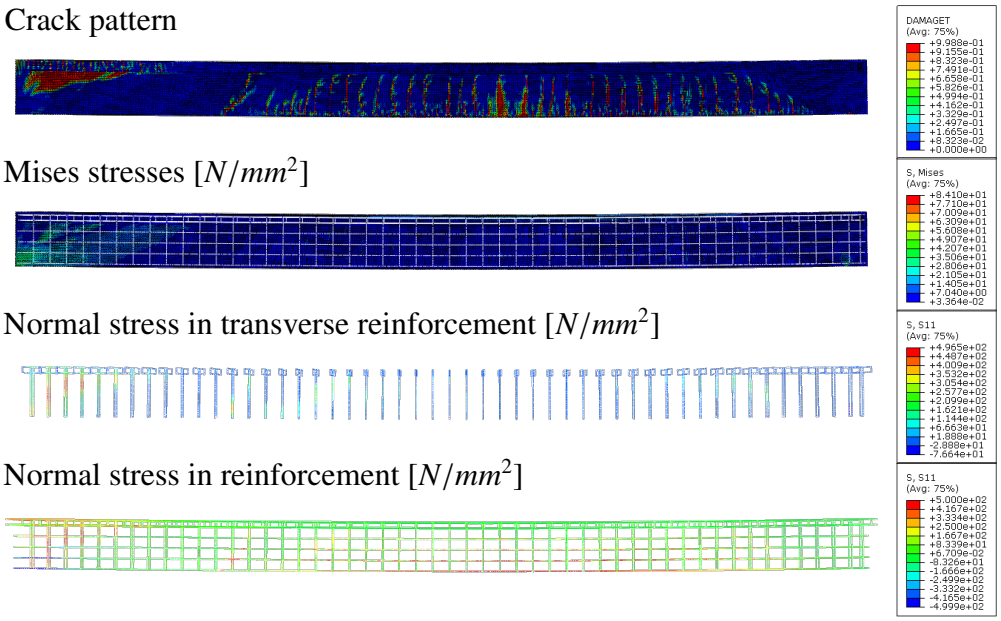

Figure A.20.: Numerical results for T15-0-2 at $F_{crit,tot}$

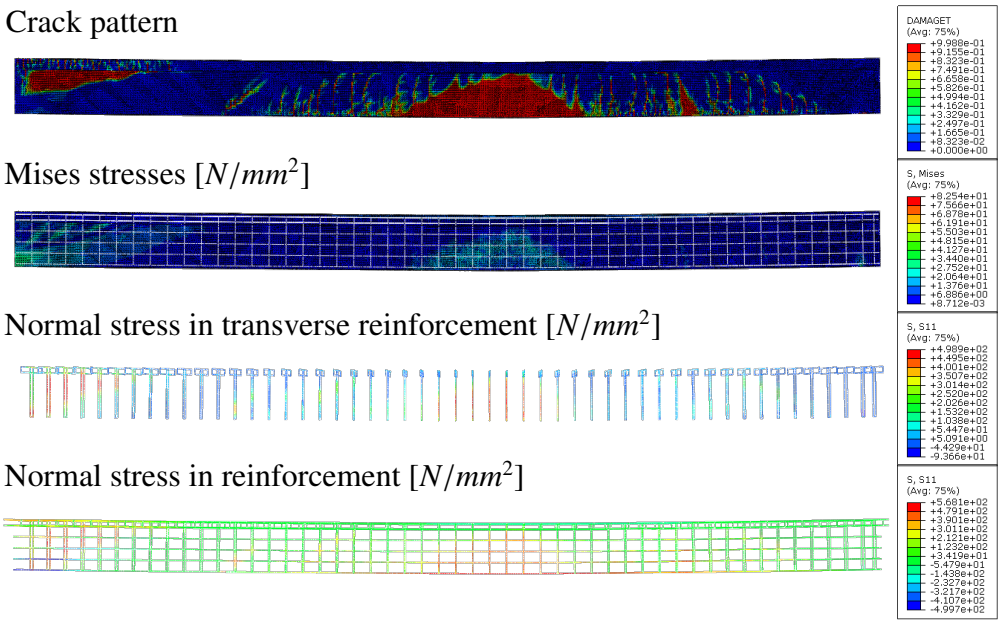

Figure A.21.: Numerical results for T15-0-0 at $F_{crit,tot}$

B. Numerical Test Series Equivalent Cantilever

This appendix provides the set up and results of the cantilever simulations that are equivalent to the numerical test series. They are split up into the following sections:

- B.1 Setup and Dimensions: Test setup as well as specimen dimension of the numerical simulation are provided in figures,
- B.2 Tables: Simulation results are provided in tabulated form,
- B.3 Diagrams: Simulation results are provided in diagrams for the test series,
- B.4 Visuals: Simulation results are provided in visual form.

B.1. Setup and Dimensions

In this section the test setup as well as the specimens cross-sections are provided. They are provided in figure B.1. Material data as well as the dimensions of the reinforcement are provided in section 4.5 table 4.8 for the equivalent one-sided clamped single span beams.

The cantilever tests were only simulated for tests T10-2-1, T10-2-2, T20-2-1 and T20-2-2, since their results proved to coincide with the full scale tests.

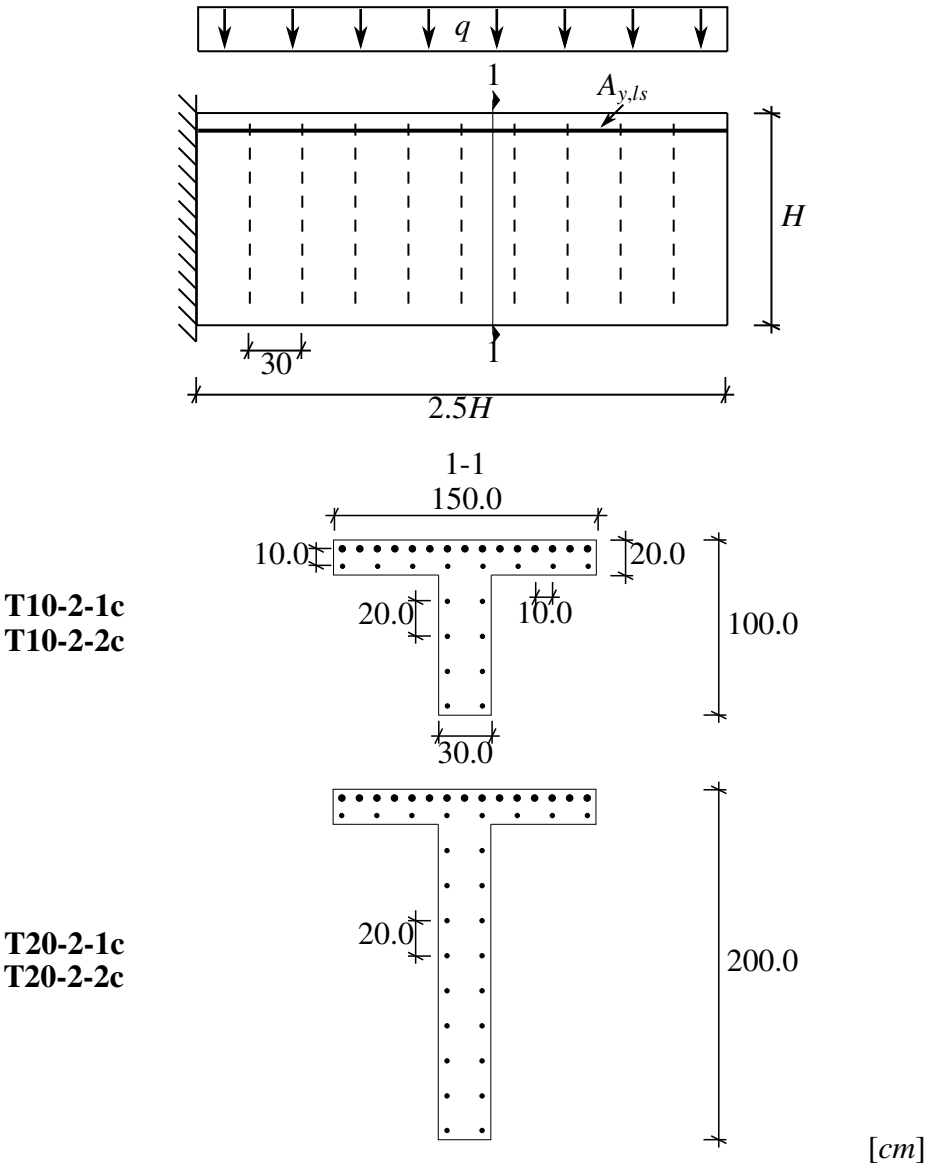

Figure B.1.: Setup of the numerical cantilever tests, equivalent to the one-sided clamped single span girders

B.2. Tables

Table B.1 provides the maximal critical failure loads $F_{crit,sc}$ for the test series equivalent cantilever simulations. These are directly comparable to $F_{crit,sc}$ from table A.1 for the respective tests.

Table B.1.: Maximal values of the cantilever tests at the clamped support $F_{crit,sc}$

Test ID	$F_{crit,sc}$ [kN]
T10-3-1	1067.44
T10-3-2	1106.04
T20-3-1	1607.55
T20-3-2	1623.22

B.3. Diagrams

In this section the load displacement curves of the cantilever simulations provided. For reference on their quality, the same curves for the normal tests on the one-sided clamped single span tests are included. Additional information on the full scale numerical simulations are provided in section 4.5 as well as appendix A.

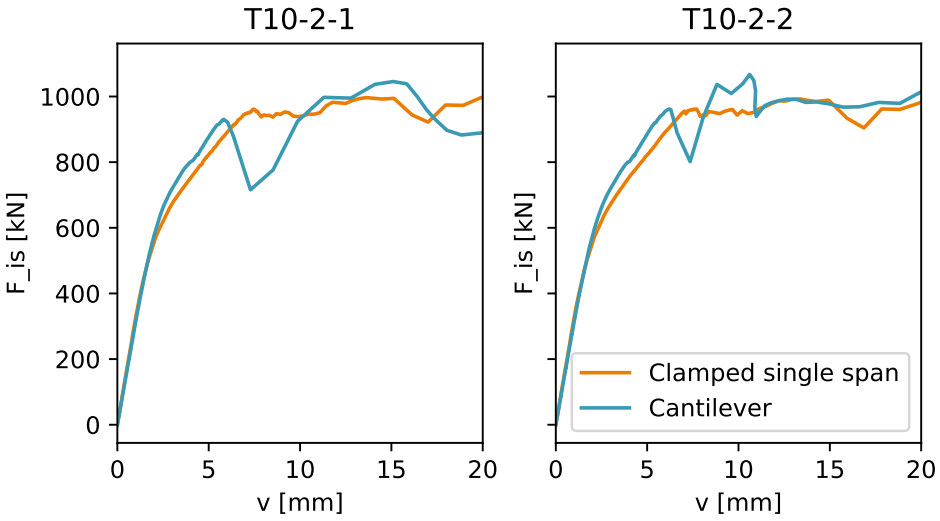

Figure B.2.: Diagrams showing the load displacement curves for T10-2-1c and T10-2-2c in comparison with their full scale counterparts T10-2-1 and T10-2-2

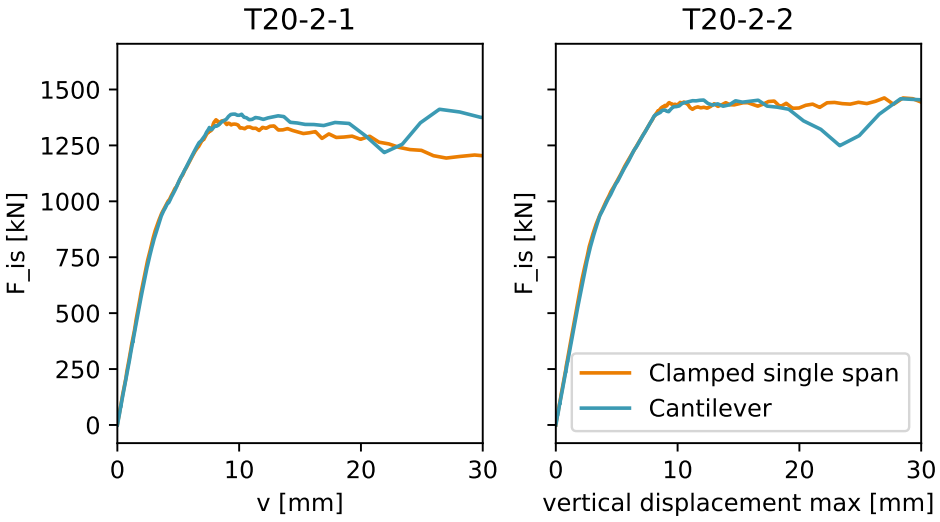

Figure B.3.: Diagrams showing the load displacement curves for T20-2-1c and T20-2-2c in comparison with their full scale counterparts T20-2-1 and T20-2-2

B.4. Visuals

In this section the visual results of the numerical simulations are documented. The four parameters shown are the crack pattern as provided by the tension damage parameter, the main stresses given as the van Mises stresses as well as the normal stress within the transverse reinforcement and the longitudinal reinforcement.

Crack pattern

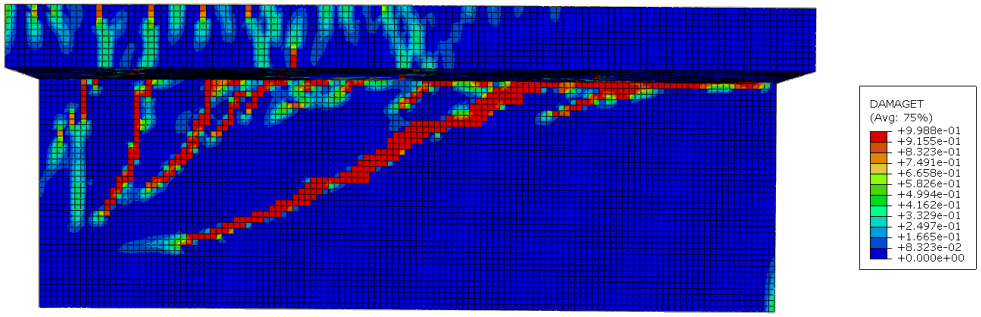

Mises stresses $[N/mm^2]$

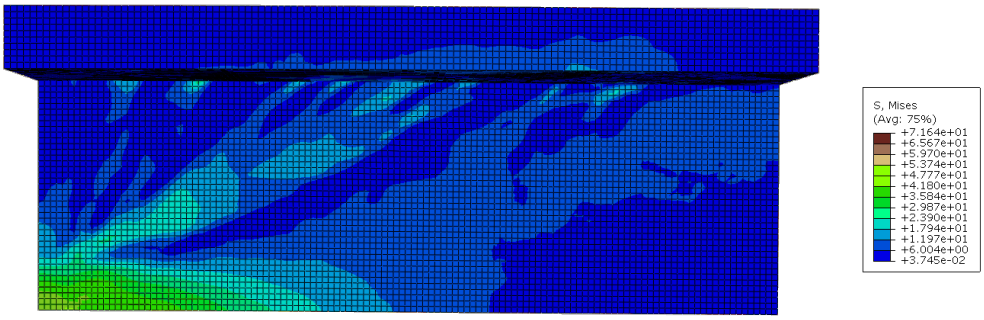

Normal stress in transverse reinforcement $[N/mm^2]$

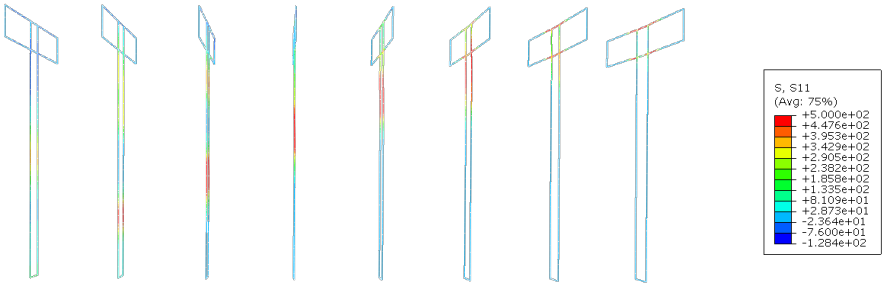

Normal stress in reinforcement $[N/mm^2]$

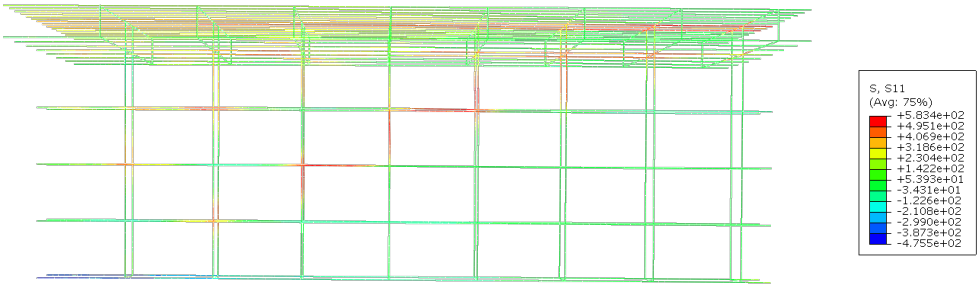

Figure B.4.: Numerical results for T10-3-1 at $F_{crit,tot}$

Crack pattern

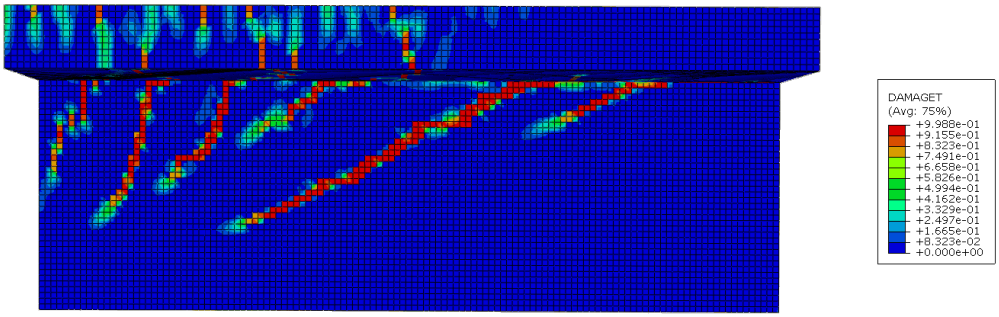

Mises stresses $[N/mm^2]$

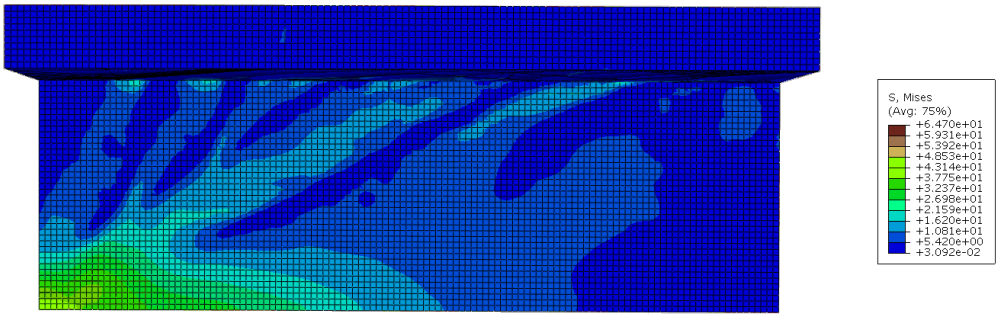

Normal stress in transverse reinforcement $[N/mm^2]$

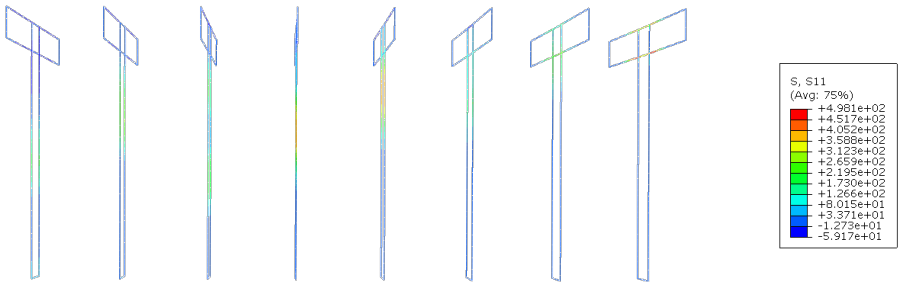

Normal stress in reinforcement $[N/mm^2]$

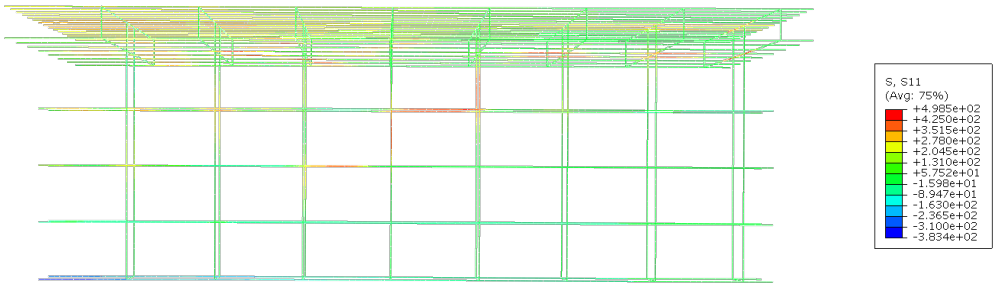

Figure B.5.: Numerical results for T10-3-2 at $F_{crit,tot}$

Crack pattern

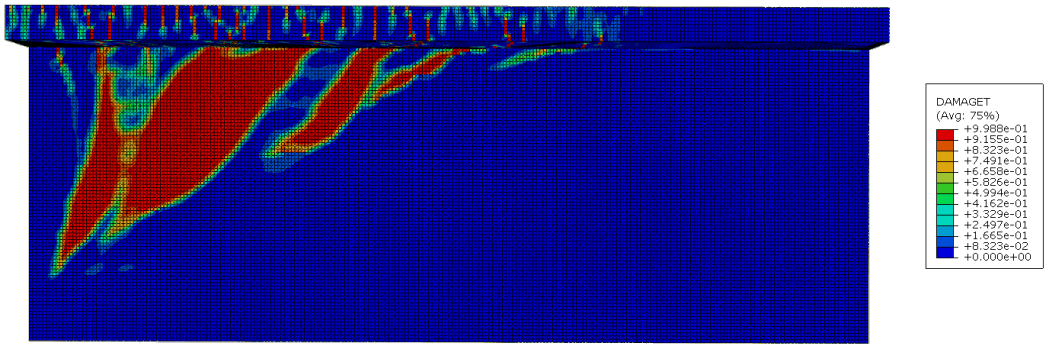

Mises stresses $[N/mm^2]$

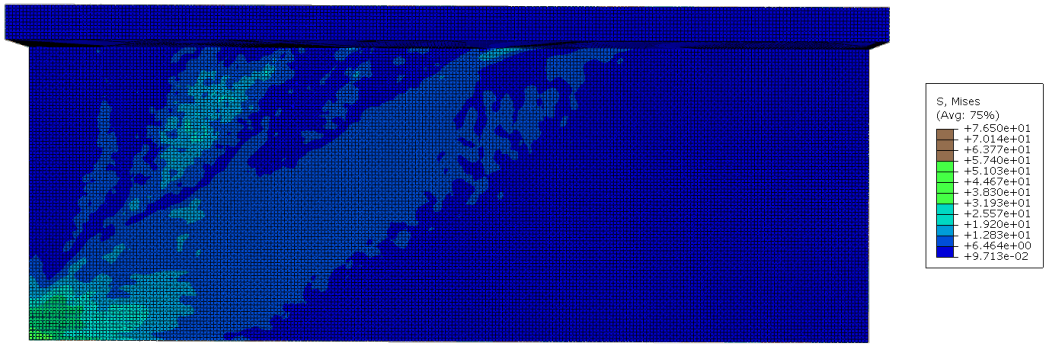

Normal stress in transverse reinforcement $[N/mm^2]$

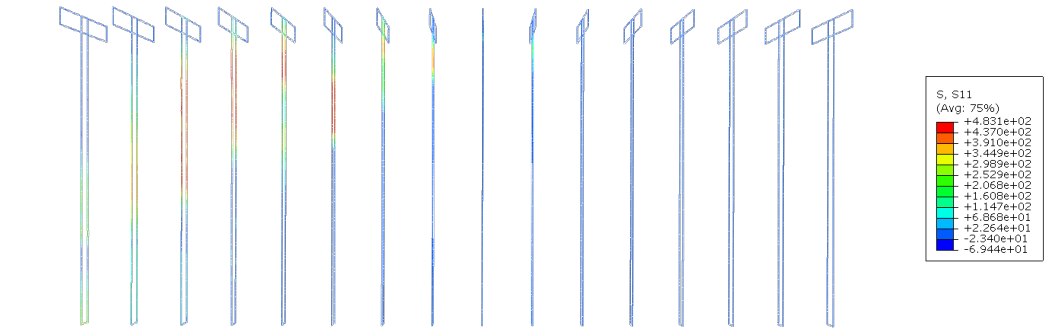

Normal stress in reinforcement $[N/mm^2]$

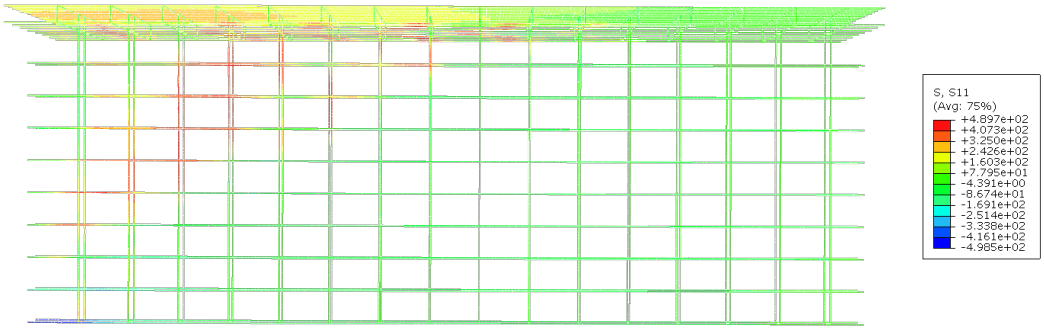

Figure B.6.: Numerical results for T20-3-1 at $F_{crit,tot}$

Crack pattern

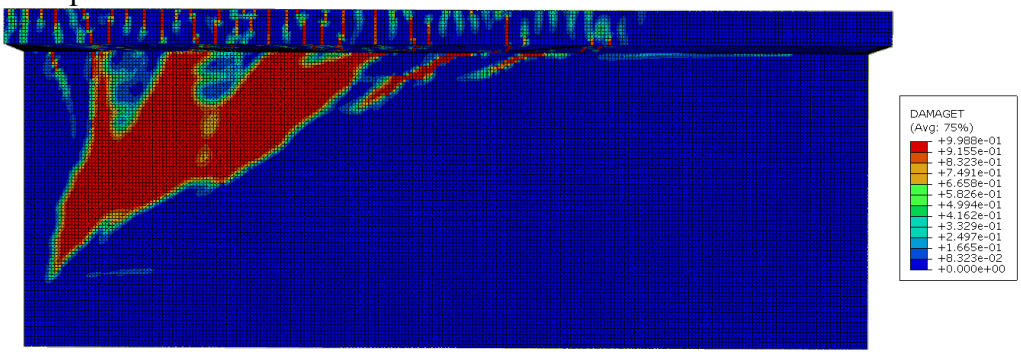

Mises stresses $[N/mm^2]$

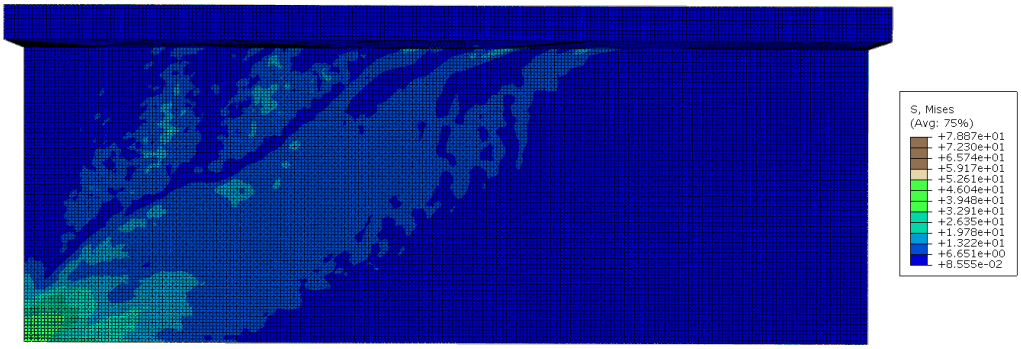

Normal stress in transverse reinforcement $[N/mm^2]$

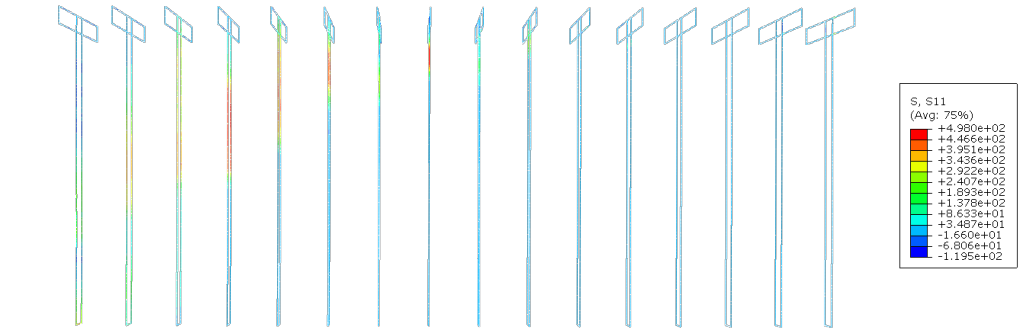

Normal stress in reinforcement $[N/mm^2]$

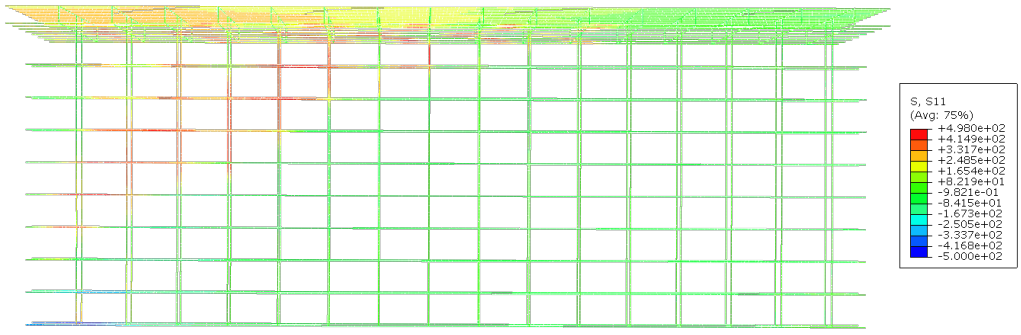

Figure B.7.: Numerical results for T20-3-2 at $F_{crit,tot}$

C. Evaluation of the Numerical Test Series using the Engineering Model

This appendix provides the set up and results of the cantilever simulations that are equivalent to the numerical test series. They are split up into the following sections:

- C.1 Effect Diagrams: Normalised effect diagrams show differences between trends resulting from varying variables,
- C.2 Diagrams: Comparison of the critical failure loads.

C.1. Effect Diagrams

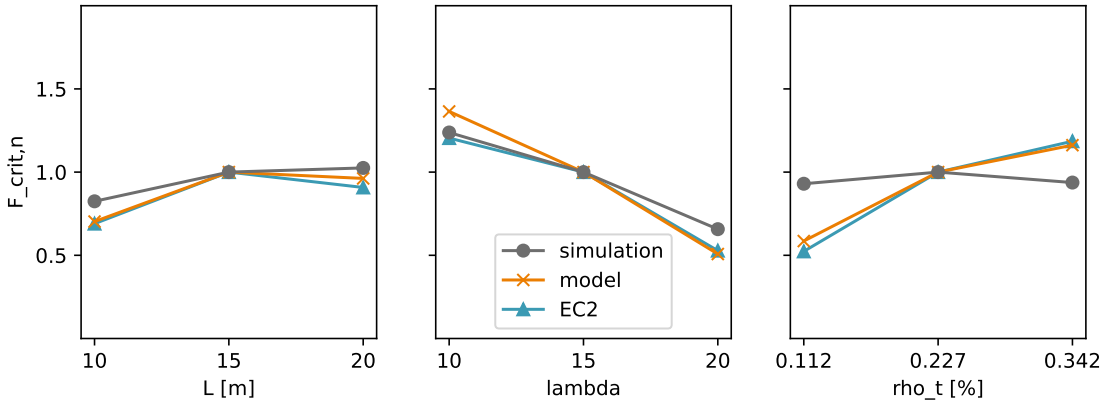

Figure C.1.: Normalised effect diagrams for the variables span length, slenderness and reinforcement ratio for a 30° angle excluding T20-1-2 and T20-2-2

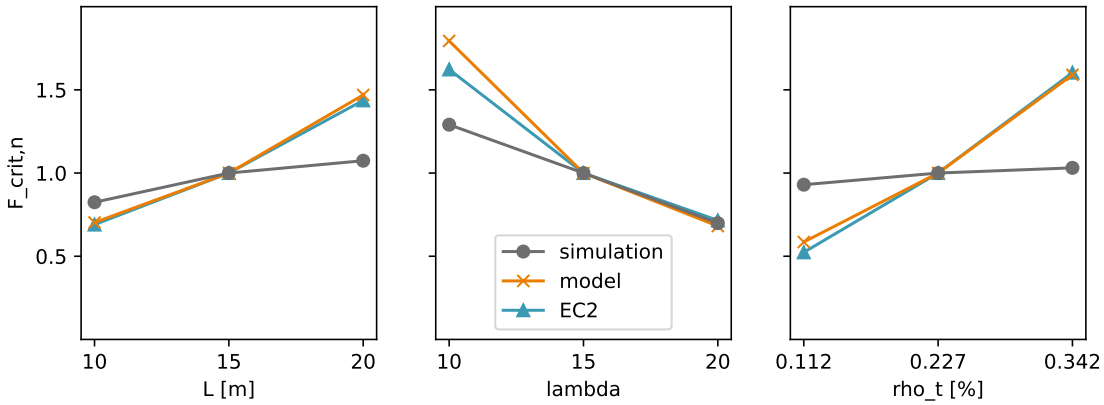

Figure C.2.: Normalised effect diagrams for the variables span length, slenderness and reinforcement ratio for a 30° angle

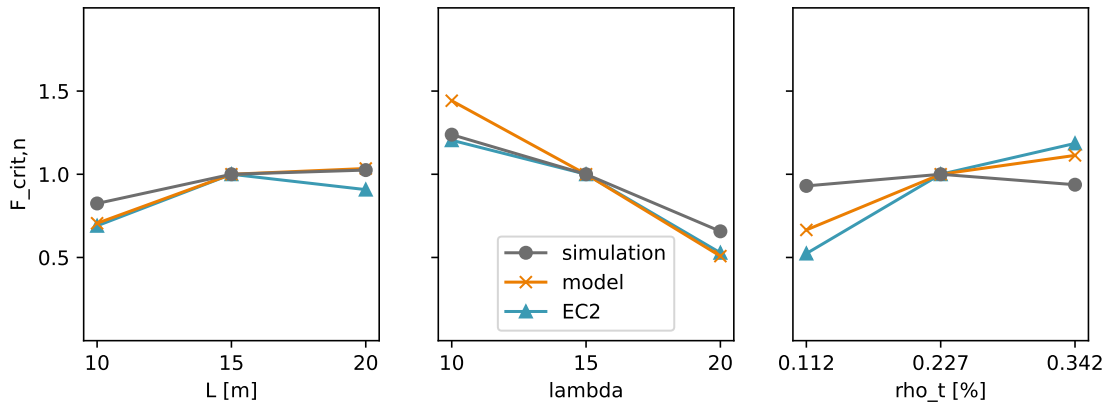

Figure C.3.: Normalised effect diagrams for the variables span length, slenderness and reinforcement ratio for a 45° angle excluding T20-1-2 and T20-2-2

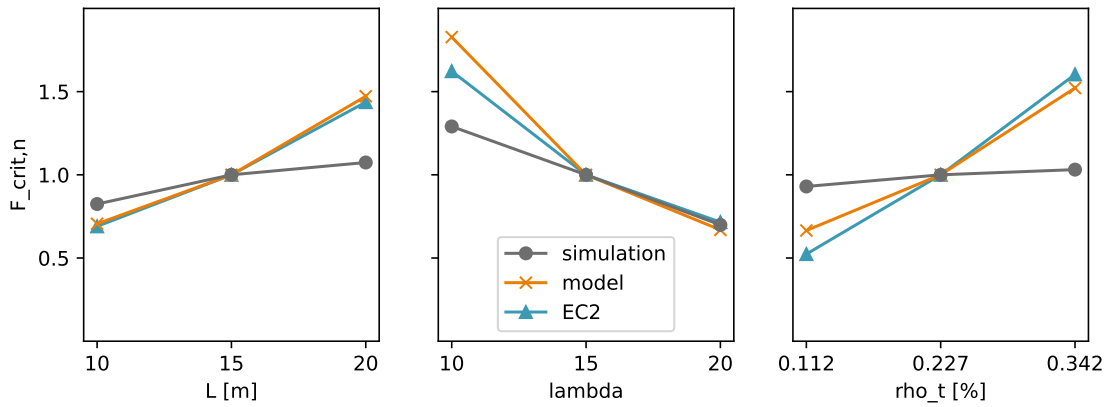

Figure C.4.: Normalised effect diagrams for the variables span length, slenderness and reinforcement ratio for a 45° angle

C.2. Diagrams

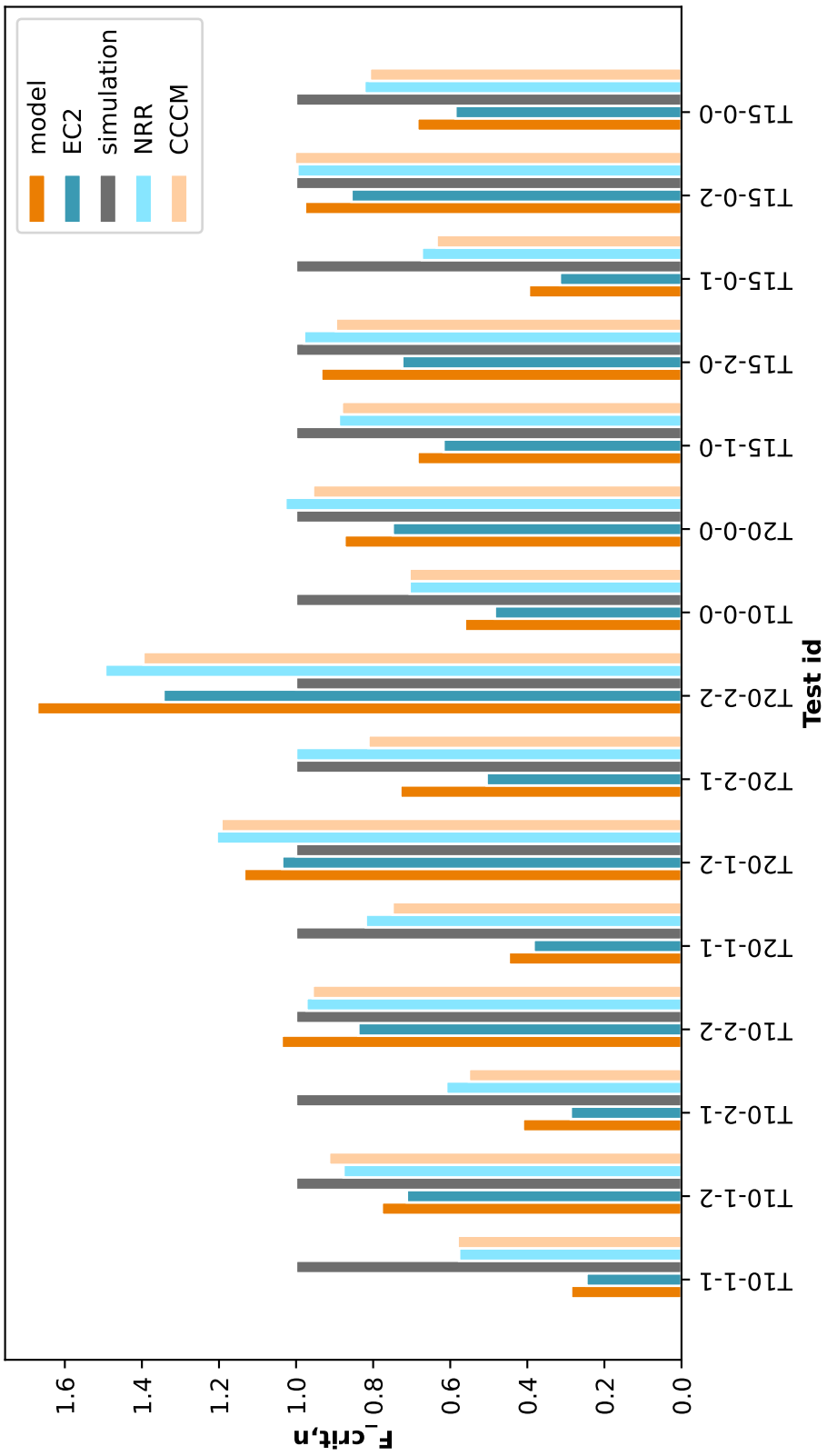

Figure C.5.: Standardised failure loads of the test series for a 30° angle

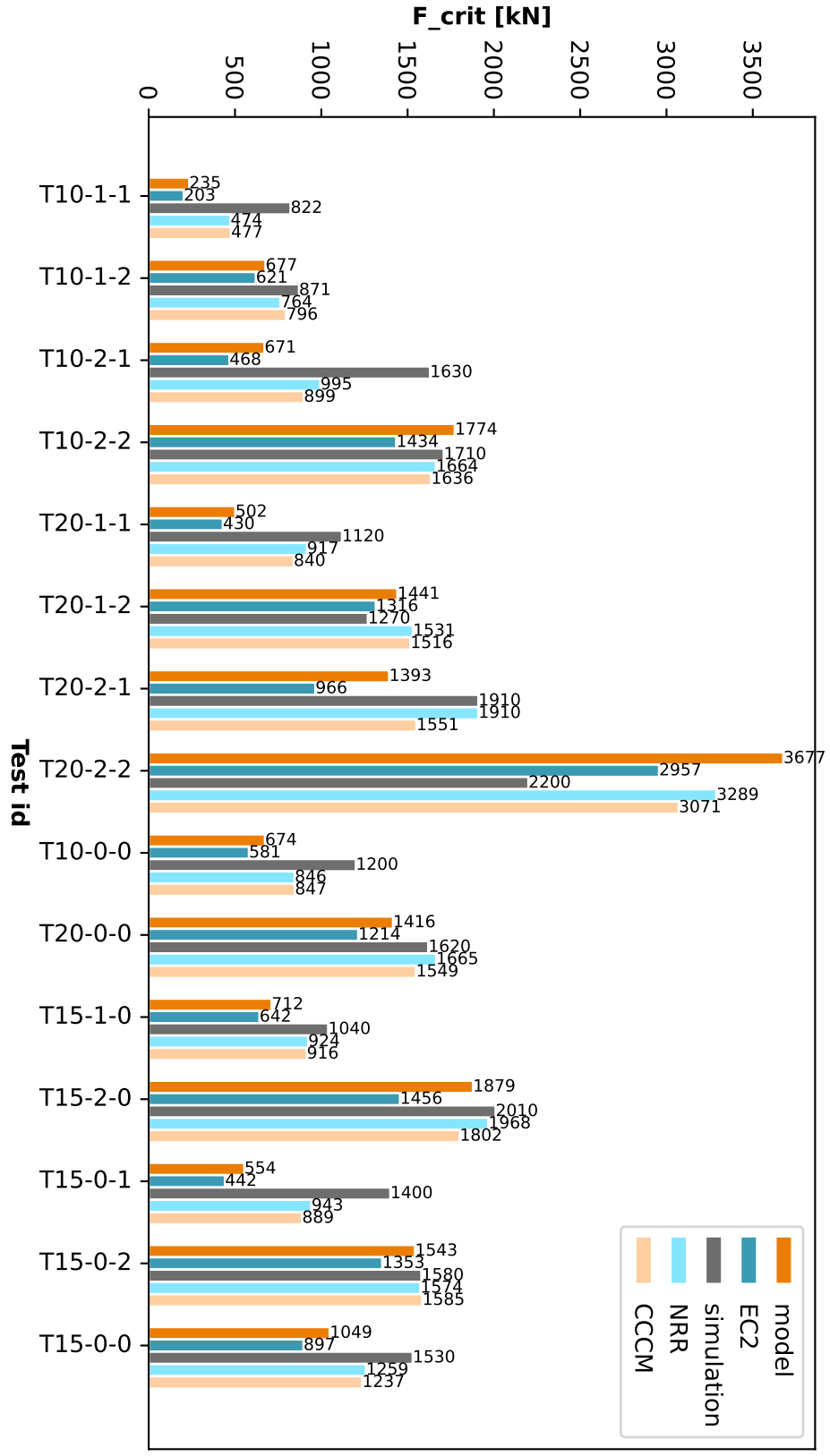

Figure C.6.: Failure loads of the test series for a 30° angle

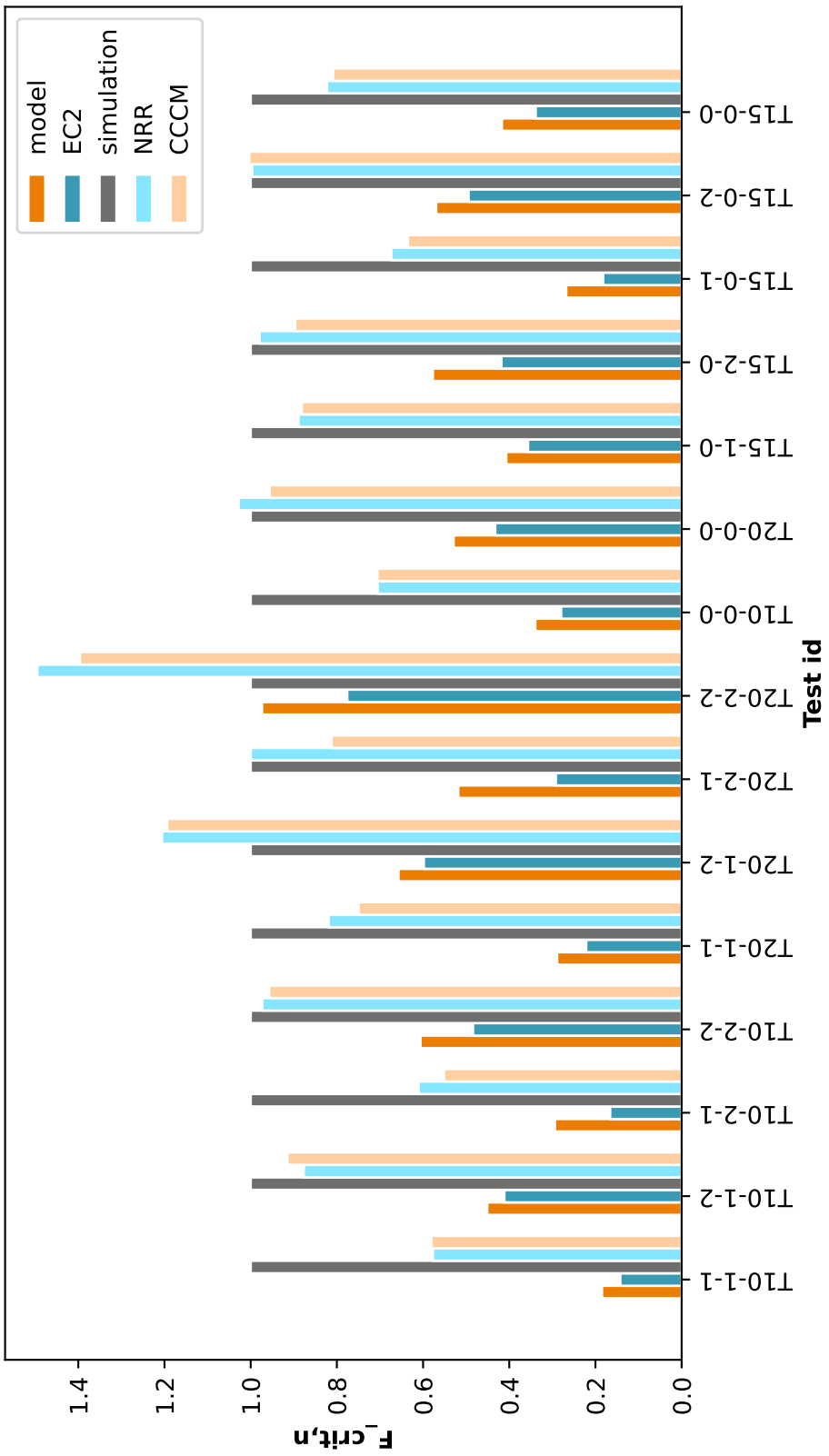

Figure C.7.: Standardised failure loads of the test series for a 45° angle

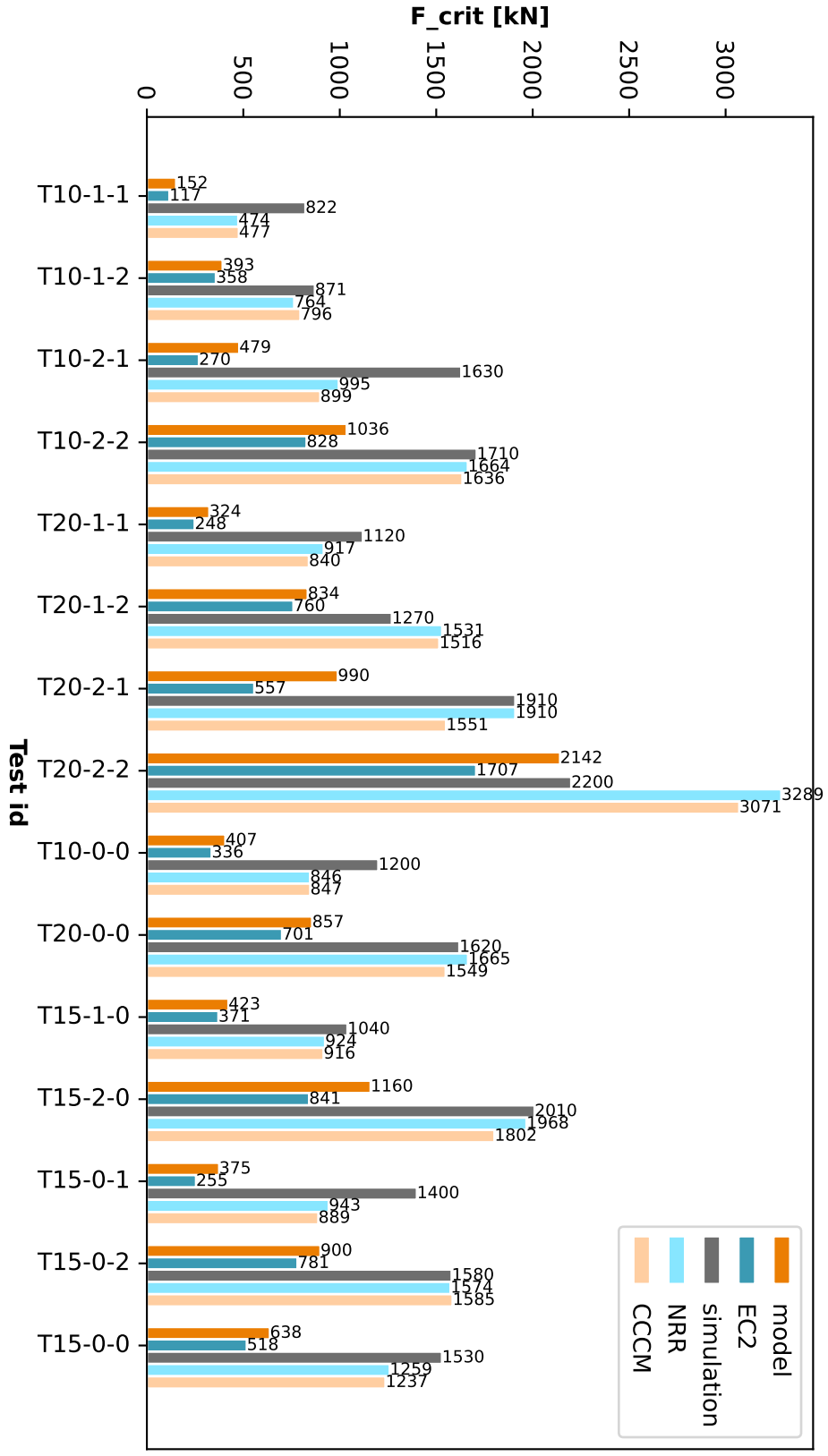

Figure C.8.: Failure loads of the test series for a 45° angle